THE UNIVERSITY *of* EDINBURGH

Identification and quantification of noise sources in marine towed active electromagnetic data

Axel Laurel Tcheheumeni Djanni

Thesis presented for the degree

Doctor of Philosophy

THE UNIVERSITY
of EDINBURGH

School of GeoSciences

2016

Identification and quantification of noise sources in marine towed active electromagnetic data

Ph.D. Thesis
01/05/2012–06/06/2016

Submission 30/06/2016
Viva Voice 08/11/2016
Final Version 01/05/2017

The University of Edinburgh
School of GeoSciences

Axel Laurel Tcheheumeni Djanni
tcheheumeni@gmail.com

B.Sc. Earth Sciences 2008
The University of Douala

M.Sc. Geophysics Exploration 2011
Université de Pau et des Pays de l'Addour

Supervisors

Prof. Anton Ziolkowski
Royal Academy of Engineering
Research Professor of Petroleum Geoscience

Dr. David Wright
Research Fellow

Abstract

The towed streamer controlled source electromagnetic (CSEM) system collects data faster than the conventional static node-based CSEM system. However, the towed streamer CSEM is typically much noisier than the conventional static node-based CSEM. Identifying and quantifying various sources of noise is important for the development of future robust electromagnetic streamer system. This is the problem I address in this thesis. I achieve this in three parts.

First, I examine the idea that the towed streamer suffers from noise induced by its motion through the Earth's magnetic field according to Faraday's law of induction. I derive expressions for the motionally-induced noise for the cases of a horizontal streamer parallel to the acquisition vessel's path and a curved streamer caused by a constant cross-current. These expressions demonstrate that the motionally-induced noise is sensitive to the magnitude of the feather angle at the head and at the tail of the streamer, and to the vertical and lateral motion of the streamer. The key finding is that no motionally-induced noise is generated when the streamer is horizontal and moving in a constant magnetic field. By contrast, when the streamer shape is curved because of cross-currents, motionally-induced noise is generated if the velocity of the streamer varies over time.

Second, I analyse and compare the noise recorded using the first generation of towed streamer with the noise recorded using a static ocean bottom cable (OBC) CSEM. I find out that within the frequency range of interest, 0.01–1 Hz the towed streamer noise is 20 dB greater (factor of 10) than the noise recorded with the OBC CSEM. I show also that the motion of the telluric cable between the pair of electrodes in the towed streamer is responsible for this difference in amplitude between the two systems. In the frequency ranges, 0.03–0.1 Hz and 0.03–0.2 Hz, the motionally-induced noise is shown to be uncorrelated across all channels. However, within the frequency band 0.1–0.3 Hz, the motionally-induced noise correlation gradually increases and becomes well correlated at about 0.2 Hz. This correlated noise could be caused by ocean swell from surface waves, water flowing around the streamer or cross-currents.

Finally, to identify and quantify the contribution of several distinct sources of noise, and to describe the mechanisms generating each source of noise, I co-designed a prototype towed streamer CSEM. I carried out an experiment with the prototype streamer suspended 1 m below the water surface in the controlled environment of the Edinburgh wave tank located in King's building campus (the University of Edinburgh). I then subjected the streamer to flow running at velocities of 0–1 $\mathrm{m\,s^{-1}}$ along its length and to waves propagating in the same direction, at 45°, and perpendicular relative to the streamer direction.

From the data obtained in the tank, I identify, quantify and characterise two separate sources of noise: the motionally-induced electric field noise due to flow rates (referred to as flow noise) and the motionally-induced electric field noise due to wave motion (referred to as wave motion noise). I show that the motion of the streamer in response to an increase of flow rate increases the noise level. However, most of the flow noise occurred from 0 $\mathrm{m\,s^{-1}}$ to 0.5 $\mathrm{m\,s^{-1}}$. Above 0.5 $\mathrm{m\,s^{-1}}$, the increase of flow noise is modest. The initial large flow noise difference observed when the flow increases from 0 $\mathrm{m\,s^{-1}}$ to 0.5 $\mathrm{m\,s^{-1}}$ is caused by local hydrodynamic effects due to flow over the electrode surfaces. The wave motion noise is 12 dB (about a factor of 4) above the flow noise at the wave frequency of 0.29 Hz. I show that this wave motion noise is due to the motion of the telluric cable connecting two electrodes in response to wave motion. In addition, I calculate the motionally-induced electric field noise based on the cable's displacement data and compare the result with the measured electric field noise. The key findings are that the calculated motionally-induced electric field noise is correlated with the measured electric field noise. I also observe that the measured electric field noise is greater than the estimated wave motion noise by a factor of about 3. This discrepancy is likely caused by additional noise in the telluric cable between the electrodes and the amplifier.

The results of my investigations contribute to the understanding of the relation between the motion of the streamer when towed in the sea and the electric field noise recorded. The main source of noise in the towed streamer CSEM system is the motion of the telluric cable connecting two electrodes) through the Earth's magnetic field. From these results, I conclude that the effects of wave motion could be reduced in three ways: use of rigid telluric cables between a pair of electrodes, tow the streamer deeper, and increase the cable and the telluric cable tension.

Lay Summary

Controlled source electromagnetic (CSEM) is a method used for the exploration of oil and gas reservoirs in marine environment and also to offset the cost associated with drilling dry wells. CSEM relies on the difference in electrical resistivity between oil and the water-bearing sediments. Resistivity information is the primary oil and gas indicator since the 1920s. In fact, a sediment saturated with oil displays higher resistivity than the water-bearing sediment.

Conventionally, in marine CSEM, the receivers (also called nodes) are deployed on the seafloor at 1 to 3 kilometers apart at the start of the survey and log autonomously. After, a high-powered source of electromagnetic energy is towed over these receivers at about 30 m above the seafloor to ensure good coupling of the signals with the earth. The receivers detect and record the refracted energy from the subsurface layers. At the end of the survey, the receivers are recovered to deck and the data downloaded for processing and interpretation. By studying the collected data, the resistivity of the seafloor can be determined. However, this method is expensive and time-consuming.

A towed system where about the high-powered source and receiver (placed in a cable called streamer) are towed simultaneously at depths 10–100 m below the sea surface enables faster and more efficient data acquisition compared to the conventional node-based system. However, the noise level in the towed streamer is significant compared with the noise level in the node-based system. Identifying and quantifying various sources of noise is important for the development of future robust electromagnetic streamer cables. This is the problem I address in this thesis.

I examine noise data collected using the first generation of the towed streamer CSEM in the sea and the noise data collected with a prototype streamer CSEM in a wave tank. From the data collected in the sea, I show that the towed streamer noise level is a factor 10 greater than the conventional node-based system. From the data collected in the controlled environment of the wave tank, I investigated the effect of increasing water current and wave motion around the prototype streamer. The main finding is that the motion of the telluric cable connecting two electrodes (to form a receiver) is the major mechanism responsible for the generation of the noise level. I also demonstrate that the major source of noise is from wave motion perpendicular to the streamer direction. The noise caused by wave motion is about 4 times greater than the noise due to cross-currents.

From the above results, I conclude that the effects of wave motion on the streamer could be reduced in three ways: use of rigid telluric cables between the receivers, tow the streamer deeper, and increase the cable and the telluric cable tension.

Declaration

I declare that this thesis has been composed solely by myself and that it has not been submitted, either in whole or in part, in any previous application for a degree or professional qualification. Except where otherwise acknowledge, the work presented is entirely my own.

Parts of this work have been published in Djanni et al. (2016), Djanni et al. (2015), Djanni et al. (2014), Tcheheumeni et al. (2013), Wright et al. (2016), and Wright et al. (2015).

Axel Laurel Tcheheumeni Djanni
May 2016

8

Acknowledgements

I would like to take this opportunity to express my gratitude towards my supervisors: Prof. Anton Ziolkowski and Dr. David Wright. My time spent as one of their students has helped me to sharpen my geophysics knowledge and to improve my scientific writing skills. Thanks so much for your encouragements and endless advice over the years.

I also wish to thank Petroleum Geo-Services (PGS) for funding my research.

Thanks to Dr. Jack King and Dr. Dieter Werthmüller for contributing to my understanding of Latex. This thesis is writing based on a modified version of Dieter's template.

I wish also to thank Carlos Alberto Da Costa Filho for very interesting discussions that contribute to my understanding of the programming language Matlab. Thanks also for your Latex and Inkscape tips.

Each chapter of this thesis was reviewed by a number of people who pointed out corrections or suggested clarifications. These people include Amelia Bain, Dr. Andrew Frazer-Harris, Dr. Andy Bell, Carlos Alberto Da Costa Filho, Dr. Dieter Werthmüller, Ellen Mears, Elisabeth Salter, Dr. Erica Galetti, Matthew Holloway, Dr. Mark Chapman, and Philli Cilli of the School of Geosciences; Matthew Day of Wood Mackenzie; Rachel May of the Homeless World Cup.

I wish to thank my flat mates, Nicola Rigonat, Dr. Rami Eid, and Elisabeth Salter for creating a fun and entertaining environment.

Outside the campus, I actively participate in many activities that contribute to release the stress of working in front of a computer. I would like to thank friends of the University African Dance Society, the Australian Football League Edinburgh team ("The Bloods"), and the Volleyball club.

I am incredibly grateful for the encouragement and support of my family members at the early stage of my program and at the writing stage. My family member includes: Stella (mum), Bibiane (2nd mum), Michel (dad), Patrice (twin brother), Pamela, Hermann, Steve, Japhet, and Romario. Your financial supports help me to focus on my work.

The understanding and forbearance of Pamela Nathalie Nkoue Ngako is gratefully acknowledged. The time and effort spent these last years have been reflected on being away from my 1 year and 4 months old baby Imani Clemence Stella Djanni. I thank you for the joy you are bringing in my life and I hope you will understand why daddy has been away for a very long time. I love so much! Papaaa, as you call me, miss you so much.

Contents

List of Figures

List of Tables

•

Conventions and Notations

SI and Derived Units

A measurement of any physical quantity requires a unit. This unit is shown commonly in it abbreviated form. This section associates quantities to the units used in this thesis. It follows the International System of Units (SI) base (metre, second, and ampere) and derived units, except for angles.

Quantity	**Unit**		**Abbreviations**
Length	metre		m
Time	second		s
Electric current	ampere		A
Electric potential	volt		V
Frequency	hertz		Hz
Magnetic flux	weber	$\mathrm{Wb} = \mathrm{V\,s}$	Wb
Angle	degree		°
Electric charge	coulomb	$\mathrm{C} = \mathrm{A\,s}$	C
Electrical capacitance	farad		F
Electrical inductance	henry		H
Electrical conductance	siemens		S
Magnetic field strength	tesla	$\mathrm{T} = \mathrm{V\,s\,m^{-2}}$	T

Notations

The symbols listed here are used consistently throughout the whole thesis. I list only the most common subscripts. All symbols are presented in alphabetical order and have a unique name. Some are chosen following SI guidelines, and the others are derived notations.

In this thesis, vectors are designated by letters in bold, e.g. $\mathbf{E}$. The magnitude of the vector is designated by the same letter in italics, e.g. E.

Symbol	Description	Unit
θ	Feather **angle**	$^\circ$
α	Streamer incidence **angle**	$^\circ$
x^*	**Complex conjugate** of x	
$x * y$	The **Convolution** of x and y	
$\mathbf{J}$	**Current conductivity density**	$\mathrm{A\,m^{-2}}$
$\mathcal{G}$	**Earth impulse response**	
$\mathbf{E}$	**Electric field intensity**	$\mathrm{V\,m^{-1}}$
$\mathbf{D}$	**Electric displacement**	$\mathrm{C\,m^{-2}}$
E_n	Total **electric field noise**	$\mathrm{V\,m^{-1}}$
E_i	Magnetetolluric **electric field noise**	$\mathrm{V\,m^{-1}}$
E_T	Towing **electric field noise**	$\mathrm{V\,m^{-1}}$
V_r	**Electrodes and amplifiers noise**	$\mathrm{V\,m^{-1}}$
$\mathcal{V}$	**Electromotive force**	V
ε	**Electrical permittivity**	$\mathrm{F\,m^{-1}}$
σ	**Electrical conductivity**	$\mathrm{S\,m^{-1}}$
ϵ	**Error**	
f	**Frequency**	Hz
ω	Angular **frequency**, $\omega = 2\pi f$.	$\mathrm{rad\,s^{-1}}$
$\hat{}$	**Hat** Denotes change of domain from time to frequency.	
i	**Imaginary unit**, $i = \sqrt{-1}$.	
$\int_a^b ()$	**Integration**	
$\Delta x_{s/r}$	**Length of the source/receiver dipole**	m
$\log_{10}$	**logarithm to the base 10**	
Φ	**Magnetic flux**	V s
$\mathbf{B}$	**Magnetic flux density**	T
$B_{x/y/z}$	Magnitude of the north/east/vertical component of the **magnetic field**	T
$\mathbf{H}$	**Magnetic field intensity**	$\mathrm{A\,m^{-1}}$
μ	**Magnetic permeability**	H m
V	**Measured voltage response**	V
$\mathcal{I}$	**Measured input current**	A
$\mathcal{N}$	**Noise**	V
$\mathbf{n}$	**Normal to the surface** S	
δ	**Skin depth**	m
$\sum_a^b ()$	**Summation**	
S	**Surface** form by the telluric cable	$\mathrm{m^2}$
v	**Streamer velocity**	$\mathrm{m\,s^{-1}}$

Constants of Free Space

In electromagnetics, there are three universal constants which are related to the properties of the free space (vacuum): the velocity of electromagnetic waves (including light), the permittivity of free space, and the permeability of free space.

Constant	Symbol	Value
Permittivity	ϵ_0	$\sim \frac{1}{36\pi} \times 10^{-9}\ \mathrm{F\,m^{-1}}$
Permeability	μ_0	$\sim 4\pi \times 10^{-7}\ \mathrm{H\,m^{-1}}$
Velocity of light	c_0	$\sim 3 \times 10^{8}\,\mathrm{m\,s^{-1}}$

Function

Fourier transform

Let $x(t)$ be a time series. The Fourier transform of $x(t)$ is defined as

$$\hat{X}(w) = \int_{-\infty}^{\infty} x(t) e^{-i\omega t}\,\mathrm{d}t\,, \tag{0.1}$$

and the inverse Fourier transform (IFT) as

$$x(t) = \frac{1}{2\pi} \int_{-\infty}^{\infty} \hat{X}(\omega) e^{i\omega t}\,\mathrm{d}\omega\,, \tag{0.2}$$

where $i = \sqrt{-1}$ is the imaginary unit, $\omega = 2\pi f$ is the angular frequency (in $\mathrm{rad\,s^{-1}}$), and f is the frequency (in Hz).

Discrete Fourier Transform

Let $x(n)$, $n = 0, 1, 2, ..., N-1$ be sampled at equispaced intervals of Δt to produce a discrete sequence $x(n\Delta t)$ from the input signals $x(t)$ and let N be the total number of samples. In addition, suppose that $x(n\Delta t)$ is measured in volts (V). Following Brigham (1974), the discrete Fourier transform (DFT) $x(n\Delta t)$ is expressed as:

$$\hat{X}(k) = \Delta t \sum_{n=0}^{N-1} x(n\Delta t) e^{-i\frac{2\pi}{N}kn}\,, \qquad [\mathrm{V\,s}] \text{ or } [\mathrm{V\,Hz^{-1}}] \tag{0.3}$$

where $\hat{X}(k)$ is the kth output component of the DFT, and $k = 0, 1, 2, ..., N-1$ is the index of the DFT output in the frequency domain.

Fast Fourier Transform

The Fast Fourier Transform (FFT) is an algorithm used to compute the DFT of discrete signal (equation (0.3)). The programming language, Matlab, that is used for the computation of the DFT throughout this thesis is based on library Fast Fourier Transform in the West (FFTW) (Frigo and Johnson, 1998). FFTW is known as the fastest free software implementation of the FFT algorithm.

Running FFT in Matlab returns a two-sided spectrum. Since, the signal I am dealing with throughout this thesis are real, so the frequency spectrum between 0 and $N/2+1$ appears to have a mirror image of frequencies that run between 0 and $-N/2+1$, that is, the spectrum estimates for the positive and negative frequencies is similar. Thus, I only plot the frequencies ranging between 0 and $N/2+1$. Therefore, every frequency is multiplied except for the DC by 2 in order to conserve the total power.

To analyse the frequency content of the data, I divide the discrete sequence $x(n\Delta t)$ into K-second-long windows each. Each window is then multiplied by a Hanning taper of the same length before applying the FFT. This is done to avoid spectral leakage introduced by sudden changes at the start and at the end of the data. The DFT expressed in equation (0.3) is rewritten as:

$$\hat{X}'(k) = \Delta t \sum_{n=0}^{N-1} x(n\Delta t)h(n\Delta t)e^{-i\frac{2\pi}{N}kn}\,, \qquad [\mathrm{V\,s}] \text{ or } [\mathrm{V\,Hz^{-1}}] \quad (0.4)$$

where, $\hat{X}'(k)$ is the kth output component of the DFT of $x(n\Delta t)h(n\Delta t)$, and $h(n\Delta t)$ denotes the Hanning window.

Power and amplitude spectral density

The power spectral density (PSD) describes the power per hertz in a signal. Using equation (0.4), the PSD of $x(n)$, $\hat{\mathcal{P}}(k)$ is defined as (Kay and Marple, 1981; Brigham, 1974):

$$\hat{\mathcal{P}}(k) = \frac{1}{N\Delta t} \mid \hat{X}'(k) \mid^2, \qquad [\mathrm{V^2 s}] \text{ or } [\mathrm{V^2 Hz^{-1}}] \quad (0.5)$$

Windowing a signal as shown in equation (0.4) reduces its power (Hayes, 1996). Therefore, a normalisation factor is applied to each window to compensate for the loss of power. This normalisation factor is expressed as (Hayes, 1996):

$$U = \frac{1}{N}\sum_{n=0}^{N-1} h^2(n\Delta t)\,. \quad (0.6)$$

Following Hayes (1996), equation (0.6) is applied to equation (0.5) as follows:

$$\hat{\mathcal{P}}'(k) = \frac{2}{UN\Delta t} \mid \hat{X}(k) \mid^2, \qquad [\mathrm{V^2 s}] \text{ or } [\mathrm{V^2 Hz^{-1}}] \quad (0.7)$$

The factor of 2 in Equation (0.7) accounts for the fact that only half of the PSD array is used as explained on the second paragraph of the "Fast Fourier Transform" section.

The amplitude spectrum density (ASD), $\hat{\mathcal{A}}$, is derived from equation (0.5) following the formula:

$$\hat{\mathcal{A}}(k) = \sqrt{\hat{\mathcal{P}}'(k)}\,. \qquad [\mathrm{V}\sqrt{\mathrm{s}}] \text{ or } [\mathrm{V}\,(\sqrt{\mathrm{Hz}})^{-1}] \qquad (0.8)$$

Graphing the PSD and the ASD

The index of the programming language, Matlab, used for the processing of the data, starts at 1. Therefore, the indices for the DFT are integers from 1 to N.

The discrete-time series $x(n)$ is assumed to be separated by

$$\Delta t = \frac{1}{f_s}\,, \qquad [\mathrm{s}] \qquad (0.9)$$

where Δt is the time increment per sample, and f_s is the sampling frequency (in hertz (Hz)). In the frequency domain, $\hat{X}(k)$ is complex-value. Each index or bin (k) in the DFT is spaced by the frequency resolution

$$\Delta f = \frac{1}{N\Delta t} = \frac{f_s}{N}\,. \qquad [\mathrm{Hz}] \qquad (0.10)$$

The PSD of $\hat{X}'(k)$ at index k measures the amount of frequency f (in hertz) present in the data. The frequency is expressed as

$$f = k\Delta f\,. \qquad [\mathrm{Hz}] \qquad (0.11)$$

The highest frequency component in the spectrum is expressed as:

$$f_{max} = \frac{f_s}{2}\,. \qquad [\mathrm{Hz}] \qquad (0.12)$$

Given equations (0.10) and (0.12), the entire frequency axis is computed in the following frequency range:

$$f = [0 : \Delta f : f_{max}]\ . \qquad (0.13)$$

In this thesis, the power spectral density (equation (0.7)) and the amplitude spectral density (equation (0.8)) are plotted versus the frequency axis defined in equation (0.13).

Cross-correlation

In this thesis, the relationship between different time series is explored intensively. To achieve this, the cross-correlation function is used for analysis in the time domain, and the magnitude squared coherence function is used in the frequency domain.

Given two time series $x(t)$ and $y(t)$, we can delay $x(t)$ by T samples, and then calculate

the cross-covariance between this pair of signals. That is:

$$\sigma_{xy}(T) = \frac{1}{N-1}\sum_{t=1}^{N}(x(t-T)-\mu_x)(y(t)-\mu_y)\,, \tag{0.14}$$

where μ_x and μ_y are the means of each respective time series, and N is the number of samples in each of them. The cross-correlation is the normalised version of $\sigma_{xy}(T)$. It is expressed as:

$$r_{xy}(T) = \frac{\sigma_{xy}(T)}{\sqrt{\sigma_x^2\,\sigma_y^2}}\,, \tag{0.15}$$

where σ_x^2 and σ_y^2 are the variance of $x(t)$ and $y(t)$, respectively. For simplicity, $\sigma_x \equiv \sigma_{xx}$ and $\sigma_y \equiv \sigma_{yy}$.

Vector Analysis

Cartesian coordinates

For a given cartesian coordinate system as shown in Figure 0.1, we can define three orthogonal unit vectors parallel to the three axes OX, OY, OZ, and designate them by a right-handed system with based vectors $\mathbf{a_x}$, $\mathbf{a_y}$, and $\mathbf{a_z}$ in the three coordinate directions satisfying the following relation:

$$\mathbf{a_y} \times \mathbf{a_z} = \mathbf{a_x}\,, \tag{0.16}$$

$$\mathbf{a_z} \times \mathbf{a_x} = \mathbf{a_y}\,, \tag{0.17}$$

$$\mathbf{a_x} \times \mathbf{a_y} = \mathbf{a_z}\,, \tag{0.18}$$

where "$\times$" denotes the cross product. The position vector of a point $P(x_1, y_1, z_1)$ in that coordinate system can be considered as the sum of three orthogonal vectors as illustrated in Figure 0.1:

$$\mathbf{OP} = \mathbf{a_x}x_1 + \mathbf{a_y}y_1 + \mathbf{a_z}z_1\,. \tag{0.19}$$

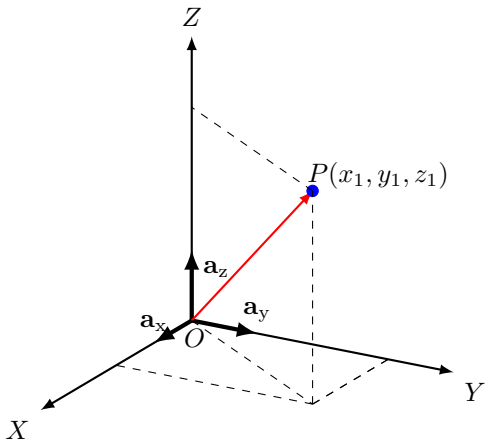

Figure 0.1: Cartesian coordinates.

Following equation (0.19), vectors **A** and **B** in Cartesian coordinates can be written as:

$$\mathbf{A} = \mathbf{a_x} A_x + \mathbf{a_y} A_y + \mathbf{a_z} A_z \,, \tag{0.20}$$

$$\mathbf{B} = \mathbf{a_x} B_x + \mathbf{a_y} B_y + \mathbf{a_z} B_z \,. \tag{0.21}$$

Using equations (0.20) and (0.21), the dot product of the two vectors is:

$$\begin{aligned} \mathbf{A} \cdot \mathbf{B} &= (\mathbf{a_x} A_x + \mathbf{a_y} A_y + \mathbf{a_z} A_z) \cdot (\mathbf{a_x} B_x + \mathbf{a_y} B_y + \mathbf{a_z} B_z) \,, \\ &= A_x B_x + A_y B_y + A_z B_z \,, \end{aligned} \tag{0.22}$$

and the cross product is:

$$\begin{aligned} \mathbf{A} \times \mathbf{B} &= \begin{vmatrix} \mathbf{a_x} & \mathbf{a_y} & \mathbf{a_z} \\ A_x & A_y & A_z \\ B_x & B_y & B_z \end{vmatrix} \,, \\ &= \mathbf{a_x}(A_y B_z - A_z B_y) + \mathbf{a_y}(A_z B_x - A_x B_z) + \mathbf{a_z}(A_x B_y - A_y B_x) \,. \end{aligned} \tag{0.23}$$

Integrals containing vector functions

In this thesis, we perform line and surface integrals. To evaluate the integral, one must properly define the differential elements of length and area in Cartesian coordinates. The expressions for differential length and differential surface are:

$$d\ell = \mathbf{a_x} dX + \mathbf{a_y} dY + \mathbf{a_z} dX \,, \tag{0.24}$$

$$d\mathbf{s} = \mathbf{a_x} dY\, dZ + \mathbf{a_y} dX\, dZ + \mathbf{a_Z} dX\, dY \,. \tag{0.25}$$

The line integral of a vector field along a given path may be expressed as:

$$\int_C \mathbf{A} \cdot d\ell \,, \tag{0.26}$$

where C is the path of integration. If the integration is to be carried out from a point P_1 to another point P_2, Combining equation (0.20) and equation (0.24) into equation (0.26) yields:

$$\int_{P_1}^{P_2} \mathbf{A} \cdot d\ell = \int_{P_1}^{P_2} A_x dX + A_y dY + A_z dZ \,. \tag{0.27}$$

If $\mathbf{A}$ is replaced by the electric field vector $\mathbf{E}$, then the integral represents the work done by the electric field in moving a unit charge from P_1 to P_2.

The surface integral of a vector, is the flux of this vector through a surface. It is written as:

$$\int_S \mathbf{A} \cdot d\mathbf{s} \,, \tag{0.28}$$

where $d\mathbf{s} = \mathbf{n}ds$ is the vector differential surface element, $\mathbf{n}$ is the normal unit vector that points in a direction perpendicular to the surface S, and ds is the element of the surface defined in equation (0.25). Since ds is the product of two variables, the surface integral is a double integral. Thus the notation in equation (0.28) is in short-form notation.

Trapezoidal rule

For a domain discretised into N non-equally space panel, $a = x_1 < x_2 ... < x_{n+1} = b$, to approximate a definite integral, we use the trapezoidal rule defined as:

$$\int_a^b f(x)dx \approx \frac{1}{2} \sum_{k=1}^{N} (f(x_{k+1}) + f(x_k))(x_{k+1} - x_k) \,. \tag{0.29}$$

Vector differential operator

A vector differential operator "nabla" (∇) is used thoroughly in Chapter 2. This section aims to provide its expression in Cartesian coordinates. In fact, the presence of this operator instructs the reader to take derivatives of the quantity on which the operator is acting. The operator can take different forms:

$$\nabla \equiv \mathbf{a_x}\frac{\partial}{\partial x} + \mathbf{a_y}\frac{\partial}{\partial y} + \mathbf{a_z}\frac{\partial}{\partial z} \qquad \text{Gradient}$$

$$\nabla \cdot \mathbf{A} = \left(\frac{\partial A_x}{\partial x} + \frac{\partial A_y}{\partial y} + \frac{\partial A_z}{\partial z}\right) \qquad \text{Divergence}$$

$$\nabla \times \mathbf{A} = \begin{vmatrix} \mathbf{a_x} & \mathbf{a_y} & \mathbf{a_z} \\ \dfrac{\partial}{\partial x} & \dfrac{\partial}{\partial y} & \dfrac{\partial}{\partial z} \\ A_x & A_y & A_z \end{vmatrix} \qquad \text{Curl}$$

List of Acronyms

ADC	Analog-to-digital converter
CSEM	Controlled-source electromagnetic
DC	Direct current
DFT	Discrete Fourier transform
EM	Electromagnetic
EMF	Electro-motive force
FFT	Fast Fourier Transform
FFTW	Fast Fourier Transform in the West
HED	Horizontal electric dipole
IFFT	Inverse fast Fourier Transform
PRBS	Pseudo-random binary sequence
QC	Quality control
RMS	Root mean square
MSC	Magnitude squared coherence
MT	Magnetetolluluric
SNR	Signal-to-noise ratio

Companies

Companies are solely named by their abbreviations in the thesis.

EMGS	Electromagnetic Geoservices ASA
PGS	Petroleum Geo-Services ASA

Thesis

1

Introduction

If we knew what it was we were doing, it would not be called research, would it?

Albert Einstein (1879–1955)
Physicist

1.1 Background and motivation

The marine controlled source electromagnetic (CSEM) method is a geophysical tool sensitive to variations of electrical resistivity (or its reciprocal, electrical conductivity). This technology was first used for academic applications to measure the conductivity of the lithosphere (Young and Cox, 1981; Cox, 1981). It has since been used in industry applications to sense resistive bodies, which can indicate the presence of hydrocarbons (Eidesmo et al., 2002; Ellingsrud et al., 2002; Srnka, 1986). MacGregor and Tomlinson (2014), Constable (2010) and Constable and Srnka (2007) provide a detailed history of the use of the marine CSEM method.

Three configurations can be used for the marine CSEM method as shown in Figure 1.1.

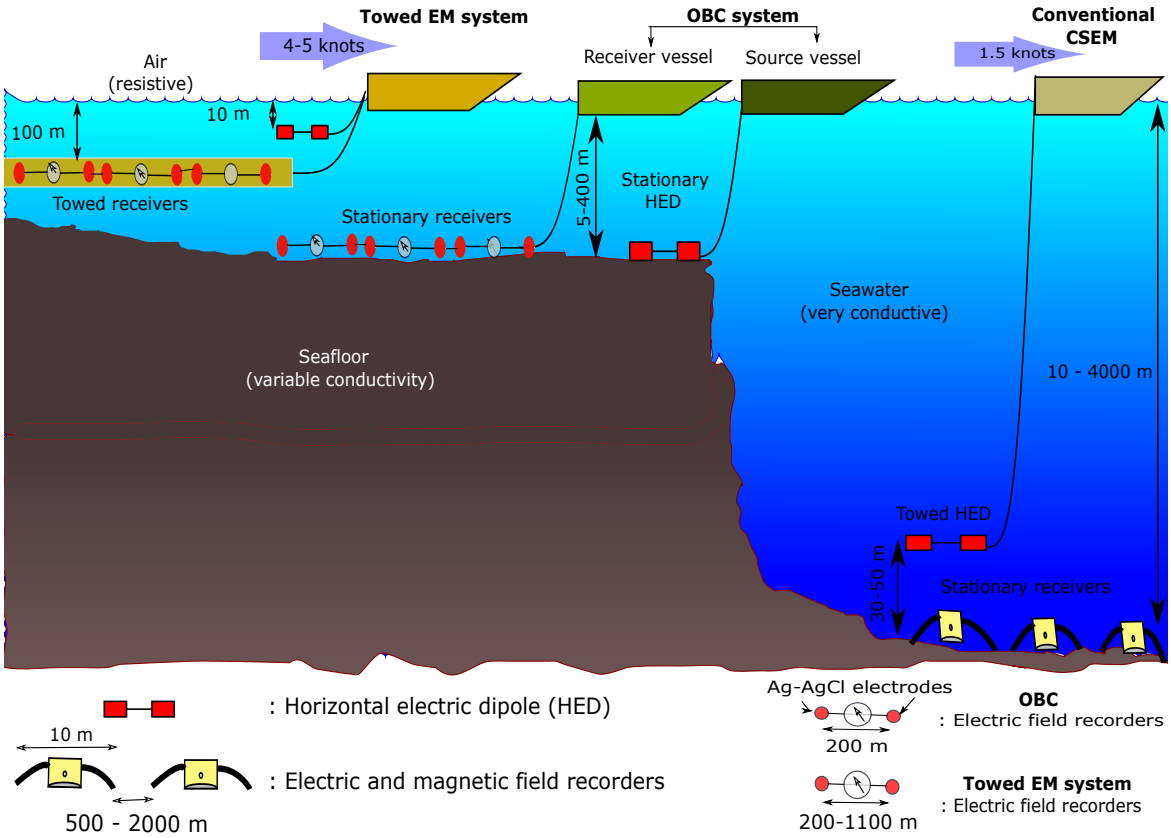

Figure 1.1: Schematic representation of marine node-based, OBC and towed CSEM concepts.

The conventional marine CSEM configuration uses a towed source above an array of receivers (called nodes) which are stationary on the seafloor. This system is mostly used in water depths greater than 1000 m. The ocean bottom cable (OBC) configuration features two vessels. One vessel deploys the source on the seafloor; this transmits a

signal to receivers in a linear configuration on the seafloor which are connected to the other vessel (Ziolkowski et al., 2010). Like the conventional marine CSEM, the receivers in the OBC configuration are stationary during data acquisition. This was designed to operate in water depths in the range 10–500 m. The OBC system has been developed into a fully towed streamer EM system, where the source and receiver are towed simultaneously. This system operates in water depths of 400 m or less (Mattsson et al., 2013). In the rest of this Ph.D. thesis, the node-based CSEM and towed streamer CSEM are used to refer to the conventional seafloor receiver and towed streamer EM configurations, respectively.

The marine CSEM method in its conventional setup uses a mobile horizontal electric dipole (HED) as a source to transmit a low-frequency electromagnetic (EM) signal, typically in the range 0.01–10 Hz, that diffuses through the sea water and sub-sea sediments, and also propagates through the air. The HED length is 100–300 m and transmits a current in the range 1000–1500 A (MacGregor and Tomlinson, 2014) although Barker et al. (2012) reported currents up to 7500 A for the deck mounted in shallow towed system. The HED is towed at a speed of 1.5 knots (compared with 4–5 knots for seismic 2D) and is kept at about 30 m above the seafloor to maximize the amount of EM energy transmitted into the subsurface while minimising the risk of collision with the seabed (MacGregor and Tomlinson, 2014). A tail buoy which includes positioning sensors, recording depth meter, is attached to the end of the HED transmitter. The Receiver electrodes measure the resulting field modified by the conductivity of the subsurface.

In node-based CSEM, receivers are deployed at known locations on the seafloor anchored by concrete blocks. The anchor helps to stabilise the receiver against forces such as water currents. Figure 1.2 shows a typical receiver node and its deployment. Traditionally, the receiver has four long orthogonal polypropylene pipe arms, each about 8–10 m in length and 5 cm diameter, with silver-silver chloride (Ag-AgCl) electrodes. A pair of electrodes forms a dipole which senses a voltage difference. Induction coil magnetometers sense magnetic field variations in three orthogonal directions. Constable (2013) provides a review of node-based CSEM survey instrumentation. Alternative node receivers have also been developed. Nielsen et al. (2009) describe a new type of receiver that uses capacitive electrodes as electric field receivers. The innovation is that these electrodes are inside the receiver module and therefore eliminate the need for long electric field arms.

Node-based CSEM is time consuming compared with 2D seismic surveying, mainly due to the time it takes to deploy and recover the receiver nodes. In an effort to improve acquisition efficiency and reduce costs, a long flexible neutrally-buoyant EM streamer cable has been developed to be towed simultaneously with an electric current dipole

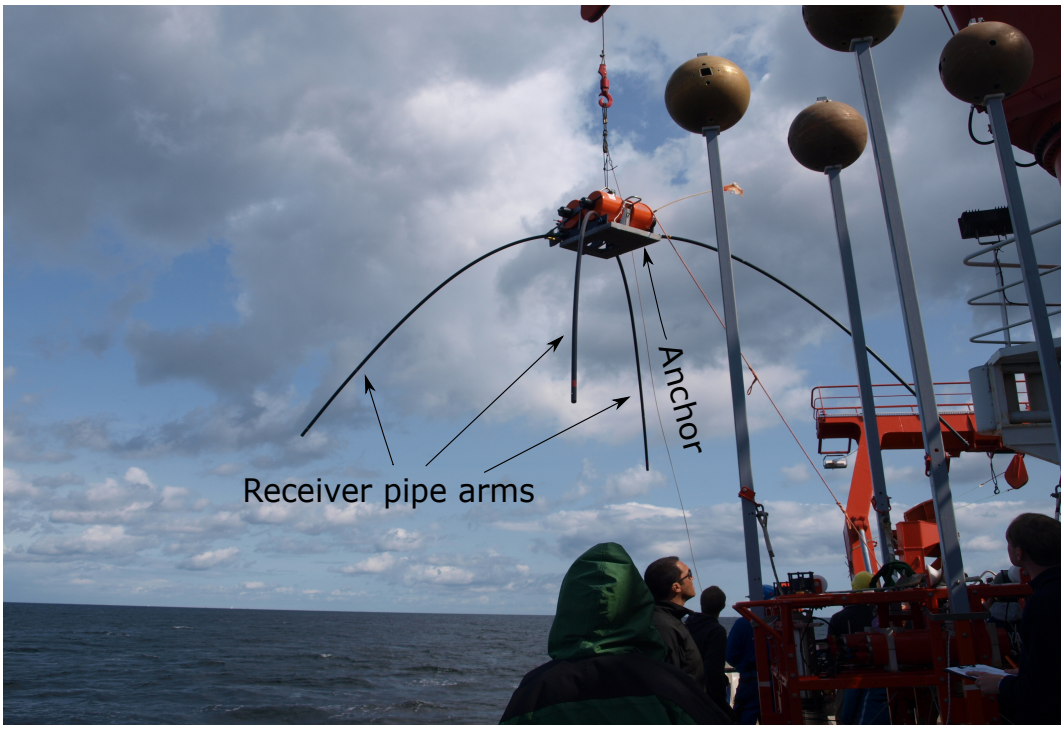

Figure 1.2: Node-based receiver showed being deployed from a ship. The electrodes are housed in the ends of the flexible arms.

source at 4–5 knots (Anderson and Mattsson, 2010). The source and receiver are towed at nominal depths of 10–100 m below the sea surface, or shallower depending on the water depth. The source is towed at the front of an EM streamer with offsets in the range 500–8000 m (Mattsson et al., 2013). The EM streamer is 8 km long maximum and configurable with a series of electrode pairs distributed along its length, each connected by a telluric cable. The near offset has a receiver separation of 200 m, and this separation increases as the offset increases in length to reach a maximum of 1100 m long (Engelmark et al., 2014).

This method has the advantages of allowing a common platform for both seismic and EM operations and permitting real-time quality control (QC). The QC aims to determine and verify that CSEM data acquisition process and transmission meets or exceeding the customer requirements. A QC professional on the vessel will assess the suitability of the survey' equipment and focus on defect identification.

The EM streamer has a dense receiver spacing - typical spacing is 200 m compared with 500–2000 m for the node-based CSEM system (Mattsson et al., 2013). This results in superior data density compared with the node-based CSEM. Constable et al.

(2012) developed a towed system that provides information at near offsets (up to 1 km) during conventional CSEM surveying to enable better characterisation of the near surface resistivity, which is important in the inversion of deeper data. Table 1.1 gives a comparison of the node-based and towed streamer CSEM.

Criteria	**Marine CSEM**	
	Node-based CSEM	**Towed streamer CSEM**
Source type	HED	HED
Source length	300 m	800 m
Source amplitude	1000 A	1500 A
Source speed	Source towed at 1.5 kn	Source-receiver towed at 4–5 kn
Receiver length	1–10 m	200–1100 m
Receiver type	Static receiver	Towed receiver
Operational depth	10–4000 m	5–400 m

Table 1.1: Comparison of marine node-based and towed streamer CSEM

Although the increase in acquisition efficiency is obvious, various sources of noise affect the towed system and can degrade considerably the desired signal transmitted through the earth. Therefore, its performance is to a great extent dependent on noise levels in the acquired data. Some sources of noise affecting the towed streamer CSEM have already been identified in the node-based CSEM: magnetotelluric noise (Ziolkowski and Wright, 2012), electrode and amplifier noise (Constable et al., 1998) and motionally-induced noise (Mittet and Morten, 2012; Summerfield et al., 2005). This last source is due to swell, microseisms and water currents which cause the receiver arms to vibrate. When towing the EM streamer in the sea at depths of 100 m or less, the noise levels are substantially greater than the noise levels in the node-based CSEM. This is because of additional noise generated by the movement of the streamer in the Earth's magnetic field. It has been suggested by Constable (2013); Engelmark et al. (2012); Tenghamn et al. (2007), and Burrows (1972) that the dominant source of noise is motionally induced. However, none of these papers estimate the noise levels. The benefits of towing the EM streamer in water depths of 400 m or less (Mattsson et al., 2013), such as ease of operation, are counteracted by an increase in noise level within the frequencies of interest (0.01–10 Hz). These observations give rise to three questions that need to be addressed in order to improve the performance of the towed streamer CSEM:

- How large is the motionally-induced noise compared with other noise presents in

the towed streamer CSEM, and relative to the node-based CSEM noise level?

- What is the distribution or nature of the noise: frequency and correlation properties?
- What is the physical mechanism that generates the noise?

For a transmitter frequency of 0.25 Hz, the present depth limit of imaging is about 2500 m below the seafloor (Engelmark et al., 2014). This is controlled by the noise levels, the sensitivity and accuracy of the instrumentation and the source moment (Spies, 1989). Therefore, successfully addressing the noise issue may enable higher quality electric field data to be obtained and may improve the depth of imaging of resistive bodies. In addition, better characterisation of noise may help to develop methods to minimise their effect.

A further challenge is to obtain data with an adequate signal-to-noise ratio (SNR) given the constraint of a fixed data acquisition period of 100 seconds per shot (McKay et al., 2015). SNR provides a quantitative measure of performance of a system. The SNR of the system can be enhanced by different methods:

- Maximising signal. This can be achieved by increasing the length of the source dipole or by increasing the source current. Various techniques have been proposed to increase the source signal and have reached their practical limitation, as shown in detail in Chapter 3.
- Reducing noise. One way to reduce noise levels could be to filter the data in a specific frequency range. Filtering decreases the noise levels but is detrimental to the resolution. An optimal filter can be designed only when one knows the characteristics of the noise and the signal in the data.

As a result, understanding the nature of noise is very important. In towed streamer CSEM, the main source of noise is poorly understood. Describing the causative mechanisms and quantifying different types of noise in the system constitute the core of this thesis.

1.2 Claim

I show in this thesis that the noise in the towed streamer CSEM system is about 20 dB greater than the noise in the OBC EM system in the frequency range 0.01–1 Hz.

At frequencies above 1 Hz, for a receiver separation of 200 m, the noise has the same amplitude and is strongly correlated from one receiver to another. The same observation

is made with the OBC data. This noise mainly originates from MT fields. At frequencies below 1 Hz, the noise on any channel does not correlate with the neighbouring channels.

To understand the physical mechanism that generates the major source of noise, a prototype EM streamer was designed and tests were carried in the controlled environment of the new FloWave tank located at the University of Edinburgh. From these tests, I show that the motion of the streamer due to the wave motion is the major source of noise in the towed streamer CSEM. The increase in noise due to the increase of flow rate around the streamer is approximately half that which is related to wave motion.

I also estimate the motionally-induced field noise level based on the streamer displacement data. I show that this noise is correlated with the measured electric field. This estimated field is found to be about three times smaller than the measured electric field.

From these results, I suggest that wave motion noise could be reduced by towing the streamer deeper, by using rigid cable or increasing the cable tension.

1.3 Layout of this thesis

The thesis covers aspects of noise sources and estimates the contribution of each of these sources in marine towed-streamer CSEM.

Chapter 2 introduces the equations which govern EM wave behaviour and derives the skin depth.

Chapter 3 focusses on investigating the similarities and differences between noise levels in the static CSEM system and towed-streamer CSEM. The chapter also contains a definition of the signal-to-noise ratio (SNR) and suggests ways to improve the SNR of the system.

Chapter 4 analyses electric field noise acquired with the OBC system and the towed streamer CSEM. It contains root means square analysis, spectral analysis and correlation analysis of the data.

Chapter 5 focuses on theory and estimation of the motionally-induced noise. It also provides an explanation of different mechanisms that could generate a motionally-induced field in towed streamer CSEM.

Chapter 6 describes the experiment carried out in the FloWave Tank to study the mechanisms of noise generation in the streamer in a controlled manner. Using the

FloWave tank data, I investigate the effect on noise levels of increasing water flow rates of 0, 0.5, 1, and 1.5 $\mathrm{m\,s^{-1}}$ and wave motion at different frequencies (0.29 Hz and 0.45 Hz) and amplitude of 0.1 m around the prototype EM streamer. Motion capture data of the streamer moving are recorded to analyse the relation between the electric field and the cable motion.

Chapter 7 shows experimental results and analysis of the data collected in the Flowave Tank. It shows that the wave motion noise is approximately 12 dB above the flow noise. This flow noise is due to flow over the electrode surfaces, and the wave motion noise is due to the motion of the telluric cable in the Earth's magnetic field in response to wave motion.

Finally, Chapter 8 summarises the findings, provides recommendations to mitigate the flow noise and wave motion noise. To improve the signal-to-ratio of the towed streamer CSEM, one could tow the streamer deeper, increase the tension of the streamer and the telluric cable or the use of rigid telluric cables.

2

Behaviour of Electric and Magnetic fields

I consider that I understand an equation
when I can predict the properties of its solutions,
without actually solving it.

Paul A. M. Dirac - (1902–1984)
Physicist

This chapter deals with electromagnetic wave propagation governed by Maxwell's Equations. From these equations, the electromagnetic wave equations have been derived when electromagnetic wave propagates in free space and inside a typical electrical conductivity values of rocks which are of an interest in electromagnetic prospecting and where there are free currents. The depth of penetration electromagnetic waves is also derived. From this, it is clear that the frequency of the incident electromagnetic wave and the conductivity of the medium are the key parameters controlling the penetration depth of EM fields. In the last section, the electric field equation generated by a point dipole sources is also derived from Maxwell's Equations.

2.1 Theory of electromagnetic fields

Following Zhdanov (2009), the behaviour of electromagnetic (EM) waves in an inhomogeneous conducting earth is described by the four Maxwell's Equations in differential form. These are for S.I units:

$$\nabla \times \mathbf{H} = \mathbf{J} + \frac{\partial \mathbf{D}}{\partial t} \qquad \text{Ampère-Maxwell law}, \tag{2.1}$$

$$\nabla \times \mathbf{E} = -\frac{\partial \mathbf{B}}{\partial t} \qquad \text{Faraday's law}, \tag{2.2}$$

$$\nabla \cdot \mathbf{B} = 0 \qquad \text{Gauss' law for magnetic fields}, \tag{2.3}$$

$$\nabla \cdot \mathbf{D} = q \qquad \text{Gauss's law for electric fields}, \tag{2.4}$$

in which the vector $\mathbf{H}$ and $\mathbf{B}$ are the vectors magnetic and induction fields, respectively; $\mathbf{E}$ and $\mathbf{D}$ are the vector electric and displacement fields, respectively; the vector $\mathbf{J}$ is the current conduction density and q is the electrical charge density. Equation (2.1) represents two kinds of current flow: the first, $\mathbf{J}$, in which charge carriers flow through the medium without resistance. This is often called ohmic. The second, $\partial\mathbf{D}/\partial t$, in which charge separation, and hence an impediment electric field, arises. This is often known by the name displacement current.

Constitutive relations

The pairs of $\mathbf{E}$ and $\mathbf{D}$, $\mathbf{H}$ and $\mathbf{B}$, and $\mathbf{E}$ and $\mathbf{J}$ are linked by the following constitutive relations:

$$\mathbf{D} = \varepsilon(\omega, \mathbf{E}, \mathbf{r}, t, T, P, ...)\mathbf{E}\ , \tag{2.5}$$

$$\mathbf{B} = \mu(\omega, \mathbf{E}, \mathbf{r}, t, T, P, ...)\mathbf{H}\ , \tag{2.6}$$

$$\mathbf{J} = \sigma(\omega, \mathbf{E}, \mathbf{r}, t, T, P, ...)\mathbf{E} \qquad \text{Ohm's law}, \tag{2.7}$$

where the tensors ε, μ, and σ are the dialectic permittivity, the magnetic permeability, the electrical conductivity as function of angular frequency ω (where $\omega = 2\pi f$ and f is the EM wave frequency), electric field strength $\mathbf{E}$ or magnetic induction $\mathbf{B}$, position $\mathbf{r}$, time t, temperature T, and pressure P, respectively.

In geophysical problems, it is the electrical conductivity that we want to find. Assume a right-hand Cartesian coordinate system, x, y, z, where the z - axis is directed downwards as shown in Figure 2.1.

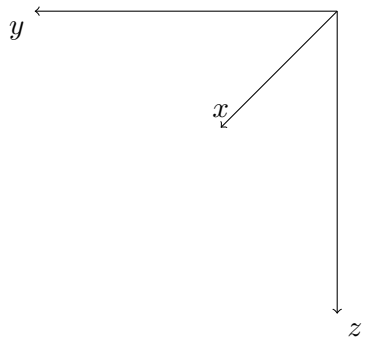

Figure 2.1: Right-handed Cartesian coordinate system

The conductivity in Cartesian coordinates is expressed as:

$$\sigma = \begin{vmatrix} \sigma_{xx} & \sigma_{xy} & \sigma_{xz} \\ \sigma_{yx} & \sigma_{yy} & \sigma_{yz} \\ \sigma_{zx} & \sigma_{zy} & \sigma_{zz} \end{vmatrix} . \tag{2.8}$$

Following Keller (1989), the conductivity tensor has a simple form if two of the orthogonal coordinate directions are selected to lie in the direction of maximum conductivity and minimum conductivity (the principal direction of the conductivity tensor). Equation 5.22 becomes

$$\sigma = \begin{vmatrix} \sigma_{xx} & 0 & 0 \\ 0 & \sigma_{yy} & 0 \\ 0 & 0 & \sigma_{zz} \end{vmatrix} . \tag{2.9}$$

To simplify analysis in electromagnetic earth problem, Ward and Hohmann (1989) suggest the following assumptions:

(1) All media are linear, isotropic, homogeneous and posses electric properties which are independent of time, temperature, or pressure. This implies that the diagonal terms in equation (5.24) have equal values, that is, $\sigma_{xx} = \sigma_{yy} = \sigma_{zz}$. Therefore, the electrical conductivity σ is a scalar.

(2) For non-magnetic earth, the magnetic permeability μ is assumed to be that of free space, that is, $\mu = \mu_0 = 4\pi\times10^{-7}$ H m^{-1}. The variation in permittivity is ignored and we use the permittivity of free space $\varepsilon_0 = 8.854\times 10^{-12}$ F m^{-1}.

Following assumptions (1) and (2), equations (2.5) to (2.7) are rewritten as:

$$\mathbf{D} = \varepsilon_0 \mathbf{E} \,, \tag{2.10}$$

$$\mathbf{B} = \mu_\mathbf{0} \mathbf{H} \,, \tag{2.11}$$

$$\mathbf{J} = \sigma \mathbf{E} \,. \qquad \text{Ohm's law} \tag{2.12}$$

Interpretation of Maxwell's Equations

Equation 2.1 is the *Ampere-Maxwell law*, which states that a current flowing in a conductor and a changing displacement current with time induce a magnetic field.

Equation 2.2 is *Faraday's law* of induction, which states that a varying magnetic field with time generates an electric field whose magnitude is proportional to the rate of change of the magnetic field. The direction of that induced electric field is such that it opposes the causes of its production. This is known as *Lenz's law*.

Equation 2.3 is *Gauss's law* for magnetic fields. It is essentially stated that there is no magnetic analogue for electric charge. In order words, there are no magnetic monopoles.

Equation 2.4 is *Gauss's law* for electric fields. It states that electric charges are the source of electric displacement, $\mathbf{D}$.

To sum up, from Equation 2.2, a time-varying magnetic field induces an electric field, while according to Equation 2.1 the same electric field gives rise to a magnetic field. The electric and magnetic fields, continuously interact, reinforcing each other and consequently probing great distances in space (Zhdanov, 2009). This is exploited in electromagnetic exploration.

2.2 Electromagnetic wave equation

From equation (2.1) and substituting in the constitutive relation for displacement fields in equation (2.10) and for current density in equation (2.12), we obtain

$$\nabla \times \mathbf{H} - \varepsilon_0 \frac{\partial \mathbf{E}}{\partial t} - \sigma \mathbf{E} = 0 \,. \tag{2.13}$$

From equation (2.2) and substituting in the constitutive relation for magnetic flux density in equation (2.5) we have

$$\nabla \times \mathbf{E} + \mu_0 \frac{\partial \mathbf{H}}{\partial t} = 0 \,. \tag{2.14}$$

First, we determine the wave equation for the electric field.
Take the curl of equation (2.14) to yield

$$\nabla \times (\nabla \times \mathbf{E}) = -\mu_0 \left(\nabla \times \frac{\partial \mathbf{H}}{\partial t} \right) . \tag{2.15}$$

if the vector $\mathbf{H}$ is piecewise continuous and has continuous first and second derivatives, the curl $\nabla\times$ and derivative $\partial/\partial t$ may be interchanged in equation (2.15), yielding

$$\nabla \times (\nabla \times \mathbf{E}) = -\mu_0 \frac{\partial}{\partial t} (\nabla \times \mathbf{H}) . \tag{2.16}$$

Using the vector identity

$$\nabla \times (\nabla \times \mathbf{F}) = \nabla(\nabla \cdot \mathbf{F}) - \nabla^2 \mathbf{F} , \tag{2.17}$$

equation (2.16) becomes

$$\nabla (\nabla \cdot \mathbf{E}) - \nabla^2 \mathbf{E} = - - \mu_0 \frac{\partial}{\partial t} (\nabla \times \mathbf{H}) . \tag{2.18}$$

The free charge dissipates almost immediately in conductive media, which means that

$$\nabla \cdot \mathbf{E} = 0 , \tag{2.19}$$

inserting equation (2.19) and substituting for $\nabla \times \mathbf{H}$ from equation (2.1) in equation (2.18) yields:

$$\nabla^2 \mathbf{E} = \mu_0 \left(\sigma \frac{\partial \mathbf{E}}{\partial t} + \varepsilon_0 \frac{\partial^2 \mathbf{E}}{\partial t^2} \right) . \tag{2.20}$$

This is the wave equation for the electric field in the time domain.

Second, we determine the wave equation for the magnetic field. Similarly, by performing the curl operation of equation (2.13) yields

$$\nabla \times \nabla \times \mathbf{H} - \varepsilon_0 \frac{\partial}{\partial t} (\nabla \times \mathbf{E}) = \nabla \times (\sigma \mathbf{E}) . \tag{2.21}$$

As above, the operators $\nabla\times$ and $\partial/\partial t$ may be interchanged if $\mathbf{E}$ is piecewise continuous and has first and second derivatives. In addition, σ is locally a constant (homogeneous medium), therefore, it is taken outside the operator $\nabla\times$ on the right-hand side of equation (2.21) to yield

$$\nabla \times \nabla \times \mathbf{H} - \varepsilon_0 \frac{\partial}{\partial t} (\nabla \times \mathbf{E}) = \sigma \nabla \times \mathbf{E} , \tag{2.22}$$

substituting for $\nabla \times \mathbf{E}$ from equation (2.14) into equation (2.22) yields

$$\nabla \times \nabla \times \mathbf{H} + \varepsilon_0 \mu_0 \frac{\partial^2 \mathbf{H}}{\partial t} + \mu_0 \sigma \frac{\partial \mathbf{H}}{\partial t} = 0\,. \tag{2.23}$$

Using the vector identity defined in equation (2.17), equation (2.23) can be rewritten as

$$\nabla(\nabla \cdot \mathbf{H}) - \nabla^2 \mathbf{H} + \varepsilon_0 \mu_0 \frac{\partial^2 \mathbf{H}}{\partial t} + \mu_0 \sigma \frac{\partial \mathbf{H}}{\partial t} = 0\,. \tag{2.24}$$

Using the third Maxwell's equation (2.3) and equation (2.5), we see that $\nabla \cdot \mathbf{H} = 0$, so the first term in equation (2.24) is zero and equation (2.24) becomes

$$\nabla^2 \mathbf{H} = \mu_0 \left(\sigma \frac{\partial \mathbf{H}}{\partial t} + \varepsilon_0 \frac{\partial^2 \mathbf{H}}{\partial t^2} \right)\,. \tag{2.25}$$

This is the wave equation for the magnetic field in the time domain. It is identical in form to the electric wave equation for the electric field shown in equation (2.20).

Equations (2.20) and (2.25) completely describe the electric and magnetic fields in a homogeneous medium that apply in source-free regions.

Electromagnetic propagation in free space

Air is typically a very low conductive environment with electrical conductivity ranging between 3 to 8×10^{-15} $\mathrm{S\,m^{-1}}$ (Constable, 2010). Thus, in many applications of electromagnetic prospecting, the air electrical conductivity is approximated zero. It follows that the term containing σ in equations (2.20) and (2.25) disappears. Therefore, the electric and magnetic fields wave equations become:

$$\nabla^2 \mathbf{E} = \mu_0 \varepsilon_0 \frac{\partial^2 \mathbf{E}}{\partial t^2}\,, \tag{2.26}$$

$$\nabla^2 \mathbf{H} = \mu_0 \varepsilon_0 \frac{\partial^2 \mathbf{H}}{\partial t^2}\,. \tag{2.27}$$

Equations (2.26) and (2.27) are called wave equations because they are similar in form to the general wave equation, which describes the propagation of sound and light in free space. The wave equation is expressed as:

$$\nabla^2 \mathbf{u} = \frac{1}{c_0^2} \frac{\partial^2 \mathbf{u}}{\partial t^2}\,, \tag{2.28}$$

where u is the displacement amplitude. By analogy to equations (2.26) and (2.27), we can write:

$$\frac{1}{c_0^2} = \mu_0\varepsilon_0 \Rightarrow c_0 = \sqrt{1/\mu_0\varepsilon_0} \approx 3 \times 10^8\,, \qquad [\mathrm{m\,s}] \tag{2.29}$$

where c_0 is the speed of light. From these equations, it is clear that electric and magnetic fields in air propagate at the speed of light.

Electromagnetic propagation in conducting media: the diffusion equation

Transforming equations (2.20) and (2.25) to the frequency domain. The Fourier transform (F. T) of $\partial/\partial t$ is given by

$$\frac{\partial}{\partial t} \xrightarrow{\text{F.T}} i\omega\,, \tag{2.30}$$

where $i = \sqrt{-1}$ is the complex number. It follows that:

$$\frac{\partial^2}{\partial t^2} \xrightarrow{\text{F.T}} -\omega^2\,. \tag{2.31}$$

Therefore, equations (2.20) and (2.25) become

$$\nabla^2\hat{\mathbf{E}} + \hat{\mathbf{E}}\left(\omega^2\mu_0\varepsilon_0 - i\omega\mu_0\sigma\right) = 0\,, \tag{2.32}$$

and

$$\nabla^2\hat{\mathbf{H}} + \hat{\mathbf{H}}\left(\omega^2\mu_0\varepsilon_0 - i\omega\mu_0\sigma\right) = 0\,, \tag{2.33}$$

where $\hat{\mathbf{E}}$ and $\hat{\mathbf{H}}$ denote frequency domain of $\mathbf{E}$ and $\mathbf{H}$, respectively. To simplify the notation of equations (2.32) and (2.33), we introduce the following notation:

$$k^2 = \omega^2\mu_0\varepsilon_0 - i\omega\mu_0\sigma\,, \tag{2.34}$$

where k is the propagation constant or complex wave number in the medium. The term $\omega^2\mu_0\varepsilon_0$ describes displacement currents while $\omega\mu_0\sigma$ represents the conduction currents in Maxwell's Equations.

Using equation (2.34), equations (2.32) and (2.33) can be rewritten as:

$$\left(\nabla^2 + k^2\right)\hat{\mathbf{E}} = 0\,, \tag{2.35}$$

$$\left(\nabla^2 + k^2\right)\hat{\mathbf{H}} = 0. \tag{2.36}$$

Equation (2.32) through equation (2.36) are the wave equations in the frequency domain, or, the Helmholtz equations in $\hat{\mathbf{E}}$ and $\hat{\mathbf{H}}$. They represent the separation of the variable $\mathbf{E}$ and $\mathbf{H}$ in Maxwell's Equations.

Typical rocks in marine EM exploration have conductivity values σ ranging between 10^0 and 10^{-6} $\mathrm{S\,m^{-1}}$, magnetic permeability in the free space $\mu_0 = 4\pi \times 10^{-7}$ $\mathrm{H\,m^{-1}}$ and an electric permittivity $\varepsilon_0 = 8.854\times 10^{-12}$ $\mathrm{F\ m^{-1}}$. As a consequence, σ is typically 10^9 times bigger than ε_0. Therefore, the displacement current term $\partial\mathbf{D}/\partial t$ is negligible. Also, the frequencies used in CSEM range from 10^{-2} to 10 Hz. Moreover, the value of the conductivity relative to the electric permittivity and the relatively low frequencies used in CSEM exploration yield to the following assumption:

$$\sigma \gg \varepsilon_0\omega\,. \tag{2.37}$$

Thus the first term of k^2 in equation (2.34) is negligible compared to the second term. The complex number k can be rewritten as:

$$k = (-i\omega\mu_0\sigma)^{\frac{1}{2}} = (i)^{\frac{1}{2}}(-i\omega\mu_0\sigma)^{\frac{1}{2}}\,. \tag{2.38}$$

Using Euler formula, the imaginary factor of equation (2.38) can be rewritten as:

$$i^{\frac{1}{2}} = \pm\left(\frac{\sqrt{2}}{2} + i\frac{\sqrt{2}}{2}\right) = \pm\frac{\sqrt{2}}{2}(1+i)\,. \tag{2.39}$$

Using equation (2.39) in equation (2.38), it follows that

$$k = (1-i)(\frac{\omega\mu_0\sigma}{2})^{\frac{1}{2}}\,. \tag{2.40}$$

Equation (2.40) can be expressed as

$$k = \alpha - i\beta\,, \tag{2.41}$$

in which $\alpha = \beta = \left(\dfrac{\omega\mu_0\sigma}{2}\right)$.

Following equation (2.37), the term containing ω^2 in equation (2.32) is negligibly small. Equations (2.32) and (2.33) become

$$\nabla^2\hat{\mathbf{E}} - i\omega\mu_0\sigma\hat{\mathbf{E}} = 0\,, \tag{2.42}$$

and

$$\nabla^2\hat{\mathbf{H}} - i\omega\mu_0\sigma\hat{\mathbf{H}} = 0\,. \tag{2.43}$$

The inverse Fourier transform of equation (2.42) and equation (2.43) yield to

$$\nabla^2\mathbf{E} - \mu_0\sigma\frac{\partial\mathbf{E}}{\partial t} = 0\,, \tag{2.44}$$

and

$$\nabla^2\mathbf{H} - \mu_0\sigma\frac{\partial\mathbf{H}}{\partial t} = 0\,. \tag{2.45}$$

Equation (2.42) through equation (2.45) represent diffusion equations. It is clear that the diffusion heavily depends on the frequencies of the measured field and on the conductivity σ that we want to find. It also depends on the depth of attenuation of the measured fields, which is discussed in the next section.

2.3 skin depth

The distance it takes to reduce the amplitude by a factor of $1/e$ is called the skin depth. It is a measure of how far the wave penetrates into the conductor.

Let us assume that the planar EM wave propagates vertically, that is, in the positive and negative $z-$direction, in our homogeneous and isotropic medium. This means that:

$$\frac{\partial\mathbf{E}}{\partial x} \equiv \frac{\partial\mathbf{E}}{\partial y} \equiv \frac{\partial\mathbf{H}}{\partial x} \equiv \frac{\partial\mathbf{H}}{\partial y} \equiv 0, \tag{2.46}$$

and

$$\frac{\partial\hat{\mathbf{E}}}{\partial x} \equiv \frac{\partial\hat{\mathbf{E}}}{\partial y} \equiv \frac{\partial\hat{\mathbf{H}}}{\partial x} \equiv \frac{\partial\hat{\mathbf{H}}}{\partial y} \equiv 0. \tag{2.47}$$

Therefore, for such a plane wave and using equation (2.46) and equation (2.47) in equation (2.42) through equation (2.45), the decomposition of the Laplace operator gives the following expression:

$$\frac{\partial^2\mathbf{H}}{\partial z^2} + k^2\mathbf{H} = 0\,, \tag{2.48}$$

$$\frac{\partial^2\mathbf{E}}{\partial z^2} + k^2\mathbf{E} = 0\,, \tag{2.49}$$

$$\frac{\partial^2\hat{\mathbf{E}}}{\partial z^2} + k^2\hat{\mathbf{E}} = 0\,, \tag{2.50}$$

and

$$\frac{\partial^2 \hat{\mathbf{H}}}{\partial z^2} + k^2 \hat{\mathbf{H}} = 0\,. \tag{2.51}$$

Equation (2.48) through equation (2.51) are second order linear differential equations and have solutions in the form of

$$\hat{\mathbf{E}}(\omega, z) = \hat{\mathbf{E}}^{+}(\omega) e^{-i(kz-\omega t)} + \hat{\mathbf{E}}^{-}(\omega) e^{i(kz+\omega t)}\,, \tag{2.52}$$

and

$$\hat{\mathbf{H}}(\omega, z) = \hat{\mathbf{H}}^{+}(\omega) e^{-i(kz+\omega t)} + \hat{\mathbf{H}}^{-}(\omega) e^{i(kz+\omega t)}\,, \tag{2.53}$$

where $\hat{\mathbf{E}^{+}}(\omega)e^{-i(kz-\omega t)}$, $\hat{\mathbf{H}^{+}}(\omega)e^{-i(kz-\omega t)}$ represent the EM wave in the frequency domain propagating in the positive $z-$direction and $\hat{\mathbf{E}^{-}}(\omega)e^{i(kz-\omega t)}$, $\hat{\mathbf{H}^{-}}(\omega)e^{i(kz-\omega t)}$ represent the EM wave in the frequency domain propagating in the negative $z-$direction.

Now, we consider the propagation in the positive $z-$direction, and so, we can set the terms containing the propagation of the wave in the negative $z-$direction to zero. Equations (2.52) and (2.53) may be rewritten:

$$\hat{\mathbf{E}}(\omega, z) = \hat{\mathbf{E}}^{+}(\omega) e^{-i\alpha z} e^{-\beta z} e^{i\omega t}\,, \tag{2.54}$$

and

$$\hat{\mathbf{H}}(\omega, z) = \hat{\mathbf{H}}^{+}(\omega) e^{-i\alpha z} e^{-\beta z} e^{i\omega t}\,, \tag{2.55}$$

From equations (2.54) and (2.55) we may draw the following conclusions:

(1) Since β is positive, $e^{-\beta z}$ gets smaller as z gets larger. Hence it represents the attenuation. The intensity of an EM field decreases exponentially with increasing z by a factor of e^{-1} or to about 37% of its initial value. This is described by the skin depth δ, where

$$\delta = \frac{1}{\beta} = \sqrt{\frac{2}{\sigma \mu_0 \omega}} \approx 503 \left(\frac{1}{\sigma f}\right)^{1/2}\,. \qquad [m] \tag{2.56}$$

For propagation through a known distance z, the percentage of the original signal remaining A is given by

$$A = 100 \times (e^{-z/\delta})\,. \tag{2.57}$$

(2) $e^{-i\alpha z} = \cos(\alpha z) - i\sin(\alpha z)$ states that the wave varies sinusoidally with z.

(3) $e^{i\omega t} = \cos(\omega z) - i\sin(\omega t)$ states that the wave varies sinusoidally with t.

Skin depth is the most important concept in any EM method. As shown in equation (2.56), the skin depth heavily depends on:

1- The conductivity of the structures surveyed. Higher conductivity (or lower resistivity) materials attenuate EM fields more rapidly and have smaller skin depths than lower conductivity (or higher resistivity) materials for a given frequency. Figure 2.2 shows how the skin depth varies as the resistivity increases from 0.2 Ω m to 1000 Ω m. For example, at a frequency of 1 Hz (orange line), the skin depth in sea water with resistivity of 0.02 Ω m, is about 270 m; this means that over each 270 m the amplitude of EM energy decays by a factor of e^{-1}. If however, the material has a resistivity of 1 Ω m, the same EM field decays by a factor e^{-1} after travelling 500 m. In basalt with resistivity of 1000 Ω m, the skin depth is 16 000 m. It is clear that skin depth in seafloor sediments are larger than in seawater. This means that, in the case of marine CSEM, EM energy will propagate from the source dipole to the receivers mostly through seafloor sediment, making the method sensitive to seafloor geology.

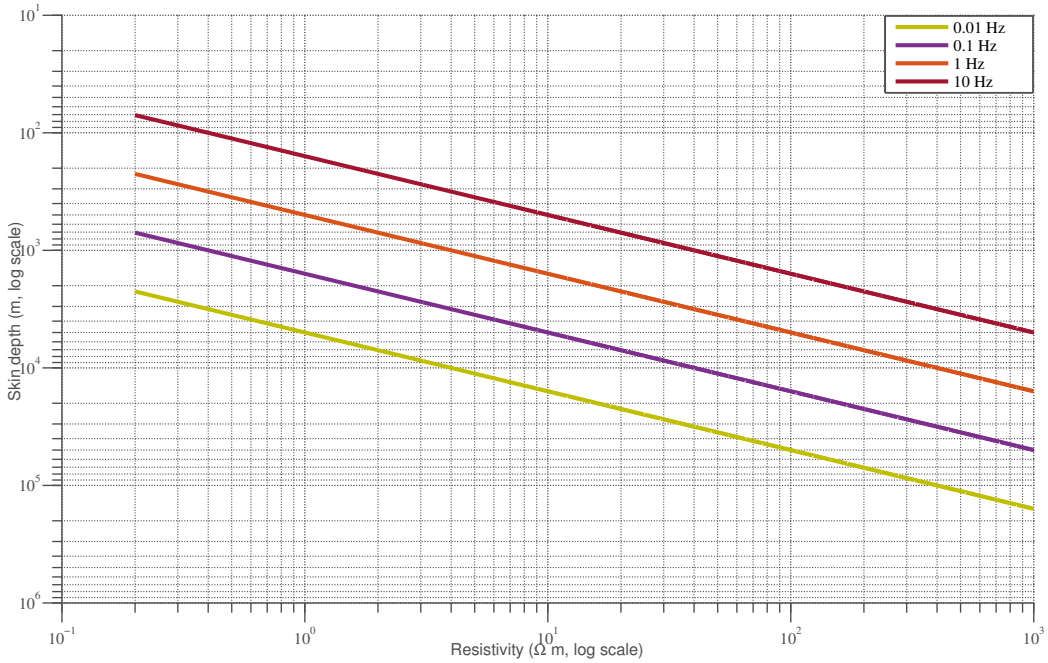

Figure 2.2: Skin depth as a function of resistivity for four frequencies:0.01 Hz (light green), 0.1 Hz (purple), 1 Hz (orange) and 1 Hz (red)

2- The frequency of the field and varies as f^{-1}, that is, the lower the frequency, the

larger the skin depth. This behaviour allows different depths to be probed by a set of discrete frequencies.

2.4 Point electric dipole source in an unbounded medium

Maxwell's equations 2.1-2.4 are known as the homogeneous equations that apply in source-free regions. In this section, we consider an electromagnetic field generated by a point dipole sources and propagated in a medium with a given distribution of electromagnetic parameters ε_0, μ_0, and σ. We consider the inclusion of electric current sources and ignore magnetic sources. Furthermore, we also ignore displacement currents because they are negligible in conducting materials in the earth at frequencies below about 10^5 Hz. Equations (2.13) and (2.14) become:

$$\nabla \times \mathbf{E} + \mu_0 \frac{\partial \mathbf{H}}{\partial t} = 0\,, \tag{2.58}$$

$$\nabla \times \mathbf{H} - \sigma \mathbf{E} = \mathbf{J_s}\,, \tag{2.59}$$

in which equation (2.58) is the same as equation (2.13) and equation (2.59) is from equation (2.14) without the displacement current term and with the new source current term on the right-hand side. We proceed as above. First, take the curl of equations (2.58) and (2.59) to obtain

$$\nabla \times \nabla \times \mathbf{E} + \mu_0 \frac{\partial}{\partial t} (\nabla \times \mathbf{H}) = 0\,, \tag{2.60}$$

$$\nabla \times \nabla \times \mathbf{H} - \sigma (\nabla \times \mathbf{E}) = \nabla \times \mathbf{J_s}. \tag{2.61}$$

Substitution for $\nabla \times \mathbf{H}$ from equation (2.60) into equation (2.61) yields a vector diffusion equation for the electric field:

$$\nabla \times \nabla \times \mathbf{E} + \mu_0 \sigma \frac{\partial \mathbf{E}}{\partial t} = -\mu_0 \frac{\partial \mathbf{J_s}}{\partial t}\,, \tag{2.62}$$

and substitution for $\nabla \times \mathbf{E}$ from equation (2.58) into equation (2.61) yields a diffusion equation for the magnetic field:

$$\nabla \times \nabla \times \mathbf{H} + \mu_0 \sigma \frac{\partial \mathbf{H}}{\partial t} = \nabla \times \mathbf{J_s}\,. \tag{2.63}$$

Ward and Hohmann (1989) derive the response to a point dipole source located at the origin and pointing in the $x-$direction in Cartesian coordinates. The coordinate system, with the source included, is shown in Figure 2.3. Since the source current is point dipole, it can be represented by a line current of length ds. That is, the source is defined as:

$$\mathbf{J_s}(\mathbf{r}) = Ids\delta(x)\delta(y)\delta(z)H(t)\mathbf{i}\,. \tag{2.64}$$

in which I is the current amplitude (amp) and Ids is the dipole moment (amp-m), $H(t)$ is the Heaviside step function, and $\mathbf{i}$ (coming out of page) is the unit vector in the $x-$direction.

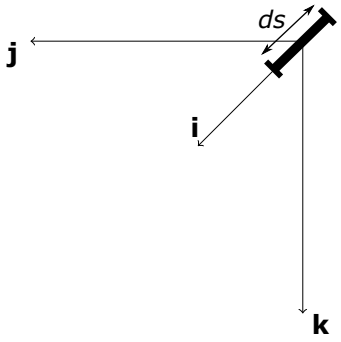

Figure 2.3: The Cartesian coordinate system is shown with the point source dipole included. $\mathbf{i}$ is coming out of page. The dipole is oriented in the $x-$direction.

The solution for equation (2.62) with the source equation (2.64) is given by Ward and Hohmann (1989) as their equation (2.50)

$$\begin{aligned}\mathbf{E}_{step} = \frac{Ids}{4\pi\sigma r^3}\left\{\left[\left(\frac{4}{\pi^{1/2}}\theta^3 r^3 + \frac{6}{\pi^{1/2}}\theta r\right)e^{-\theta^2 r^2} + 3erfc(\theta r)\right]\left[\frac{x^2}{r^2}\mathbf{i} + \frac{xy}{r^2}\mathbf{j} + \frac{xz}{r^2}\mathbf{k}\right]\right\} \\ - \frac{Ids}{4\pi\sigma r^3}\left[\left(\frac{4}{\pi^{1/2}}\theta^3 r^3 + \frac{2}{\pi^{1/2}}\theta r\right)e^{-\theta^2 r^2} + erfc(\theta r)\right]\mathbf{i}\,,\end{aligned} \tag{2.65}$$

in which $\mathbf{i}$, $\mathbf{j}$, and $\mathbf{k}$ are unit vectors in the x, y and z directions,

$$r = (x^2 + y^2 + z^2)^{1/2}\,, \tag{2.66}$$

$$\theta = \left(\frac{\mu_0\sigma}{4t}\right)^{1/2}\,, \tag{2.67}$$

and *erfc* is the complementary error function. It is expressed as

$$erfc(\theta r) = 1 - erf(\theta r) = 1 - \frac{2}{\pi^{1/2}} \int_0^{\theta r} e^{-\xi^2} d\xi \,. \tag{2.68}$$

where a new variable $\xi = \sqrt{\omega t}$.

Following Ziolkowski's CSEM course note, we can think of this solution as the step response of the linear electromagnetic system. To obtain the impulse response, we differentiate the step response. That is, the input current becomes the impulse

$$\frac{\partial \mathbf{J_s}}{\partial t} = \frac{\partial (Ids\delta(x)\delta(y)\delta(z)H(t))}{\partial t}\mathbf{i} = Ids\delta(x)\delta(y)\delta(z)\delta(t)\mathbf{i}\,, \tag{2.69}$$

and the impulse response is the time derivative of equation (2.65), we obtain

$$\begin{aligned} \mathbf{E}_{impulse} = \frac{\partial \mathbf{E}_{step}}{\partial t} = \frac{Idse^{-\theta^2 r^2}\theta^3}{\pi^{3/2}\sigma t}\{1 - \theta^2(y^2 + z^2)\}\mathbf{i} \\ + \frac{Idse^{-\theta^2 r^2}\theta^5 xy}{\pi^{3/2}\sigma t}\mathbf{j} \\ + \frac{Idse^{-\theta^2 r^2 \theta^5 xy}}{\pi^{3/2}\sigma t}\mathbf{k}\,. \end{aligned} \tag{2.70}$$

which is a simpler expression than equation (2.65) for electric field.

In conclusion, the depth of investigation and resolution of marine CSEM is limited by the frequency content. To image a target buried at a given depth below seawater, EM fields have to reach the target and travel back up to the receiver with an amplitude much greater than the noise floor. It has been shown that the skin depth of EM fields increases with decreasing frequencies. So, high frequencies are limited to sensing shallower targets. To image a deep target, low frequencies are required, but if the target is small compared to the transmitted wavelength, the resolution of the object will be lost (Mittet and Morten, 2012). Chosen the frequency bandwidth in marine CSEM is a trade-off between the high frequencies to have a good resolution and low frequencies to image deeper.

Summary

The equations governing the behaviour of electromagnetic waves in source-free regions and with a point dipole sources have been expounded in this chapter. From the source-free regions equations, the diffusion equation and skin depth have been derived. The latter is a serious impediment to imaging and to resolving small targets at depth. In addition, noise originating from various sources such as environmental types and from the receiver itself may limit the depth of investigation of marine CSEM if they are not addressed.

■

3

Sources of Noise in the Node-based and Towed Streamer CSEM Systems

One man's meat is another man's poison.

Titus Lucretius Carus (c. 99 BC - c. 55 BC), De rerum natura
Latin writer

I investigate various sources of noise which affect data acquired with a towed streamer CSEM. This chapter presents a definition of shallow, intermediate and deep water, which is used throughout this thesis. I analyse the sources of noise and review the approaches in the literature to identify and reduce noise levels in node-based CSEM. Motionally-induced noise, magnetotelluric noise, and electrode noise are believed to be the sources of noise affecting towed streamer CSEM. The analysis contained in this chapter demonstrates that the key to improving the signal-to-noise ratio of towed streamer CSEM is to reduce the effect of motionally-induced noise and to use a pseudo random binary sequence as source waveform.

3.1 Shallow, intermediate and deep water

Throughout this Ph.D. thesis, shallow water is defined as 400 m or less. This corresponds to the operational depth of the towed streamer CSEM system (Mattsson et al., 2013). Intermediate depth is between 400 m and 1000 m, and deep water is greater than 1000 m. The difference between these water depth terms is summarised in Figure 3.1.

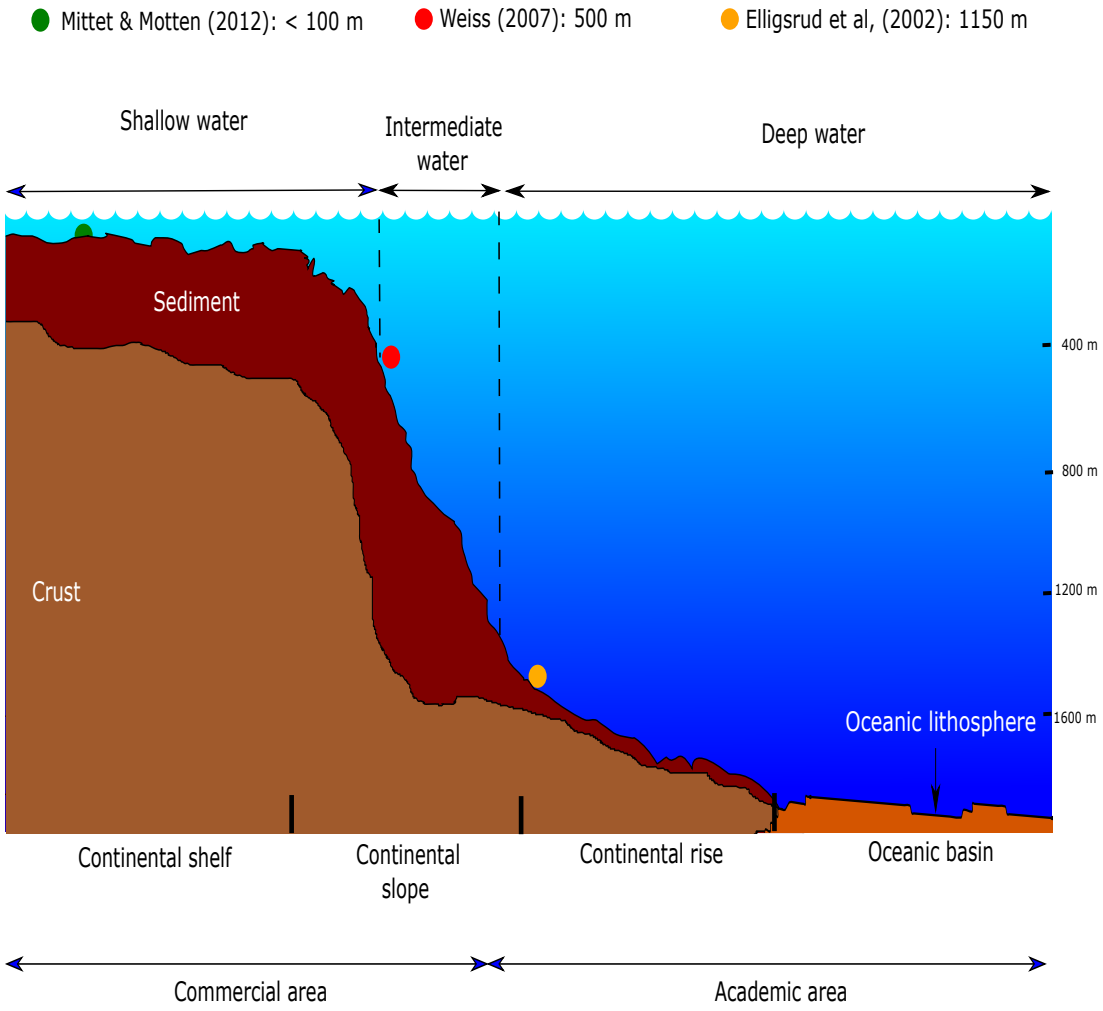

Figure 3.1: Illustration of the difference between shallow, intermediate and deep water. Definitions according to some authors are also plotted.

However, within the large number of the publications on marine CSEM reviewed for this Ph.D. project, I found no consistent definition for shallow, intermediate, and deep water. The difference between these terms in previous publications is based either on operational depths of the receiver system or is simply an arbitrary choice. Table 3.1 summarises the variety of definitions that have been used for deep, shallow, and interme-

diate water depths. The large variability in depth definitions contributes to confusion. The change in the meaning attached to these terms is more striking between commercial compared with academic applications. For academic applications, CSEM is mostly used in water depths greater than or equal to 3000 m to study the shallow resistive part of the oceanic lithosphere (Constable and Cox, 1996) and to detect features such as conductive magma chambers (MacGregor et al., 2001). For commercial applications, CSEM is used in water 40 m (Darnet et al., 2010) to 1200 m (Ellingsrud et al., 2002) depth to sense horizontal resistors of a sufficient size that may contain hydrocarbons.

Definition	Water depth (m)	Authors
Deep water	$\geqslant 3000$	Constable and Cox (1996); Evans et al. (1991) and Young and Cox (1981).
	$\geqslant 1000$	Shantsev et al. (2012),Constable (2010), Constable and Srnka (2007) and Ellingsrud et al. (2002).
	$\geqslant 500$	Shantsev et al. (2013) and Ziolkowski et al. (2011).
	$\geqslant 300$	Darnet et al. (2010), Sasaki and Meju (2009) and Andrés and MacGregor (2007).
Shallow water	$\leqslant 500$	Connell and Key (2012) and Ziolkowski et al. (2011).
	$\leqslant 300$	Ziolkowski and Wright (2010), Sasaki and Meju (2009) and Weiss (2007).
	$\leqslant 200$	Barker et al. (2012).
	$\leqslant 100$	Mittet and Morten (2012).
Intermediate water	$\geqslant 500$	Weiss (2007).
	$1900 - 2200$	Weitemeyer and Constable (2010).

Table 3.1: Water depth definitions based on published papers.

3.2 Definition and units

The performance of a towed streamer CSEM system in shallow water greatly depends on the amplitude of the source signal and the level of noise present in the recorded data.At one receiver dipole (channel), marine towed streamer CSEM acquisition and processing may be described by means of the convolutional model:

$$v(t) = \underbrace{\Delta x_r \Delta x_s \mathcal{I}(t) * \mathcal{G}(t)}_{Signal} + \underbrace{\mathcal{N}(t)}_{Noise}, \qquad [\mathrm{V}] \qquad (3.1)$$

in which $v(t)$ is the measured voltage at the receiver dipole, Δx_r is the length of the receiver dipole, Δx_s is the length of the source dipole, $\mathcal{I}(t)$ is the input current, $\mathcal{G}(t)$ is the unknown impulse response of the earth, the asterisk $*$ denotes convolution and $\mathcal{N}(t)$ is the noise, which is what would be measured if the source were switched off during the recording (that is, $\mathcal{I}(t) = 0$). Figure 3.2 is a sectional view of one possible marine towed streamer CSEM setup showing a dipole source and a line of electrode pairs in-line with the source.

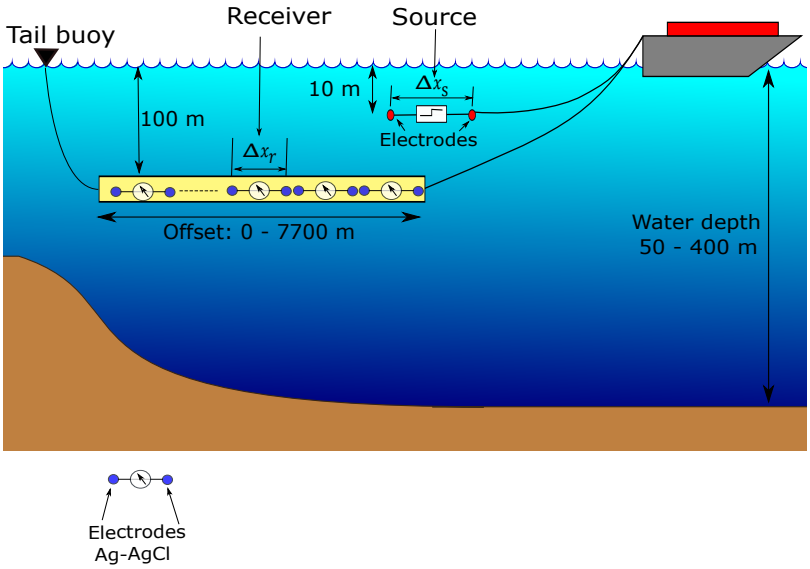

Figure 3.2: Sketch showing the towed streamer CSEM source-receiver configuration. A source antenna powered by the source vessel's generator. The receiver streamer is almost inline with the source and consists of an array of silver-silver chloride electrodes. A tail buoy is a floating unit that enables monitoring the position and direction of the streamer.

Equation 3.1 contains two independent terms - a source signal part $\Delta x_r \Delta x_s \mathcal{I}(t) * \mathcal{G}(t)$ and a noise part $\mathcal{N}(t)$. A CSEM signal is a time-varying EM field that is sensitive to resistivity variation at various locations and depths. Changing the source signal has no effect on the noise level and vice versa.

When a time-varying current is injected between two source electrodes, the resulting time-varying voltage is measured simultaneously at the receiver. The units of measurement for an electric field receiver are volts (V), as shown in equation (3.1). Since receiver lengths can vary, the measured voltage is normalised by receiver length to enable measurements made over different receiver lengths to be compared. The result of this normalisation is the electric field expressed in volts per metre ($\mathrm{V\,m^{-1}}$). Equation 3.1 therefore becomes:

$$\frac{v(t)}{\Delta x_r} = \underbrace{\Delta x_s \mathcal{I}(t) * \mathcal{G}(t)}_{S(t)} + \frac{\mathcal{N}(t)}{\Delta x_r}\,. \qquad [\mathrm{V\,m^{-1}}] \qquad (3.2)$$

However, it is common practice amongst many practitioners to scale the noise level by the source dipole moment: the source dipole length multiplied by the source current (Constable, 2010; MacGregor et al., 2001). This results in the electric field being expressed in volts per ampere per metre squared ($\mathrm{V\ A^{-1}m^{-2}}$). Constable and Srnka (2007) state that "data for interpretation are normalized by the dipole moment, so the system noise floor gets lower as the input current gets larger". MacGregor et al. (2001) give the noise level as approximately 10^{-11} $\mathrm{V\ A^{-1}m^{-2}}$ at 10^{-1} Hz, based on a notional dipole moment of 4500 A m measured by a 10 m long receiver. Using the same receiver and increasing the source dipole moment to 12 000 A m, the noise level is reduced to approximately 10^{-14} $\mathrm{V\ A^{-1}m^{-2}}$ at 10^{-1} Hz. Increasing the source dipole moment increases the signal-to-noise ratio but has absolutely no effect on the noise level recorded at the receiver.

This practice of normalizing by the source dipole moment is not helpful in understanding the noise. Therefore, here, and in the rest of my Ph.D. thesis, I have chosen to quantify the noise in units of V if referring to the electrode noise or in $\mathrm{V\,m^{-1}}$ if referring to electric field sources (MT noise and motionally-induced noise).

Since seismic acquisition is well known and understood, it is useful to present the CSEM acquisition principles in relation to seismic data acquisition. In seismic acquisition, the receiver measures the motion (e.g velocity) or the pressure at a point as shown in Figure 3.3(a). In CSEM we measure the voltage difference between two electrodes that have instantaneous potentials. The two electrodes are connected by a telluric cable which is connected to an amplifier as illustrated in Figure 3.3(b). The electrode pair length varies between 8 m (EMGS receiver length, (Mittet and Morten, 2012)) and 10 m (Scripps Institution of Oceanography) for the node-based CSEM method, and ranges from 200–1100 m for the towed streamer CSEM system (Mattsson et al., 2013).

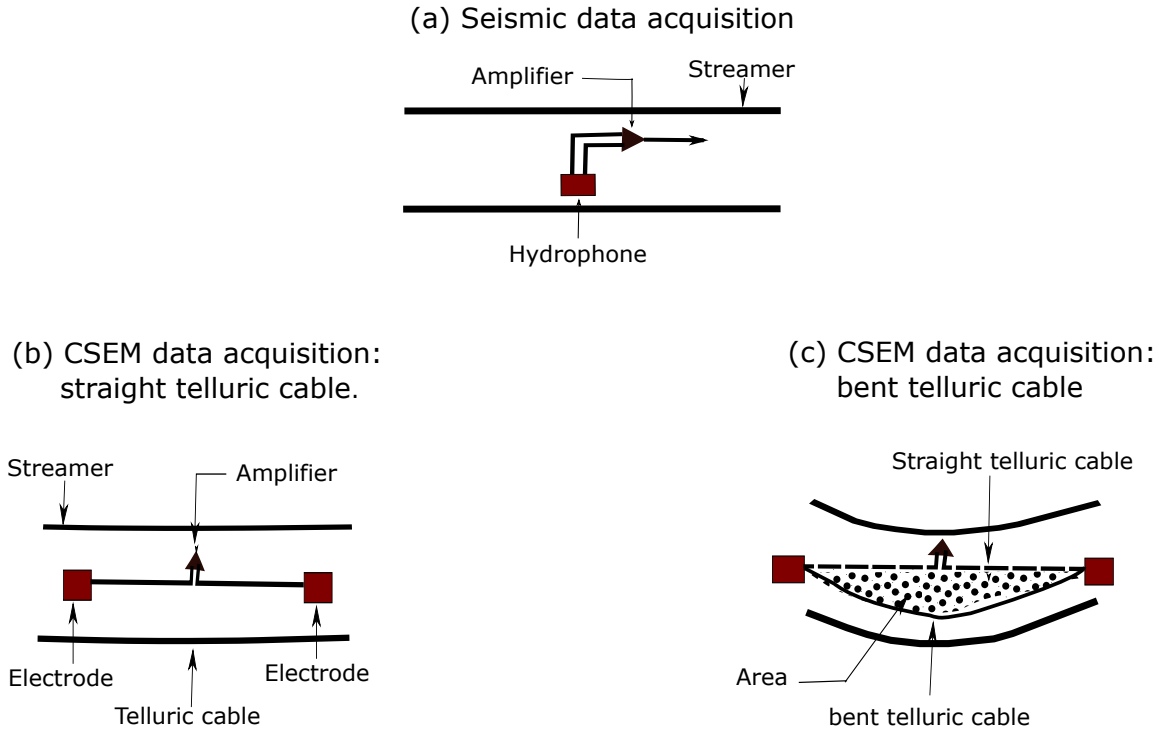

Figure 3.3: Schematic representation seismic and EM data acquisition. Top: (a) A hydrophone measures the pressure at a point. Bottom: Two electrodes measure the instantaneous potential difference between two points to give a voltage. (b) The telluric cable connecting the two electrodes is straight (ideal position). (c) The telluric cable connecting the two electrodes is bent. This may be caused by wave motion or cross-currents on the sea.

Given the CSEM measurement configuration, there are two principal sources of CSEM noise at the receiver:

- Environmental electric field noise is due to sources such as the magnetotelluric (MT) field and the motionally-induced field. The latter is induced when the telluric cable between two electrodes is not fully stretched or bent (as the area shown in Figure 3.3(b)) because of water currents, microseisms, swell and tides. This is discussed further in Chapter 5. This type of noise is frequency, receiver length, and water depth dependent. In a deep water setting, the contribution of MT noise is limited since it is significantly attenuated by the thick water layer (Key, 2003). Motionally induce noise is also not a limiting factor because of the restricted influence of current on the cable in water depths greater than or equal to 3000 m. However, in shallower water, the intensity of water currents, swell, and tides increases substantially (Constable et al., 1998; Chave et al., 1991). As a consequence, because of its towing depth, the towed streamer CSEM is more affected by the motionally-induce noise than the static node-based CSEM. The environmental electric field is expressed in volts per metre ($\mathrm{V\,m^{-1}}$).

- Instrument noise (the electrodes and the electronics) generates noise by the contact of the electrodes surface or electronics (if there is a break in the receiver insulation) with an ionic conductor (salt or fresh water). The majority of instrument noise sources are independent of the antenna length (Webb et al., 1985) and are expressed in volts (V).

In the time domain, the sources of noise recorded by a channel can be expressed as (Connell and Key, 2012):

$$E_n(t) = E_i(t) + \frac{V_r(t)}{\Delta x_r}, \qquad [\mathrm{V\,m^{-1}}] \tag{3.3}$$

where $E_n(t)$ is the total noise measured at a channel, $E_i(t)$ is the environmental electric field noise, $V_r(t)$ is the noise originating from the electrodes and amplifiers, and Δx_r is the length of the electric receiver dipole in metres (m).

When towing the EM streamer in the sea, there are other sources of noise which must be taken into consideration. The direct consequence is an increase of $E_n(t)$ with equation (3.3) rewritten as:

$$E_n(t) = E_T(t) + E_i(t) + \frac{V_r(t)}{\Delta x_r}, \qquad [\mathrm{V\,m^{-1}}] \tag{3.4}$$

where $E_T(t)$ is the component of the noise generated due to the motion of the streamer in the Earth's magnetic field. It is expressed in $\mathrm{V\,m^{-1}}$. Equation (3.4) shows that the contribution from the motionally-induce noise $E_T(t)$ and the magnetotelluric noise $E_i(t)$ is independent of the measuring receiver length, however, the contribution from the electrode and amplifiers noise $V_r(t)$ can be reduced by increasing the receiver length. Webb et al. (1985) show that the use of very long receiver length reduces the effect of electrode noise. Details are given in Section 3.3.

The total uncertainty in the recorded data in marine CSEM can be estimated using the following formula (Mittet and Morten, 2012):

$$\epsilon = \sqrt{(\alpha F^m)^2 + (E_n(t))^2}\,, \tag{3.5}$$

where F^m is the magnitude of a measured field component. The quantity α is the uncertainty that arises because of inaccuracies in source and receiver positions and orientations. The quantity $E_n(t)$, is noise which can be caused by instrumentation or by any environmental electric field noise. α and $E_n(t)$ vary with water depth (Barker et al., 2012).

In the node-based CSEM system in deep water, the source is deep-towed at 10–50 m

above the seafloor at a nominal speed of 1.5 kn. This is the minimum speed to keep some control of the source (Ziolkowski and Wright, 2012). Even at this low speed, the source electrodes may be perturbed by lateral sea currents leading to their deviation from the tow direction. Short-baseline acoustic system on both the source vessel and on the receiver electrodes combined with the transponders on the source electrodes are typically used to obtain the source and receiver in water depths of less than 3 km (Ziolkowski and Wright, 2012; Barker et al., 2012). When operating in deep water, a long tow cable from the source vessel pulls the source through the water at 30–50 m above the seafloor (Shantsev et al., 2012). Uncertainties in the source position are significant because of the difficulty to maintain source electrodes at fixed depth and to measure their lateral position accurately. Constable (2010) argues that α in equation (3.5) are the biggest limitations on node-based CSEM data quality. That is, the effect of $E_n(t)$ (see equation (3.3)) is small compared with αF^m in deep water.

In the towed streamer CSEM system, the source and receiver are towed close to the sea surface, at a depth of 10–100 m below the sea surface. Therefore, their positions are known accurately with GPS (Global Positioning System). Therefore the relative uncertainty of the source and receiver positions α is reduced significantly and is not a limiting factor. So, the noise term $E_n(t)$ (see equation (3.4)) is the biggest source of noise as it is independent of the source-receiver position. The identification and quantification of the different sources of noise in the towed streamer CSEM system may lead to

(1) modification of the acquisition parameters in order to reduce the noise during data acquisition,

(2) the prediction and subsequent subtraction of this noise from the recorded data.

Working on sources of noise for the marine towed streamer CSEM system, it is worth considering noise sources found in state-of-the-art node-based CSEM systems.

Regardless of their source, noise can be divided into two categories: incoherent and coherent (correlated) noise. In a multichannel dataset, incoherent noise does not correlate either with neighbouring channels (i.e no spatial correlation) or along the time series of the same channel (no temporal correlation). In contrast, coherent noise correlates spatially and/or temporally from channel to channel.

The nature of some noise is known: MT noise is described as spatially-correlated from receiver to receiver (Ziolkowski et al., 2010). In the literature, microseism and swell are described as noise which occur at a specific frequency and create spurious peaks in the measured signals: they have been observed between 0.05 and 1 Hz (Weitemeyer

and Constable, 2010; Kedar et al., 2008; Webb et al., 1985). However, the nature of motionally-induced noise in the towed streamer CSEM is not well understood. Resolving the nature of these noise sources is the major goal of my thesis.

3.3 Electrode and amplifier noise

Electrodes used in the node-based CSEM system are similar to those used in the towed streamer CSEM.

A pair of electrodes is used to measure the electric field in seawater. Since the conductive sea water filters EM fields, the electrodes used in marine CSEM have to be extremely sensitive in order to measure the small electric field on the seafloor (Brady et al., 2009). All electrodes fall into two categories:

Non-polarisable electrodes are robust and have excellent long term stability. One example of this electrode is the silver-silver chloride (Ag-AgCl) electrode, which is commonly used to make contact with seawater in marine CSEM electric field measurements.

The Ag-AgCl electrodes consist of metallic silver (Ag) that is coated with a thin layer of solid silver chloride (AgCl). In a commercial application, the electrode is encapsulated and immersed in a solution containing ions of the metal in high concentration (Corwin, 1973; Ives and Janz, 1961). This is done to ensure that the electrode operates in a reversible in order to give meaningful readings (Corwin, 1973). The contact with the sea water is made through a porous barrier that has a low fluid leakage rate. The electrode reversible reaction is:

$$\mathrm{Ag} + \mathrm{Cl}^- \rightleftharpoons \mathrm{AgCl} + \mathrm{e}^- \,. \tag{3.6}$$

The relative insolubility of AgCl and its compatibility with the major anion in seawater makes this a stable and practical electrode for marine use (Constable, 2013). However, electrodes that are not immersed in their own ions work and can be used for academic applications. This is the type of electrodes that were used during the experiments in the FloWave tank described in Chapter 6.

Traditionally, in marine CSEM, the electrodes are housed in the receiver unit arms, 8–10 m in length, and are connected to an amplifier through telluric cables. This amplifier generates noise which is very small compared with the electrode noise (Connell and Key, 2012). In the following analysis, I have chosen to group the amplifier noise with the electrode noise.

Despite the recent innovations, there are still factors limiting the detection and imaging of the reservoir in marine CSEM. The electrode self-noise rather than natural ambient noise is a source of electric field noise above 1 Hz (Mittet and Morten, 2012; Constable and Weiss, 2006; Hoversten et al., 2006; Constable et al., 1998; Filloux, 1980). According to Cox et al. (1978) and Corwin (1973), noise related to the electrodes arises from random rearrangements, temperature, salinity variations (the result of electrochemical processes on the electrode surfaces) and chemical reactions within the electrodes. Concerning its characteristic, Mittet and Morten (2012); Hoversten et al. (2000) and Cox et al. (1978) reported that the electrode noise spectrum seems to follow a f^{-1} law up to 0.1 Hz, and has a constant level above this frequency. This constant level is associated with noise from the amplifier (Constable et al., 1998). Another limiting factor is the related to the receiver noise-floor.

In node-based CSEM, the noise floor of the receivers in use today in 40 m water is about 8×10^{-10} V (8 m long receiver) (Mittet and Morten, 2012) and about 2×10^{-10} V (10 m long receiver) in 900 m water (Constable, 2013). This noise is so important that the current depth of investigation could double if the receiver noise floor could be decreased by a factor of 10 (Mittet and Morten, 2012).

The necessity to keep the Ag-AgCl electrode wet and electrochemical effects at the surface of the electrode (due to temperature changes or variation of the salinity of the local environment) encouraged the use of polarisable or capacitive electrodes such as gold, titanium, and carbon fibre (Crona et al., 2001). Gold and titanium are never used for commercial purposes because they are too expensive. These electrodes are inert in the seawater and do not need an electrochemical interaction with the ionic solution. Quasar Federal System Inc. (QFS), a company specialised in the design and production of low-frequency electromagnetic sensing systems has developed and commercialised a new type of electric field receiver that employs chemical inert electrodes that couple capacitively to electric potentials in the Earth (Nielsen et al., 2009; Hibbs and Nielsen, 2008). Unlike the conventional node-based receiver, this new receiver does not require any long arms to obtain measurements and does not suffer from electrochemical problems. This capacitive interaction couple directly to the electric potential at a given point in the medium via the rate of change of the local electric flux density (Hibbs and Nielsen, 2008). Zhang (2011) compares QFS receiver (a pair of electrodes separated by 0.84 m) with the Scripps Institution of Oceanography (SIO) receiver (a pair of electrodes separated by 10 m) off the Australian coast. Zhang (2011) shows that the sensitivity of the capacitive electrodes is similar to the SIO Ag-AgCl electrodes in the frequency bandwidth 0.003–1 Hz.

3.4 Magnetotelluric noise

The magnetotelluric (MT) signal originates from sources such as the magnetosphere and ionosphere. It is spatially correlated over many kilometers and is time-variant (Gamble et al., 1979). For MT studies, the MT signal is present at frequencies ranging from 0.001–10^4 Hz (Vozoff, 1991). Within this frequency range, three source regions are important. At frequencies below 1 Hz, the amplitude of the MT field increases rapidly with decreasing frequency. Solar wind interaction with the Earth's magnetosphere is the dominant cause of fields in this frequency range (Simpson and Bahr, 2005). At about 1 Hz, is the so-called *dead-band* where MT fields are typically weak. At frequencies above 1 Hz, MT fields have their origins in meteorological activity such as lightning discharges (Simpson and Bahr, 2005). In marine CSEM, MT signals are noise.

In water deeper than 3000 m, the contribution of MT fields to the noise level is small because the "skin effect" of the thick conductive seawater layer attenuates the signal (Constable et al., 1998). However, in towed streamer CSEM, the streamer is towed 100 m from surface. This water layer is not deep enough to attenuate the strong arrival of MT fields (Ziolkowski and Wright, 2012).

Efforts have been made to reduce the effect of MT noise in shallow water. de la Kethulle de Ryhove and Maaø (2008) propose a survey design method to partially remove MT signals recorded by the receiver during periods of high MT activity. The method consists of subtracting MT signals by multi-station analysis since MT signals are spatially correlated. This method consists of: first, deploying two or three receiver nodes outside the survey area (remote) as well as inside the survey area when the source dipole is not transmitting a signal. Calculate transfer functions between the remote and the survey area. These transfer functions are dependent on the frequency, survey geometry, subsurface conductivity structure and seawater conductivity but are independent of the MT signals that are recorded at different receiver nodes. When the source transmits a signal, these transfer functions are used to estimate and remove the MT signals in the data recorded in the survey area with the source signal present, based on the source-free remote measurement of the MT signal. Although the technique shows good results with node-based receiver data, it would be expensive to implement for the marine towed streamer CSEM system because of the additional cost of deploying receiver nodes away from the survey area. It comes down to doing the survey twice and using node-based receivers (for the remote survey) which one is trying to avoid by towing the receivers.

Ziolkowski et al. (2010) estimate and remove MT noise on each trace for transient data collected with a multi-channel ocean bottom cable (OBC). The technique consists

of deconvolving a source gather for the measured current. This results in the signal being compressed to impulse responses with noise still present at late times. Then, an estimate of the noise on a near-offset single trace is obtained by subtracting the short impulse response from the raw common-source gather. This noise estimate is similar to the noise on other traces. Once the noise is estimated, it can be subtracted from the trace to reveal the impulse response. This method increases the signal-to-noise ratio by up to 20 dB. This is equivalent to increasing the source signal by a factor of 10 (700 to 7000 A) or to removing 90 % of the noise. This technique works well on correlated noise present in ocean bottom cable (OBC) data and can be used for the removal of noise in the towed streamer CSEM if the source signal is transient (source signals that have a beginning and an end). On contrary, conventional CSEM source uses a continuous source signal) and the dominant noise is correlated. However, as I show in Chapter 4, in towed streamer CSEM, the majority of noise is not correlated from channel to channel within the frequency bandwidth of interest (0.01–1 Hz).

3.5 Motionally-induced noise

The motion of an electric field antenna wire at velocity $\mathbf{v}$ in Earth's magnetic field $\mathbf{B}$ results in an induced electric field (Constable, 2013):

$$\mathbf{E} = \mathbf{v} \times \mathbf{B}. \qquad [\mathrm{V}] \tag{3.7}$$

For the node-based CSEM, the physical shaking, due to mechanisms such as microseism and swell (described in the next section), or the motion of the receiver unit and electrode arms due to seafloor water currents, is troublesome for electric field measurements (Mittet and Morten, 2012; Summerfield et al., 2005). During a CSEM survey carried out in 1850 m water depth, under high tidal water currents, Summerfield et al. (2005) observed that high levels of motionally-induced noise, with peak frequencies typically around 0.3 Hz and 0.7 Hz along with harmonics, affected all data channels. The noise was caused by the vibration of the receiver electrode arms in response to water currents. In fact, a small vibration of the electrode arms can induce noise levels well within the range of measurements (Constable, 2013). It is, therefore, important to mitigate their effect.

Mittet and Morten (2012) and Summerfield et al. (2005) describe two survey techniques for the attenuation of vibration-induced noise from seafloor nodes. The first technique involves designing receivers and electrode arms with a shape that reduces hydrodynamic interaction (Mittet and Morten, 2012). Summerfield et al. (2005) show that substituting the PVC receiver arms with a stiffer one moved the dominant noise frequency at about

0.7 Hz outside the operational passband at 1.5 Hz. In addition, Summerfield et al. (2005) suggest that wrapping the electric field receiver arms with a fairing material can attenuate the motionally-induce noise levels, although Summerfield et al. (2005) never explicitly state by how much.

For the towed streamer CSEM, as the receiver sensors move in the seawater within the Earth's magnetic field, the contribution of the motionally-induced noise (Equation 3.7) is significant. This is one of the reasons why the technology was not in use until 2010. Chapter 5 is dedicated to explaining and estimating the mechanisms of this noise.

3.6 Microseism and swell noise

Longuet-Higgins (1950) proposed a mechanism that leads to the generation of microseisms based on the research carried by Miche (1944) on the theoretical study of wave motion. According to Longuet-Higgins (1950), the interaction between two waves with the same wavelength and same frequency travelling in opposite directions generates a long wavelength that does not attenuate with depth and therefore can reach the deep ocean floor. In the case of the towed streamer CSEM streamer, the long waves reach the EM streamer towed 100 m below the sea level as shown in Figure 3.4. This causes the streamer to vibrate (up-and-down) at a certain frequency. Therefore, the generation of microseisms depends mainly on the wave frequency. The question that needs to be addressed is: how does this mechanism create additional EM field noise on the receiver? In an attempt to answer the question and following Bhatt (2014)'s suggestion, it is clear that the water motion near the streamer, triggered by the wave travelling at velocity ($\mathbf{v_w}$) in the geomagnetic field ($\mathbf{B_0}$), generates a primary electric field according to the Lorentz law (i.e., $\mathbf{E} = \mathbf{v_w} \times \mathbf{B_0}$, similar to Equation 3.7), which in turn creates an EM signal detected by the receivers inside the streamer. The noise is typically present in the frequency band of 0.05–1 Hz (Kedar et al., 2008). From node-based CSEM data collected in 500 m water depth, Bhatt (2014) observes a prominent peaked spectrum at 0.1 Hz which he associates with microseism events.

Ocean swell is a wave that is free of fetch (where the wind transfers energy to the water surface and raises waves) and has a regular up-and-down and back-and-forth motion (Pinet, 2003). In shallow water, the noise due to the ocean swell is far greater than in deep water. Depending on weather conditions, swell noise is present at frequencies above 0.1 Hz (Mittet and Morten, 2012). From data acquired in 100 m water depth in the Gulf of Mexico, a peak at around 0.1 Hz observed in the spectrum was associated with ocean swell noise (Hoversten et al., 2000). A way to tackle this noise would be to analyse its frequency spectrum during the deployment of the seabed receivers and

then optimize the source waveform to avoid the overlap of transmitter signal with any observed frequency bands of the swell (Mittet and Morten (2012); Shantsev et al. (2010)). In practice, the swell frequency is not constant and can vary during a survey. Therefore, swell noise can overlap with signal bandwidth.

Since the towed streamer CSEM streamer is towed 100 m below the sea surface, microseism and swell noise are particularly troublesome for the measurement of high-quality data.

In summary, Figure 3.4 illustrates the sources of noise in the towed streamer CSEM system. The sources of noise include the electrode and amplifier noise, MT field, and the motion of the streamer. This motion can be caused by three factors: water currents, the indirect effect of ocean swells that causes the motion of the towing cable, and the direct effect of ocean swells on the streamer. MT activity affects both the node-based and towed streamer CSEM system. However, it has already been identified and its nature is understood as described in Section 3.2. On the other hand, even though some progress has been made in the understanding and limitation of the effect of electrode and motionally-induced noise in the node-based CSEM, their contributions (in terms of noise level) is greater in the towed streamer CSEM. It is clear that the identification and quantification of the contribution of each source of noise in the towed streamer CSEM is required to improve the system.

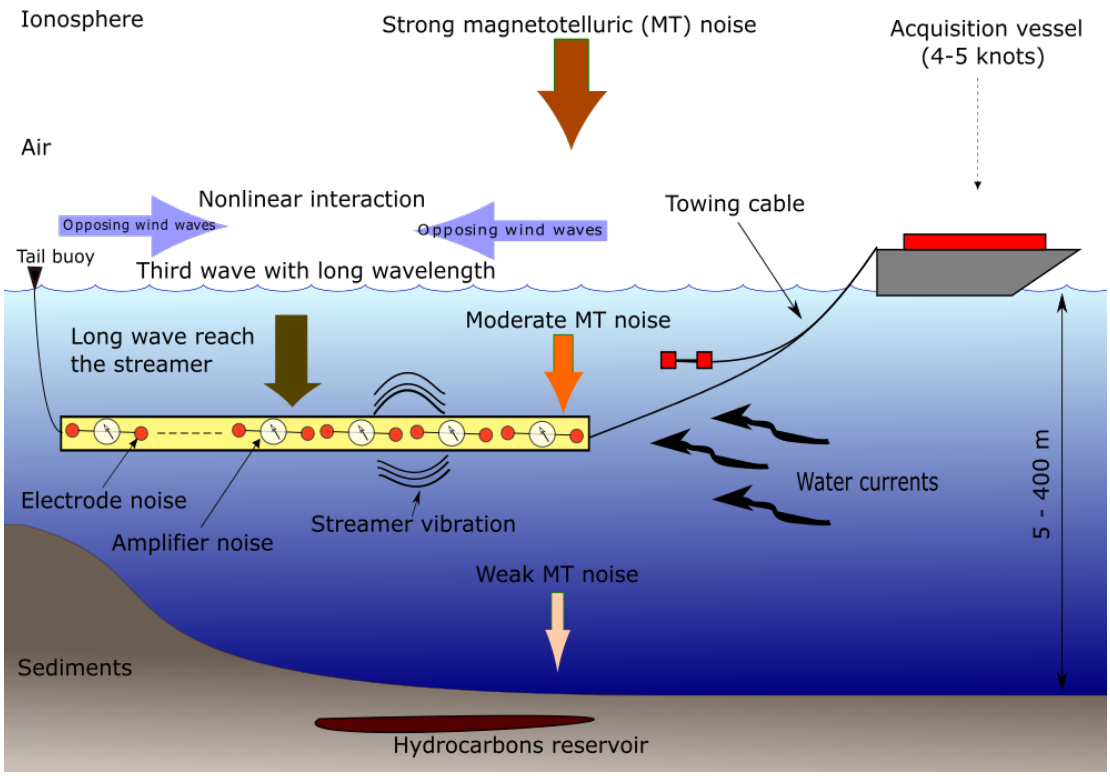

Figure 3.4: Illustration of the sources of noise in the towed streamer CSEM system (not to scale). Towing noise originates from the electrode and amplifier noise, MT field, and the motion of streamer due to water currents and ocean swells.

3.7 What does the signal-to-noise ratio look like?

Signal-to-noise ratio (often abbreviated to SNR) is a measure of signal strength relative to noise. It is used in signal processing as a quantitative measure of the performance of a system (Rutten et al., 1972) and is generally expressed in decibel (dB). The SNR is expressed as:

$$\text{SNR} = 20 \times \log_{10}\left(\frac{\text{Signal Amplitude (e.g V)}}{\text{Noise Amplitude (e.g V)}}\right). \qquad [\text{dB}] \qquad (3.8)$$

Node-based CSEM surveying was originally designed to operate in water depth greater than 1000 m (Eidesmo et al., 2002). As shown in the previous section, noise originating in the ionosphere is not a limiting factor, since the receiver nodes are deployed at the bottom of the deep ocean. In contrast, the towed streamer CSEM is towed at 100 m from the surface and is designed for water depth less than 400 m. As Barker et al. (2012), Anderson and Mattsson (2010) and Ziolkowski et al. (2010) explain, at this water depth there is more MT noise as there is less water to attenuate it. When towing the EM streamer there is an additional noise due to the movement of the receiver

electrodes in the water column (see equation (3.7)). In Chapter 4, it is shown that this towing noise is typically 20 dB above the level of the Ocean Bottom Cable system in the bandwidth of interest (0.01–1 Hz).

Therefore the benefits of towing an electromagnetic streamer in water, such as the ease of operation and the cost effective acquisition of EM data are counteracted by the increase noise levels. Increasing the signal-to-noise ratio by 20 dB is the biggest challenge associated with the towed streamer CSEM system. This leads to two questions that need to be addressed (with respect to Equation 3.8). First, by how much does the signal need to be increased? And second, by how much does noise amplitude need to be decreased? To address these questions, equation (3.8) can be rewritten as:

$$SNR = 20 \times \log_{10}\left(\frac{S(t)}{\frac{n(t)}{\Delta x_r}}\right) = 20 \times \log_{10}\left(\frac{S(t)}{E_T(t) + E_i(t) + \frac{V_r(t)}{\Delta x_r}}\right). \quad \text{[dB]} \qquad (3.9)$$

From equation (3.9), there are two ways to improve the signal-to-noise ratio. The first method consists of increasing the source amplitude, $S(t)$, specifically by increasing the source dipole moment (SDM): either by increasing the output current or lengthening the transmitter dipole or both. The second way to increase the SNR is to decrease the noise level, $E_T(t) + E_i(t) + \frac{V_r(t)}{\Delta x_r}$.

Let us start by analysing different ways to increase the SDM:

Increasing the source dipole moment (SDM): the signal has an amplitude proportional to the SDM. In the node-based CSEM method, dipole lengths are in the range of 100–300 m (Constable and Srnka, 2007) and the source current output up to 1000 A (Constable, 2010). That is, conventionally, the SDM is in the range 100–300 kA m

In the towed streamer CSEM, the current SDM in operation is 1200 kA m, with the source dipole typically 800 m and the source current output up to 1500 A (Mattsson et al., 2012). Using equation (3.9), an increase of the current SDM by a factor of 10 must be implemented to achieve the 20 dB increase in SNR. This increase could be possible if one uses a surface-towed configuration with the current source mounted on the deck of the vessel instead of using a traditional subsea encapsulation. EMGS uses this technique in water depths in the range 10–700 m. In this way, Barker et al. (2012) have been able to increase substantially the SDM, going from 350 kA m (conventional SDM) to 2160 kA m. This causes a 16 dB of the SNR of the measured data.

Although the increase in SDM increases the SNR, there are limitations associated with the source output amplitude and the length of the source. During a towed streamer CSEM survey, the source and receiver are intended to to stay straight behind the

acquisition vessel. The source is towed 10 m below the sea water, therefore, a source dipole longer than 800 m could increase the possibility for the source dipole to not accurately follow its acquisition path because of the strong effects of wave and water motion at such shallow depth. Increasing the source current amplitude above 1500 A increases the danger and complexity of shipboard operation, increases the cost of transmitting a high power through the tow cable down to the source unit, and could raise environmental concerns (Constable, 2010). More likely, increasing the SNR could be done by reducing the noise levels.

Following equation (3.9), a decreasing in the noise can be achieved in three ways:

1. **Increase the receiver length, Δx_r:** Constable (2013); Connell and Key (2012) and Webb et al. (1985) argue that the length of the receiver can be increased to overcome the presence of electrode noise, thereby improving signal-to-noise ratio for electric field measurements. The reason for this is clear from the third term of the denominator of equation (3.9). Ideally, this implies that

$$\Delta x_r \to \infty, \quad \text{therefore,} \quad \frac{V_r(t)}{\Delta x_r} \to 0. \tag{3.10}$$

   In practice, the receiver length is not infinite. In the node-based CSEM, the receiver length is 10 m. In deep water, it has been shown that receiver lengths up to 3000 m (Webb et al., 1985) are three times less noisy than 1000 m (Constable and Cox, 1996) long receivers. These receivers are also proven to be two orders of magnitude smaller in noise levels than the conventional 10 m long receivers. Doing this works because E_T and $E_i(t)$ have a limited effect in water at these depths, and proves that the major source of noise in their system was caused by electrode noise, V_r. This is shown in Figure 3.5(a). However, if one assumes that the electrode noise in 40 m water depth is 8×10^{-10} V above 0.1 Hz (Mittet and Morten, 2012), and that E_T is equal to 10^{-7} V m^{-1} (Constable, 2013), then one can conclude from Figure 3.5(b) that having receiver length up to approximately 500 m causes an increase in SNR of only 0.04 dB. In short, given the state of equipment used today, this demonstrates that making the receiver significantly longer (more than 500 m) would not have any change in the SNR. Increased SNR cannot be achieved unless the dominating term E_T is reduced as a first step.

2. **Reduce the electrode noise level, $V_r(t)$:** the present electrode noise value is 10^{-10} V m^{-1} for 8 m long receiver (Mittet and Morten, 2012). For $E_T = 10^{-7}$ V m^{-1} (Constable, 2013) and using equation (3.9), one can show that the increase of SNR is only 0.02 as V_r decreases by a factor up to 10 for example. Further

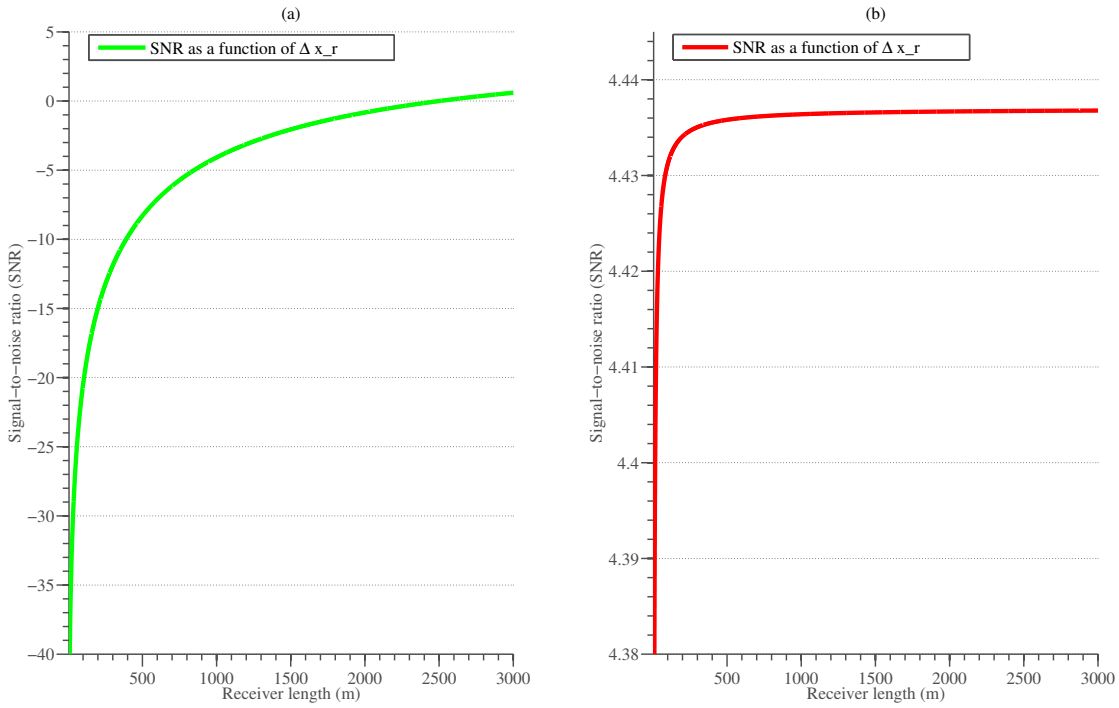

Figure 3.5: Signal-to-noise ratio as a function of increasing receiver length. (a) V_r is the major source of noise. (b) V_r not the major source of noise.

reducing the electrode noise makes almost no difference. This is true because V_r is not the major source of noise.

3. **Reduce the electric field noise due to the motion of the streamer, $E_T(t)$:** when towing the receiver in the sea, the streamer motion and its subsequent tugging or strumming are inevitable. This motion induces a noise which falls within the range of electric field measurements (Constable, 2013). Therefore, mitigating its effect is important for the efficiency of the towed streamer CSEM. Assuming a 200 m receiver length, Figure 3.6 shows that reducing the motion of the streamer by a factor of 10 and 100, for example, increases the SNR by approximately 16.8 and 19.5 dB, respectively. Further reducing $E_T(t)$, for example by a factor of 1000, is shown not to provide a significant change in the SNR improvement. To prevent the motion of the streamer, one could tow the streamer deeper or increase the streamer tension.

4. **Modifying the waveform:** the transmitter generates a pre-determined waveform that controls the frequency content, the distribution, and the relatives amplitudes of the component frequencies. Since CSEM is sensitive to thin electrical structure (resistive bodies) which lie between conductive bodies, it is desirable to

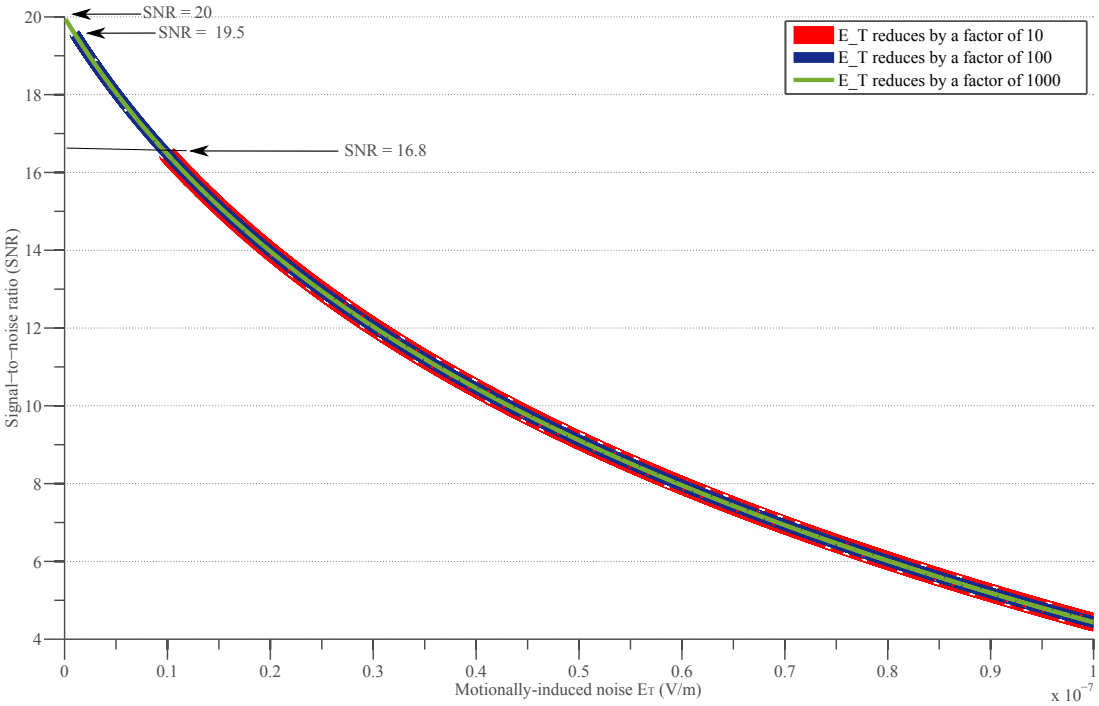

Figure 3.6: Signal-to-noise ratio as a function reducing the motionally induced field. Decreased noise level E_T from 10^{-7} to 10^{-10} V m^{-1}. The red, blue and green curve correspond to the effect of reducing E_T by a factor of 10, 100 and 1000, respectively.

use a waveform that contains multiple frequencies so that several depths can be probed. Ideally, the energy transmitted at each frequency should be as equal as possible and cover a decade of frequencies (Lu and Srnka, 2009). Square waves or a sequence of square waves are generally used in CSEM because they are easy to generate and contain a useful range of frequencies (MacGregor, 1997). However, its energy is concentrated at the fundamental frequency and odd harmonics and sequentially decreases in magnitude with increasing frequency. Waveforms which concentrate the energy in selected frequencies to resolve the target of interest have been customized (Myer et al., 2011; Mittet and Shaug-Pettersen, 2008; Constable and Cox, 1996) and patented (Lu and Srnka, 2009). However, Ziolkowski et al. (2011) demonstrated the use of a pseudo-random binary sequence (PRBS) waveform in 380 m water depth using towed streamer CSEM. This waveform has the advantage of containing all frequencies at equal amplitude within the desired bandwidth. Ziolkowski et al. (2011) showed that compressing the receiver energy of the pseudo random binary sequence into an impulse response by deconvolution result in a gain in SNR of 32.5 dB.

Table 3.2 summarises the five recommended approaches for increasing the SNR in the towed streamer CSEM: reducing the motionally-induced noise by a factor of 100, increasing the receiver length up to 500 m, reducing the electrode noise by a factor 10, using PRBS waveforms and increasing the source current by a factor of 10. It is clear that the biggest challenge in towed streamer CSEM is related to the identification, quantification and perhaps the attenuation of the component of the noise associated with the motionally-induced noise, E_T. Addressing the first two points is the major objective of my Ph.D. project.

	Increase parameter factor by	**Reduction parameter factor by**	**Gain in SNR (dB)**
$V_r(t)$	-	10	0.02
Δx_r (max. length 500 m)	-	-	0.04
$E_T(t)$	-	100	16
PRBS	-	-	32.5
	Factor increase in Δx_s or $i(t)$		**Gain in SNR (dB)**
SDM	10		20

Table 3.2: Increase in signal-to-noise ratio associated with increasing SDM and decreasing noise level.

Summary

A towed streamer CSEM system enables faster and more efficient data acquisition compared with traditional node-based receivers. However, the system can be affected by noise from various sources. Most of the noise sources identified in node-based CSEM are observed in the towed streamer CSEM. I have summarised research on this issue and shown how these sources of noise contribute in the towed streamer CSEM system. However, because of motionally-induced noise, the noise level in the towed streamer CSEM is substantially higher than noise levels in the node-based CSEM. I then presented different parameters in the source signal that one needs to change in order to improve the signal-to-noise ratio of the towed streamer CSEM. Increasing the signal has reached practical limitations, so the only option is to reduce the noise. Two approaches have been shown to increase the signal-to-noise ratio. First, reducing the effect of motionally-induced noise by a factor of 100. Second, using a pseudo-random binary sequence (PRBS) waveform. A clear identification and quantification of the sources of noise could help to predict and then subtract the noise in data. It could also help to modify the acquisition system to prevent the noise being generated in the first place.

■

4

Noise Analysis: Towed Streamer and Ocean Bottom Cable CSEM

The most exciting phrase to hear in science, the one that heralds the most discoveries, is not "Eureka! " (I found it!) but "That's funny..."

Isaac Asimov (1920–1992)
Author and Biochemist

I analyse the noise recorded using first the 1st generation towed streamer controlled source electromagnetic (CSEM) with the noise recorded using a static ocean bottom cable (OBC) CSEM. The main findings are that within the frequency range of interest, 0.01–1 Hz, the towed streamer CSEM noise is 5–30 dB greater than the noise recorded with the OBC-based CSEM. I show also that the motion of the telluric cable between the pair of electrodes in the towed streamer CSEM is responsible for this difference in amplitude between the two systems. Within 0.03–0.1 Hz and 0.3–0.2 Hz, the motionally-induced noise is uncorrelated across all channels. However, within 0.1–0.3 Hz, the motionally-induced noise correlation coefficient gradually increases and becomes well correlated at about 0.2 Hz. I conclude that movements of the lead-in cable due to ocean swells cause this correlated noise. This mechanism is the major mechanism responsible for the generation of noise in the towed streamer CSEM. I suggest that the signal-to-noise ratio on towed streamer CSEM can be improved by increasing the channel length to at least 500 m, towing the streamer deeper or by increasing the tension between the streamer head and the tail buoy.

Parts of this chapter (4.1-4.3) were presented under the title *Noise investigation of a towed marine active source EM system* at the Bristish Geophysical Association Postgraduate Research Meeting. The abstract is published in Tcheheumeni et al. (2013).

4.1 OBC (static) and towed streamer CSEM noise datasets

For the purpose of my Ph.D. thesis, I analyse ocean bottom cable (OBC) and towed streamer controlled source electromagnetic (CSEM) data collected by Petroleum Geo-Services (PGS) while the transmitter was switched off. The data were collected with the 1st generation towed streamer CSEM streamer. The same system was used to acquire noise data in the North Sea presented in Mattsson et al. (2012). Acquisition parameters are provided in Table 4.1. The OBC data were obtained in water 100 m deep at a sampling rate of 20 Hz. The system consisted of 11 channels, each 200 m long.

Towed streamer CSEM noise measurements consisted of a 6500 m long streamer towed 100 m below the sea surface at a speed of 4 knots (2.06 $\mathrm{m\,s^{-1}}$). The noise was collected in a total of 11 straight survey lines, at the beginning (pre-noise) and at the end (post-noise) of each line, at a sampling rate of 120 Hz. This makes a total of 22 datasets. The streamer contained 22 channels that were laid out as shown Figure 4.1. The channel layout was subdivided into two main groups as shown in Table 4.2. The first group consisted of 11 inline (non-overlapping) channels in which the separation of the electrodes in each pair was 200 m. The second group consisted of 11 inline (overlapping) channels in which 10 channels were 500 m length and a 650 m long single channel.

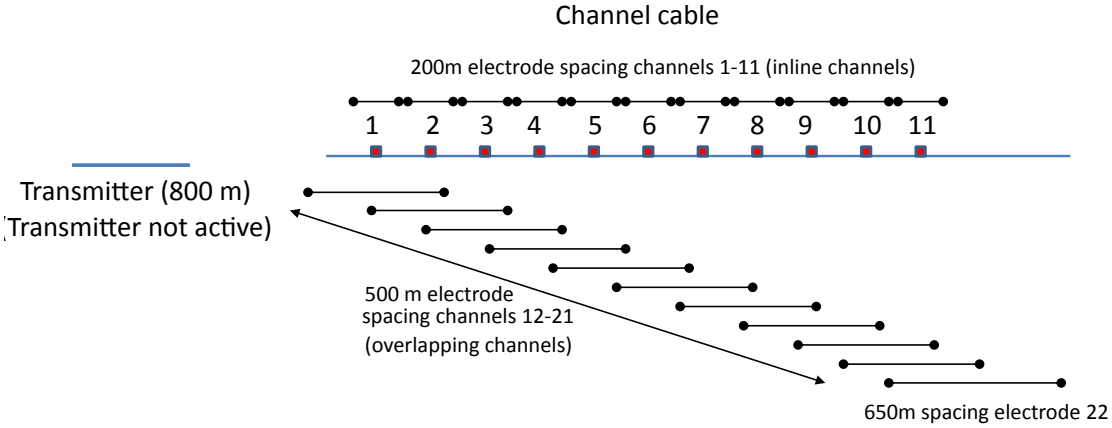

Figure 4.1: Towed streamer CSEM electrode configuration. The near offset has a channel separation of 200 m (Channel 1) and 500 m (Channel 12), and the separation between the far offset channel pair is 650 m (Channel 22). Notional offsets for Channel 1–11 are the same as Channel 2–22 so the mid-point of Channel 1 is the same as Channel 12 (from Dr. David Wright).

Parameters	OBC CSEM	Towed streamer CSEM
Number of lines	1	13
Number of channels	11	22
Channel length (m)	200	200, 500 and 650
Length of record	216450 samples, 832.5 s	1303743 samples, 864.5 s
Sampling frequency (Hz)	20	120

Table 4.1: OBC and towed streamer CSEM data acquisition parameters.

The abbreviation "Ch" followed by a number in Table 4.2 corresponds to the channel position along the towed streamer. The same abbreviation is used to display the OBC CSEM data.

Electrode configuration	Length (m)	Channel number										
Group 1 (non-overlapping)	200	Ch1	Ch2	Ch3	Ch4	Ch5	Ch6	Ch7	Ch8	Ch9	Ch10	Ch11
Group 2 (overlapping)	500	Ch12	Ch13	Ch14	Ch15	Ch16	Ch17	Ch18	Ch19	Ch20	Ch21	
	650	Ch22										

Table 4.2: Electrode configuration. Group 1 consisted of 11 non-overlapping channels (Ch1 until Ch11), and Group 2 consisted of 11 overlapping channels (Ch12 until Ch22).

The frequency range of interest is 0.01–1 Hz.

4.2 OBC and towed CSEM noise quality control analysis

To examine and characterise the measured data, several quality control (QC) methods are used. These include analysis in the time domain and in the frequency domain.

Time domain analysis

OBC and towed streamer CSEM data were collected as time series. These time series were divided into 120-second windows that correspond to a typical towed streamer CSEM acquisition shot length. The mean was subtracted to remove the direct current (DC) contribution.

The distribution of noise along a streamer can be obtained by averaging the root mean square (RMS) values from several statistically independent records (Elboth et al., 2009).

Let $E(n)$ denote a one-dimensional discrete-time series containing the electric field noise, n be the time-domain index of the input samples, $n = 1, ..., N$, and N be the total number of samples used to calculate the RMS. The RMS value of a quantity is the square root of the mean value of the squared quantity taken over an interval. It is defined as:

$$E_{rms} = \sqrt{\frac{1}{N}\sum_{n=1}^{N} E(n)^2}\,, \qquad [\mathrm{V\,m^{-1}}] \tag{4.1}$$

To compute E_{rms}, the following steps were implemented:

1) The noise data were divided into several windows of 120-second length.
2) The mean was removed from each of the windows.
3) E_{rms} was calculated in each window following equation (4.1).
4) The mean E_{rms} was obtained by averaging the vector containing the E_{rms} values.
5) The standard deviation and standard error of the mean were computed to give a measure of the RMS variability. The standard deviation is defined as:

$$E_{std} = \sqrt{\frac{1}{M-1}\sum_{j=1}^{M}(E_{rms}(j) - \overline{E_{rms}})^2}\,, \tag{4.2}$$

where E_{std} is the standard deviation, j is the sample RMS number, $\overline{E_{rms}}$ is the RMS mean, and M is the number of RMS values. The standard deviation is a measure that summarises the amount by which every value within a data set varies or deviates from the mean. On the other hand, the standard error of the mean is defined as:

$$E_{sem} = \frac{E_{std}}{\sqrt{M}}\,, \tag{4.3}$$

where E_{sem} is the standard error. The standard error of the mean tells how close each sample of a data set is to the mean.

If the sampling distribution is normal, the standard error of the mean will be used to produce a range we can be 95 % confident it will contain the true mean. This is called confidence interval and it is expressed as:

$$CI = E_{rms} \pm 2 \times E_{sem}\,, \tag{4.4}$$

where CI is the confidence interval.

Spectral analysis

Spectral analysis is useful for analysing the contribution of noise at different frequencies. This is performed with the power spectral density (PSD).

To calculate the PSD, the discrete-time series $E(n)$, was divided into 120-second-long windows, and the DC was removed in each time window. Each time window was multiplied with a Hanning window of the same length before applying the FFT. The product was put through the real-to-complex FFT algorithm following equation (0.4). The squared magnitude in each window was computed, averaged and scaled according to equation (0.7).

Coherence analysis

The magnitude squared coherence (MSC) is a signal processing tool that provides a measure of how well 02 time series $x(t)$ and $y(t)$ are correlated as a function of frequency. It varies between 0 and 1, where 0 indicates complete uncorrelation and 1 denotes perfect correlation:

$$C_{xy}(f) = \frac{\mid P_{xy}(f) \mid^2}{P_{xx}(f)P_{yy}(f)}\,, \tag{4.5}$$

where $P_{xy}(f)$ is the cross power spectral density at frequency f between two time-series $x(t)$ and $y(t)$ with power spectral density $P_{xx}(f)$ and $P_{xy}(f)$. The MSC can also be interpreted as a correlation coefficient in the frequency domain (Stoica and Moses, 2005). In the following, the MSC is called the correlation coefficient for simplicity.

Let $x(n)$, $n = 1, ..., N$ and and $y(n)$, $n = 1, ..., N$ be samples from the input signals. The cross power spectral density is the distribution of power per unit frequency and is defined as:

$$P_{xy}(f) = \frac{1}{f_s}\sum_{m=1}^{N} R_{xy}(m)e^{-2\pi imf/f_s}\,, \tag{4.6}$$

where m is the lag between two samples, $R_{xy}(m)$ is the cross-correlation sequence. It is defined as:

$$R_{xy}(m) = \sum_{n=1}^{N-m} x(n+m)y^{\star}(n)\,, \tag{4.7}$$

where * indicates the complex conjugate.

The power spectral density estimates are given by

$$P_{xx}(f) = \frac{1}{f_s}\left|\sum_{n=1}^{N} x(n)h(n)e^{-2\pi inf/f_s}\right|^2, \tag{4.8}$$

$$P_{yy}(f) = \frac{1}{f_s}\left|\sum_{n=1}^{N} y(n)h(n)e^{-2\pi inf/f_s}\right|^2. \tag{4.9}$$

The power spectrum for the coherence is calculated following the Welch method (Welch, 1967). First the time-series is divided into a number of windows of the same length. Then each window is multiplied by a window function; in this case, a Hanning function is used. The power spectral density of each window is calculated, and then the average is obtained to find the MSC $C_{xy}(f)$ in equation (4.5).

4.3 Noise in a towed streamer and OBC CSEM

Towed streamer and OBC CSEM noise data were collected at a rate of 120 Hz and 20 Hz, respectively. To compare the two datasets, a high pass filter at 0.02 Hz was applied to OBC CSEM dataset. This was done because the towed streamer noise data were acquired with an analogue high-pass filter at 0.02 Hz. A low pass filter of 10 Hz was applied on the towed noise data. The output was then re-sampled to 20 Hz, that is the same sample rate as the OBC CSEM data. Finally, an FFT was applied over the same window length on both datasets. Figure 4.2(a) shows typical time series with amplitude measured in volts per metre. Figure 4.2(b) shows the amplitude spectrum obtained from the data shown in Figure 4.2(a).

Considering the PSD plots in Figure 4.2(b), the following observations can be made:

- Above 3 Hz the noise on the towed streamer CSEM is comparable with that of the OBC CSEM. The peak at approximately 7.83 Hz is present on all datasets and observed at the same amplitude on both systems. This peak corresponds to the first Schumann resonance (Madden and Thompson, 1965). Schumann resonance is the global low-frequency electromagnetic oscillations of the earth-ionosphere cavity that occurs at frequencies of about 7.8 Hz, 14.1 Hz, 20.3 Hz, 26.4 Hz, and 32.5 Hz (Nickolaendro and Hayakawa, 2013; Matsushita and Campbell, 1967).
- Below 3 Hz the difference between the towed streamer and static system becomes clear. As the frequency decreases, the OBC and towed streamer CSEM noise increase rapidly in amplitude. Towing noise is about 32 dB higher than in the OBC system at 0.07 Hz, and 10 dB higher at 0.7 Hz. Typically, towing adds on

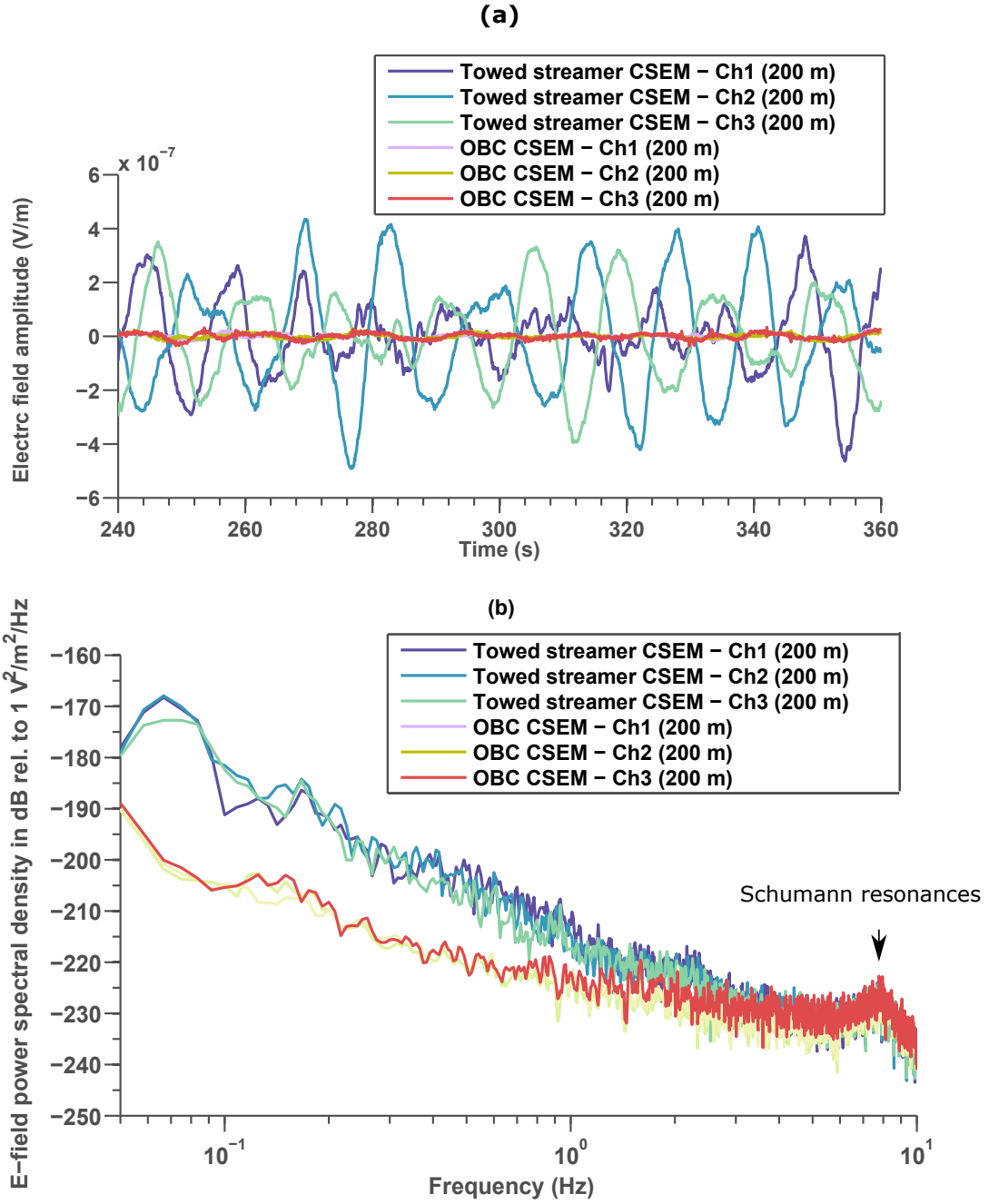

Figure 4.2: (a) Typical time series in V m^{-1} for 120 s of noise recorded during the two surveys. (b) Typical PSD of data shown in (a).

average about 20 dB to the noise level over the frequency range of interest in marine CSEM for hydrocarbon exploration.

Coherence analysis

Figures 4.3 and 4.4 were produced by computing the coherence of the electric field noise measured by one channel with all other channels using the data collected during the OBC and towed streamer CSEM survey, respectively. The diagonal elements (red) represents the perfect correlation of each channel with itself and is equal to 1. The off-diagonal elements represent the correlation coefficients of one channel with the other channels. The vertical and horizontal axes represent the channel number. Figure 4.4 shows the average of the correlation coefficient over the 22 noise datasets recorded during the towed streamer survey.

Figures 4.3(a), (b) and (d) display values of the correlation coefficient in the range of 0.8–0.9 . This shows that the noise present in the OBC CSEM is correlated across different channels. This is a characteristic of MT noise. However, at 1 Hz (Figures 4.3(c)), the correlation coefficient dramatically decreases to about 0.4. This is likely due to the so-called "MT dead band" (Chave and Jones, 2012; Milsom and Eriksen, 2011) which considerably reduces the amplitude of MT fields.

Figure 4.4(a) and (c) show that the correlation coefficient is on average below 0.2 at 0.05 Hz and 1 Hz, respectively. However, at 0.2 Hz, as shown in Figure 4.4(b), the correlation coefficient is about 0.6. The poor correlation coefficient of about 0.05 observed at this frequency, and at 10 Hz in Channel 1, Channel 9, and Channel 11 is likely due to possible faulty channels. The overall high correlation across all channels observed at approximately 0.2 Hz is likely due to ocean swell that causes motions of the various vessel. These motions are transferred through the lead-in cable to the streamer. Another source of this high correlation could be attributed to the direct effect of ocean swell on the streamer. At 10 Hz (Figure 4.4(d)), the correlation coefficient is about 0.9. This means that the noise is well correlated across different channels. Therefore, MT noise is the dominant component of noise at 10 Hz in the towed streamer CSEM.

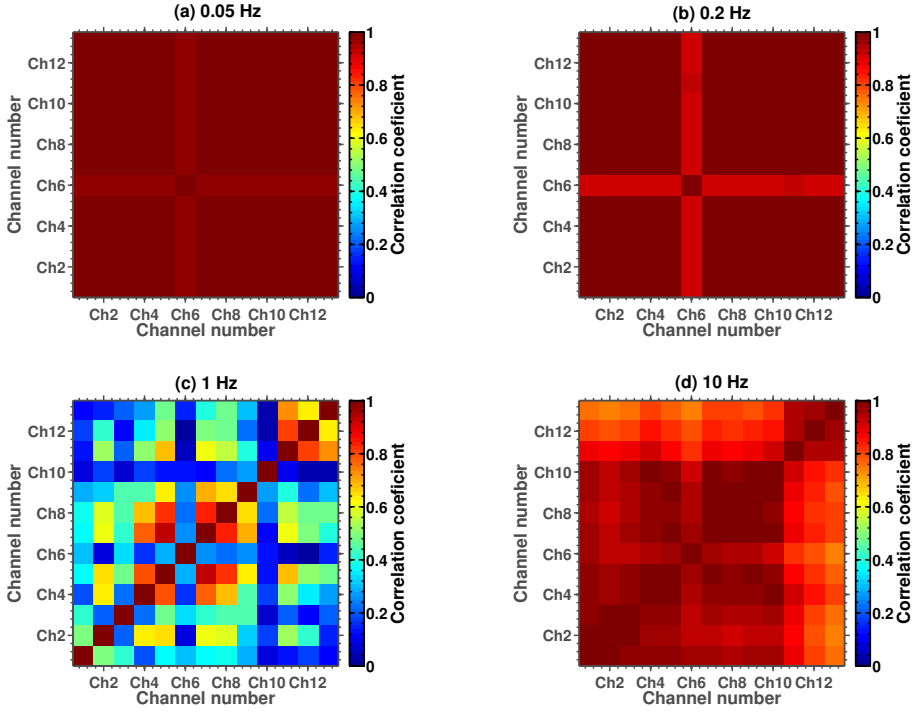

Figure 4.3: Coherence matrix of the electric field noise recorded with the OBC CSEM. (a) 0.05 Hz. (b) 0.2 Hz. (c) 1 Hz. (d) 10 Hz.

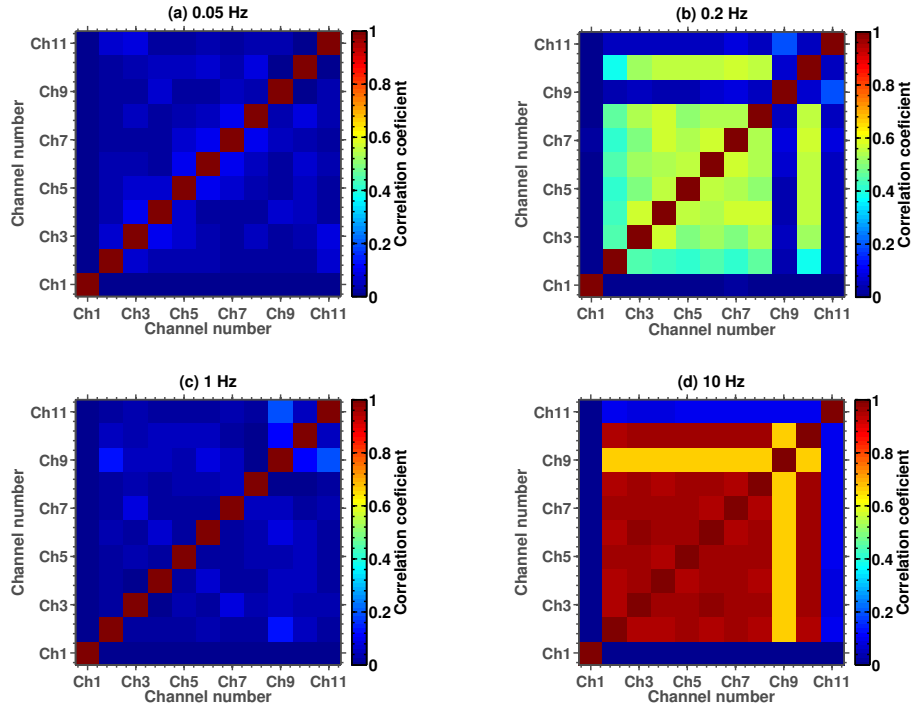

Figure 4.4: Coherence matrix of the electric field noise recorded with the towed streamer CSEM - non-overlapping channels. (a) 0.05 Hz. (b) 0.2 Hz. (c) 1 Hz. (d) 10 Hz.

These results are important as they contribute to the understanding of the degree of similarity as a function of frequency between noise recorded across different channels in a static system such as the OBC CSEM and to the towed streamer CSEM. By comparing Figures 4.3 and 4.4, it is clear that in both systems, the dominant component of noise above 3 Hz is due to MT fields. However, below 1 Hz, the dominant component of the OBC CSEM noise data is correlated MT noise, and the dominant component of the towed streamer CSEM noise is towing noise. The peak observed at about 0.2 Hz in the frequency spectrum (Figure 4.2) of the towed streamer CSEM is found to be correlated across all channels.

4.4 OBC CSEM data

An example time series of electric field noise collected by three channels using the OBC CSEM system is shown in Figure 4.5. The noise appears to be well correlated at low-frequencies. By plotting only the data between 589 and 593 s, as shown the window in the upper right of Figure 4.5, one can observe that noise measurements also contain high-frequency peaks (indicated by the black arrows) that are also spatially correlated across all channels.

The relative amount of correlated background noise in a measurement can be estimated by the peak of the cross-correlation coefficient of noise records from different channels (Elboth et al., 2010a). Figure 4.6 was produced by cross-correlating the noise measured by Channel 1 with all the other channels. The value at zero lag was then picked for each cross-correlation.

Figure 4.6 shows that the noise is very well correlated, and it is about 0.96. This indicates that correlated noise makes up to 96 % of the overall noise recorded by Channel 1.

The low and high-frequency features associated with the strong correlation features of the noise are characteristic of the natural occurring magnetotelluric (MT) signal (Dobrin and Savit, 1988), that is viewed as noise.

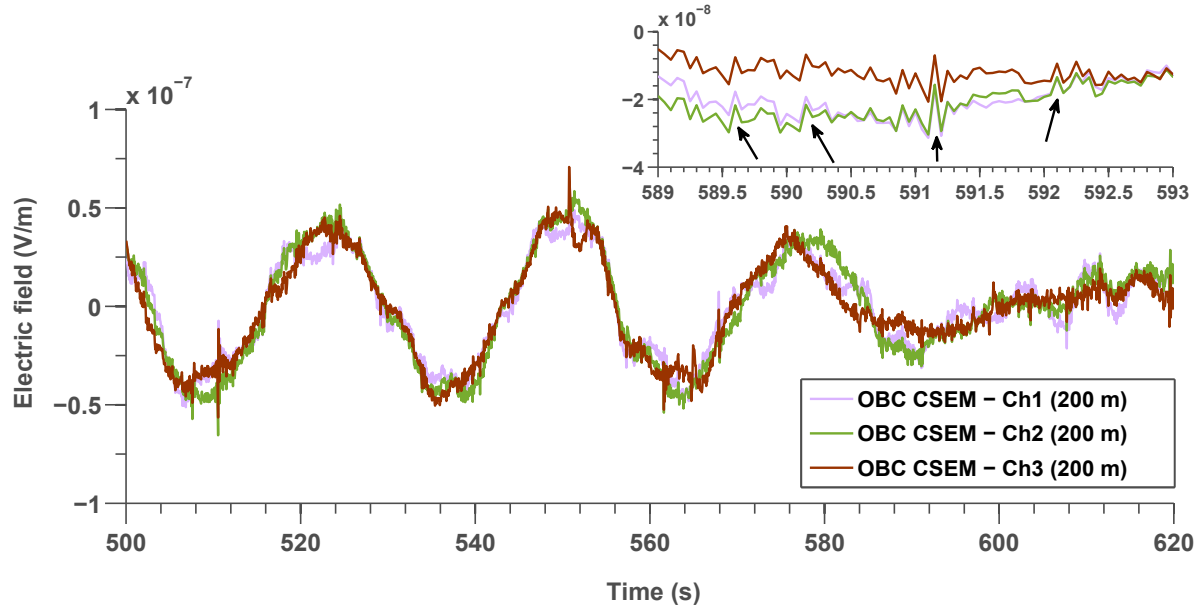

Figure 4.5: OBC CSEM: time series of noise records acquired with the OBC CSEM. The window in the upper right represents 4 *s* of the data.

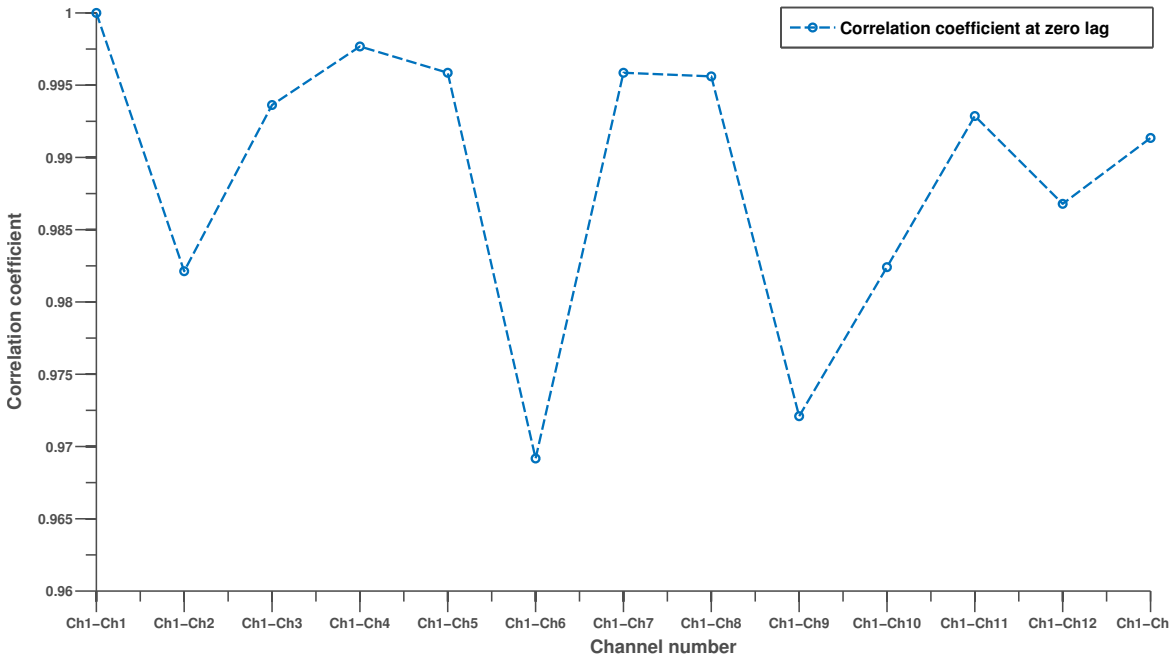

Figure 4.6: Cross-correlation of Channel 1 with all the others 13 channels

Recalling equation (3.4), and multiplying by the the channel length Δx_r yields:

$$\Delta x_r E_n(t) = \Delta x_r (E_i(t) + E_T(t)) + V_r(t)\,, \qquad [\mathrm{V}] \tag{4.10}$$

where $\Delta x_r E_n(t)$ represents the noise measured by the OBC CSEM system (V), $E_i(t)$ is the MT noise ($\mathrm{V\,m^{-1}}$), $E_T(t)$ is the motionally-induced noise ($\mathrm{V\,m^{-1}}$), and $V_r(t)$ is the electrode noise (V). The average RMS computed from Equation (4.10) is shown in Figure 4.7. The error bars represent the standard error and show the distribution of errors in estimating the average RMS. The red dotted line represents an estimation of the relative amount of the correlated MT noise in the OBC data from 98 % in Channel 1 (Figure 4.6), represented by $E_i(t)$ in equation (4.10). In fact, MT noise contribution is the same across all channels (since they all have the same length). In addition, since the OBC CSEM noise measurements are made in shallow water, tidal currents and waves can cause motion of the telluric cable connecting pairs of electrodes (Ziolkowski et al., 2010). As a consequence, $E_T(t)$ is induced. Therefore, the variability in noise level observed in each channel above the dotted red line in Figure 4.7 is likely caused by $E_T(t)$, $V_r(t)$ or a combination of $E_T(t)$ and $V_r(t)$. Error bars are small for all channels. This suggests that the average RMS plotted in Figure 4.7 is reliable.

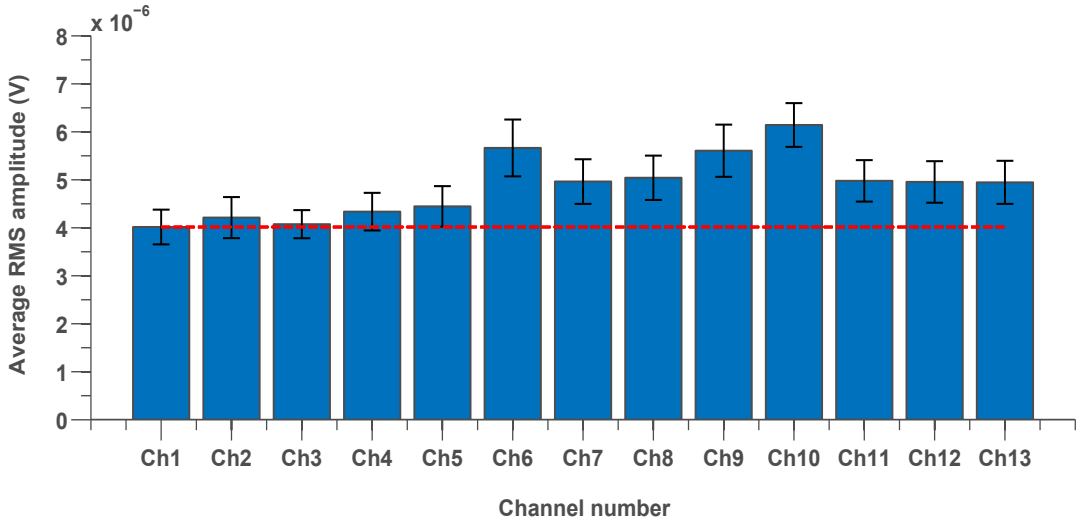

Figure 4.7: Average RMS noise level in the time domain (error bars represent standard error). The RMS level above the red dotted line shows the contribution of either $E_T(t)$, $V_r(t)$ or the combination of both noise sources. Error bars represent standard error of the mean.

The PSD computed from the time series shown in Figure 4.5 is displayed in Figure 4.8.

In general, the spectra in Figure 4.8 decay as frequency increases. This is due to the inherent feature of the MT signal. At frequencies below 0.05 Hz, the main source of noise is the spatially coherent MT noise (Connell and Key, 2012). The peak near 0.13

Hz is attributed to ocean swell noise (Ziolkowski et al., 2010). Furthermore, the peak near 7.9 Hz is characteristic of the first Schumann resonance.

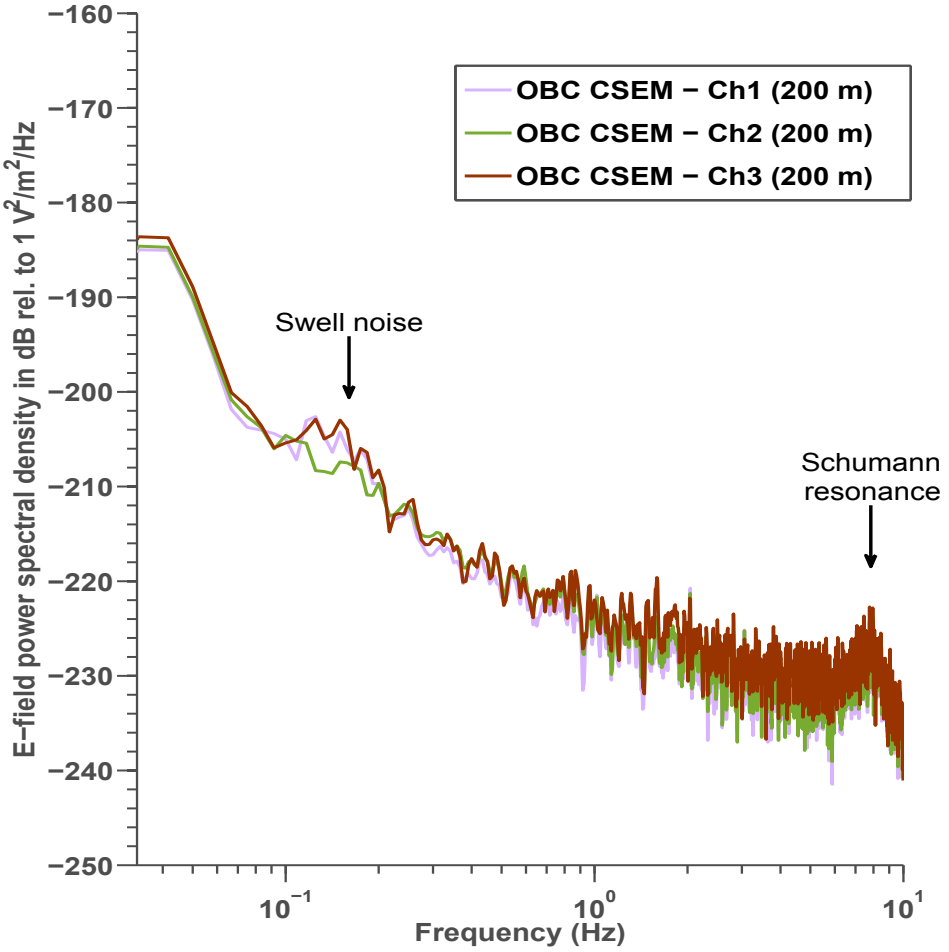

Figure 4.8: OBC CSEM: PSD in dB relative to 1 $V^2m^{-2}Hz^{-1}$ for Channel 1 (200 m), Channel 2 (200 m), and Channel 3 (200 m) of the data shown in Figure 4.5.

4.5 Towed streamer CSEM data

Time domain analysis

Figure 4.9 shows typical time series in $\mathrm{V\,m^{-1}}$ of three channel lengths for the towed streamer system. The green, yellow and red lines show recordings made by Channel 1 (200 m), Channel 15 (500 m) and Channel 22 (650 m), respectively. Figure 4.9 is dominated by low-frequency noise that is uncorrelated across all channels. On the other hand, the high-frequency noise peaks observed, for example just after 620-s and 660-s on all three channels, are correlated. The window in the upper right highlights the peaks observed after 664-s. These correlated peaks are characteristic of MT noise.

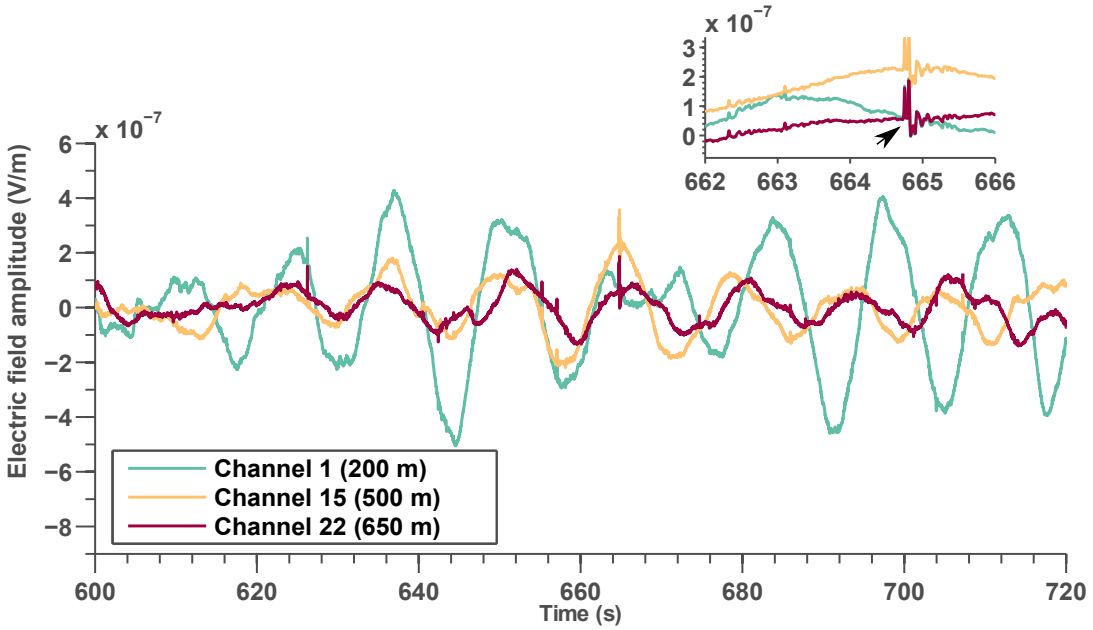

Figure 4.9: Towed streamer CSEM: time series in $\mathrm{V\,m^{-1}}$ measured by Channel 1 (200 m) - green, Channel 15 (500 m) - orange, (orange) and Channel 22 (650 m) - red. The window in the upper right highlights the peaks observed after 664-s

Figures 4.10(a) and (c) show the average bar plots from all runs for individual channels in volts and volts per metre, respectively. Figures 4.10(b) and (d) show the same result obtained by averaging the RMS of channels that have the same length. Error bars represent the standard error of the mean. They are used to access the precision of the RMS' average and represent interval within with each average value falls. Analysis of the mean RMS shows that Channel 8, Channel 10, Channel 17, Channel 18, and Channel 19 are possibly faulty and are excluded from further analysis.

From Figures 4.10(a) and (c), we observe that the average RMS of same length channels

is not similar. The reason for this is that the electrodes are affected by uncontrollable and small changes in the streamer environment or within each electrode. These changes may be due to mechanical motions of the streamer (subsequently causing the each electrode to vibrate) triggered by the motion of the lead-in cable. Figure 4.10(a) shows that short channels (200 m) record less noise than longer channels (500 m and 600 m). From Figure 4.10(b), we can observe that the RMS level increases with increasing channel length, with the 650 m channel 1.3 times greater than the 500 m, and this 1.1 times higher than the 200 m channel. However, when the RMS level at each channel is normalised by the channel length in order to enable measurements made over different channel lengths to be compared (Figures 4.10(c) and (d)), we observe that the average RMS level drops off as the channel length increases. From Figure 4.10(d), the average RMS level during the survey is typically 1.4×10^{-7} V m^{-1} for the 200 m channels. This value is about 2.5 times higher than the 500 m and the 650 m channels. This indicates that the noise due to motions of the lead-in cable is local at every channels. It also shows that increasing the channel length is one way to reduce this noise.

The recorded noise level corresponds to $E_n(t)$ in equation (3.4). Following this equation, MT noise, $E_i(t)$, is the same across all channels. The noise components that depend on the motion of the telluric cable between electrodes, and the channel length are $E_T(t)$ and $V_r(t)/\Delta x_r$, respectively. From Figure 4.10(b) the noise level increases with channel lengths but this increase is not proportional to the channel length. Therefore, following equation (4.10), term $E_i(t)$ cannot be considered as a major source of noise. The more likely major contributors to noise levels are therefore attributed to $E_T(t)$ or $V_r(t)$. Furthermore, when scaling the noise level by the channel lengths as shown in Figure 4.10(d), we see that on average the RMS level is the inverse of channel length from 200 m to 500 m. This could suggest that the noise is dominated by electrode noise $V_r(t)/\Delta x_r$. However, this observation does not hold when the channel length increases from 500 m to 650 m. In fact, the average RMS of the 500 and 600 m channels length is similar. As a consequence, $V_r(t)/\Delta x_r$ cannot explain the electric field noise level across the channels. The only parameter remaining is the motionally-induced noise term $E_T(t)$.

The similar values or the slight difference of the RMS average amplitude at the 500 m and 650 m channels are likely due to the self-cancelling of the motionally-induced noise. According to Burrows (1972), the self-cancelling effect occurs when the channel length is greater than transverse waves during data acquisition. In this case, this effect takes place when the channel length is greater than 500 m. Thus, for channels length greater than 500 m the subsequent motion of the streamer generates smaller motionally-induced noise, almost similar to the noise induced in the 500 m channel. In contrast, for the 200 m channel, the RMS level is high compared with the 500 and 650 m channels

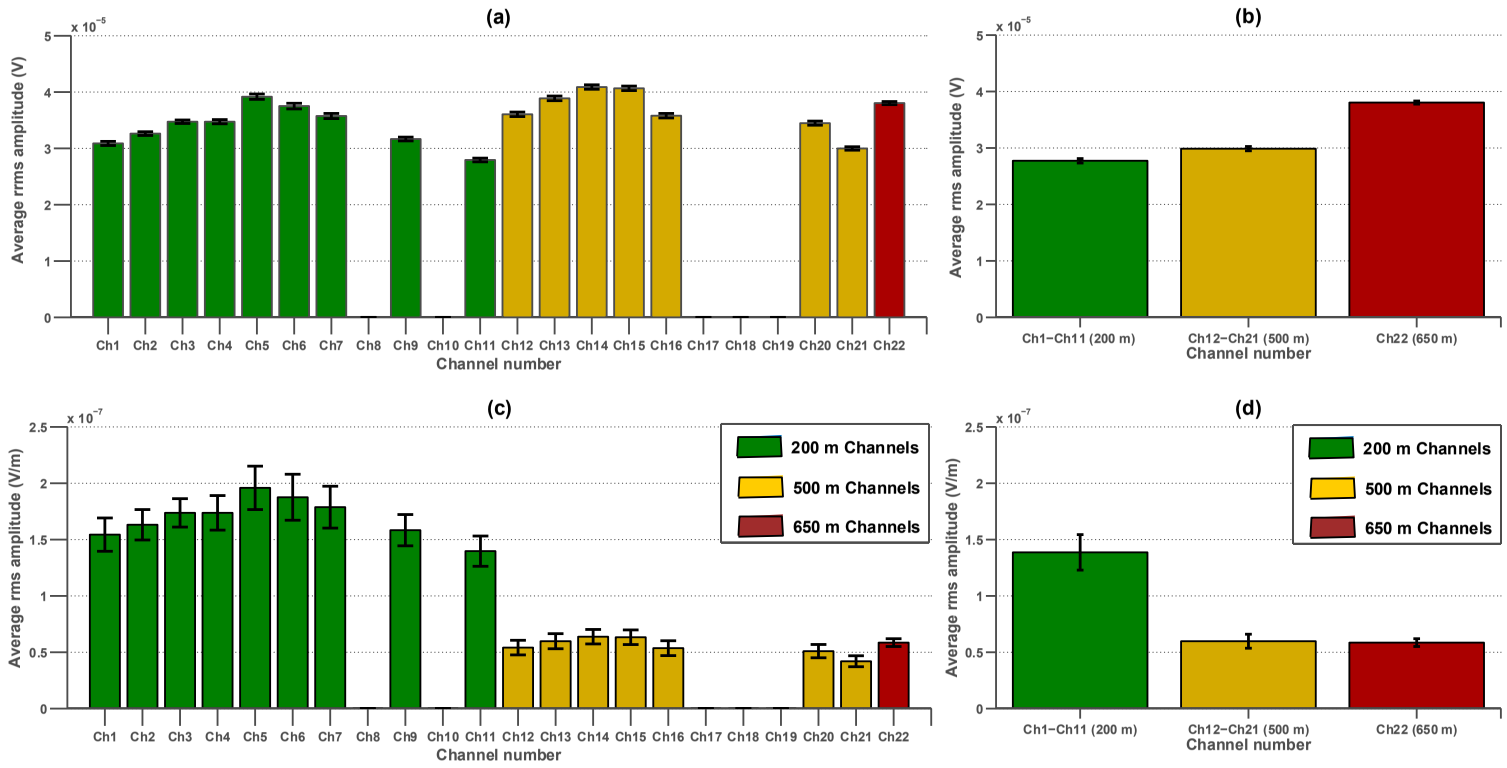

Figure 4.10: Average RMS amplitude as a function channel length. (a) Average RMS (V). (b) The average RMS (V) for channels in (a) that have the same lengths. (c) Average RMS ($\mathrm{V\,m^{-1}}$). (d) The average RMS ($\mathrm{V\,m^{-1}}$) for channels in (c) that have the same lengths. Error bars represent the standard error of the mean. Ch8, Ch10, Ch17, Ch18, and Ch19 are possible faulty channels.

because the motion or vibration of the telluric cable is in phase along the whole length. The motionally-induced noise is therefore large. This occurs when the channel length is smaller than transverse waves on the sea (Burrows, 1972). One question is: can we quantify the contribution of $E_T(t)$ and $V_r(t)$?

However, even though the 500 and 650 m channels length have similar RMS amplitude in average as shown in Figure 4.10(d), a close analysis of the respective standard error of the mean bar demonstrates that the 500 m one is about twice longer than the 600 m channel. The average RMS of the 500 m is given as $5.9 \times 10^{-8} \pm 0.6 \times 10^{-8}$ V m^{-1}. The actual RMS value is asserted to be between 6.5×10^{-8} and 5.3×10^{-8} V m^{-1}. Similarly, the average RMS of the 650 m channel length is about $5.9 \times 10^{-8} \pm 03 \times 10^{-8}$ V m^{-1}. In this last case, the true RMS average value is between 6.2×10^{-8} and 5.6×10^{-8} V m^{-1}. The fact that the average difference between the maximum RMS amplitude of the 500 and 600 m channels length is 0.3×10^{-8} V m^{-1} indicates the limitation of the interpretation given in the previous paragraph.

Estimation of the contribution of $E_T(t)$ and $V_r(t)$

MT noise is not the major contributor of noise, therefore we assume that the term $E_i(t)$ in equation (3.4) is negligible. For our problem of fitting the $E_n(t)$ recorded by each channel length over the 22 noise datasets data recorded with the towed streamer CSEM, equation (3.4) is rewritten as:

$$\overline{E_n(\Delta x_r)} = E_T + \frac{V_r}{\Delta x_r}\,, \tag{4.11}$$

where $\overline{E_n(\Delta x_r)}$ is the mean of the RMS of $E_n(t)$ for each channel length, and E_T and V_r are the constants to be estimated using non-linear least-squares. We fit the model in equation (4.11) by assigning two random starting points to E_T and V_r. The non-linear least-squares criterion consists of finding the value of E_T and V_r that minimizes

$$f(E_T, V_r) = \sum_{j=1}^{P} \left[\overline{E_n(\Delta x_r)_j} - (E_T + \frac{V_r}{(\Delta x_r)_j}) \right]^2 , \tag{4.12}$$

where P is the total number of points (22 in our case) and $f(E_T, V_r)$ is the function that is the sum of the squares of the errors, ε_j, associated with each point j defined as:

$$\varepsilon_j = \overline{E_n(\Delta x_r)_j} - (E_T + \frac{V_r}{(\Delta x_r)_j})\,. \tag{4.13}$$

For each value of $\overline{E_n(\Delta x_r)}$ recorded at the same time by the 200, 500, and 650 m channel, we find the best fitting curve so we can estimate the value of E_T and V_r. It is important to point out that regardless of the starting value given to E_T and V_r at the beginning of each iteration, the E_T and V_r solutions were always the same. The final result, shown as a brown dashed line in Figure 4.11, is the average of the fitting curve obtained from each of the 22 runs. The green diamond points denote the measure RMS data from each channel length. From the iteration, we obtained the average of $E_T = 3 \times 10^{-7}$ V m^{-1} and $V_r = 0.4 \times 10^{-4}$ V. For 200 m, 500 m, and 650 m channel length, $E_T(t)$ is 1.5, 4, and 5 times greater than $V_r(t)/\Delta x_r$, respectively. It follows that $E_T(t)$ is the major source of noise.

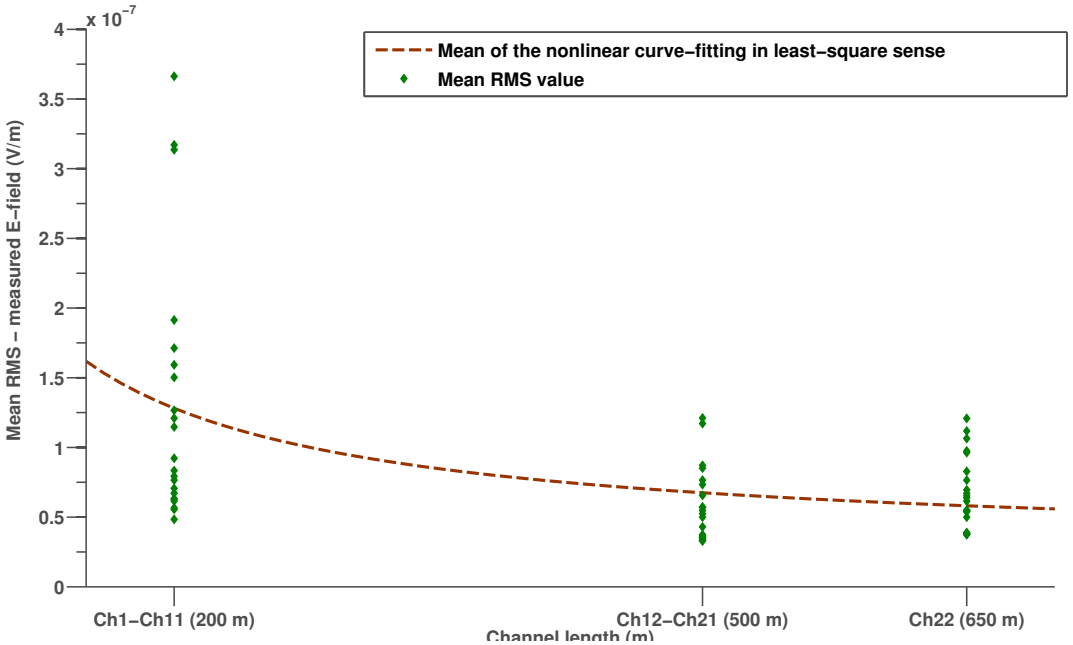

Figure 4.11: Towed CSEM system: average RMS amplitude as a function of channel length. The red dashed curve is the mean of the non-linear curve fitting in the least squares sense.

The Pearson residual is calculated to evaluate the relevance of the model (the brown dashed curve line) for each data and how well it fits the data. The Pearson residual is useful at detecting the measured RMS values that differs substantially from others — these points are called *outliers*. Identifying these outliers are very important because they may distort the model, resulting in an inappropriate model (Chen and Liu, 1993). Following Dunn and Smyth (1996), the Pearson residual for each jth mean RMS value is given by:

$$\Delta E(\Delta x_r)_j = \frac{\overline{E_n(\Delta x_r)_j}^{\text{measured}} - \overline{E_n(\Delta x_r)_j}^{\text{fitted}}}{\sqrt{std(\overline{E_n(\Delta x_r)_j}^{\text{fitted}})}} \qquad [\text{V m}^{-1}] \tag{4.14}$$

where $\Delta E(\Delta x_r)_j$ is the residual, $\overline{E_n(\Delta x_r)_j}^{\text{measured}}$ the measured RMS number at each channel length, and $\overline{E_n(\Delta x_r)_j}^{\text{values}}$ the estimate RMS number at each channel length. Chen and Liu (1993) and Ryan (1997) pointed out that any residual points exceeding 3 standard deviation should be considered as outliers.

Figure 4.12 shows the Pearson residual plot obtained from Figure 4.11. The red cross denotes residual points at each channel length calculated using equation (4.14), the small dashed line passing through 0 is the mean, and the blue long dashed line denotes ± 3 standard deviation cut-off. The outliers are encircled.

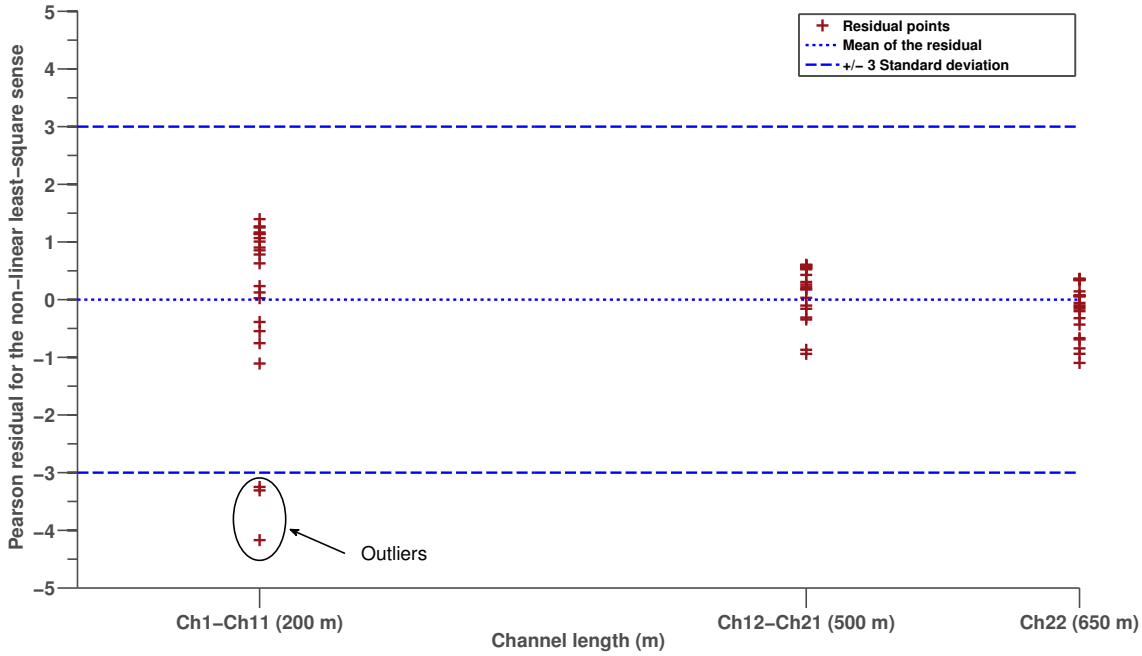

Figure 4.12: Towed CSEM system: Residual plot from Figure 4.11 Notice that most of the residual points are around 0 and well within ± 2 standard deviation for all channels. However, they are 3 outliers in the 200 m channel length.

In Figure 4.12, most the residual points are scattered around 0 and within ±2 standard deviation, although they are 03 outliers in the 200 m channel lengths. This means that the model fits well the data when the channels are 500 and 650 m long and could be improved for 200 m channel lengths. However, removing the outliers and running the iteration again did not considerably change the result (estimation of E_T and $V_r/\Delta x_r$)

and the fit. This suggests that the model is acceptable.

Spectral analysis

It is important to remember that the noise recorded at each receiver is the total noise, $E_n(t)$, which is the contribution of the three sources of noise: $E_i(t)$, $E_T(t)$, and $V_r(t)/\Delta x_r$ expressed in equation (3.4) as:

$$E_n(t) = E_i(t) + E_T(t) + \frac{V_r(t)}{\Delta x_r}\,. \qquad [\mathrm{V\,m^{-1}}]$$

To be consistent with the noise model in the time domain, the Fourier Transform of equation (3.4) is written as:

$$\hat{E}_n(f) = \int_{-\infty}^{\infty} \left[E_i(t) + E_T(t) + \frac{V_r}{\Delta x_r}(t)\right] e^{-2\pi i f t} dt\,. \qquad [\mathrm{V\,m^{-1}\,Hz^{-1}}] \tag{4.15}$$

From equation (4.15), the PSD is defined as:

$$|\,\hat{E}_n(f)\,|^2 = \hat{E}_n(f)\hat{E}_n{}^*(f)\,. \qquad [\mathrm{V^2 m^{-2} Hz^{-1}}] \tag{4.16}$$

Expanding equation (4.16), we obtain

$$\begin{aligned}
\hat{E}_n(f)\hat{E}_n{}^*(f) &= \int_{-\infty}^{\infty} \left[E_i(t) + E_T(t) + \frac{V_r}{\Delta x_r}(t)\right] e^{-2\pi i f t} dt \int_{-\infty}^{\infty} \left[E_i(s) + E_T(s) + \frac{V_r}{\Delta x_r}(s)\right] e^{2\pi i f s} ds \\
&= \iint_{-\infty}^{\infty} \left[E_i(t) + E_T(t) + \frac{V_r(t)}{\Delta x_r}\right] \left[E_i(s) + E_T(s) + \frac{V_r(s)}{\Delta x_r}\right] e^{2\pi i f (s-t)} dt ds \\
&= \hat{E}_i(f)\hat{E}_i{}^*(f) + \hat{E}_T(f)\hat{E}_T{}^*(f) + \frac{1}{\Delta x_r^2}\hat{V}_r(f)\hat{V}_r{}^*(f) \\
&+ \hat{E}_i(f)\hat{E}_T{}^*(f) + \hat{E}_i(f)\frac{\hat{V}_r{}^*(f)}{\Delta x_r} + \hat{E}_T(f)\hat{E}_i{}^*(f) \\
&+ \hat{E}_T(f)\frac{\hat{V}_r{}^*(f)}{\Delta x_r} + \frac{\hat{V}_r(f)}{\Delta x_r}\hat{E}_i{}^*(f) + \frac{\hat{V}_r(f)}{\Delta x_r}\hat{E}_T{}^*(f)\,.
\end{aligned} \tag{4.17}$$

Assuming that $E_i(t)$, $E_T(t)$, and $V_r(t)$ are three independent physical processes, we may suppose that they are uncorrelated stochastic processes. Then

$$\mathbb{E}[E_T(t)E_i(t+\tau)] = 0\,. \tag{4.18}$$

Where $\mathbb{E}$ is the expected value of the cross-correlation. Thus, on average, their cross-correlations have an expected value of zero:

$$\int_{-\infty}^{\infty} E_T(t)E_i(t+\tau)dt = 0\,. \tag{4.19}$$

As a result, the expected values of the cross terms in equation (4.17) are all zero:

$$\hat{E}_i(f)\hat{E_T}^*(f) = 0\,. \tag{4.20}$$

The same is valid for the other cross terms, that is,

$$\hat{E}_i(f)\frac{\hat{V_r}^*(f)}{\Delta x_r} = 0\,, \tag{4.21}$$

$$\hat{E_T}(f)\hat{E_i}^*(f) = 0\,, \tag{4.22}$$

$$\hat{E_T}(f)\frac{\hat{V_r}^*(f)}{\Delta x_r} = 0\,, \tag{4.23}$$

$$\frac{\hat{V_r}(f)}{\Delta x_r}\hat{E_i}^*(f) = 0\,, \tag{4.24}$$

$$\frac{\hat{V_r}(f)}{\Delta x_r}\hat{E_T}^*(f) = 0\,. \tag{4.25}$$

Therefore substituting equations (4.20) to (4.25) in equation (4.17), we obtain

$$\begin{aligned} |\,\hat{E_n}(f)\,|^2 &\approx \hat{E}_i(f)\hat{E_i}^*(f) + \hat{E_T}(f)\hat{E_T}^*(f) + \frac{1}{\Delta x_r^2}\hat{V_r}(f)\hat{V_r}^*(f) \\ |\,\hat{E_n}(f)\,|^2 &\approx |\,\hat{E_i}(f)\,|^2 + |\,\hat{E_T}(f)\,|^2 + \left|\frac{\hat{V_r}(f)}{\Delta x_r}\right|^2 . \qquad [\mathrm{V^2 m^{-2} Hz^{-1}}] \end{aligned} \tag{4.26}$$

To demonstrate that equation (4.26) holds, towed streamer CSEM noise data collected by the same channel during three independent runs over a period of 120 s were used. These runs included "Pre-noise 6", "Post-noise 6", and "Pre-noise 7". Figure 4.13 shows these data in the time domain. In the time domain, let Pre-noise 6, Post-noise 6, and Pre-noise 7 be expressed as $a(t)$, $b(t)$, and $c(t)$, respectively. Let's also assume that $x(t) = a(t) + b(t) + c(t)$. In the frequency domain, $a(t)$, $b(t)$, $c(t)$, and $x(t)$ become $\hat{A}(f)$, $\hat{B}(f)$, $\hat{C}(f)$, and $\hat{X}(f)$, respectively.

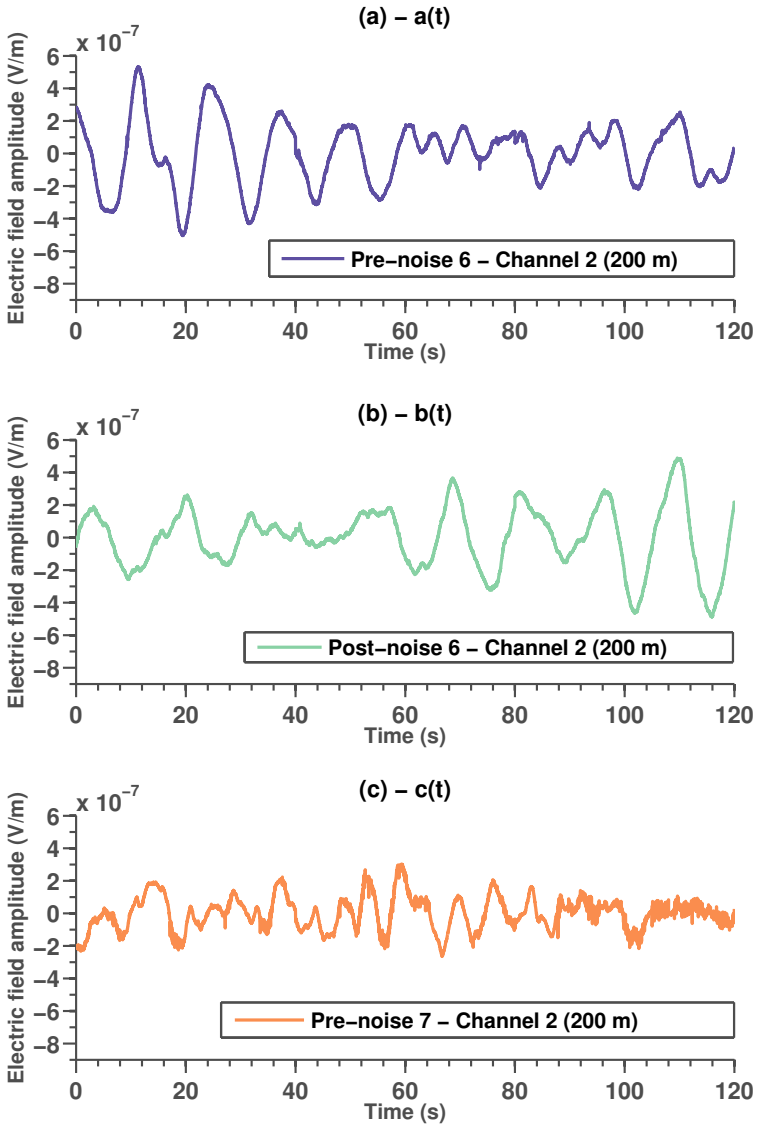

Figure 4.13: Towed streamer CSEM time domain. (a) Pre-noise 6, Channel 2. (b) Post-noise 6, Channel 2. (c) Pre-noise 7, Channel 2.

In the frequency domain, Figure 4.14(a) shows the PSD in decibel of the data display in Figure 4.13. From Figure 4.14(b), one can observe that displayed

$$| \hat{X}(f) |^2 \approx | \hat{A}(f) |^2 + | \hat{B}(f) |^2 + | \hat{C}(f) |^2 \ . \tag{4.27}$$

This shows that equation (4.26) holds given only if $E_i(t)$, $E_T(t)$, and $V_r(t)/\Delta x_r$ are uncorrelated stochastic process.

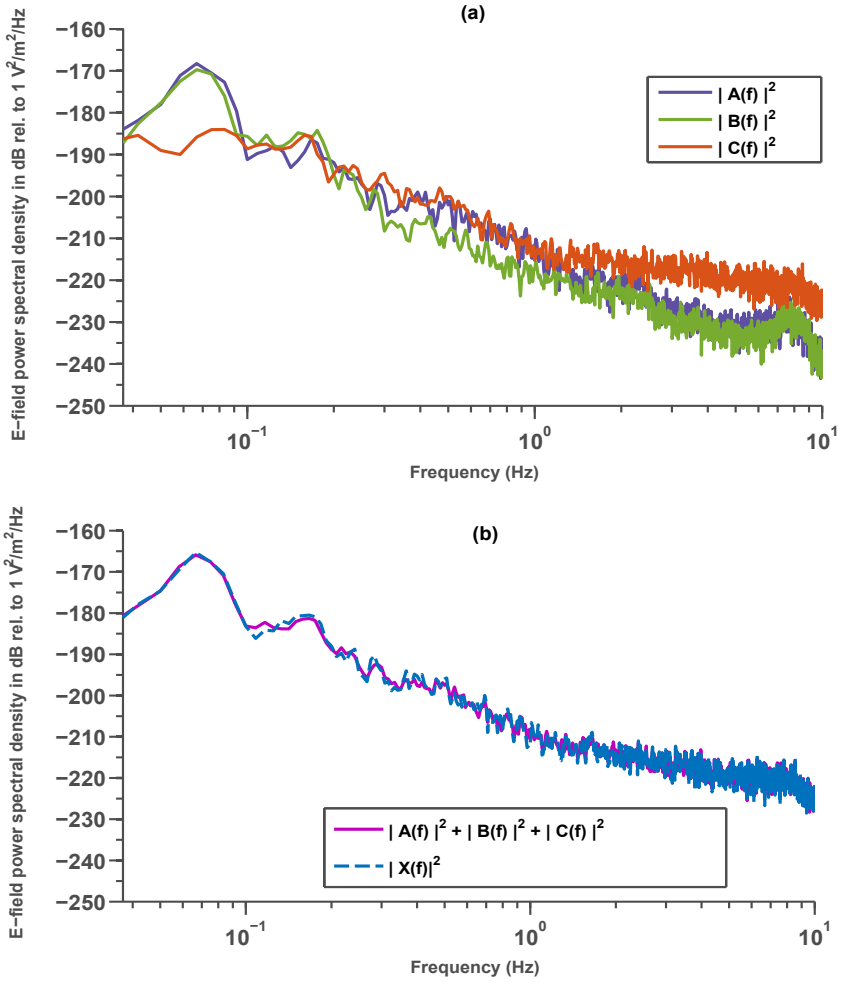

Figure 4.14: Towed streamer CSEM frequency domain. (a) PSD of data displayed in Figure 4.13. (b) PSD of $\mid \hat{A}(f) \mid^2 + \mid \hat{B}(f) \mid^2 + \mid \hat{C}(f) \mid^2$ (in red) and $\mid \hat{X}(f) \mid^2$.

Multiplying equation (4.26) by the square of the channel length Δx_r^2 gives the expression for $\mid \hat{E_n}(f) \mid^2$ in volts squared per hertz

$$\Delta x_r^2 \mid \hat{E_n}(f) \mid^2 \approx \Delta x_r^2 (\mid \hat{E_i}(f) \mid^2 + \mid \hat{E_T}(f) \mid^2) + \mid \hat{V_r}(f) \mid^2 \ . \qquad [\mathrm{V^2 Hz^{-1}}] \quad (4.28)$$

Figures 4.15(a) and (b) show an example of $\Delta x_r^2 \mid \hat{E_n}(f) \mid^2$ and $\mid \hat{E_n}(f) \mid^2$ for three different channel lengths, respectively. These PSD were computed using the data displayed in Figure 4.13. In general, the noise power decreases as the frequency increases. The following observation can be made:

- At frequencies above 3 Hz, in Figure 4.15(a), the PSD increases as the channel length increases. However, in Figure 4.15(b), the 200 m, 500 m and 650 m channels converge. This shows that MT noise, highlighted in equations (4.26) and (4.28) by the term $\mid \hat{E_i}(f) \mid$, is the dominant source of noise. In addition, the noticeable

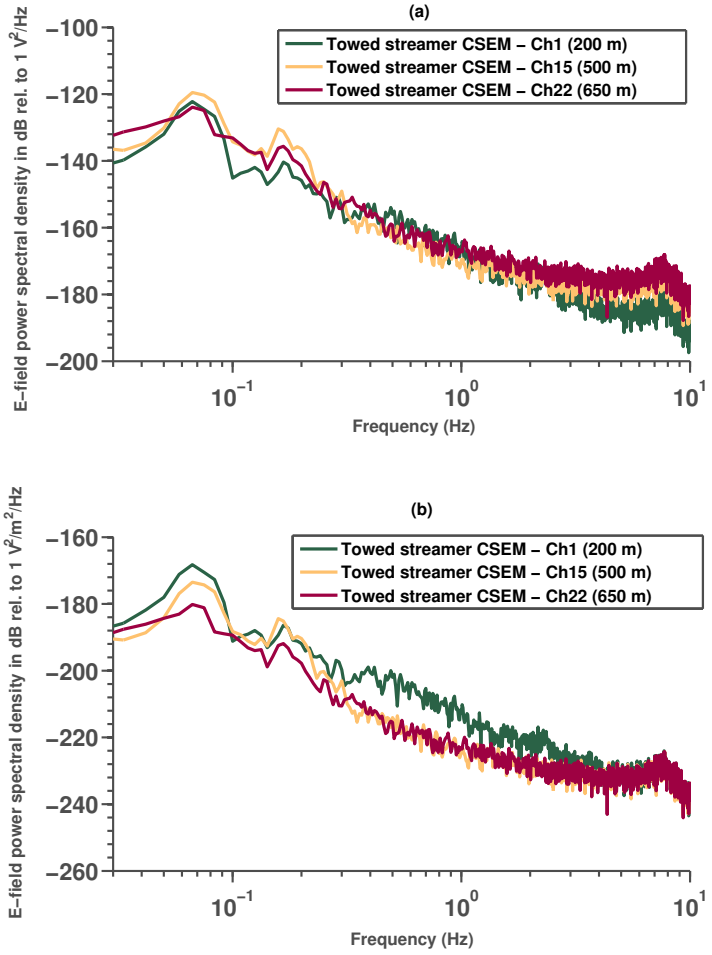

Figure 4.15: (a) Towed streamer CSEM PSD in dB relative to 1 V^2Hz^{-1} of the data shown in Figure 4.9(a). (b) PSD in dB relative to 1 $V^2m^{-2}Hz^{-1}$.

peak visible on all the channels near 7.83 Hz corresponds to the first Schumann resonance. A similar peak was observed in the OBC CSEM noise amplitude as shown in Figure 4.8.

- At frequencies 1–3 Hz, in Figure 4.15(a), the noise level is the same for all channels up to 2 Hz. In the bandwidth 2–3 Hz, the noise level is proportional to the channel length. However, scaling by the receiver length as displayed in Figure 4.15(b), the 500 m channel amplitude is similar to the 650 m channels but the 200 m channels lengths noise level is 5–10 dB above the other two.
- At frequencies 0.3–1 Hz, in Figure 4.15(a), the noise level is the same for all the channels. However, scaling with the channel length as shown in Figure 4.15(b), the noise level becomes higher for shorter channel lengths, with the 200 m being 10–15 dB higher than the 500 m and 650 m channels. The similar power of the 500

m and 650 m could be explained by the self-cancelling process of the motionally-induced noise for channel lengths equal to or greater than 500 m as explained in the time domain analysis subsection (page 88, paragraph 4). Therefore, the term $|\hat{E_T}(f)|$ in equations (4.26) and (4.28), is the dominant component of noise, although MT noise $|\hat{E_i}(f)|$ is still present within this frequency range.

- Below 0.3 Hz in Figure 4.15(b), the noise level is inversely proportional to the channel length. This means that noise originating from the electrodes and amplifiers, highlighted in equations (4.26) and (4.28) by term $|\hat{V_r}(f)|$, is one of the dominant source of noise. The prominent peak centered at 0.07 Hz in Figure 4.15 observed in all channels is noise likely due to the direct effect of ocean swell on the streamer as similar peak was observed in conventional marine CSEM noise data acquired in 109 m of water (Connell and Key, 2012). The peak at about 0.2 Hz is likely attributed the indirect effect of ocean swell on the vessel. Ocean swell causes motions of the vessel that are transferred down to the streamer through the lead-in cable. Simultaneous measurements made over receivers of different lengths, as displayed in Figure 4.15, show that frequencies of peaks are constant but amplitude decreases as the receiver length increases. The same observation was made on other runs.

  Figure 4.16 was obtained by picking prominent peak powers and frequencies recorded over the 22 noise measurements for a 200 m receiver length. The peak frequency at 0.07 Hz is sometime negligible, but the peak at about 0.2 Hz is always present on data from all runs. In general the two peaks are present in the PSD as displayed in Figure 4.15. One can observe that during the survey, peak frequencies are almost constant but power varies. This suggests that the direct or indirect effect of ocean swell on the streamer streamer affects low frequencies, and impacts each recording at varying powers. This also means that the wave height varied considerably during the entire survey. Therefore, measuring the swell amplitude prior to acquisition, and choosing the survey frequencies above this level as suggested by Mittet and Morten (2012) cannot be efficient because of swell noise variability in power.

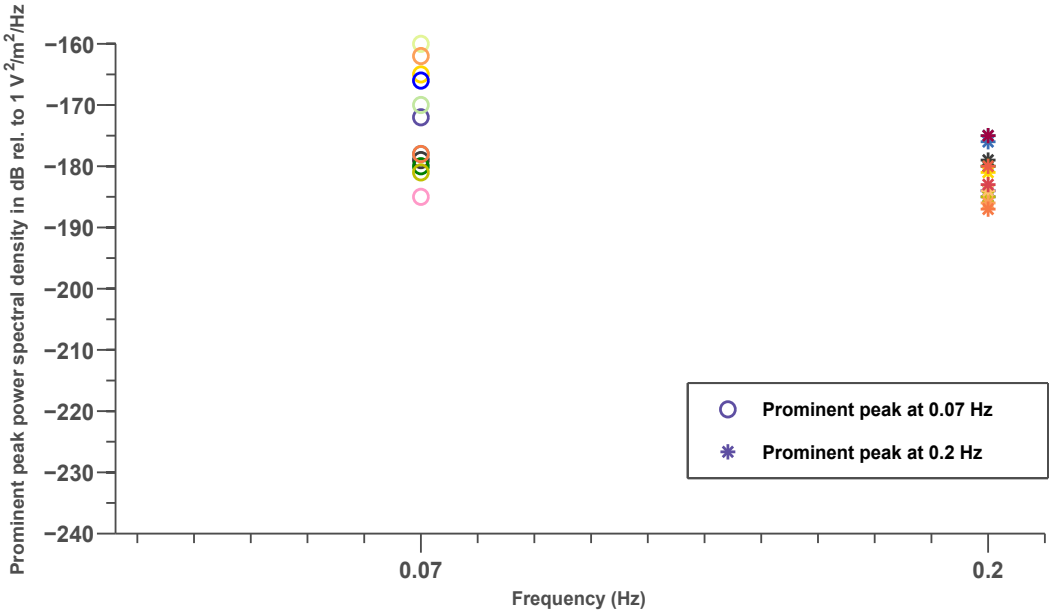

Figure 4.16: Prominent peaks powers as a function of frequency. The color of the markers denotes the peak obtained from different runs.

Coherence analysis

The purpose of coherence analysis is, first, to investigate the similarity in electric field noise between non-overlapping channels and overlapping channels, and second, to refine further the Frequency Domain Analysis section.

Figure 4.17 was obtained by calculating the coherence between the electric field noise recorded by Channel 4 and the non-overlapping channels (Figure 4.17(a)), and the coherence between Channel 4 and the overlapping channels (Figure 4.17(b)). Channel 4 (200 m) and Channel 15 (500 m) share the same mid-point. Similar figures were also obtained at other channels.

From Figure 4.17, four frequency ranges of interest are observed and marked: Range 1 (0.03–0.1 Hz), Range 2 (0.1–0.3 Hz), Range 3 (0.3–2 Hz) and Range 4 (2–60 Hz).

- Range 1 (0.03–0.1 Hz): the correlation coefficient, between Channel 4 and the non-overlapping channels (Figure 4.17(a)), and between Channel 4 and the overlapping channels (Figure 4.17(b)), is on average below 0.15 and shows a similar pattern. However, when the coherence is computed between Channel 4 and Channel 15 (see purple broken line in Figure 4.17(b)), the correlation coefficient is 0.8 at 0.03 Hz, drops to about 0.2 at 0.07 Hz, and starts to increase at 0.1 Hz.

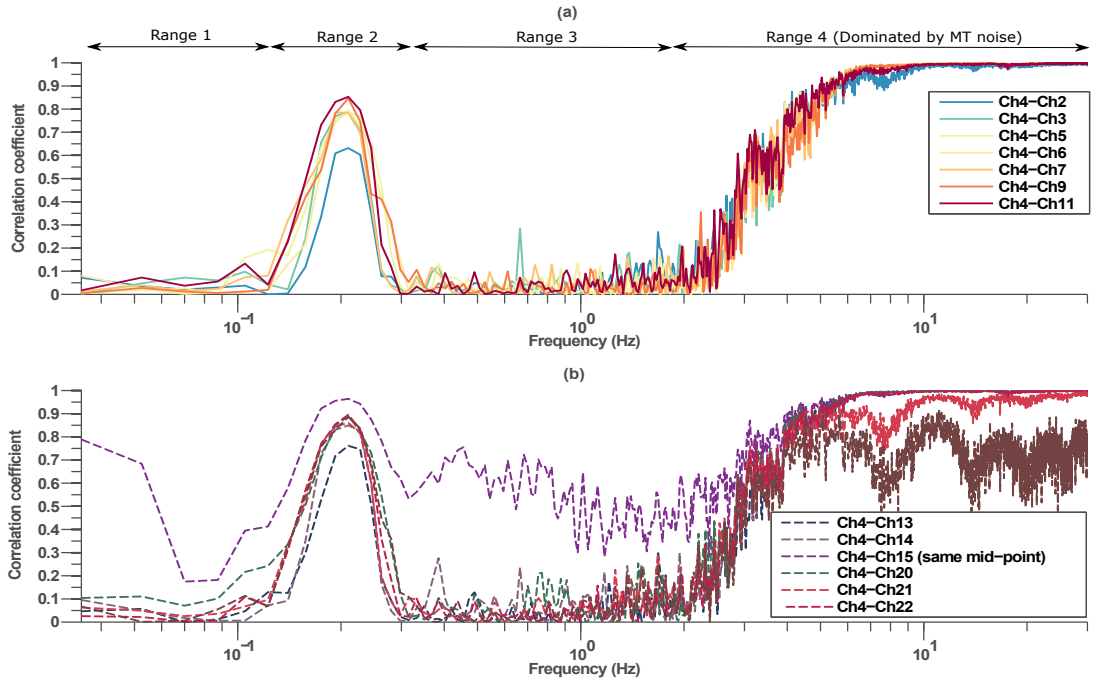

Figure 4.17: (a) Coherence between Channel 4 with non-overlapping channels. (b) Coherence between Channel 4 and overlapping channels (dashed lines). The purple broken line represents the coherence between Channel 4 and Channel 15.

- Range 2 (0.1–0.3 Hz): the correlation coefficient progressively increases and reaches its peak at around 0.2 Hz, where it is approximately 0.8. The same pattern is observed when the coherence is calculated between Channel 4 and Channel 15, but with the correlation coefficient peaking at approximately 0.95 at about 0.2 Hz. The prominent peak observed at about 0.2 Hz is probably related to the peak observed in the amplitude spectrum displayed in Figure 4.15. This peak is likely associated with the motion of the streamer vibrating with a period of about 5 s.
- Range 3 (0.3–2 Hz): the correlation coefficient between Channel 4 with most of the channels is as described in Range 1. However, the correlation coefficient between Channel 4 and Channel 15 is even higher, approximately 0.7.
- Range 4 (2–60 Hz): the correlation coefficient between Channel 4 with most of the channels is similar and gradually increases until about 7 Hz, although the correlation coefficient between Channel 4 and Channel 15 is still above the others. Above 7 Hz, the correlation coefficient between Channel 4 and all the channels (Channel 15 included) converge and is constant with an average of 0.9. This frequency range is dominated by MT noise.

These observations suggest that within the Range 1 and Range 3 frequency ranges of interest, the electric field noise recorded by the non-overlapping and the overlapping

channels is uncorrelated. However, the electric field noise of channels sharing the same mid-point is well correlated. This suggests that channels sharing the same mid-point are affected by the same noise. Within the Range 2 frequency range, the noise is very well correlated at about 0.2 Hz.

In the following, the spatial coherence of the electric field noise between Channel 4 and the non-overlapping channels (Figure 4.18), and Channel 4 and the overlapping channels (Figure 4.19), at typical frequencies chosen within the defined four ranges (0.05, 0.2, 1 and 10 Hz, respectively) is presented in more detail. The same analysis is done for Channel 15 and the overlapping channels (Figure 4.20).

In Figure 4.18, Figure 4.19, and Figure 4.20, the vertical axis represents the magnitude of the correlation coefficient obtained by computing the coherence between channels. The horizontal axis denotes the channel number that is used to compute the coherence with Channel 4 or Channel 15. For example, in Figure 4.18, "Ch2" means that the coherence is computed between Channel 4 and Channel 2. In Figure 4.19, "Ch14" means that the coherence is calculated between Channel 4 and Channel 14. In Figure 4.20, "Ch14" means that the coherence is calculated between Channel 15 and Channel 14.

Figures 4.18(a) and (c) show that the correlation coefficient between Channel 4 and Channel 3 (left), and Channel 4 and Channel 5 (right) is very low (≈ 0.05) at 0.05 and 1 Hz. As the separation between channels increases, the correlation coefficient gradually shrinks. However, at 0.2 Hz, see Figure 4.18(b), the correlation coefficient is high (≈ 0.8) and the same for all channels. At 10 Hz, as shown in Figure 4.18(d), the correlation is high (≈ 1) and constant over all channels.

Figures 4.19(a) and (b) show that the correlation coefficient between the channels sharing the same mid-point (Channel 4 and Channel 15: "Ch15") is about 8 times greater than the correlation coefficient between Channel 4 and Channel 13 ("Ch13"), and Channel 4 and Channel 16 ("Ch16"), respectively. The same feature is observed in Figure 4.19(c). Again the correlation coefficient decreases as the distance increases. Figures 4.19(c) and (d) display the same feature as described in Figures 4.18(a) and (b).

Figure 4.20 was produced by calculating the coherence between Channel 15 and the other overlapping channels without a common mid-point. The overlap distance between Channel 15 and the other channels is displayed in Table 4.3.

Figures 4.20(a) and (c) show that the correlation coefficient between Channel 15 with the channels that have an overlapping distance of 300 m is about 5 times greater than the correlation coefficient between Channel 15 and the channels that have an overlap distance of 100 m. The correlation coefficient substantially decreases as the overlapping

Channel number	Overlapping length (m)
Channel 15 - Channel 13 (“Ch13”)	100
Channel 15 - Channel 14 (“Ch14”)	300
Channel 15 - Channel 16 (“Ch16”)	300
Channel 15 - Channel 17 (“Ch17”)	100
Channel 15 - Channel 20 (“Ch20”)	0
Channel 15 - Channel 21 (“Ch21”)	0
Channel 15 - Channel 22 (“Ch22”)	0

Table 4.3: Overlapping length between Channel 15 and the overlapping channels without a common mid-point.

decreases. Therefore, within the frequency bands 0.03–0.1 Hz and 0.3–2 Hz, the correlation coefficient is a function of the overlap length between channels. In Figure 4.20(b), however, the correlation coefficient is closed to 1 for the coherence between Channel 15 and Channel 4, and slightly decreases to be 0.95 and 0.9 as the overlapping length decreases from 300 m to 100 m, respectively. Thus, the decrease of the correlation coefficient as the overlapping length between channels decreases (Figures 4.20(a) and (c)), has no effect at 0.2 Hz. Figure 4.20(d) displays the same feature as described in Figure 4.18(d) and Figure 4.19(d).

From the analysis made in Figures 4.18(a) and (b), and Figures 4.20(a) and (b), one can deduce that the non-overlapping channels have lower levels of correlated noise compared with the overlapping channels. For example, at 0.05 Hz the correlation coefficient between Channel 4 and the non-overlapping channels (Figure 4.18), Channel 3 (left), and Channel 5 (right), is 30 times less than the correlation coefficient between Channel 15 and the overlapping channels (Figure 4.20), Channel 14 (left), and Channel 15 (right).

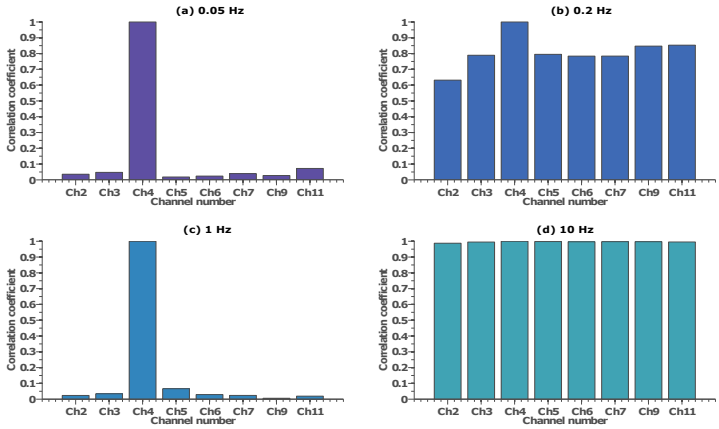

Figure 4.18: Coherence between Channel 4 and the non-overlapping channels. (a) At 0.05 Hz. (b) At 0.2 Hz. (c) At 1 Hz. (d) At 10 Hz.

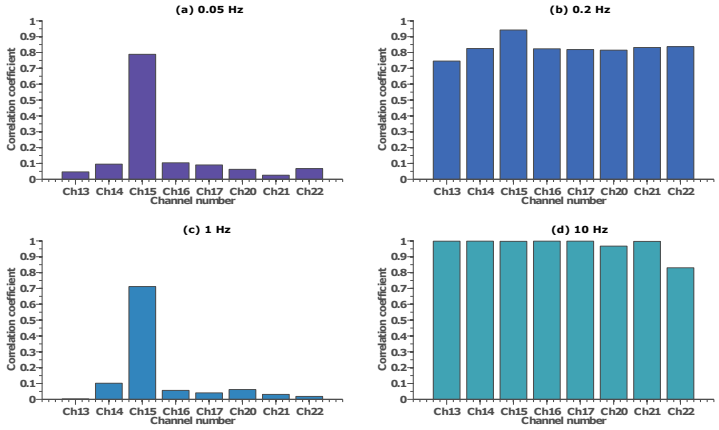

Figure 4.19: Coherence of Channel 4 and overlapping channels. Channel 4 and Channel 15 share the same mid-point. (a) At 0.05 Hz. (b) At 0.2 Hz. (c) At 1 Hz. (d) At 10 Hz.

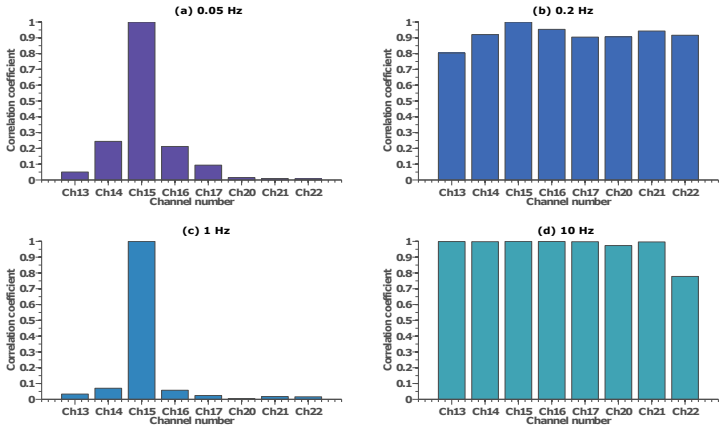

Figure 4.20: Coherence of Channel 15 and the overlapping channels. (a) At 0.05 Hz. (b) At 0.2 Hz. (c) At 1 Hz. (d) At 10 Hz.

In summary, below 1 Hz, the correlation coefficient is higher for channels sharing the same mid-point (Figure 4.19) than for non-overlapping (Figure 4.18) or overlapping (Figure 4.20) channels without a common mid-point. At the 0.03–0.1 Hz and 0.3–2 Hz frequency ranges, the correlation coefficient decreases with increasing distance separating individual channels. At 0.2 Hz, however, the noise is well correlated and does not depend on the distance separating individual channels. MT noise, represented by $\mid \hat{E}_i(f) \mid$ in equation (4.26), is correlated across all channels. However, within the frequency range of interest, the recorded noise is mostly uncorrelated. Therefore, MT noise can not be the major source of noise.

The electrode noise represented by $\mid \hat{V}_r(f)/\Delta x_r \mid$ in equation (4.26), is expected to be uncorrelated across all channels, and to decrease as the receiver length increases. However, as shown in Figure 4.15(b), the amplitude of the noise is almost the same in the frequency range 1–0.2 Hz. Therefore, $\mid \hat{V}_r(f)/\Delta x_r \mid$ cannot explain the poor correlation coefficient ($\leqslant 0.15$) between a non-overlapping or overlapping channel and its neighbouring channels, and the good correlation observed at about 0.2 Hz.

At about 0.2 Hz, the noise is very well correlated across all channels compared to the uncorrelated noise (Figure 4.15). This suggests that noise due to the motion of the telluric cable, represented by $\mid \hat{E}_T(f) \mid$ in equation (4.26), is the major source of noise. The high correlation between the channels sharing the same mid-point suggests that as the streamer moves, these channels experience the same type of motion.

Discussion

It is challenging to separate the contribution from various sources of noise in data collected with a towed streamer. Several distinct sources contribute to the overall noise picture: magnetotelluric noise, electrode noise, and motionally-induced noise. The last of these is suggested to be the largest part of the noise (Constable, 2013; Burrows, 1974, 1972). The analysis undertaken in this chapter and displayed in Figures 4.10, 4.15 and 4.17 gives an indication of what is happening in the case of a towed streamer CSEM. It appears that within the frequency range of interest, the noise is uncorrelated in the 0.03–0.1 Hz and 0.3–2 Hz frequency bands, and very well correlated at 0.2 Hz. Therefore, two mechanisms probably can cause the motionally-induced noise: ocean swell and the pressure fluctuations within the turbulent boundary layer (TBL) around the streamer.

During a survey, the streamer is towed behind a vessel by a lead-in cable. The vessel constantly experiences a linear vertical motion (up/down) due to the sinusoidal movement of a wave. Swell also can suddenly push the vessel sideways or break violently

into the vessel. The motion of the vessel creates both an extreme pulling and drag force on the lead-in cable which are subsequently transferred to the streamer. This generates various motions of the telluric cable inside the streamer. This mechanism is responsible for the correlated noise observed at 0.2 Hz as shown in Figure 4.4 and Figure 4.17. My overall results suggest that this is likely the dominant mechanism that generates motionally-induced noise.

Ocean swell may also have a direct effect on the streamer by inducing vertical motion of the streamer (Elboth et al., 2010b) and causes the two end points of the telluric cable connecting each channel to vibrate in a similar manner. This is further investigated in Chapter 7, where the direct effect of swell on the motion of the streamer is simulated in a controlled environment of the FloWave tank.

Based on experiments conducted in a laboratory environment, Keith et al. (2005) and Furey (2005) show that seismic streamers are surrounded by a TBL that grows from a few millimetres near the front to likely several decimetres near the tail. Elboth et al. (2010a) carried out an experiment in a Norwegian fjord to seek insight into the complex TBL that surrounds commercial seismic streamers in the ocean. Elboth et al. (2010a) were able to visualise the TBL based on a dye release along the streamer. A snapshot of the TBL is shown in Figure 4.21. Similar TBL is likely observed around the towed streamer CSEM. Based on experiments carried out on a 31 m and a 300 m submarine-towed Extremely Low Frequency (ELF) antennas, Burrows (1972, 1974) concluded that the pressure fluctuations in the TBL surrounding the ELF antenna cable cause it to vibrate in the Earth's magnetic field. This vibration causes a temporal variation of the angle between the Earth's magnetic field vector and the local center of the cable. Thus a voltage is induced according to Faraday's law of induction. This is investigated in Chapter 5. These pressure fluctuations are essentially uncorrelated from point to point along the cable, and so do not predispose the cable to vibrate at a specific wavelength (Burrows, 1974). This mechanism could explain the uncorrelated noise observed within the 0.03–0.1 Hz and 0.3–2 Hz frequency ranges shown in Figure 4.17.

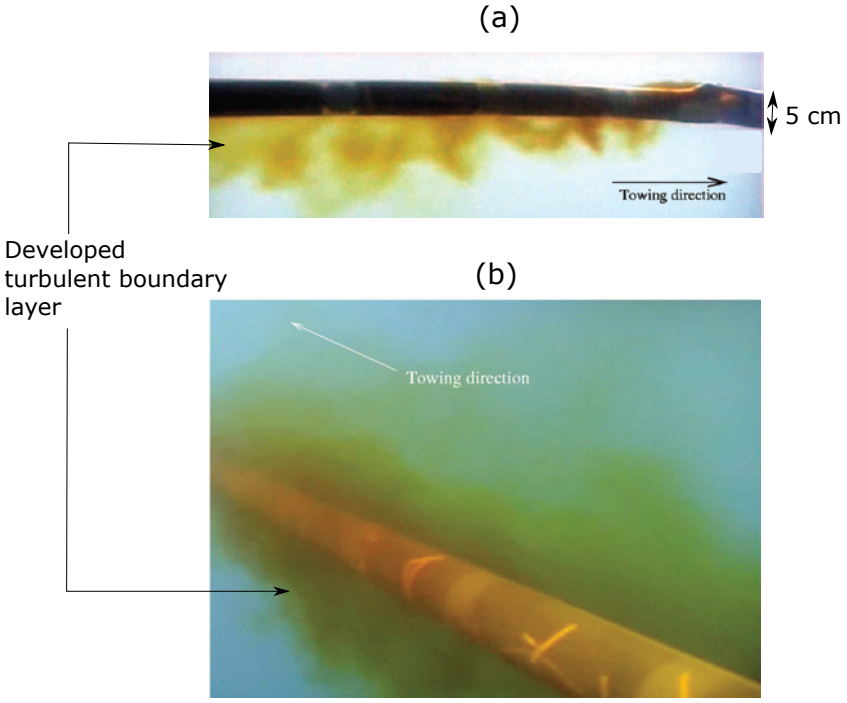

Figure 4.21: Snapshot showing a developed turbulent boundary layer (coloured dye) surrounding a 5 cm thick seismic streamer cable in the ocean. (a) Cross-section view visualized by a single hole dye release. (b) 3-D view by a multi-hole dye release. These two pictures were taken in Elboth et al. (2010a).

Summary

This chapter describes the noise recorded in 100 m water depths with an OBC and the PGS' prototype towed CSEM streamer. By comparing the recorded noise from the two methods within the frequency range of interest, 0.03–1 Hz, it is found that the towing noise is on average 20 dB greater than the noise recorded with the OBC system for 200 m channels lengths. I show also that within this frequency range, motionally-induce noise amplitude decreases with the increase of the channel length; with the noise level in the 500 and 650 m channel length being about 5–15 dB lower than the 200 m channel length. In addition, I show that motionally-induce noise is uncorrelated within the 0.03–0.1 Hz and 0.3–2 Hz frequency bands. I suspect that the pressure fluctuations within the turbulent boundary layer surrounding the streamer, that cause it to vibrate within the Earth's magnetic field, is responsible for this uncorrelated noise. At 0.2 Hz the noise is very well correlated. This high correlation is likely due to motions the vessel that are transferred to the streamer through the lead-in cable. This causes the telluric cable to vibrate at the same frequency. This is the most important mechanism that generates motionally-induce noise. In the OBC system, however, the noise is correlated across all channels in the 0.03–1 Hz frequency range. This noise is mainly due to MT fields.

The decrease in noise level as the channel length increases in the towed system, suggests that one way to reduce the motionally-induced noise could be to increase the channel length. Another way to reduce the vibration of the streamer due to ocean swell is to tow the streamer deeper and to increase the tension of the streamer.

■

5

Motionally-induced Noise Mechanisms in the Towed Streamer CSEM

Imagination is more important than knowledge. Knowledge is limited. Imagination encircles the world.

Albert Einstein
Physicist (1879-1955)

I examine the idea that towed streamer CSEM suffers from motionally-induced noise according to Faraday's law of induction. The theory is set out in detail to illustrate the cases of a horizontal and curved streamer in a constant and time-varying magnetic field, moving in water. The effect of cross-currents and ocean swell on the amplitude of the motionally-induced noise is also investigated. It is shown that no motionally-induced noise is generated when the streamer is straight in a constant magnetic field. By contrast, when the streamer shape is curved because of a cross-current, motionally-induced noise is generated if the velocity of the streamer varies over time. I derive an expression for motionally-induced noise which demonstrates that the motionally-induced noise is sensitive to the magnitude of the feather angle at the head and at the tail of the streamer and to the vertical and lateral motion of the streamer.

I presented part of this chapter during the EAGE meeting in 2014 under the title: *Estimation of Induction noise in a towed EM streamer* in Djanni et al. (2014).

5.1 Theory of motionally-induced noise: Faraday's law of induction

We consider a right-handed Cartesian coordinate system with $\mathbf{a_x}$, $\mathbf{a_y}$ and $\mathbf{a_z}$ as unit vectors in the X, Y, and Z directions, respectively. For our problem, two electrodes are connected by a cable in the presence of a spatially uniform magnetic field $\mathbf{B}(t)$, as shown in Figure 5.1. The Earth's magnetic field does not vary spatially over the area S bounded by the loop of the cable, although it does vary with time. If the cable between the electrodes is not fully stretched, the straight line between the electrodes and the cable creates an electric loop C with an area S (Filloux, 1973).

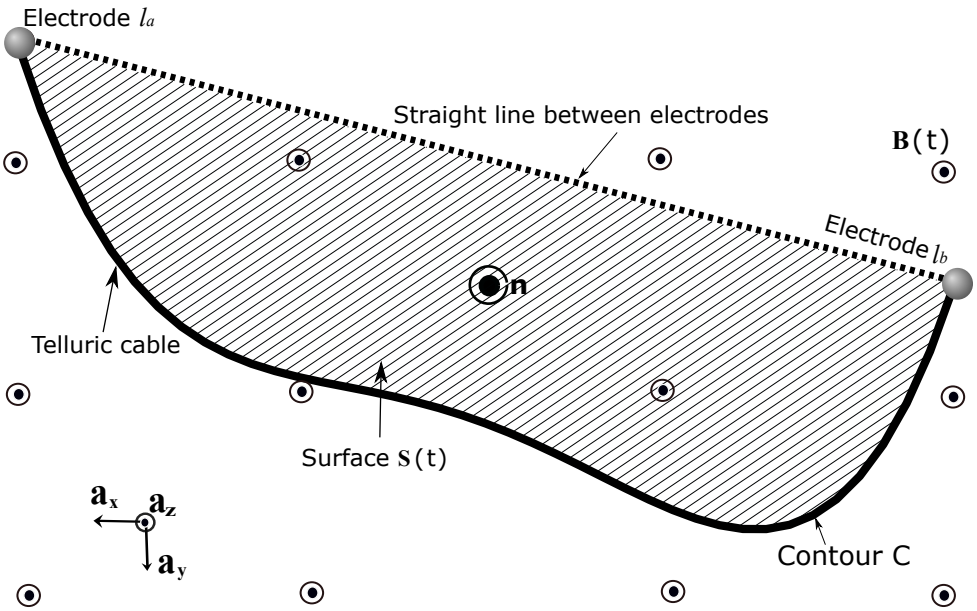

Figure 5.1: Electric loop created by the cable connected to the electrodes and the straight line between the electrodes (after, Filloux (1973)). **B** is pointing upwards (black crosses) and the normal to the surface **n** is pointing upward. The hatched area is the surface S.

The magnetic flux crossing the surface S is given by:

$$\Phi = \int_S \mathbf{B} \cdot d\mathbf{S}\,. \qquad [\mathrm{T\,m^2}] \tag{5.1}$$

The magnetic field **B** can be written as:

$$\mathbf{B} = \mathbf{a_x} B_x + \mathbf{a_y} B_y + \mathbf{a_z} B_z\,, \tag{5.2}$$

where B_x and B_y are the horizontal components of **B**. B_z is the upwards component of **B**.

The electromotive force (emf) or induced voltage, $\mathcal{V}$, around the loop is generated when the magnetic flux (in equation (5.1)), linking the loop, changes over time. This phenomenon is known as Faraday's law. It is expressed as:

$$\mathcal{V} = -\frac{\partial \Phi}{\partial t} = -\frac{\partial}{\partial t}\int_S \mathbf{B}\cdot d\mathbf{S} \qquad [\mathrm{V}] \tag{5.3}$$

Consider an electrode pair with contour C and area S that moves from C_1 at time t to C_2 at time $t+\Delta t$ with a velocity $\mathbf{v}$ in a time-varying magnetic field $\mathbf{B}(t)$ as illustrated in Figure 5.2.

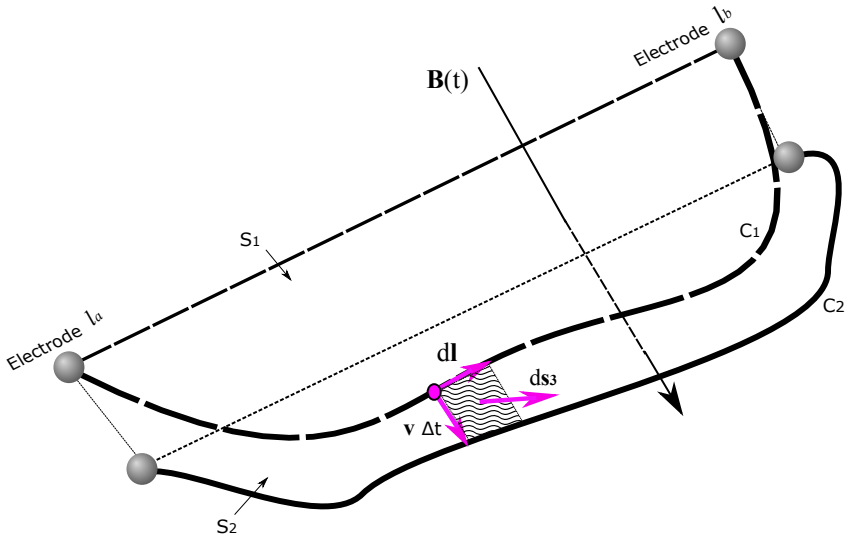

Figure 5.2: A moving electrode pair in a time-varying magnetic field. Modified from Cheng (1989).

Equation (5.4) through equation (5.13) are defined following Cheng (1989). Rewritten equation (5.3), the time-rate of change of magnetic flux through the contour is:

$$\begin{aligned}\frac{\partial \Phi}{\partial t} &= \frac{\partial}{\partial t}\int_S \mathbf{B}\cdot d\mathbf{S} \\ &= \lim_{\Delta t\to 0}\frac{1}{\Delta t}\left[\int_{S_2}\mathbf{B}(t+\Delta t)\cdot d\mathbf{S_2} - \int_{S_1}\mathbf{B}(t)\cdot d\mathbf{S_1}\right].\end{aligned} \tag{5.4}$$

$\mathbf{B}(t+\Delta t)$ in equation (5.4) can be expanded as a Taylor's series:

$$\mathbf{B}(t+\Delta t) = \mathbf{B}(t) + \frac{\partial \mathbf{B(t)}}{\partial t}\Delta t + \mathrm{H.O.T.}, \tag{5.5}$$

where the higher order terms (H.O.T) contain the second and higher powers of (Δt). Substitution of equation (5.5) into equation (5.4) yields

$$\frac{\partial}{\partial t}\int_S \mathbf{B}\cdot d\mathbf{S} = \int_{S_2}\frac{\partial \mathbf{B}}{\partial t}\cdot d\mathbf{S_2} + \lim_{\Delta t\to 0}\frac{1}{\Delta t}\left[\int_{S_2}\mathbf{B}\cdot d\mathbf{S_2} - \int_{S_1}\mathbf{B}\cdot d\mathbf{S_1} + \text{H.O.T.}\right]. \tag{5.6}$$

where $\mathbf{B}(t)$ has been written $\mathbf{B}$ for simplicity. In going from C_1 to C_2 the electrode pair covers a region that is bounded by S_1, S_2, and S_3. Side surface S_3 is the area swept out by the contour in time Δt. An element of the side surface is

$$d\mathbf{S_3} = d\mathbf{l}\times\mathbf{v}\,\Delta t\,. \tag{5.7}$$

The differential length change $d\mathbf{l}$ and the velocity $\mathbf{v}$ in an arbitrary direction can be written as the vector sum of the component length- and velocity changes, respectively:

$$d\mathbf{l} = \mathbf{a_x}dl_x + \mathbf{a_y}dl_y + \mathbf{a_z}dl_z\,, \tag{5.8}$$

$$\mathbf{v} = \mathbf{a_x}v_x + \mathbf{a_y}v_y + \mathbf{a_z}v_z\,, \tag{5.9}$$

where dl_x, dl_y are the horizontal components of $d\mathbf{l}$ and dl_z is the vertical component of $d\mathbf{l}$. The scalar v_x, v_y are the horizontal components of $\mathbf{v}$ and v_z is the vertical component of $\mathbf{v}$.

We now apply the divergence theorem for $\mathbf{B}$ at time t to the region sketched in Figure 5.2:

$$\int_V \nabla\cdot\mathbf{B}dv = \int_{S_2}\mathbf{B}\cdot d\mathbf{S_2} - \int_{S_1}\mathbf{B}\cdot d\mathbf{S_1} + \int_{S_3}\mathbf{B}\cdot d\mathbf{S_3}\,, \tag{5.10}$$

where a negative sign is included in the term involving $d\mathbf{S_1}$, because outward normals must be used in the divergence theorem. Using equation (5.7) in equation (5.10) and noting Maxwell's equation that $\nabla\cdot\mathbf{B} = 0$ because magnetic monopoles do not exist, we have

$$\int_{S_2}\mathbf{B}\cdot d\mathbf{S_2} - \int_{S_1}\mathbf{B}\cdot d\mathbf{S_1} = -\Delta t\int_C(\mathbf{v}\times\mathbf{B})\cdot d\mathbf{l}\,. \tag{5.11}$$

Combining equation (5.6) and equation (5.11), we obtain

$$\frac{\partial}{\partial t}\int_S \mathbf{B}\cdot d\mathbf{S} = \int_S\frac{\partial\mathbf{B}}{\partial t}\cdot d\mathbf{S} - \int_C(\mathbf{v}\times\mathbf{B})\cdot d\mathbf{l}\,. \tag{5.12}$$

Substituting equation (5.12) into equation (5.3), we obtain the equation that constitutes the general form of Faraday's law for a moving system in a time-varying magnetic

field:

$$\mathcal{V} = -\int_S \frac{\partial \mathbf{B}}{\partial t} \cdot d\mathbf{S} + \int_C (\mathbf{v} \times \mathbf{B}) \cdot d\mathbf{l}\,. \qquad [\mathrm{V}] \qquad (5.13)$$

In equation (5.13), the first term on the right-hand side is the emf induced voltage in a stationary loop due to the time variation of **B** through the surface; and the second term is the flux cutting emf or the motional emf due to the motion of the electrodes in **B**.

From Equation 5.13 it can be seen that an emf voltage at each pair of electrodes can be generated in four ways:

(1) A change in the magnetic field strength ($\partial B/\partial t$) over the surface S as shown in Figure 5.3;

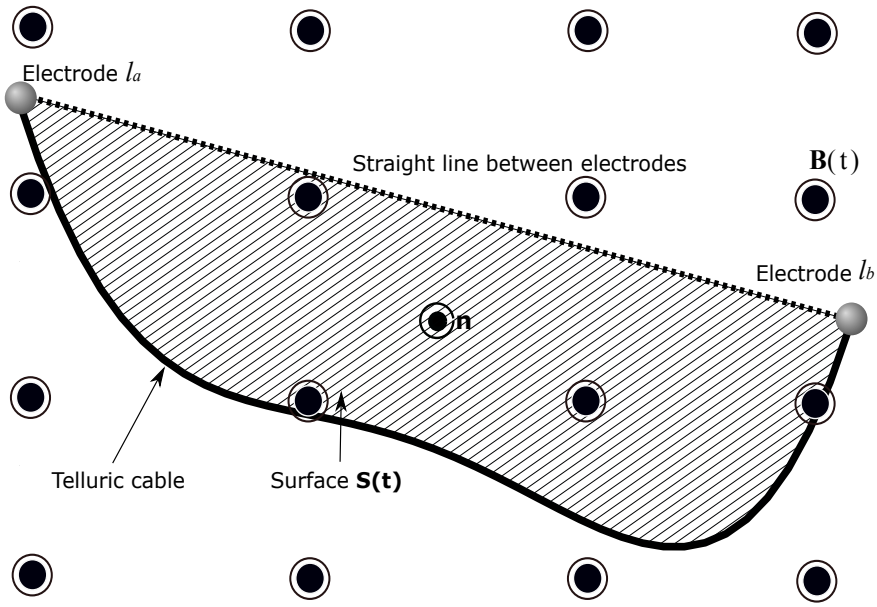

Figure 5.3: An electric field is induced by increasing the magnetic field amplitude over time. The bold circles indicate an increase in the magnitude of the geomagnetic field compared with Figure 5.1.

(2) Variation of the surface area S enclosed by the loop with time as illustrated in Figure 5.4.

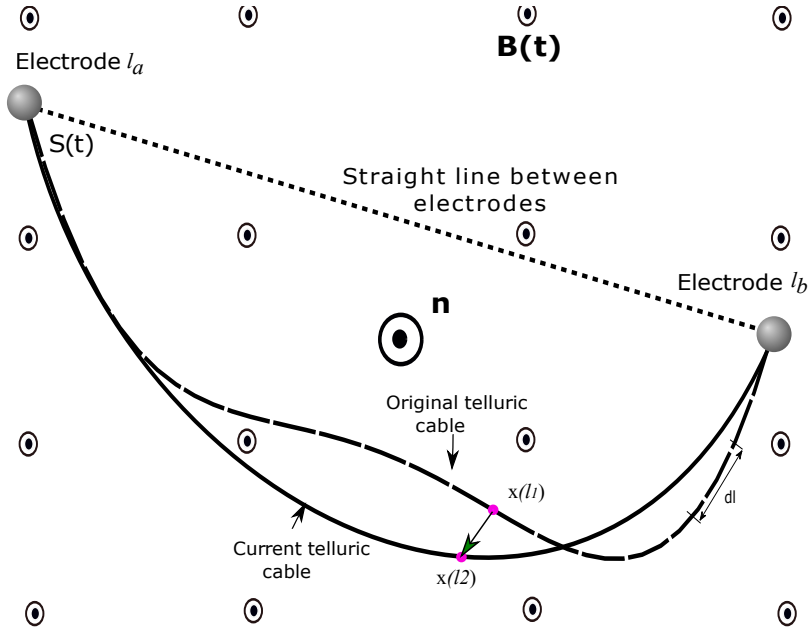

Figure 5.4: An electric field is induced by the variation of the surface S over time. The arrow moving from the position $x(l_1)$ to the position $x(l_2)$ shows how a change of the a position can change the surface area.

(3) Variation of the angle $(\partial\alpha/\partial t)$ between the magnetic field and the area vector with time, as shown in Figure 5.5.

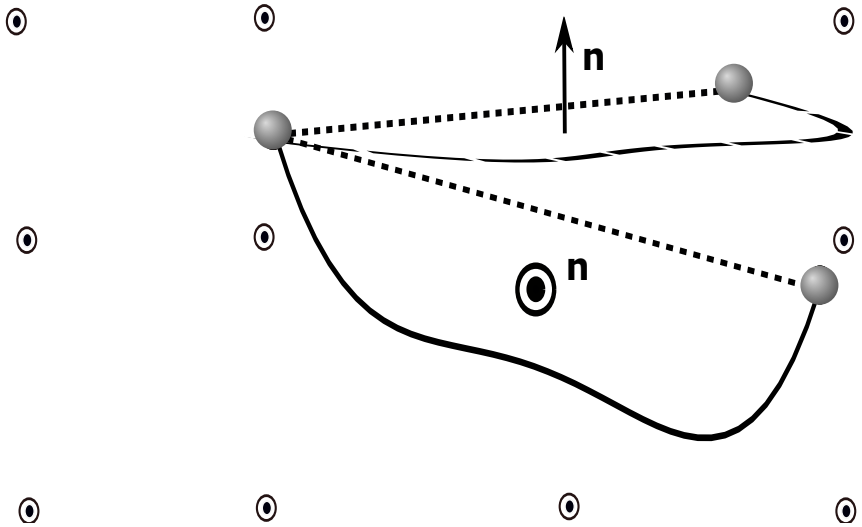

Figure 5.5: An electric field is induced by the variation the angle α (The angle between **n** and **B**) over time.

(4) Velocity's variation of the moving conductor as shown in Figure 5.2.

Stationary streamer in a constant geomagnetic field

When the streamer is stationary in a geomagnetic field assumed to be constant, the telluric cable is straight and the sea is calm, the parameters in equation (5.13) become:

$$\mathbf{S} = 0\,, \mathbf{v} = 0\,, \frac{\partial B}{\partial t} = 0\,. \tag{5.14}$$

This implies that

$$\mathcal{V} = 0\,. \tag{5.15}$$

Therefore, if nothing changes, the induced emf is zero.

Stationary streamer in a time-varying geomagnetic field

There are fluctuations which occur in the geomagnetic field. The total magnetic field is approximately 50,000 nT and the disturbance may be as much as 100 nT during magnetic storms and only 1 nT on magnetic quiet day (Longuet-Higgins et al., 1954). Because $\partial B/\partial t$ is not zero and $v = 0$, equation (5.13) can be rewritten as:

$$\mathcal{V} = -\int_S \frac{\partial \mathbf{B}}{\partial t} \cdot d\mathbf{S}\,. \qquad [\mathrm{V}] \tag{5.16}$$

From equation (5.16), it is clear that when the electrodes are stationary, the induced voltage between them is due to a variation of the magnetic field with time through the surface S. Therefore, this voltage is induced only if $S \neq 0$

Moving streamer in a constant magnetic field

When an electrode pair moves with a velocity $\mathbf{v}$ in a constant (non-time-varying) magnetic field $\mathbf{B}$, the rate of change of the magnetic field ($\partial \mathbf{B}/\partial t$) is equal to zero. Therefore, equation (5.13) is rewritten as:

$$\mathcal{V} = \int_C (\mathbf{v} \times \mathbf{B}) \cdot d\mathbf{l}\,. \qquad [\mathrm{V}] \tag{5.17}$$

For computational purposes, to find the motionally-induced voltage, the path may be thought of as a series of short segments (dl_i) over each of which the component of the vector $\mathbf{v} \times \mathbf{B}$ is constant or changing with respect to time as shown in Figure 5.6. The incremental motionally-induced voltage ($\mathcal{V}_i$) generated over each segment is the

component of the vector $\mathbf{v}\times\mathbf{B}$ along the path of that segment times the segment length. Thus,

$$\mathcal{V}_i = (\mathbf{v}(t)_i \times \mathbf{B}) \cdot d\mathbf{l}_i = (\mathbf{F}_i(t)) \cdot d\mathbf{l}_i = F_i(t) dl_i \cos(\alpha_i)\,, \tag{5.18}$$

where $\mathbf{F}_i(t)$ is the voltage equal to $\mathbf{v}_i \times \mathbf{B}$, α_i is the angle between $\mathbf{F}_i(t)$ and $d\mathbf{l}_i$, and an approximation of the motionally-induced voltage along the entire path expressed in equation (5.17) is then just the summation of the incremental $\mathcal{V}_i$ at each segment, which is

$$\mathcal{V} = \sum_{i=1}^{N} \mathcal{V}_i = \sum_{i=1}^{N} (\mathbf{v}_i \times \mathbf{B}) \cdot d\mathbf{l}_i\,. \tag{5.19}$$

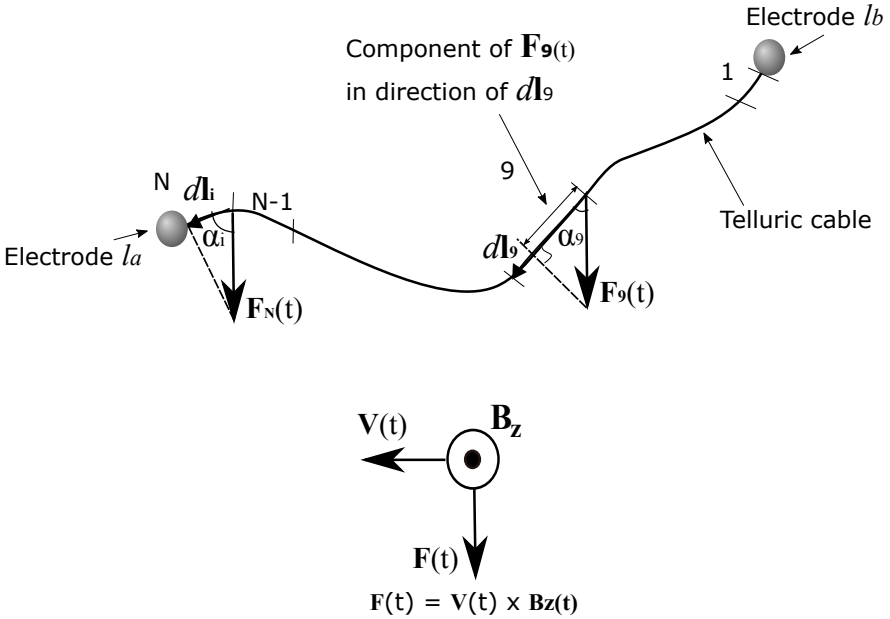

Figure 5.6: Component of $\mathbf{V} \times \mathbf{B}$ along a telluric cable between two electrodes.

Recalling equation (5.17), the cross product $\mathbf{v} \times \mathbf{B}$ can be expressed as:

$$\mathbf{v} \times \mathbf{B} = \mathbf{a_x}(v_y B_z - v_z B_y) + \mathbf{a_y}(v_z B_x - v_x B_z) + \mathbf{a_z}(v_x B_y - v_y Bx)\,. \tag{5.20}$$

Substituting equations (5.8) and (5.20), into equation (5.17) we obtain

$$\mathcal{V} = \int_{l_a}^{l_b} dl_x(v_y B_z - v_z B_y) + dl_y(v_z B_x - v_x B_z) + dl_z(v_x B_y - v_y Bx)\,. \tag{5.21}$$

In the following, three mechanisms that can generate the motionally-induced field are investigated.

Case 1: no cross-current

We assume that the CSEM streamer (containing two electrodes l_a and l_b) is towed by a vessel at a nominal and constant speed of 4 knots as illustrated in Figure 5.7. So, the direction of the vector $\mathbf{l}_b\mathbf{l}_a$ joining the electrodes may be expected to be the same as that of the velocity $\mathbf{v}$ of the ship relative to the earth. This means that

$$dl_y = dl_z = 0\,. \tag{5.22}$$

Substituting equation (5.22) in equation (5.21) we obtain

$$\mathcal{V} = \int_{l_a}^{l_b} dl_x(v_y B_z - v_z B_y)\,. \tag{5.23}$$

We assume also that the velocity of the vessel, $\mathbf{v}$, is the same as for the electrodes. The vessel is towed inline with its velocity aligned with the x-axis. So,

$$v_y = v_z = 0\,. \tag{5.24}$$

Substituting equation (5.24) in equation (5.23), we obtain

$$\mathcal{V} = 0\,. \qquad [\mathrm{V}] \tag{5.25}$$

That is, when the streamer is towed behind a vessel along the vessel's track, the electrode pair cuts no magnetic flux. Therefore, no motionally-induced voltage is generated.

Case 2: with cross-current and ocean swell

A common problem in marine acquisition is ocean water currents that cause the streamer to deviate from its desired track line to a curved shape (Krail and Brysk, 1989), as illustrated in Figure 5.8. The tangent line along the streamer curve and the line of the vessel's track is known as the feather angle (Krail and Brysk, 1989).

Following (Martin et al., 2000) who described the effect of ocean water currents on seismic 2D seismic streamer, we can imply that sea water currents generate vibrations that propagate down the EM streamer in a number of characteristic modes, amplitudes, apparent velocities and frequencies, which are partly function of the stiffness of the streamer and how the electrodes are de-coupled from various streamer vibrations.

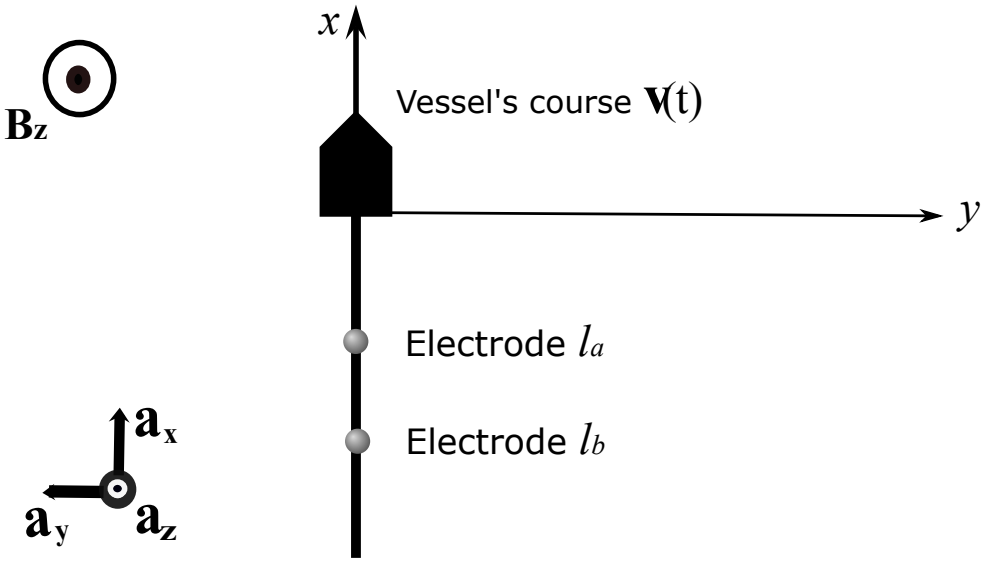

Figure 5.7: The streamer in still-water without current

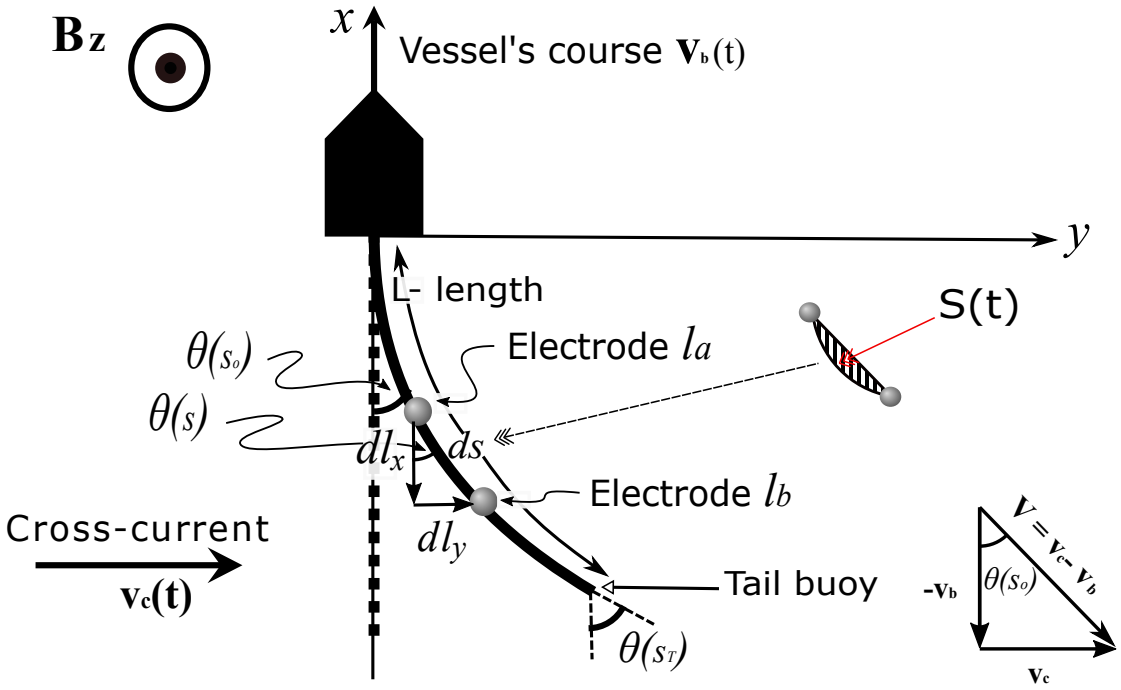

Figure 5.8: The streamer is shown as it sails in a cross-current. ds is a small element of the streamer. $\theta(s_0)$ and $\theta(s_T)$ are the feathering angles at the head of the streamer and at the tail buoy, respectively. θ is a feathering angle at a position over the streamer. S(t) is the surface area between the pair of electrodes receiver (hatched area).

In this section, we derive an expression for the motionally-induced electric field for the shape of the streamer curved by the action of drag forces from ocean water current and balanced by the tension of the mooring.

For our problem, the feather angles at the head of the streamer and at the tail buoy are denoted by $\theta(s_0)$ and $\theta(s_T)$ respectively. This is shown in Figure 5.8. The feather angle at any position along the streamer is denoted by $\theta(s)$. Let the velocity of the vessel be $\mathbf{v_b}$ and $\mathbf{v_c}$ the velocity of the cross current. The resultant velocity vector $\mathbf{v}$ of the water acting on the cable is the vector difference of the course of the vessel and the cross current; that is $\mathbf{v} = \mathbf{v_c} - \mathbf{v_b}$. Thus the vector $\mathbf{v}$ is equal to $v_x\mathbf{a_x} + v_y\mathbf{a_y} + v_z\mathbf{a_z}$. This may be estimated from accelerometers, gyroscopes, and magnetic compasses (Ronaess and Lindqvist, 2010). Following Krail and Brysk (1989), the coordinates x and y of the streamer are related to the feather angle θ and the arc length s by the relations:

$$dl_x = ds\cos(\theta(s))\,, \tag{5.26}$$

$$dl_y = -ds\sin(\theta(s))\,, \tag{5.27}$$

provided that the magnitude of $\theta(s)$ never exceeds $\pi/2$ rad. This means that the streamer does not double back. In addition, since the streamer curves away from the x-axis, the magnitude of $\theta(s)$ increases down the streamer. The assumptions made in deriving equations (5.26) and (5.27) hold for the following condition:

1) The streamer is in equilibrium; this means that all forces — tension and drag forces — acting on the streamer are constant for a time sufficient to damp all oscillations.

2) The cross-current velocity is constant - at the time that one shot is recorded.

3) The physical end points of the streamer coincide with the physical end points where the tangent angle end points are measured.

4) The feather angle both at the head of the cable and at the tail buoy cannot be equal to zero. The equation describing the shape of the streamer holds for only small angles up to about $\pi/2$ rad.

However, these assumptions do not hold if, during a time sufficient for a shot, the streamer tension is disturbed by sudden physical forces due to the change of sea state or cross-current velocity, the vessel's speed or when the vessel turns around at the end of a line.

To acknowledge the fact that the streamer shape is curved, and substituting equations (5.26) and (5.27) into equation (5.21) we obtain:

$$\begin{aligned}\mathcal{V} &= \int_{s_0}^{s_T} (v_y B_z - v_z B_y)\cos(\theta(s))ds - (v_z B_x - v_x B_z)\sin(\theta(s))ds \\ &= \int_{\theta(s_0)}^{\theta(s_T)} (v_y B_z - v_z B_y)\cos(\theta(s))\frac{ds}{d\theta}d\theta - (v_z B_x - v_x B_z)\sin(\theta(s))\frac{ds}{d\theta}d\theta\,, \end{aligned} \tag{5.28}$$

where s_0 and s_T are the arc lengths between a pair of electrodes at the head of the cable and at the tail buoy, respectively. From Krail and Brysk (1989), the expression that relates the arc length s to the feather angle at the head of the cable and at the tail buoy, and the streamer length is:

$$s(\theta) = L\left(\frac{\cot(\theta_0) - \cot(\theta)}{\cot(\theta_0) - \cot(\theta_T)}\right), \tag{5.29}$$

where $\theta(s)$, $\theta(s_T)$, and $\theta(s_0)$ have been written θ, θ_T, and θ_0 for simplicity, respectively. L is the streamer length in metres. We differentiate equation (5.29) to obtain $ds/d\theta$:

$$\frac{ds}{d\theta} = \frac{L}{\cot(\theta_0) - \cot(\theta_T)}\frac{1}{\sin^2(\theta)}, \tag{5.30}$$

or

$$\frac{ds}{d\theta} = D\frac{1}{\sin^2(\theta)}, \tag{5.31}$$

where

$$D = \frac{L}{\cot(\theta_0) - \cot(\theta_T)}. \tag{5.32}$$

Substituting equation (5.31) into equation (5.28), we find that $\mathcal{V}$ is:

$$\begin{aligned}\mathcal{V} &= \int_{\theta_0}^{\theta_T} (v_y B_z - v_z B_y)\cos(\theta)D\frac{1}{\sin^2(\theta)}d\theta - (v_z B_x - v_x B_z)\sin(\theta)D\frac{1}{\sin^2(\theta)}d\theta\,, \\ &= \int_{\theta_0}^{\theta_T} (v_y B_z - v_z B_y)D\frac{\cot(\theta)}{\sin(\theta)}d\theta - (v_z B_x - v_x B_z)D\frac{1}{\sin(\theta)}d\theta\,. \end{aligned} \tag{5.33}$$

Assuming that the velocity of the streamer (v_x, v_y, and v_z) is constant over one shot, then an integration of equation (5.33) can be performed analytically and yields:

$$\mathcal{V} = -(v_y B_z - v_z B_y)D\frac{1}{\sin(\theta)} + (v_z B_x - v_x B_z)D\ln\left(\left|\tan\left(\frac{\theta}{2}\right)\right|\right)\Bigg|_{\theta_0}^{\theta_T}. \tag{5.34}$$

After evaluating equation (5.34), we find the expression for $\mathcal{V}$:

$$\begin{aligned}\mathcal{V} &= (v_z B_y - v_y B_z) D \left(\frac{1}{\sin(\theta_T)} - \frac{1}{\sin(\theta_0)} \right) \\ &+ (v_z B_x - v_x B_z) D \left[\ln \left(\left| \tan \left(\frac{\theta_T}{2} \right) \right| \right) - \ln \left(\left| \tan \left(\frac{\theta_0}{2} \right) \right| \right) \right] , \\ &= (v_z B_y - v_y B_z) D \left(\frac{1}{\sin(\theta_T)} - \frac{1}{\sin(\theta_0)} \right) \\ &+ (v_z B_x - v_x B_z) D \ln \left(\left| \frac{\tan(\frac{\theta_T}{2})}{\tan(\frac{\theta_0}{2})} \right| \right) . \qquad [\mathrm{V}] \end{aligned} \tag{5.35}$$

Dividing equation (5.35) by the streamer length, we obtain the expression of the motionally-induced electric field $E_T = \mathcal{V}/L$:

$$\begin{aligned} E_T &= (v_z B_y - v_y B_z) K \left(\frac{1}{\sin(\theta_T)} - \frac{1}{\sin(\theta_0)} \right) \\ &+ (v_z B_x - v_x B_z) K \ln \left(\left| \frac{\tan(\frac{\theta_T}{2})}{\tan(\frac{\theta_0}{2})} \right| \right) , \qquad [\mathrm{V\,m^{-1}}] \end{aligned} \tag{5.36}$$

where

$$K = \frac{1}{\cot(\theta_0) - \cot(\theta_T)} . \tag{5.37}$$

Equation (5.36) is the general expression of the motionally-induced field generated along the tensioned streamer length when it sails through a constant cross current. Equation (5.36) shows a relation between the streamer velocity $\mathbf{v}(v_x,\ v_y,$ and $v_z)$, the geomagnetic field $\mathbf{B}(B_x,\ B_y,$ and $B_z)$, and the feathering tangent angle at the head (θ_0) and the tail (θ_T) of the streamer.

However, this expression is only valid both in a stable current zone and if the streamer has an arc length shape as a result of the current. In case of strong variability of marine currents in the area under investigation, Equation (5.36) could not be used because of the oscillation of compass values (θ_0 and θ_T). Moreover, it can be seen that when the streamer is parallel to the vessel's course, in the case that v_c is small enough to not cause the deviation of the streamer, that is θ_T and θ_0 are constant at zero, equation (5.36) does not hold. Hence, equation (5.36) is valid only when $\theta_0 \neq \theta_T$.

Following the first-order term of the Taylor series, in case the tangent angles θ_0 and θ_T (in radians) are small (approaching zero), the following small-angle approximation can

be made:

$$\sin(\theta_0) \approx \theta_0\,, \tag{5.38}$$

$$\cos(\theta_0) \approx 1 - \frac{\theta_0^2}{2!} \approx 1\,, \tag{5.39}$$

$$\tan(\theta_0) \approx \frac{\sin(\theta_0)}{\cos(\theta_0)} \approx \theta_0\,, \tag{5.40}$$

$$\cot(\theta_0) = \frac{1}{\tan(\theta_0)} \approx \frac{1}{\theta_0}\,; \tag{5.41}$$

and,

$$\sin(\theta_T) \approx \tan(\theta_T) \approx \theta_T\,, \tag{5.42}$$

$$\cos(\theta_T) \approx 1 - \frac{\theta_T^2}{2!} \approx 1\,, \tag{5.43}$$

$$\tan(\theta_T) \approx \frac{\sin(\theta_T)}{\cos(\theta_T)} \approx \theta_T\,, \tag{5.44}$$

$$\cot(\theta_T) = \frac{1}{\tan(\theta_T)} \approx \frac{1}{\theta_T}\,. \tag{5.45}$$

Substituting equations (5.38) to (5.41) and equations (5.42) to (5.45) in equation (5.36) yields a simplify expression of E_T. After some mathematical manipulations,

$$E_T = v_y B_z - v_z B_y + (v_z B_x - v_x B_z)\frac{\theta_T \theta_0}{\theta_T - \theta_0} \ln\left(\left|\frac{\theta_T}{\theta_0}\right|\right)\,. \qquad [\mathrm{V\,m^{-1}}] \tag{5.46}$$

From equation (5.46), we can deduce that the expression of E_T holds only for two conditions:

- $\theta_T \neq \theta_0\,,$
- $\theta_0 \neq 0\,.$

The model expressed equation (5.46) is a simplification of the motionally-induced field caused solely by the motion of the streamer. Equation (5.46) only takes in consideration the motionally-induced field due to motion of the streamer. However, for a real streamer at sea, in addition of the streamer motion, the whole water volume around the streamer moves as well and generates an additional motionally-induced field. Hence, the amplitude of this motionally-induced field due to water motion is connected to the size of the streamer. Reducing the streamer size could possibly reduce the amplitude of this motionally-induced field and disconnect the motion of the streamer from the water motion.

Now, if θ_T and θ_0 approach zero at different speed, then

$$\lim_{\theta_{0/T}\to 0} \frac{\theta_T \theta_0}{\theta_T - \theta_0} \ln\left(\left|\frac{\theta_T}{\theta_0}\right|\right) = 0\,. \tag{5.47}$$

After substitution of equation (5.47) into equation (5.46), we obtain an expression of E_T that relates the streamer velocity and geomagnetic field, eliminating the influence of the feathering angles at the top and head of the streamer:

$$\lim_{\theta_{0/T}\to 0} E_T = v_y B_z - v_z B_y\,. \qquad [\mathrm{V\,m^{-1}}] \tag{5.48}$$

Let θ_T and θ_0 approach zero at the same speed,

$$\lim_{\theta_{0/T}\to 0} \frac{\theta_T \theta_0}{\theta_T - \theta_0} \ln\left(\left|\frac{\theta_T}{\theta_0}\right|\right) \text{ is undefined}\,, \tag{5.49}$$

as a consequence,

$$\lim_{\theta_{0/T}\to 0} E_T \text{ is undefined}\,. \tag{5.50}$$

The motionally-induced electric field can be calculated or estimated if the value of each parameter in equation (5.36) is known. Motion sensors such as 3 components accelerometers dispose along the streamer measure the motion of the streamer in water in $\mathbf{a_x}$, $\mathbf{a_y}$, and $\mathbf{a_z}$ direction. The streamer lateral (v_x and v_y) and vertical (v_z) velocity could be derived from the integration of the accelerometer data. Earth magnetic field component (B_x, B_y, and B_z) could be measured at a fixed location by three-axis fluxgate magnetometers.

If the streamer velocity does not change over time, from one shot to another, only a direct current (DC) shift equation (5.36) will be generated. However, any change in the velocity of the streamer induces a variation of the magnetic flux passing through the electric conductive part of the streamer. As a consequence, a motionally-induced field is generated between a pair of electrodes.

Discussion and Conclusion

Following Krail and Brysk (1989), I derived the general expression of the motionally-induced electric field when the streamer has a curved shape caused by a constant cross-current (equation (5.36)). From equation (5.36), it is clear that the magnitude of the motionally-induced noise is a function of the amplitude of the earth magnetic fields (B_x, B_y, and B_z), the velocity of the streamer (v_x, v_y, and v_z) resulting from

water acting on the cable, and the tangent angle at the head (θ_0) and at the tail of the cable (θ_T). Hence, the obvious approach to estimate the motionally-induced electric field passes by estimating all the three parameters. After the motionally-induced noise has been estimated, the remain task is to correct the measured electric field data using the estimated electric field.

To start with, the magnitude of the earth magnetic field is known and cannot be reduced. The velocity of the streamer and the feather angles in the 3 Cartesian coordinates on the other hand depend on the streamer capability to resist external perturbations such as cross-currents and ocean swell. Therefore the magnitude of E_T may be reduced in two ways. The first way could be to reduce the lateral (v_x and v_z) and vertical (v_z) motion of the streamer by the mean of robust streamer control vertical and horizontal devices, by towing deeper or by having rigid telluric cable. The second way could be to reduce the angle differences between the feathering angle at the head of the streamer and at the tail buoy. This could be done by increasing the tension at the head of the streamer and at the tail buoy. The expression of the motionally-induced noise [equation (5.48)] was obtained when the tangent angle θ_0 and θ_T tends to zero at different speed.

Summary

I have explored the effect of Faraday's law of induction on a towed electric streamer and have derived expressions of the motionally-induced field in three scenarios. In the first case, the streamer was assumed to be parallel to the vessel's track line. The motionally-induced noise was found to be zero. In the second case, when the streamer shape is curved because of cross-currents, motionally-induced noise is generated if the velocity of the streamer, and the feather angle at the head and at the head of the streamer vary over time. Based on these expressions, I argued that the motionally-induced field could be reduced by towing the streamer deeper or increasing the tension of the streamer at the tail buoy.

■

6

Experiment

See now the power of truth; the same experiment which at first glance seemed to show one thing, when more carefully examined, assures us of the contrary.

Galileo Galilei (1564–1642)
Astronomer and Physicist

I describe a set of small-scale tests carried out using marine silver-silver chloride (Ag-AgCl) electrodes that are used as sensing devices on a purpose-built prototype towed controlled source electromagnetic (CSEM) streamer. I also report on an experiment carried out to measure the motionally-induced noise in the prototype streamer suspended in the Edinburgh FloWave tank, in which the streamer is subjected both to water flow along its length and to waves propagating in the same direction, at 45° and 90° to the streamer direction. To evaluate the efficiency of the new marine Ag-AgCl electrodes, I compare first the background noise sensed by the new electrodes with noise sensed by the land copper electrodes and a pair of commercially used marine Ag-AgCl electrodes. Then I compare the background noise sensed by the new electrodes when submerged in fresh and salt water, respectively. The key findings are that the new electrodes recorded the same background noise as the copper and the commercial electrodes. I also show that the new electrodes work in fresh water as well as in salt water. Finally, I describe the assembly process of the prototype streamer, the purpose of each wiring configuration, and the tests carried out in the FloWave tank.

6.1 Introduction

Analysing noise measured during a field trial in the sea with the marine towed controlled source electromagnetic (CSEM) system in Chapter 4, I observed that the noise is spatially correlated at high-frequency ($\geqslant$ 10 Hz). However, within the frequency range of interest, 0.01–0.2 Hz and 0.3–1 Hz the noise is uncorrelated and correlated at about 0.2 Hz. Evidence of motionally-induced noise has been observed in the data, but the mechanism generating it is unclear. In an effort to try to understand the mechanism generating this noise, and to simulate real offshore condition, Dr. David Wright, Prof. Anton Ziolkowski, and I planned the FloWave tank experiment. Prof. Anton Ziolkowski and Dr. David Wright raised the money for the equipment and for the use of the FloWave tank. Dr. David Wright designed the prototype CSEM streamer. This streamer was then suspended 1 m below fresh water in the Edinburgh FloWave tank, where it was subjected to water flowing along its length and to wave motion of different heights, frequencies, and travelling in different directions. These tests enable me to characterise and quantify the motionally-induced electric field noise due to flow rates around the electrodes (this will be referred to as flow noise) relative to the motionally-induced electric field noise due to wave motion (this will be referred to as wave motion noise). These tests also enable me to estimate the amplitude of the wave motion noise and to compare it to the measured electric field noise.

This chapter has two parts. It starts with the description of small-scale tests I conducted prior to the FloWave tank experiment. For the purpose of the tests, Prof. Anton Ziolkowski and Dr. David Wright bought new marine silver-silver chloride (Ag-AgCl) electrodes. I investigated their capability to sense background noise. The manufacturing specification states that the electrodes work in fresh water as well as in salt water. The objectives of these tests were:

1) To check that the Ag-AgCl electrodes were able to sense electric field noise in fresh water as well as in salt water. This is because the FloWave tank contains fresh water.

2) To test the effect of a random perturbation of water around the electrodes. The reason for carrying out this test is because one of the objectives of the FloWave tank experiment was to quantify the contribution of flow and wave motion noise around the prototype streamer.

3) To test the difference in amplitude between a pair of twisted and a non-twisted pair electrode telluric cable. Figure 6.1 illustrates a non-twisted pair cable (top), and a twisted pair cable (bottom). In fact, the electrode cables were twisted

together only on the common return path, but an electrode of each pair was submerged individually into a tank of water 0.3 m away from the other electrode, and the associated telluric cable was connected to the amplifier. Twisted pair cable is used in telecommunication to reduce magnetic interference noise (Vander-Hyde et al., 2011). Twisting the electrodes cable may, therefore, help to reduce the background noise contribution.

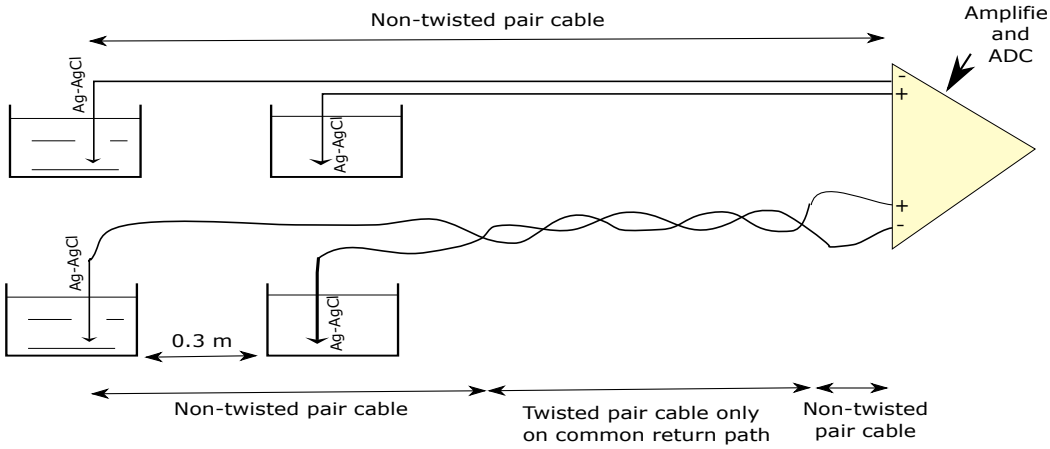

Figure 6.1: Non-twisted pair cable (top) and twisted pair cable (bottom). The electrode cables were twisted together only on their common return path.

To obtain a twisted pair of electrode cables, two cables were attached at one end. At the other end, I stripped the cables and carefully inserted them into the center of a hand drill chuck. Once the chuck was closed around the copper wires, I pulled the two cables out straight, and the twisting began when the drill started to rotate.

4) To test that the data acquisition software, namely Labview, was effective. I wrote the data acquisition codes from scratch. Without any experience in Labview, it was very important to confirm that the codes work well.

The second part focuses on the description of the experimental tests carried out in the FloWave tank. It also contains a description of the electrode wiring configurations and their respective objectives and the methods that were used during this experiment.

6.2 Small scale tests

The small scale tests were performed in front of the car park facing the Grant Institute, King's Building (The University of Edinburgh), between August 2014 and January

2015. The background noise consisted of the magnetotelluric and ionosphere field, the man-made activity (omnipresent), and the power station supply.

Materials and methods

Silver-silver chloride electrodes

For the purpose of the FloWave tank tests, 28 non-polarizing marine Ag-AgCl electrodes were bought from Castle Electrodes. Each electrode was housed in a white cylindrical nylon barrel (80 mm long $\times$ 24 mm diameter) which has 2 small holes at the bottom to allow electrical contact between the electrode and the electrolytic solution. A removable cap at the bottom of the barrel minimises the electrolytic solution fouling whilst still allowing the electrode to function. This design is referred here as the "dry electrode".

To give meaningful readings, a pair of electrode is immersed in a solution that contains soluble silver ions and chloride ions at various concentration. While this type of electrode gives a correct potential difference when the surrounding solution is constant, a change in hydrodynamic, chemistry, temperature, and salinity of the solution, will change the potential of the electrodes (Corwin, 1973). However, during a towing process through currents, a dry electrode pair may be subjected to change of temperature due to upwelling, downwelling, and internal waves for example. Additionally, I observed that when water flows in direct contact with the electrode surfaces, the reading was not stable. According to Wang et al. (2014) and Corwin (1973), the flow of water passing at the surface of an Ag-AgCl electrode may produce flow noise levels of several millivolts due to disequilibrium in the electrochemical processes acting at the Ag-AgCl electrode. Another disadvantage of this design is that the Ag-AgCl electrodes are not suitable for rapid deployment. In fact, I noted that when the electrodes were placed in contact with water for the first time, it took about 20 minutes for the reading of the field potential to be stable. As a consequence, the dry electrodes are not suitable for commercial the towed CSEM streamer.

To minimise the hydrodynamic effect of water, most of the manufacturers including Castle electrodes housed the Ag-AgCl electrode inside a protective membrane. To chemically and thermally isolate the electrodes from the sea and to make sure that chloride ions are present at a sufficiently high concentration, electrodes used in commercial marine EM applications are generally immersed in a solution of constant AgCl ions with a known concentration. This solution leaks through a porous membrane to make electrical contact with the surrounding ionic conductor. Moreover, as the electrode has sufficient time to established an equilibrium with the electrolyte before being used,

the problem of the initial unstable potential is not present here. Wang et al. (2014) and Constable (2013) described with details the fabrication process of recent marine Ag-AgCl electrode used in CSEM applications. This design is referred here as the "wet electrode".

For the small scale tests, the acquisition comprised five electrode pairs:

- 2 pairs of marine Ag-AgCl electrodes that had never used. To be tested.
- 1 pair of marine Ag-AgCl electrodes that have been commercially used in the past (they are renamed "$AgAgCl_{com}$" throughout).
- 2 pairs of land copper (Cu) electrodes.

The performance of the Ag-AgCl electrodes was evaluated relative to the performance of the Cu, and the $AgAgCl_{com}$ electrodes. At the end of each experiment, the electrodes were rinsed thoroughly with distilled water and stored in a dry area.

Amplifier, computer, and tanks

The amplifier specifications used during the tests are specified in Table 6.1. It is a 48-channel low noise amplifier system (NI USB-6289, from National Instrument) with an 18-bit analogue-to-digital (ADC) resolution. The amplifier has an onboard lowpass filter that rejects high-frequency noise above 750 kHz and prevents aliasing. The same amplifier was used both during the small scale and the FloWave tank experiment.

Connector	ADC resolution	Max rate	Small signal band-width*	Number of channels	Max input range
Screw/68 pin SCSI	18 bits	625 KS/s	750 kHz filter off	48	±10V

Table 6.1: Amplifier: NI USB-6289 specifications.*Small signal bandwidth is the cut off frequency of the onboard lowpass filter.

A laptop computer was used to displayed the measurements, and 8 plastic tanks of 25 litre each were used as water container.

Software

I programmed the code for data recording and analysis under Labview 2009 (short for Laboratory Virtual Instrument Engineering Workbench, National Instrument).

Experimental procedures

The experimental procedures were set up as shown in Figure 6.2. The electric field noise measurements were made using electrodes (marine and land) placed in pairs, with 54 m spacing, and an electrical contact with fresh or salt water. In Figure 6.2, two pairs of Ag-AgCl and four plastic tanks are shown. A receiver was formed by a pair of electrodes submerged in water in two tanks separated by 54 m. The electrodes were connected to an amplifier using insulated telluric cables stripped at the ends. The amplifier was then connected to a computer through a USB cable. The entire circuit was powered by a 12 V battery connected to a power inverter. When analysing the towed and OBC CSEM data in Chapter 4, I observed that above 10 Hz, the noise was dominated by MT noise. In addition, the fundamental frequency of mains power in the United Kingdom (UK) is 50 Hz. Therefore, the background noise in these experiments was measured at a sampling rate of 50 Hz, with the highest frequency at 25 Hz, well below mains fundamental frequency.

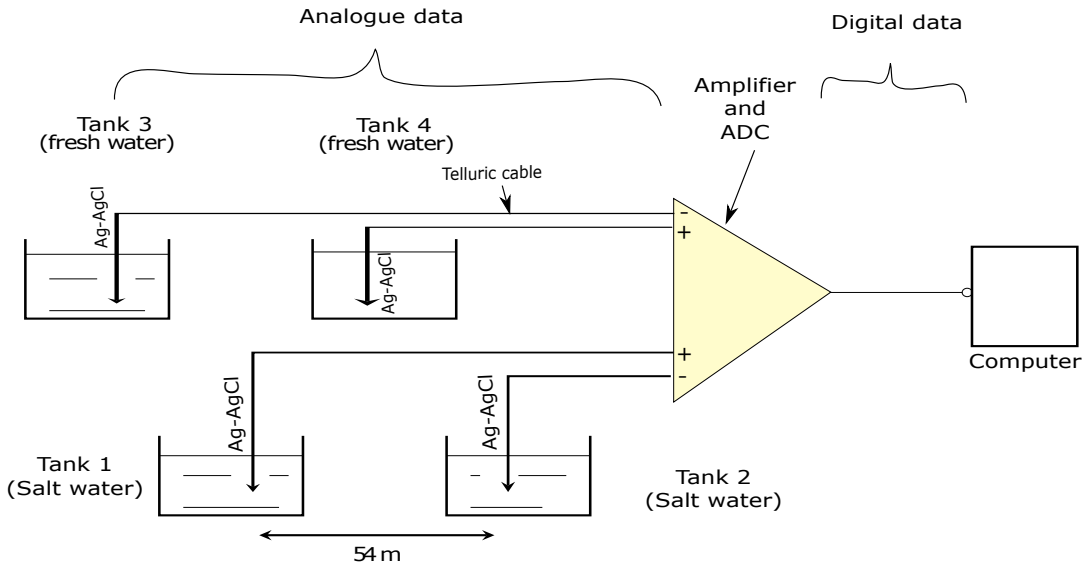

Figure 6.2: Noise measurement layout during the experiment. The analogue noise was sensed at each electrode, then was transferred to the amplifier through the telluric cable where it was digitized by an ADC before being stored/displayed on the computer.

Following Figure 6.2, the noise recording process could be summarised in three steps: (1) the analogue noise was sensed at the each channel, and (2) transferred to the amplifier through the telluric cable where it was digitized by an ADC. (3) The digital signal from the amplifier was passed finally to the computer where it was stored, and displayed.

The experiments generally were carried out during non-windy day. This means that the

electrode cables suspended in the air or laying on the ground were straight and did not move during measurements. This situation is similar to when the commercial streamer is straight and towed in a steady water with no cross currents is static. Keeping the electrode cables straight is probably not too bad since acquisition will usually cease under turbulent conditions that could cause a whiplash motion of the cable.

The experiments were divided into four parts. Each experiment consisted of a maximum of 1-hour recording and was repeated many times; during the same day or the next day.

1- **Experiment 1**. The aim of this experiment was to check that the Ag-AgCl electrodes work well. The layout is shown in Figure 6.3. All the electrodes were submerged in salt water. The materials used were two pairs of Ag-AgCl electrodes, one pair of $\mathrm{AgAgCl_{com}}$ electrodes, two pairs of Cu electrodes, and two plastic tanks separated by 54 m, filled with salt water (3.25 $\mathrm{S\,m^{-1}}$). Electrodes of each pair were installed in the corresponding tank so that the electric potential across a 54 m dipole was measured.

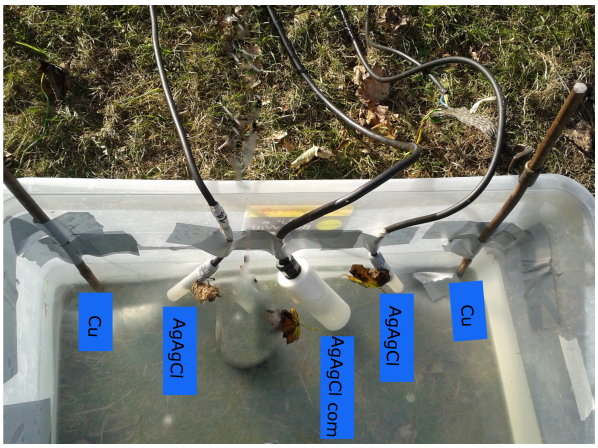

Figure 6.3: Experiment 1 - Marine Ag-AgCl and land Cu electrodes submerged into salt water

2- **Experiment 2**. The aim of this experiment was to test the effects of water salinity on the recorded background noise. The layout is shown in Figure 6.4. Four pairs of Ag-AgCl electrodes and four plastic tanks were used in this case. The electrodes were arranged in two parallel lines, with 54 m between each pair and 0.3 m separated the lines. Then, two electrode pairs were submerged in plastic tanks containing salt water, and two other pairs in fresh water (10 $\mathrm{mS\,m^{-1}}$). Noise measurements were made simultaneously.

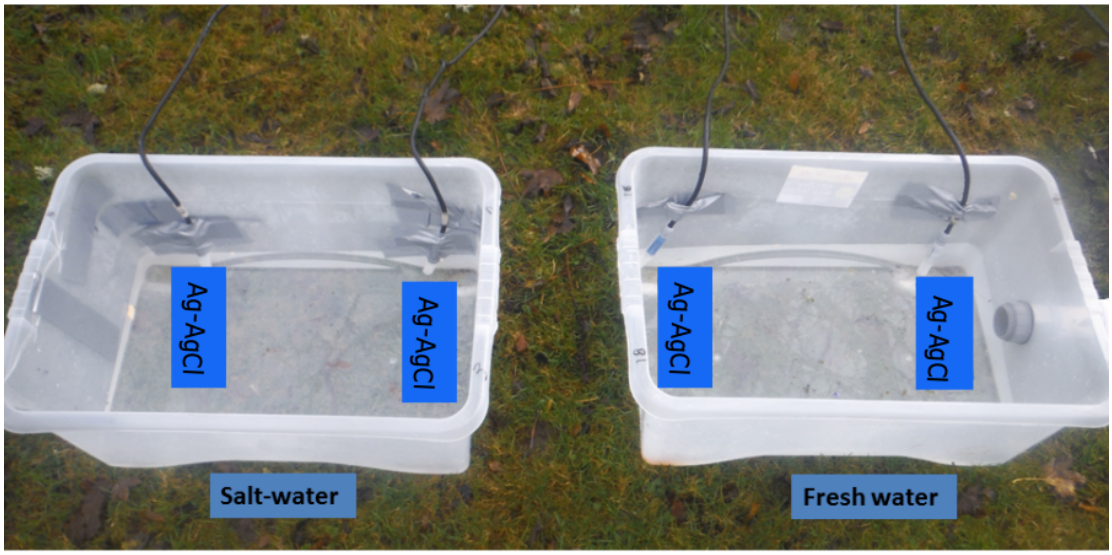

Figure 6.4: Experiment 2 - Simultaneous noise measurement: Ag-AgCl electrodes submerged into salt water (left) and into fresh water (right).

3- **Experiment 3**. The aim of this experiment was to investigate the effect on the recorded background noise of water motion around the Ag-AgCl electrodes. Similar layout as in Experiment 2 was implemented. In Chapter 5, it has been shown that the motion of an electrical conductor in the earth's magnetic result in induced electric fields noise. Moreover, I observed that the electrodes were very sensible to flow motion, even a small motion of the cable generated additional electric fields noise. To minimise this noise, each electrode and cable in the tank were taped to keep them static while water moved around the electrodes as shown in Figure 6.5. As a result, the observed electric field measurements were solely due to water motion rather than the movement of the electrodes or cable. Random water turbulence was generated with a submersible water pump around the electrodes in one tank as shown in Figure 6.5. The water was still in the other three tanks, among them, two tanks were used as reference against which to compare the noise generated by the water pump.

4- **Experiment 4**. The aim of this configuration was to investigate the effectiveness of twisted pair cables to reduce the background noise compared with non-twisted pair cables. The layout was similar to the one shown in Figure 6.2, but two plastic tanks were added on each side of the layout. Figure 6.6 shows one side of the layout. Two twisted pairs of Ag-AgCl electrodes and two pairs of non-twisted Ag-AgCl electrodes were placed in different plastic tanks. For example, following Figure 6.2, the common part of the telluric cable from the electrode submerged

Figure 6.5: Experiment 3 - Random water turbulence around the electrodes. The electrodes were taped in a corner of the tank.The water pump is shown perturbing the water contained in a tank.

in “Tank 3” and in “Tank 4” was twisted to make a twisted pair cable.

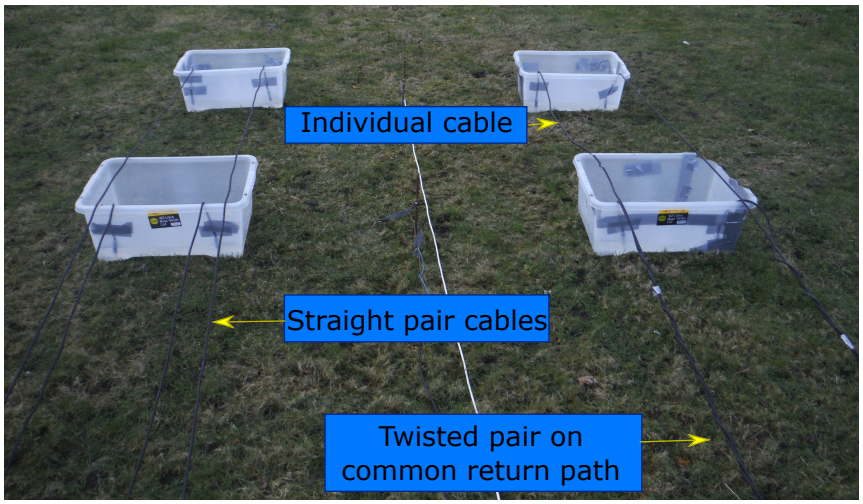

Figure 6.6: Experiment 4 - Non-twisted cables pair (left), and twisted pair cables (right).

Results and analysis

The following analysis was carried out on electric field noise recorded from different experiments enumerated in the “Experimental procedures” subsection. In processing,

I divided the data into windows of 120 s each, and each window was multiplied by a Hanning taper of the same length. This window size was the same as the one used for the processing of the towed CSEM data. The mean was removed in each of these windows. I used the result to calculate the discrete Fourier transform (DFT) and the power spectral density (PSD) as shown in equations (0.3) and (0.5) in each window. To obtain the final frequency spectra, I averaged the frequency spectra from each window.

Figures 6.7(a) and (b) respectively show the time domain and the corresponding PSD obtained when the marine and land electrodes were submerged in salt water (see Experiment 1, Figure 6.3). From Figure 6.7(a), one can observe that the new Ag-AgCl, $\mathrm{AgAgCl_{com}}$, and the land Cu electrodes, are all fluctuating around -0.004–$0.006\,\mathrm{V\,m^{-1}}$. The amplitude spectrum displayed in Figure 6.7(b) shows that all the channels follow the same path and have approximately the same amplitude within the frequency band 0.04–10 Hz. These observations show that that the new Ag-AgCl electrodes work. In addition, the PSD is contaminated with coherent large spikes in all the channels at about 0.55 Hz, 2.5 Hz, 3.5 Hz, and 4.5 Hz. The origin of these peaks is unknown.

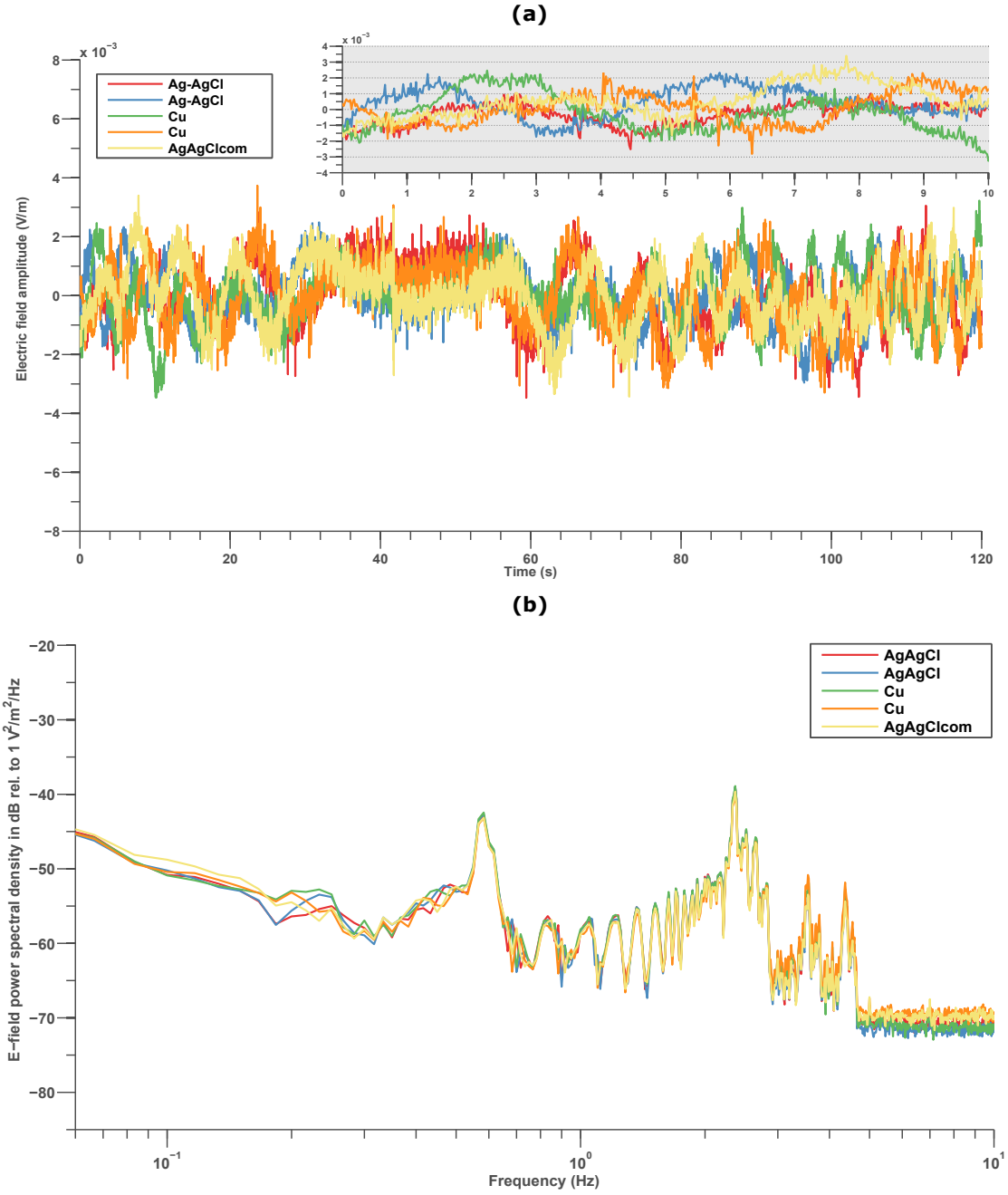

Figure 6.7: Experiment 1 - (a) Time domain with overall sample mean removed. The window in the upper right is a zoom of the first 10 seconds. (b) PSD of the background noise measured by marine and land electrodes.

Figures 6.8(a) and (b) respectively display the time domain and the corresponding PSD recorded when Ag-AgCl electrodes were placed in fresh water (green and orange) and in salt water (blue and red) (see Experiment 2, Figure 6.4).

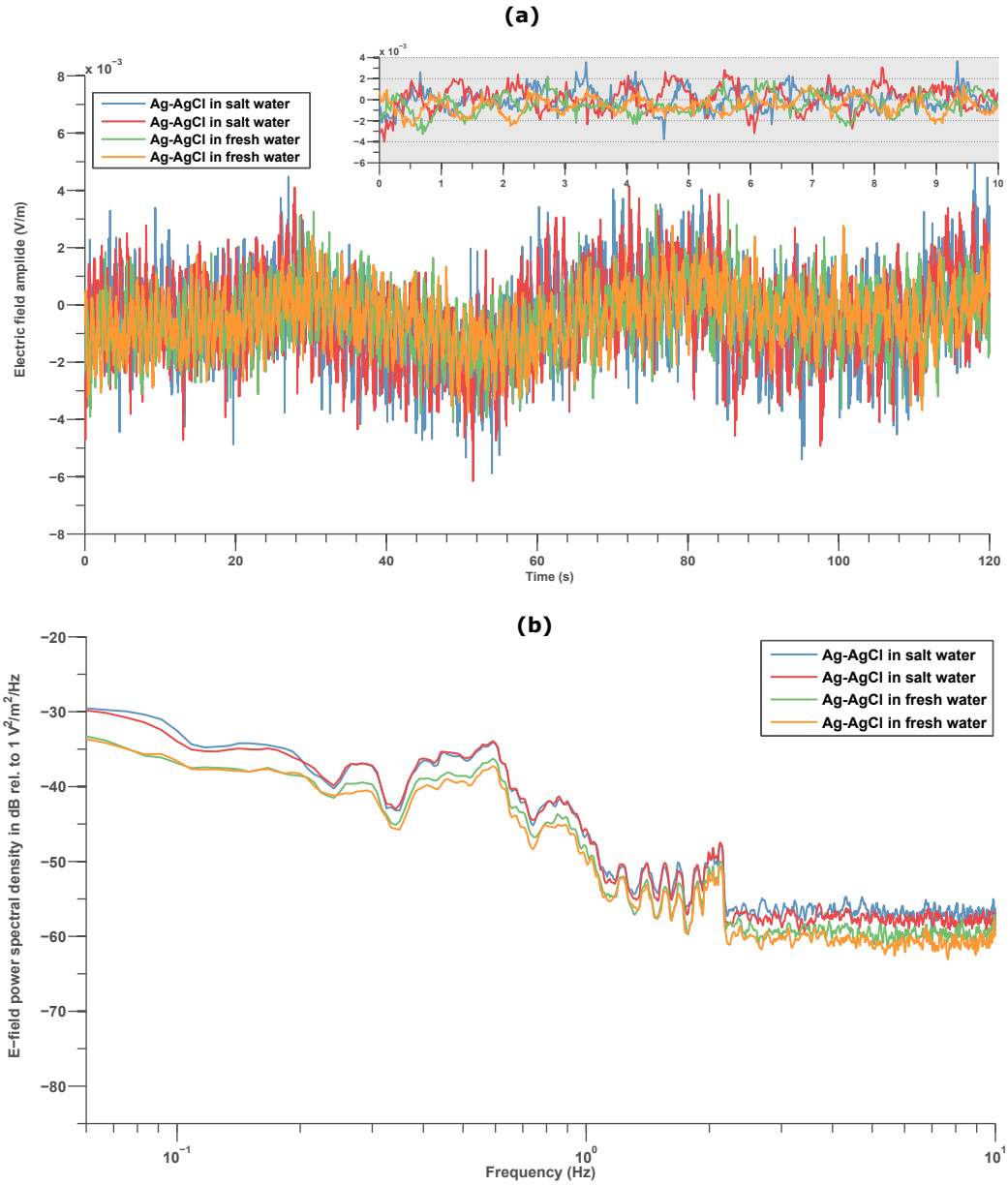

Figure 6.8: Experiment 2 - (a) Time domain with overall sample mean removed. The window in the upper right is a zoomed in of the first 10 seconds. (b) PSD of the background noise measured by Ag-AgCl electrodes submerged in fresh water and in salt water.

Figures 6.8(a) and (b) show that the Ag-AgCl electrodes work well when submerged in fresh water as well as in salt water. Figure 6.8(a) shows that the electric field noise PSD recorded by the Ag-AgCl electrodes in salt water is higher than that recorded by the electrodes in fresh water. Figure 6.8(b) shows that the spectra follow the same path regardless the salinity of the solution over all the frequencies. Within these frequencies, the spectra of the channels submerged in salt water is about 2 dB higher than the

spectra of channels in fresh water. This difference was expected because of the electrochemical reaction of salt ions on AgCl surface that generated additional noise. In addition, Figure 6.8(b) is contaminated with coherent large spikes in all the channels at about 0.55 Hz, 0.75 Hz, and 2 Hz.

Figures 6.9(a) and (b) respectively display the time domain and the corresponding PSD spectra recorded when random water turbulence water was generated around the electrodes (see Experiment 3, Figure 6.5.)

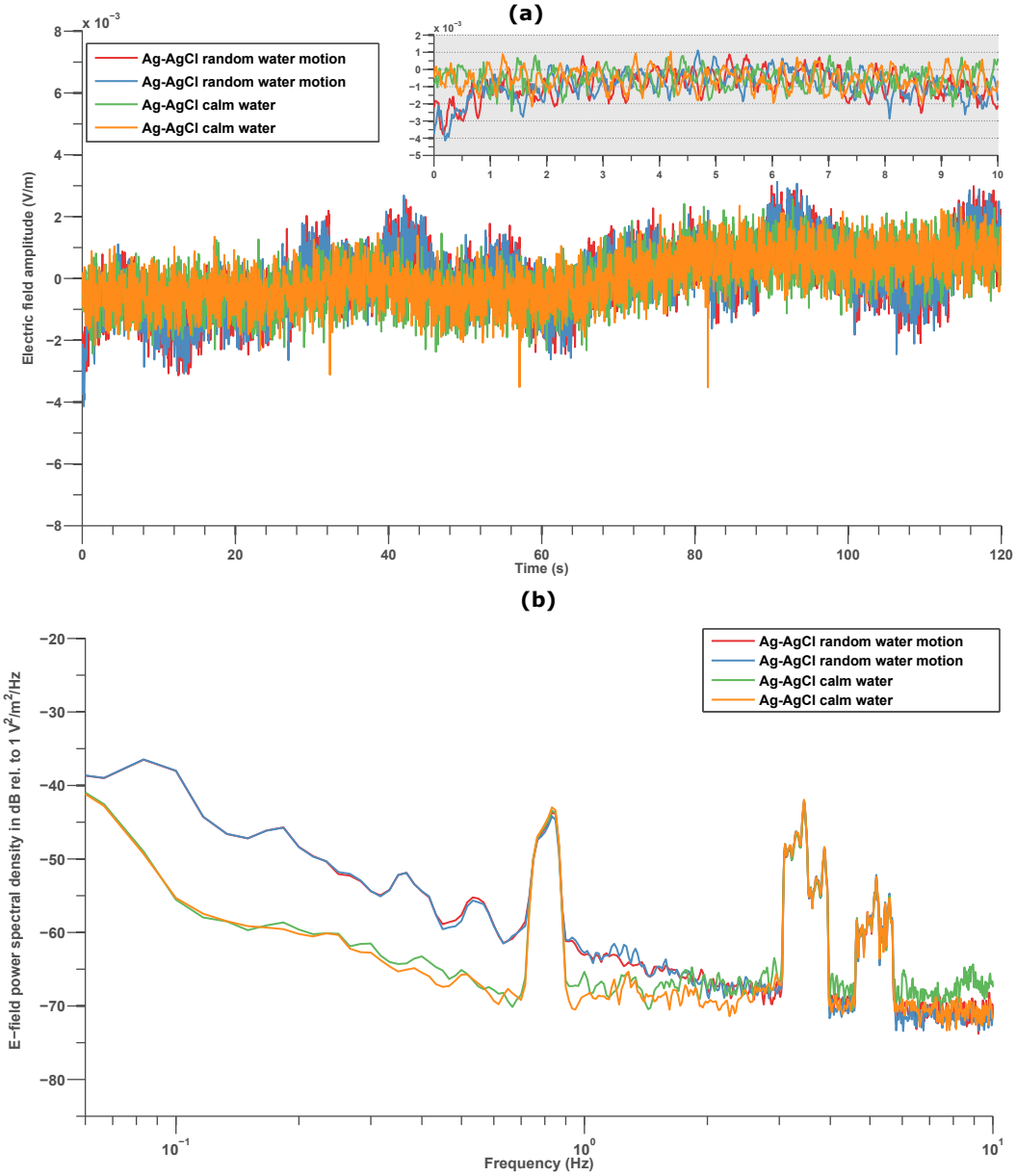

Figure 6.9: Experiment 3 - (a) Time domain with overall sample mean removed. The window in the upper right is a zoomed in of the first 10 seconds. (b) PSD of the background noise measured in a stand still water (green) and when the water is randomly moving around the electrodes (blue), respectively.

Figure 6.9(a) and (b) demonstrate that the Ag-AgCl electrodes are sensitive to the motion of the water within the frequency bandwidth 0.3–0.04 Hz. This corresponds to the frequency bandwidth of interest. Figure 6.9(b) shows that above 3 Hz the spectra are almost the same between the two water states, whereas, within the frequency band 0.04–3 Hz, the PSD spectra gradually increased when water moved randomly around an electrode. This increase is about 10 dB at 0.1 Hz. The coherent large spikes in all the

channels at frequencies of about 0.8, 3.5, and 5.5 Hz may originate from frequencies above 25 Hz (maximum frequency) and below 750 kHz (onboard lowpass filter cut off frequency) which are aliased into lower frequencies. They were probably caused by man-made activities or power line interferences.

Figures 6.10(a) and (b) respectively display the time series and amplitude spectrum recorded by two non-twisted (red and blue) and twisted pairs (green and orange) of Ag-AgCl electrode cables (see Experiment 3, Figure 6.5).

Figure 6.10(a) and (b) show that twisted pairs of Ag-AgCl cable (green and orange) helps to reduce the contribution of the background noise in the common path of both cables carrying analogue signal compared to the non-twisted pair (red and blue). From Figure 6.10(b), the background noise of the twisted pair cable is shown to be about 5 dB less in power than the amplitude of the non-twisted pair. Figure 6.10(b) is contaminated with coherent large spikes observed in all the channels. For example, the first peak is centered at 0.65 Hz, and the second at about 0.5 Hz, the third at about 0.7 Hz, and the fourth at about 1 Hz. These peaks may originate from frequencies above 25 Hz and below 750 kHz which are aliased into lower frequencies. They were probably caused by man-made activities or power line interferences.

Conclusion

The objectives of these small-scale tests were achieved successfully. I showed that the Ag-AgCl electrodes, the $AgAgCl_{com}$ electrodes, and the land Cu electrodes measured similar background noise. I showed also that the Ag-AgCl electrodes work as well in fresh water as they do in salt water. In addition, by generating random water turbulence around the electrodes, I demonstrated that the electrodes were sensitive to the motion of water. Finally, I showed that pair of electrode cables twisted on their common return path reduced the background noise compared with the non-twisted pair of electrode cables.

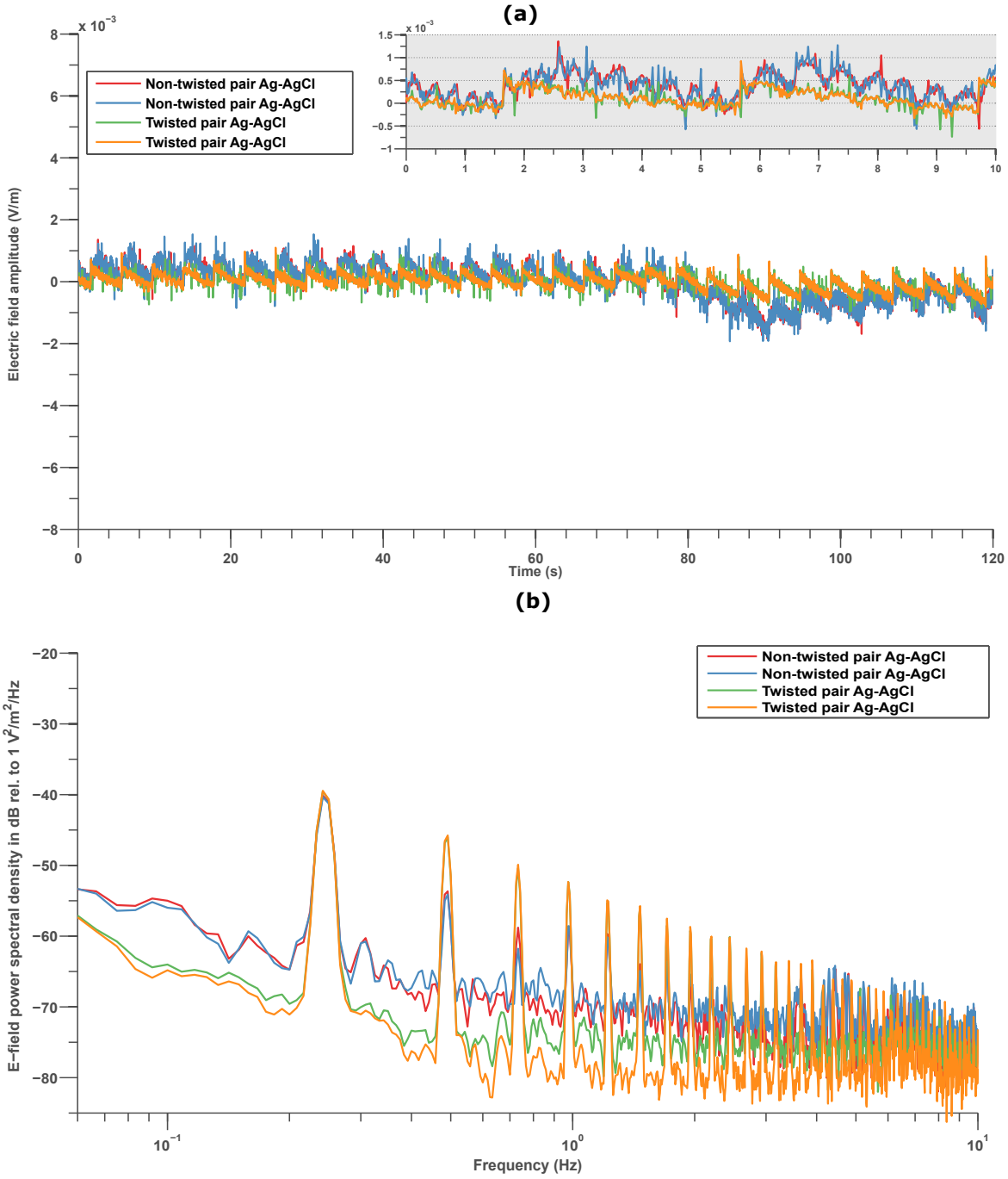

Figure 6.10: Experiment 4 - (a) Time domain with overall sample mean removed. The window in the upper right is a zoomed in of the first 10 s. (b) PSD of the background noise measured by non-twisted pair and twisted-pair of Ag-AgCl electrodes, respectively.

6.3 The FloWave tank experiment

Materials and methods

Tube

To build the prototype CSEM streamer, a 30 m long flexible PVC (84 mm in diameter) incorporating a rigid PVC Spiral as an integral part of the PVC wall was used.

Connector boards

Dr. David Wright designed two connector boards of 24 insulated panel inputs each with the purpose of allowing the wiring configuration to be changed in a few minutes. These connector boards are shown in Figure 6.11. Each input was labelled with a number corresponding to the position of an electrode along the prototype streamer. Each telluric cable from the prototype streamer was connected to an individual input in one board (namely "first connector board"), and each input from the other board (namely " second connector board") was connected to the amplifier through electronic wires. Finally, 24 flexible banana plug test leads connected to the inputs of the second board enabled the wiring configuration to be changed quickly by changing the position of the plug test leads on the first connector board.

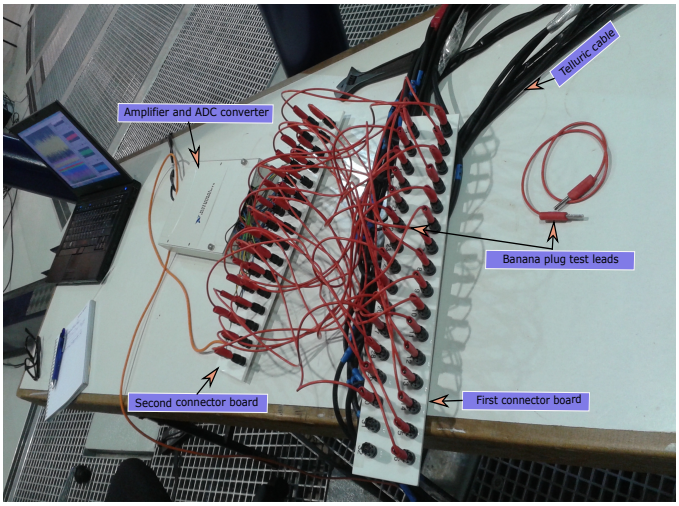

Figure 6.11: Two boards of 24 insulated panel inputs each are connected by 24 banana plug test leads. Telluric cables are shown connected to the first connector board, and the second connector board is connected to the amplifier. Banana plug test leads interconnected the two boards.

Assembly phase of the prototype streamer

Once all these experiments were completed, the electrode cables were twisted in pairs around one another. The assembly process is shown in Figure 6.12. Each twisted pair (Figure 6.12(a)) was twisted around one another. Then, they were bound all together with a tape to ease the insertion into the flexible PVC tube as illustrated in Figure 6.12(b). The flexible PVC tube containing the shielded Ag-AgCl electrode cables is shown in Figure 6.12(c).

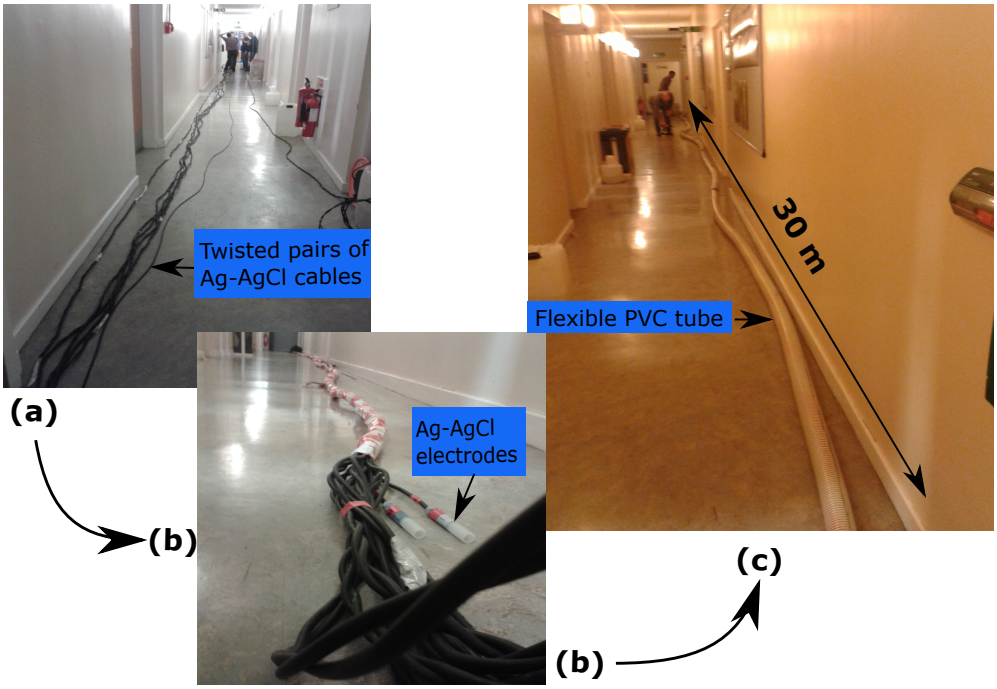

Figure 6.12: Assembly phase of the prototype streamer. (a) Twisted pairs of Ag-AgCl electrode cables on the floor. (b) Twisted pairs of Ag-AgCl electrode cables were twisted all together and shielded with a tape. (c) Flexible PVC tube that contains the shielded Ag-AgCl electrode cable displayed in (b).

The FloWave tank description

The tests were conducted in February 2015 in the world's first circular tank that allows the combination of waves and currents in any relative direction (Ingram et al., 2014). The tank is 30 m in diameter, 3 m deep, filled with fresh water and capable of generating flow rates of up to 1.5 $\mathrm{m\,s^{-1}}$. Waves of different frequencies and amplitudes can be generated from any direction by 168 wave makers. These work both to generate waves at one side and to absorb waves at the opposite side to prevent any reflection of wave energy within the tank. Flow and wave motion can be generated simultaneously. The

objective was to understand the behaviour of a CSEM streamer section under the influence of flow and wave motion, and to quantify their effects on the measured electric field.

Experimental setup

The 30 m long prototype EM streamer was instrumented over the central 16 m section with 12 electric field channels (24 Ag-AgCl electrodes). The setup is shown in Figure 6.13. In addition, three channels were fixed 1 m below the water surface. An anchor rope between the tank floor and the gantry was used to hold these electrodes in place. The telluric cable for these electrodes ran along the gantry and not through the water. So measurements made using these channels were not affected by any motionally-induced noise which might affect receivers in the streamer section. Outside the test area, the telluric cables were connected to the connector boards, and to a 24-channel digital recording system with an 18-bit ADC converter sampling at 50 Hz as shown in Figure 6.11.

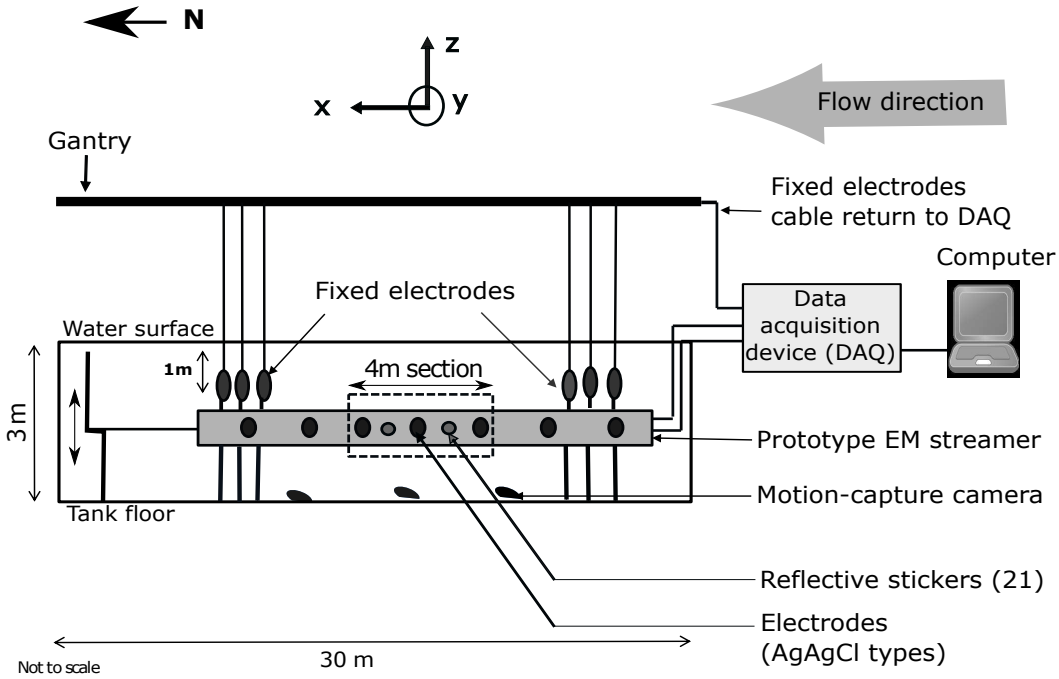

Figure 6.13: Configuration of the prototype CSEM streamer in the FloWave tank, showing the fixed electrodes and reflector sticker for the motion-capture cameras. The dashed rectangular section represents the 4 m section where the motion of streamer was recorded. The flow is parallel to the streamer.

A pre-stretched Dyneema rope inside the streamer supported much of the tension within the streamer. The streamer was further anchored at each end by a three point anchor between two points on the tank floor and the edge of the tank at ground level. This held the streamer straight at a depth of 1 m. Figure 6.14 shows the streamer being deployed in the tank.

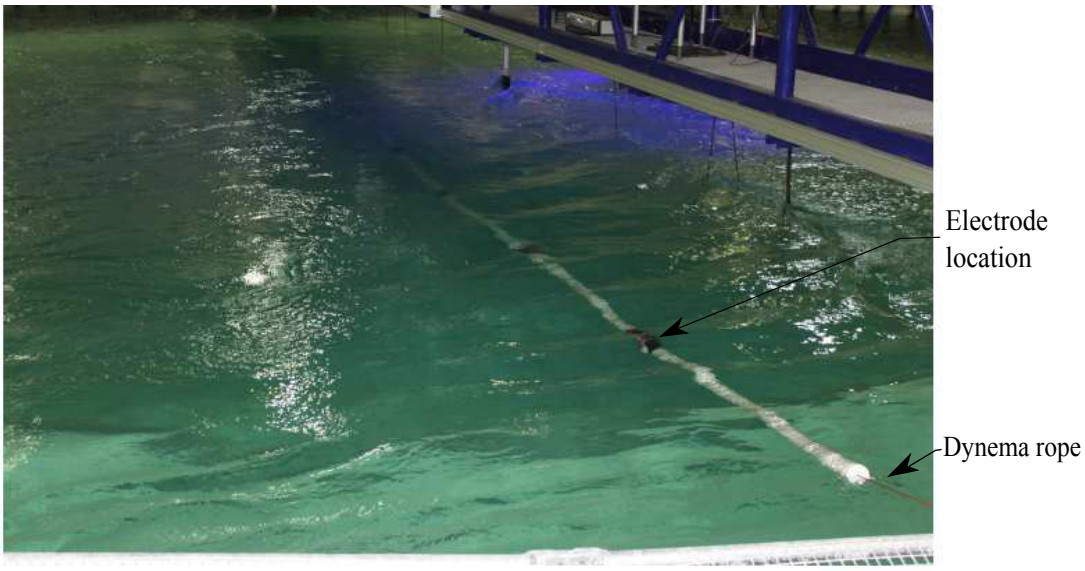

Figure 6.14: Photo of the prototype streamer (white cable) being deployed in the FloWave tank. The Dyneema rope and the location of electrodes are indicated.

Three wiring configurations were used during the test:

1) Configuration 1 layout is shown in Figure 6.15. The purpose of this configuration was to compare the noise level recorded by a single channel (Ch1) with the noise recorded by multiple non-overlapping smaller channels with the same total length as the length of the single channel. Thus, noise measurements made by Ch2 + Ch3, Ch4+Ch5+Ch6+Ch7, and CH8+Ch9+Ch10+Ch11+Ch12+Ch13+Ch14 +Ch15 were compared with noise measurements made by Ch1.

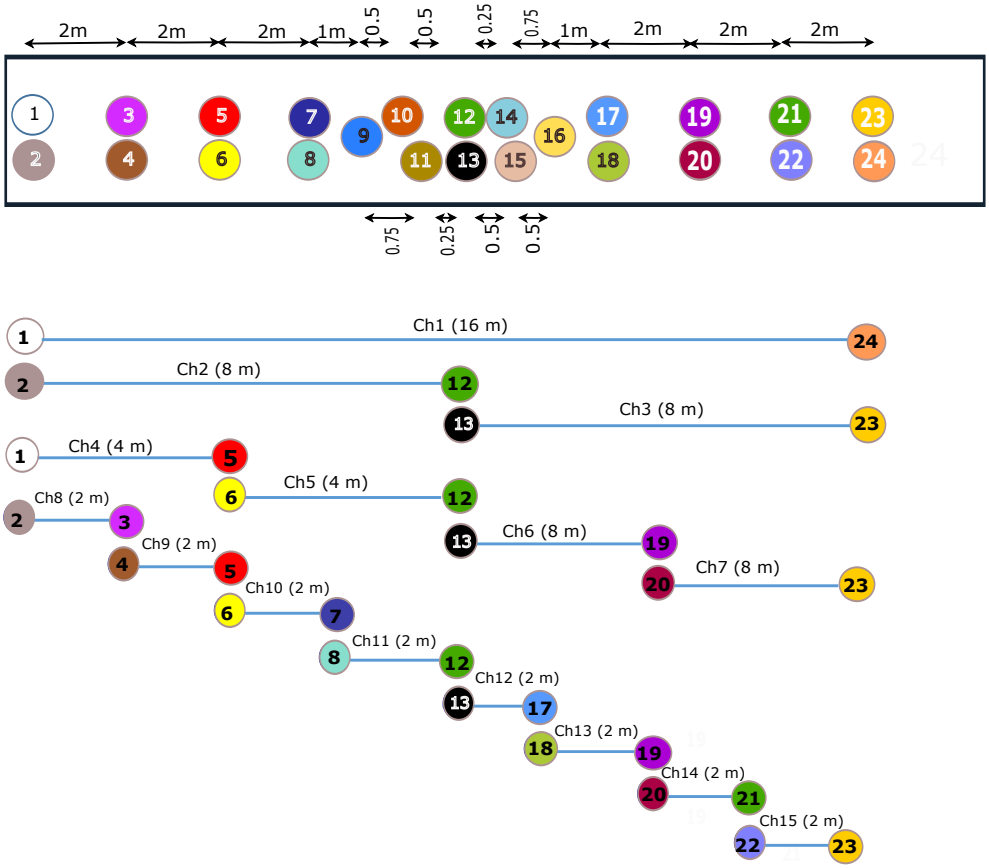

Figure 6.15: layout of the wiring configuration 1. (Top) Illustration of the prototype streamer. The circle of different colors and numbers denote the electrodes and their position along the streamer, respectively. (Bottom) The layout of the wiring configuration 1 (Not to scale).

2) Configuration 2 layout is shown in Figure 6.16. All the channels extend from the same central electrode (Ch13). There was an electrode at the centre (Ch13) which was shared by all channels. Electrode separations ranged from 0–8 m for the channels inside the streamer, and from 4–6 m for the fixed channels (Ch14-15). The objective of this configuration was to estimate the correlation length of the recorded flow and wave related noise. Doing this may help to estimate the overlap length at which the noise is uncorrelated. This configuration may help to isolate the noise related to the movement of the streamer to the one related to the increase in flow rate and wave motion.

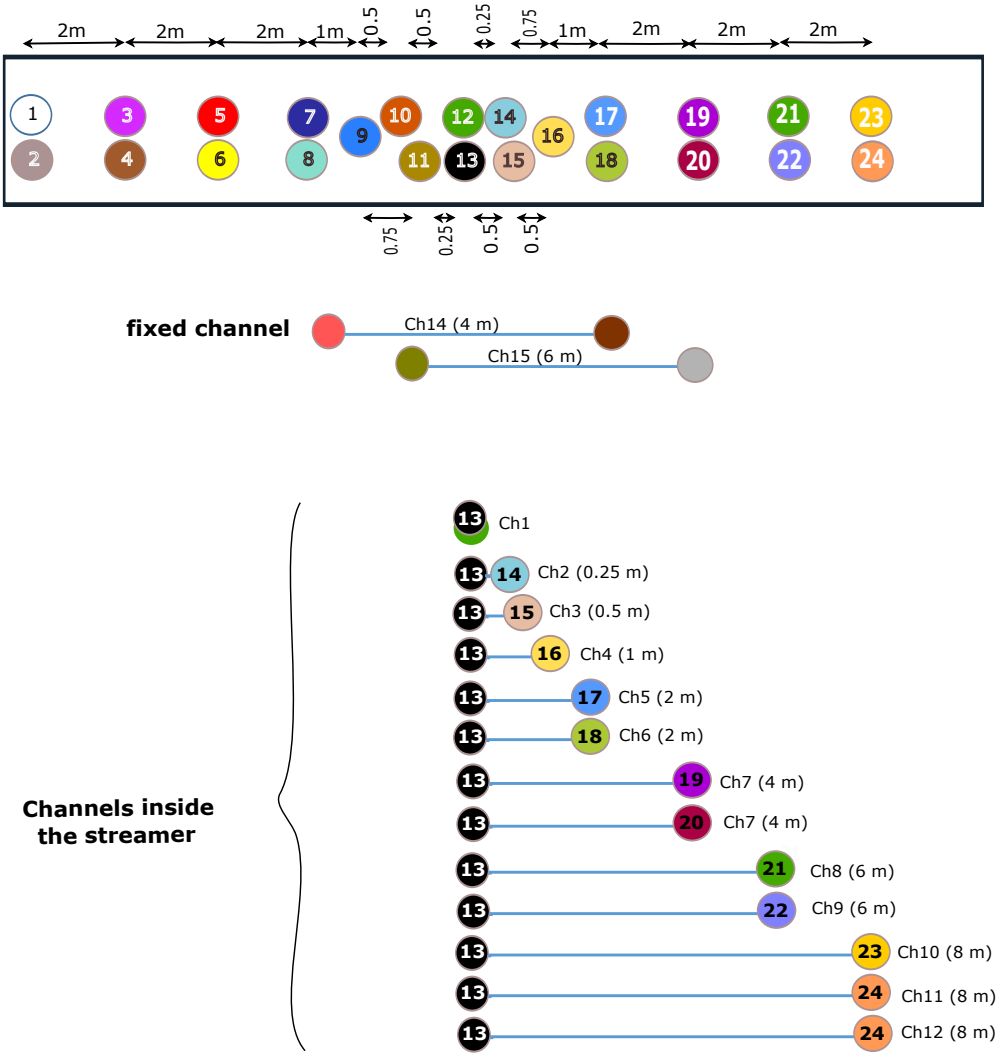

Figure 6.16: layout of the wiring configuration 2. (Top) Illustration of the prototype streamer. The round shape of different colors and numbers denote the electrodes and their position along the streamer, respectively. (Bottom) layout of the wiring configuration 3 (Not to scale).

3) Configuration 3 layout is shown in Figure 6.17. The aim of this configuration was to isolate the noise on a single channel and estimate the noise level related to the motion of streamer due to water flow rate and wave motion, respectively. There was an electrode at the centre of the streamer which was shared by all channels. Electrode separations ranged from 2–12 m, channels 13, 14, and 15 were fixed electrode pairs with 2, 4, and 6 m electrode spacing, respectively.

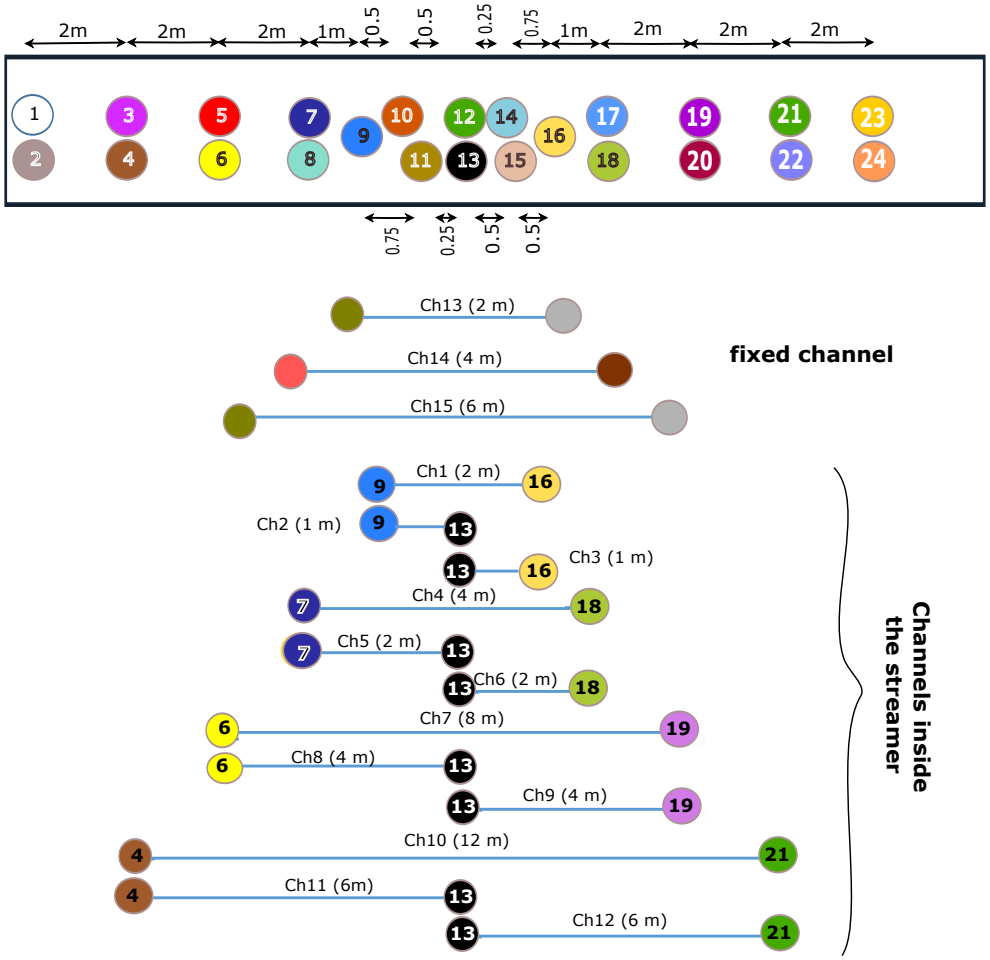

Figure 6.17: layout of the wiring configuration 3. (Top) Illustration of the prototype streamer. The round shape of different colors and numbers denote the electrodes and their position along the streamer, respectively. (Bottom) The Layout of the wiring configuration 5. Channel 13, 14 and 15 are fixed channels. (Not to scale).

Table 6.2 shows the relationship between channel number and electrode spacing for each wiring configuration.

Wiring configurations objectives - theory

The towed streamer CSEM data recorded during a survey contain signal and noise. In general, the signal is correlated whereas the noise from neighbouring channels can either be correlated or uncorrelated. One way to improve the signal-to-noise ratio (SNR) may be to increase the number of channels (Elboth et al., 2010a):

$$\text{SNR Improvement} \approx (\frac{S}{\mathcal{N}})\sqrt{\mathrm{N_c}}\,, \tag{6.1}$$

Channel	Channel length in metres		
	Config. 1	**Config. 2**	**Config. 5**
Ch 1	16	0	2
Ch 2	8	0.25	1
Ch 3	8	0.5	1
Ch 4	4	1	4
Ch 5	4	2	2
Ch 6	4	2	2
Ch 7	4	4	8
Ch 8	4	4	4
Ch 9	2	6	4
Ch 10	2	6	12
Ch 11	2	8	6
Ch 12	2	8	6
Ch 13	2	8	2
Ch 14	2	4	4
Ch 15	2	6	6

Table 6.2: Relationship between channel number and electrode spacing in metres. The cells with grey colour denote the fixed channels. Config. and Ch are the abbreviations of Configuration and Channel, respectively.

where S denotes the signal amplitude, $\mathcal{N}$ denotes the noise amplitude, and $\mathrm{N_c}$ represents the number of channels. If the noise is mostly uncorrelated, then equation (6.1) holds. However, if the noise is mainly correlated on neighbouring channels, equation (6.1) does not hold. This last case is applied in the towed CSEM streamer. In Chapter 4 I showed that the major source of noise in the towed CSEM streamer, namely motionally-induced noise, is well correlated from one channel to another at about 0.2 Hz. This noise is governed therefore by the distance between channels. Thus, there must be a correlation distance at which the motionally-induced noise becomes uncorrelated from channel to channel. For example, cross-correlating the recorded noise in Configuration 2 may help to determine the spatial extent of flow and swell noise, and one could use this to determine an overlap distance between channels where the noise becomes uncorrelated.

Motion of the EM streamer

The central 4 m section of the streamer was further instrumented with 21 reflective markers in order to monitor cable motion using Qualisys underwater infrared motion capture cameras. The locations of these markers are shown in Figure 6.18(a). The cameras record the $\mathrm{X, Y, Z}$ positions of the reflectors to a precision of $\pm$ 2 mm at a

distance of 10 m. The positions of the markers are defined by a right-handed Cartesian coordinate system, as shown in Figure 6.18(b). The X direction is aligned with the streamer while Z is in the vertical upwards direction.

Video recording

An underwater camera was placed at the same depth, and a distance far enough to capture the motion of the prototype streamer. During the filming, the flow speed was increased gradually from 0, 0.5, 1, and 1.5 $\mathrm{m\,s^{-1}}$. To visualize flow pattern surrounding the streamer, hydrodynamic tufts of 15 cm long, were attached at 1 m interval along the streamer.

Increased flow rates and wave motion

Two tests were carried out to investigate the effect on noise levels of increasing water flow rate and wave motion at different frequencies and amplitudes around the streamer.

- Test 1: The effect of flow. Water flow was generated parallel to the streamer. Data were acquired for flow rates of 0, 0.5, 1, and 1.5 $\mathrm{m\,s^{-1}}$.
- Test 2: The effect of wave motion. Data were acquired with a constant flow rate of 0.5 $\mathrm{m\,s^{-1}}$ parallel to the streamer and wave amplitudes of 0.1 m. Wave frequency of 0.29 Hz was generated (1) in parallel to the streamer, (2) at 45° to the streamer, and (2) perpendicular to the streamer.

Table 6.3 shows the tests that were carried out in each configuration.

Wiring configuration	The effect of flow	The effect of wave motion
Config.1	Yes	No
Config.2	Yes	Yes
Config 3	Yes	Yes

Table 6.3: Tests carried out on each wiring configuration.

The motion of the streamer was recorded simultaneously with the electric field in order to investigate the relationship between the electric field noise and cable motion.

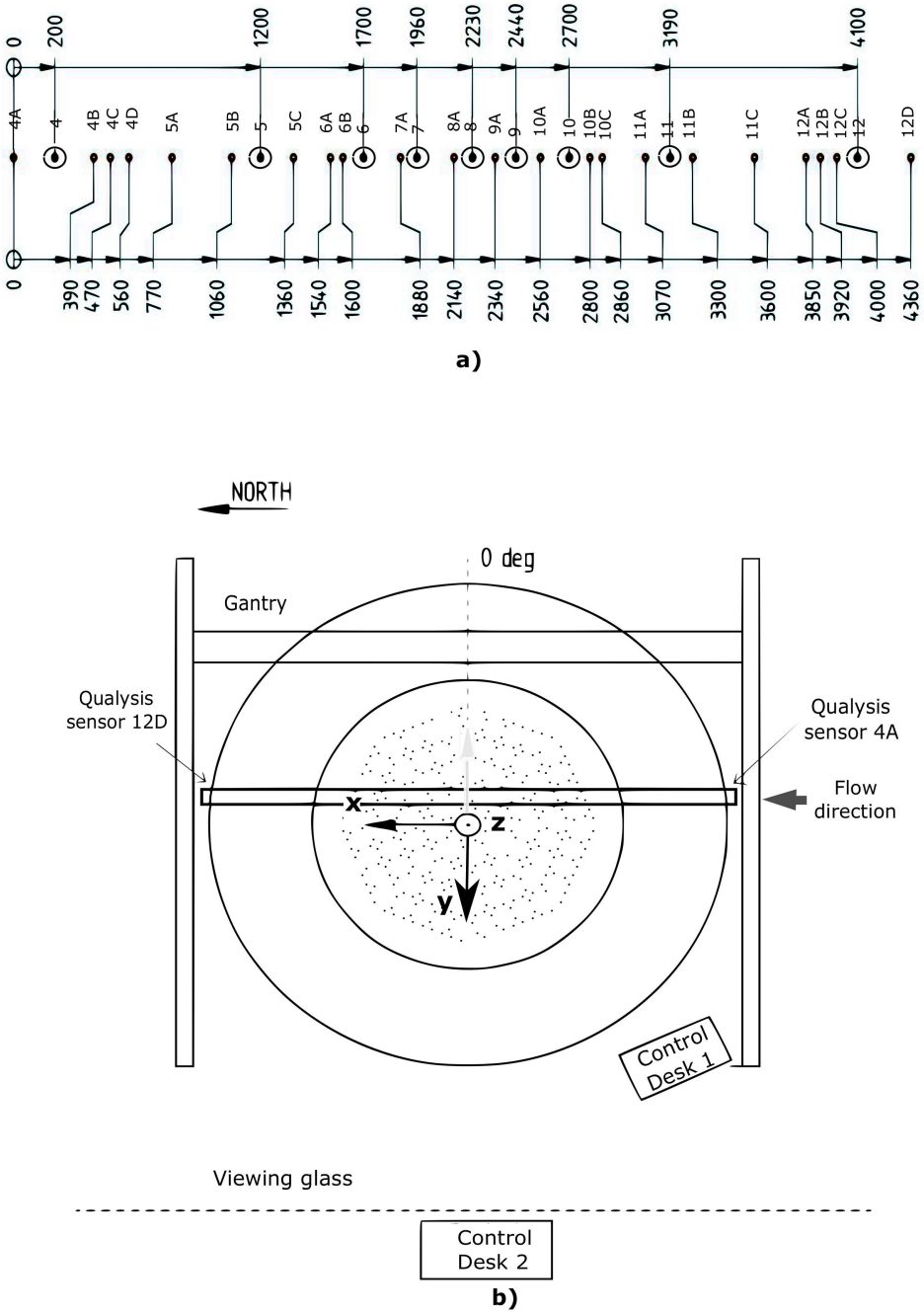

Figure 6.18: (a) Sketch of the 4 m section of the streamer. The round black spots denote the motion sensors and the circle black spots represent electrodes. (b) Layout and coordinate system for the motion detection cameras. The streamer is oriented North-South. The red arrow indicates the origin of flow.

6.4 The prototype and the conventional CSEM streamer - The differences

The FloWave tank is an excellent place to study the mechanism of noise generation in the streamer as experiments can be carried in a controlled manner. Table 6.4 shows the differences between the FloWave tank and the towed CSEM streamer. A number of artificial methods were used to give an indication of the streamer behaviour towed by a vessel. For example, the flow in the tank was gradually increased from 0 $\mathrm{m\,s^{-1}}$ until 1.5 $\mathrm{m\,s^{-1}}$ to simulate and quantify the effect of flow noise in noise measurements.

A 30 m prototype streamer is certainly different from an 8000 m conventional towed CSEM streamer in many ways. For example, the tension is much less in the FloWave tank compared to the towed CSEM streamer. In fact, the prototype streamer was manually anchored at both ends at the edge of the tank by a Dyneema rope compared with the presence of both a deflector at the head and a tail buoy at the end of the streamer. These devices create and maintain tension forces on the streamer which constraint the motion of the streamer.

Towing depth is another important parameter for the performance of the towed CSEM streamer. A commercial streamer is towed generally at a depth of 100 m which corresponds to its operational depth. During experiments in the FloWave tank, the prototype streamer was kept at a depth of 1 m. This depth discrepancy is not of any importance as the most depending depth parameters is the sea state [1].

Parameter	FloWave tank	Towed CSEM streamer
Water depth	3 m	500 m or less
Towing depth	1 m	100 m
Streamer length	30 m	up to 8000 m
Channel lengths	1–16 m	200–1100 m
Towing speed	0, 0.5, 1, and 1.5 $\mathrm{m\,s^{-1}}$	2.1–2.6 $\mathrm{m\,s^{-1}}$
Sources of noise	Provocation: flow and ocean swell noise	Natural: flow and ocean swell
Streamer configuration	Head and tail of the streamer anchored in the tank by Dyneema rope	Streamer anchors at the head by a lead-in cable and at the tail by a tail buoy

Table 6.4: Differences between the FloWave tank experiment and the towed CSEM streamer

[1] In oceanography, a sea state is the general condition of the ocean surface with respect to wind waves and swell. The sea state can be in the range of 0 to 9, where 0 is perfectly calm, and 9 is wave heights above 14 m (Elboth et al., 2010a).

Summary

This chapter described two experiments. The first one consisted of testing the marine Ag-AgCl electrodes and the data acquisition devices that were then used to build a prototype towed CSEM streamer. Comparing two pairs of marine Ag-AgCl electrodes to a pair of land Cu electrodes and a commercial marine Ag-AgCl demonstrated that the new Ag-AgCl electrodes sensed similar background noise as the two others. The success of this experiment led to the second, which involved a series of tests carried out on the prototype towed CSEM streamer suspended in the Edinburgh FloWave tank.

■

7

FloWave Tank Data Analysis

Observations should only be used to falsify possible solutions, not to deduce any particular solution.

Albert Tarantola (1949–2009)
Physicist

From the data collected in the FloWave tank (chapter 6), I identify and quantify two separate sources of noise: the motionally-induced noise due to water flow rates and to wave motion. I show that the motion of a prototype streamer in the FloWave tank in response to an increase of flow rate increases the flow noise level. However, almost all flow noise is generated as the flow increases from 0 to 0.5 $\mathrm{m\,s^{-1}}$. This initial large difference in flow noise is due to flow over the electrode surfaces which disrupts ions at the surface of the electrode. I also show that the wave motion noise is 12 dB above the flow noise. In addition, I calculate the wave motion electric field noise level and compare it with the measured electric field noise. I observe that the calculated wave motion noise is correlated with the measured electric field noise. However, the measured electric field noise is generally is a factor of about 3 greater than the calculated wave motion electric field noise. This discrepancy is likely caused by additional noise in the telluric cable between the electrodes and the amplifier. Finally, I estimate the overlap channels length for the motionally-induced noise to be uncorrelated. I find out that the "optimal" overlap length is about 1 m.

Parts of this chapter were published in Djanni et al. (2016) with the title *Electromagnetic induction in a towed electromagnetic streamer*, copyright 2016 SEG. I adjusted the original text, layout, and symbols to fit the style of the thesis.

During the FloWave tank experiment described in chapter 6, I investigated the effect on the noise level caused by a gradual increase in flow rate: from $0\,\mathrm{m\,s^{-1}}$, $0.5\,\mathrm{m\,s^{-1}}$, $1\,\mathrm{m\,s^{-1}}$ and $1.5\,\mathrm{m\,s^{-1}}$. This was done in the three wiring configurations. However, the effect of wave motion on noise level was carried out only for wiring configuration 3. This chapter shows the results obtained after processing of the data collected using these wiring configurations. The first part of this chapter describes the quality control (QC) and the processing steps carried out while analysing the prototype streamer motion and the measured electric field noise. The second and third parts focus on the effects of flow and wave motion on the motion of the streamer and on the electric field noise. The fourth part isolates and estimates the motionally-induced electric field noise due to wave motion (this will be referred to as wave motion noise) and compared it to the measured electric field noise. The fifth part investigates the distance at which the wave motion noise becomes uncorrelated with the neighbouring channels. The last part investigates the idea that the signal-to-noise ratio of the towed streamer controlled source electromagnetic (CSEM) could be improved by using multiple channels instead of a single channel.

7.1 Motion and electric field data: QC and processing steps

Flow pattern

During the FloWave tank experiment, an underwater camera was used to visualise the flow pattern around the streamer. No wave motion was generated during the recording. A recorded video showing the flow pattern and the motion of hydrodynamic tuffs is attached to the compact disc. When watching the video recorded with the underwater camera, the hydrodynamic tuffs were generally parallel to flow. This means that the flow pattern was laminar around the streamer for different flow rates.

QC of the streamer displacement data

To analyse the motion capture data, I inspected the data and identified missing values using a Matlab motion capture toolbox namely *MoCap Toolbox* (Burger and Toiviainen, 2013). Figure 7.1 displays a map of the state of the markers as the flow was increasing from $0.5\ \mathrm{m\,s^{-1}}$ to $1\ \mathrm{m\,s^{-1}}$. The vertical axis denotes the marker label and the horizontal axis displays the number of samples recorded by each marker. The thick black lines show the number of missing values in each marker, whereas, the white space shows that the

markers function well without any missing values. Figure 7.1 shows that marker 8A, 11A, 11B, 12A, 12B, and 12 C malfunctioned during this run. They were therefore excluded in the future analysis.

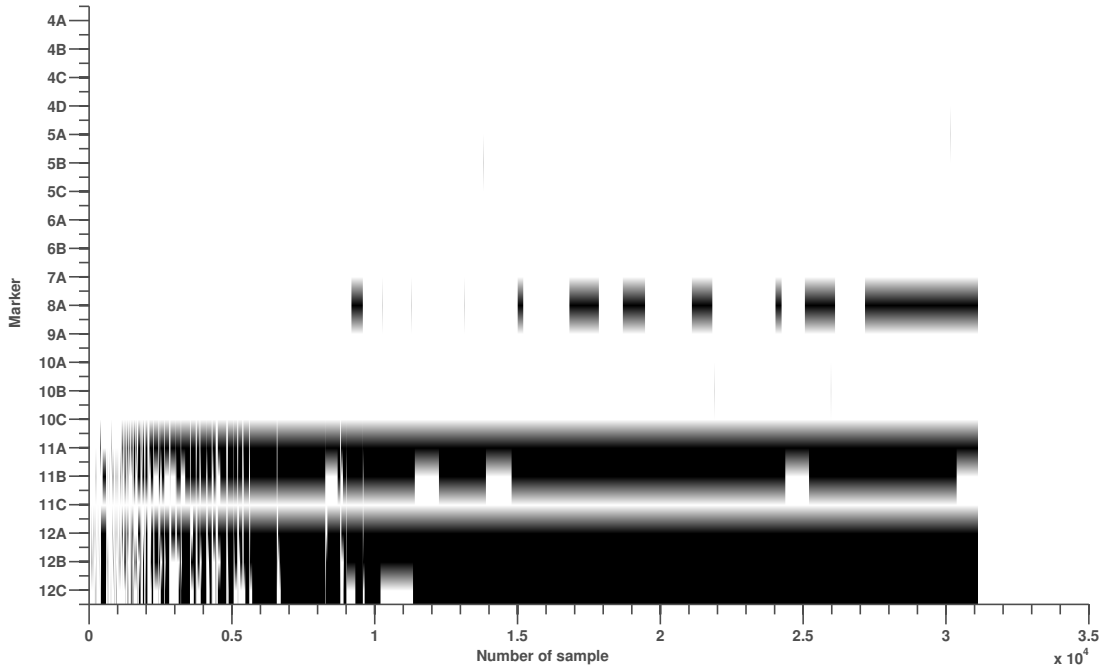

Figure 7.1: A markers map showing the missing values. Markers 8A, 11A, 11B, 12A, 12B, and 12 C malfunctioned during this run. I used the *MoCap Toolbox* to display this figure.

3D motion of the streamer

It is difficult to visualise streamer motion from the displacement of a single component. A more intuitive way to display the displacement is to plot the displacement of two components as a function of time. Figure 7.2(a) and (b) show the displacement of a single marker in the Y-Z and X-Z planes for a wave propagating along the X-direction (parallel to the streamer). Figure 7.2(c) and (d) show the displacement of the same marker in the Y-Z and X-Z planes for a wave propagating at 45° to the streamer direction. Figure 7.2(e) and (f) show the displacement of the same marker in the Y-Z and X-Z planes for a wave propagating in the Y-direction.

Regardless of the wave direction, it can be seen from Figure 7.2(b), (d), and (f) that the displacement in the X-direction is almost zero. This is because the streamer is anchored at both ends in the X-direction. Moreover, when the wave propagates in the X-direction, the Y- and Z-displacements are similar in amplitude and oscillate at the wave frequency. When the wave moves at 45° to the streamer direction, the Y-displacement increases

by about a factor of 5 while the Z-displacement stays constant. As the wave propagates perpendicular to the streamer direction, the Y-displacement increases by a factor of 10 while the Z-displacement increases by a factor 2 compared to its previous position.

Figure 7.2 demonstrates that the streamer displays a rotary motion. Figure 7.2(a) and (b) show that the streamer depicts a vertical rotary motion in both the Y-Z and X-Z plans when the wave moves parallel to streamer direction, while the streamer displays a lateral rotary motion in the Y-Z plane (Figure 7.2(c) and (d)), and a vertical rotary motion in the X-Z plan (Figure 7.2(d) and (f)) as the wave moves at 45° and 90°to the streamer direction, respectively. Figure 7.2 also shows that the biggest displacement is observed in the Y-direction when the wave is propagating perpendicular to the streamer. In offshore conditions, this signifies that the towed CSEM streamer experiences it biggest motion when the cable moves laterally or vertically.

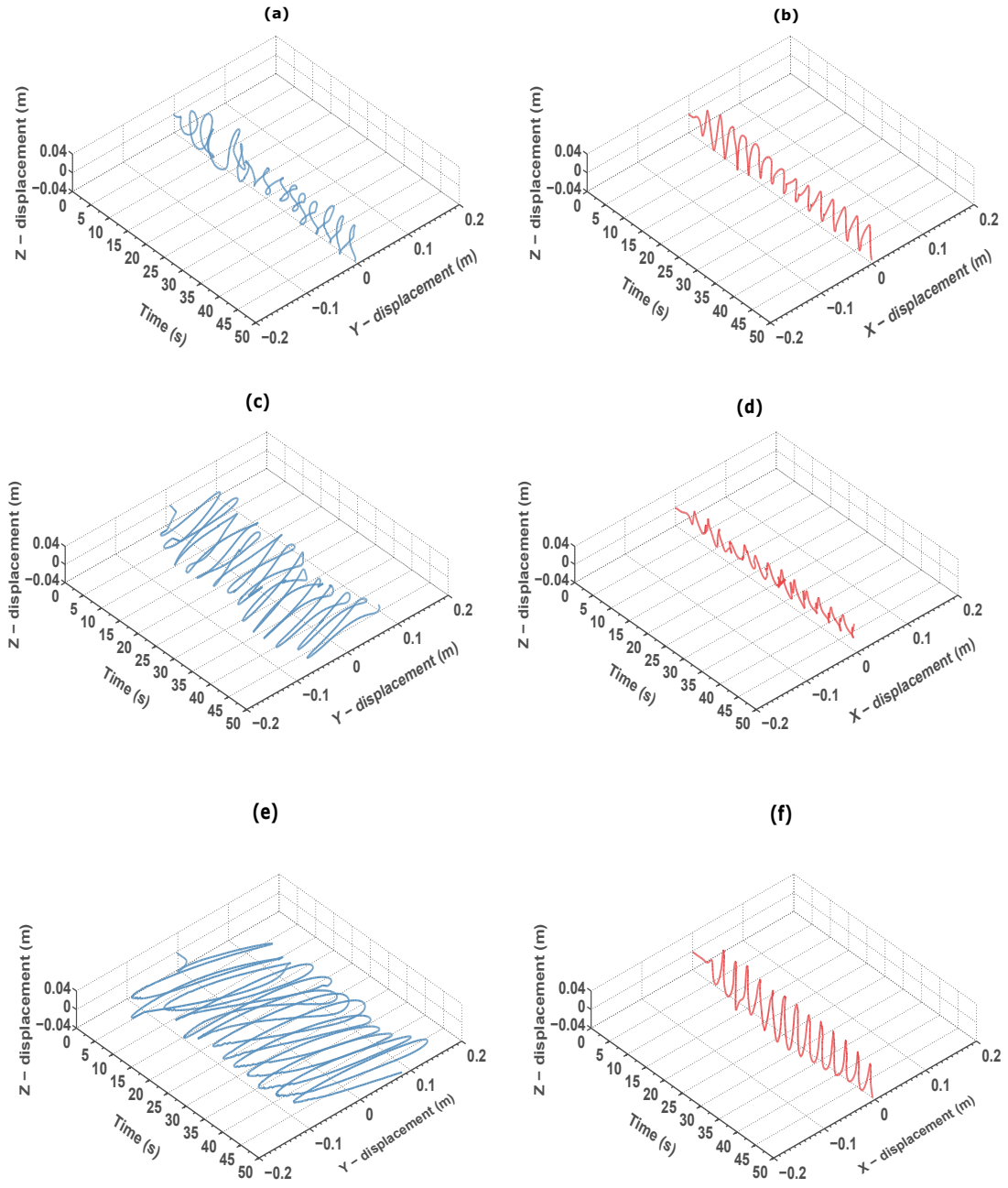

Figure 7.2: Trajectory of marker 5C. (a) Y-Z displacement when the wave was moving parallel to the streamer direction. (b) X-Z displacement when wave was moving parallel to the streamer direction. (c) Y-Z displacement when the wave was moving at 45° to the streamer direction. (d) X-Z displacement when the wave was moving was at 45° to the streamer direction. (e) Y-Z displacement when the wave was moving perpendicular to the streamer direction. (f) X-Z displacement when the wave was moving perpendicular to the streamer direction.

Motion and electric field processing steps

In the time domain, the mean of the data was first subtracted so that the data fluctuate around zero. In the frequency domain, the 70 s data were divided into 7 equal 10 s windows. I applied a Hanning taper to each window and used the result to calculate the discrete Fourier transform (DFT), power spectral density (PSD), and amplitude spectra density (ASD) as shown in equations (0.4), (0.7) and (0.8), respectively. To obtain the final frequency spectra, I averaged the obtained frequency spectra from each window.

The distribution of noise along a streamer was obtained by averaging the root mean square (RMS) values from several statistically independent records (Elboth et al., 2009). To compute the mean RMS, the following steps were implemented:

1. A low-pass filter was applied to the data to remove signals above 10 Hz. This limit is chosen because in Chapter 4, I observed that above 10 Hz, the noise was dominated by magnetotelluric (MT) noise.
2. The noise data were divided into a number of equal length windows. In our case, the 70 s noise records were divided into 7 equal 10 s windows. Doing this reduce the noise to a level that allows flow rates and waves motion features to be observed.
3. The mean was removed in each window.
4. RMS was calculated in each window.
5. Standard deviation and standard error were computed to give a measure of the RMS variability.

7.2 The effect of flow - Wiring Configuration 3

The displacement and electric field data were acquired simultaneously for flow rates of 0 $\mathrm{m\,s^{-1}}$, 0.5 $\mathrm{m\,s^{-1}}$, 1 $\mathrm{m\,s^{-1}}$, and 1.5 $\mathrm{m\,s^{-1}}$ in absence of wave motion. The time domain of the displacement data for different flow rates is plotted between -0.2 m and 0.2 m in the vertical axis to be consistent with the wave motion displacement data. The amplitude spectra density (ASD) for different flow rates is plotted between -110 dB and 0 dB for the same reason.

Displacement of the streamer

The displacement of the centre of the prototype streamer for flow rates parallel to the streamer (X-direction) at 0 $\mathrm{m\,s^{-1}}$ (purple), 0.5 $\mathrm{m\,s^{-1}}$ (green), 1 $\mathrm{m\,s^{-1}}$ (orange), and 1.5 $\mathrm{m\,s^{-1}}$ (red) in the X-, Y-, and Z-direction is shown in Figures 7.3(a), (b), and (c),

respectively. The ASD of the data shown in Figures 7.3(a), (b), and (c) are displayed in Figure 7.4(a), (b), and (c).

In the time domain, as shown in Figure 7.3, it can be seen that the effect of gradually increase the flow rate is not visible in the X-displacement (Figure 7.3(a)). However, this effect is observable in the Y-displacement(Figure 7.3(b)) and Z-displacement (Figure 7.3(c)). In fact, the largest motion is observed in the Y-direction (Figure 7.3(b)) — 18 times and 1.5 times greater than the motion in the X- and Z-direction, respectively.

In the frequency domain, as shown in Figure 7.4, the following observation can be made:

- At frequencies above 3 Hz, the effect of gradually increase the water flow rate is not visible. In fact, the displacement is almost identical for different flow rates in the X-direction (Figure 7.4(a)) and Z-direction (Figure 7.4(c)). However, in the Y-direction (Figure 7.4(b)), there is a 5 dB difference between the flow being at 0 $\mathrm{m\,s^{-1}}$ to 0.5 $\mathrm{m\,s^{-1}}$. I was not to explain this difference and the other data available were not of a good quality.
- At frequencies below 3 Hz, the effect of increasing flow rates is clearly visible. The streamer motion increases as the water flow rate increases. However, most of the increase occurred as the flow rate increased from 0 to 0.5 $\mathrm{m\,s^{-1}}$. For example, at 0.1 Hz, for flow rate increasing from 0 to 0.5 $\mathrm{m\,s^{-1}}$, the increase in the Y-direction is the largest — this increase is approximately 17 dB in the X-direction, 31 dB in Y-direction, and 24 dB in the Z-direction. Above 0.5 $\mathrm{m\,s^{-1}}$, this increase is gradual but modest, in the X-direction, the streamer motion increases is 3 dB from 0.5 to 1 $\mathrm{m\,s^{-1}}$, and approximately 4 dB from 1 to 1.5 $\mathrm{m\,s^{-1}}$.

The observations made in Figures 7.3 and 7.4 suggest that the streamer is sensitive to water flow rate. However, most of the streamer motion occurs when there is no flow to 0.5 $\mathrm{m\,s^{-1}}$. Beyond 0.5 $\mathrm{m\,s^{-1}}$, the effect of flow rates on the streamer motion is small. In practice, the streamer is generally towed at about 2.05–2.5 $\mathrm{m\,s^{-1}}$, which is the minimum velocity to ensure that the streamer can be held at the same depth by depth control devices (Anderson and Mattsson, 2010). Since increasing the flow rate has a meaningful effect above 0.5 $\mathrm{m\,s^{-1}}$ and assuming that the flow pattern around a commercial streamer is laminar as observed during our experiments, this could suggest that the current velocity of the vessel in the towed streamer CSEM is likely not a limiting factor. In the next section, the effect of this streamer motion in the electric field noise is investigated thoroughly.

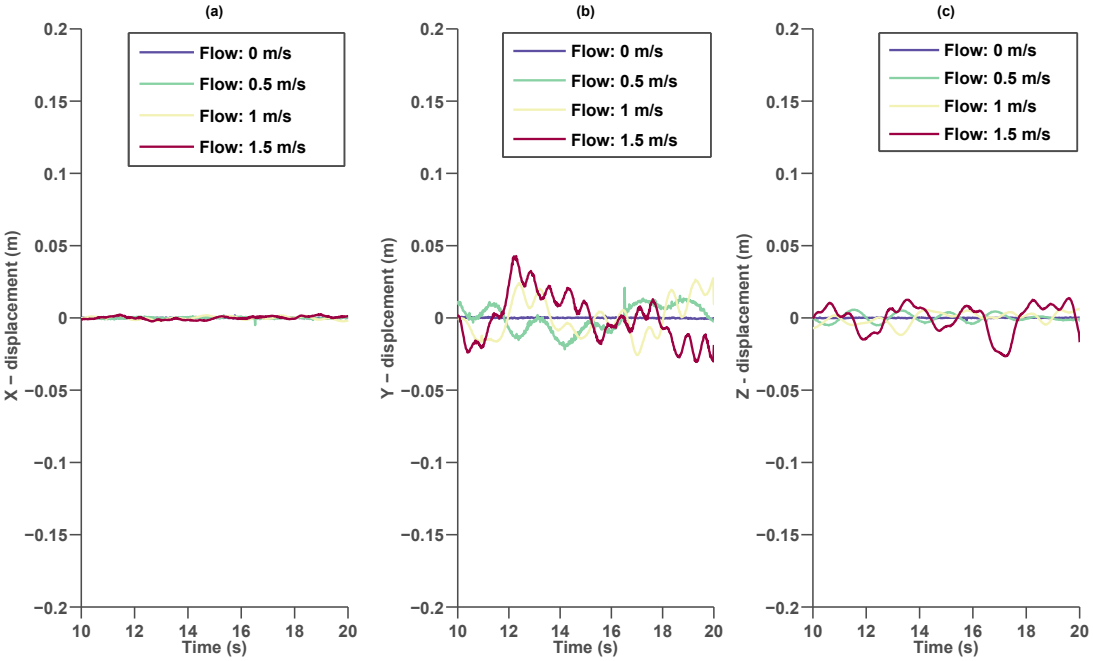

Figure 7.3: Displacement of the streamer in the X- (a), Y- (b) and Z- (c) direction for a marker in response to flow rates of 0 $\mathrm{m\,s^{-1}}$ (purple), 0.5 $\mathrm{m\,s^{-1}}$ (green), 1 $\mathrm{m\,s^{-1}}$ (orange), and 1.5 $\mathrm{m\,s^{-1}}$ (red). The data were recorded in absence of wave motion.

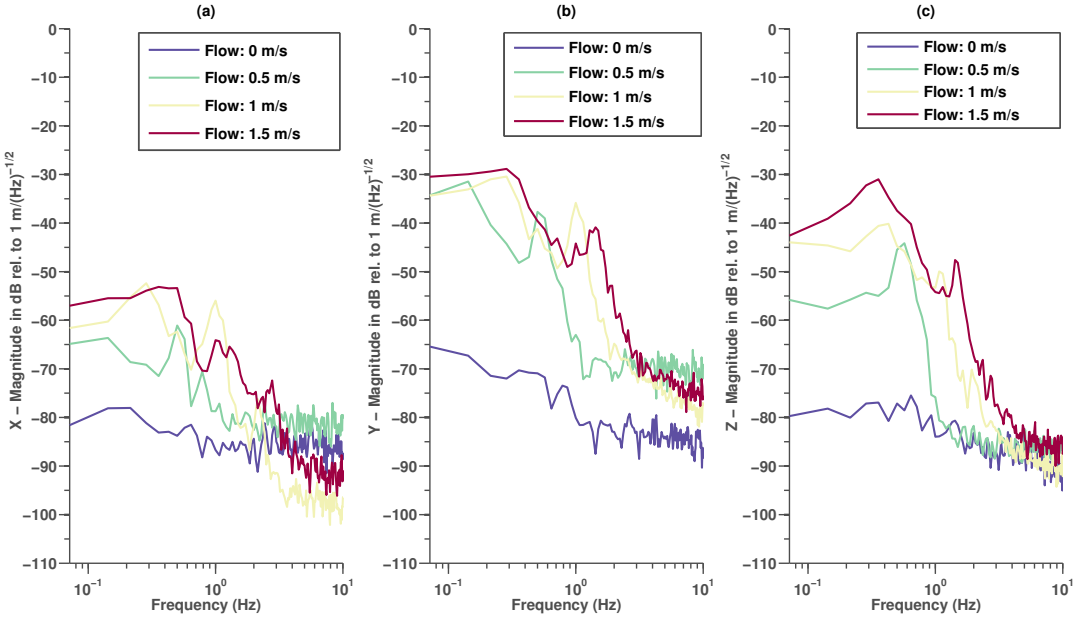

Figure 7.4: ASD of the displacement in the X- (a), Y- (b), and Z- (c) direction for data shown in Figure 7.3(a), (b), and (c), respectively.

Electric field analysis

This section focuses on electric field measurements recorded simultaneously with the streamer displacements shown Figure 7.3. The motionally-induced electric field noise due to the effect of flow rates is referred to as flow noise. Figure 7.5 was obtained by averaging RMS values of the electric field in the time domain from the 4 flow rate: 0, 0.5, 1, and 1.5 $\mathrm{m\,s^{-1}}$. Figure 7.6 was obtained by calculating the ASD of the electric field data following equation (0.8). For comparison purposes, the average RMS noise level and ASD for a flow rate of 0.5 $\mathrm{m\,s^{-1}}$ and a wave motion parallel to the streamer direction (dashed pink) is also plotted.

Analysis of the results from Figure 7.5 indicated that channels 2, 3, 7, and 10 may be faulty and were therefore excluded from my analysis. In addition, from Figure 7.5 it can be seen that the RMS electric field noise levels recorded without flow and wave motion (black bar on the graphs) vary from channel to channel. This noise corresponds to E_n in equation (3.4). Because the environmental electric noise field due to the MT signal (E_i) is the same for all channels, it is reasonable to assume that any discrepancy between channels is due to electrode noise at each channel and the motionally-induced noise (E_T).

From Figure 7.5, it can be seen that the RMS noise level increased by approximately 40% (factor of 1.6) as the flow increased from 0 to 1.5 $\mathrm{m\,s^{-1}}$. However, more than half (about 25%) of this increase occurs between there being no flow and flow of 0.5 $\mathrm{m\,s^{-1}}$. This observation is connected to the motion of the streamer as shown in Figure 7.4.

The effect of a constant laminar flow of 0.5 $\mathrm{m\,s^{-1}}$ and wave motion is shown by the brown bar in Figure 7.5. The RMS noise level increased by 180% (factor of about 3) $\mathrm{V\,m^{-1}}$ from a 0.5 $\mathrm{m\,s^{-1}}$ with no wave motion (black rectangular) to a constant flow of 0.5 $\mathrm{m\,s^{-1}}$ with wave motion (brown rectangular). Comparing the wave motion and flow noise, it is clear that wave related noise is in average more than twice than that of the flow related noise.

Analysing the ASD as shown Figure 7.6, the following observation can be made:

- Above 3 Hz, the flow and wave motion noise are relatively flat. This is likely due to white noise from the loggings electronics (Havsgård et al., 2010; Constable et al., 1998). The same observation was made in the towed CSEM streamer electric field noise in Figure 4.2 — Chapter 4 and when analysing the streamer motion due to flow motion in Figure 7.4.
- Below 3 Hz, the effect of flow and wave motion noise on the electric field is observable. The effect of increasing the flow rate is clear below 0.2 HzİIt can be

seen that the flow noise increases with flow rates. However, almost all flow noise is generated as the flow increased from 0 to 0.5 $\mathrm{m\,s^{-1}}$. The analysis made here do not match with the observation made by (Constable et al., 2015). Constable et al. (2015) claim that noise was generally lower at higher tow speeds. However, Constable et al. (2015) do not provide any data to support their argument.

Another observation we can make is that the wave motion effect is observable at the input wave frequency. At 0.29 Hz, there is a 12 dB difference between the electric field recorded when the flow is moving a parallel to the streamer at 0.5 $\mathrm{m\,s^{-1}}$ with no wave motion. This is consistent with the observation made when I analysed the average RMS noise in Figure 7.5 and the motion of the streamer as shown in Figure 7.4.

Since the flow noise increases as the water flow rate increases, this suggests, in practice, that the flow noise increases as tow velocities increase. However, because the flow noise increases only by about 0.1 $\mathrm{V\,m^{-1}}$ as the flow rate increased by 0.5 $\mathrm{m\,s^{-1}}$ could suggest that flow noise is not a limiting factor in the towed streamer CSEM. This is consistent with the streamer motion analysis showed in Figure 7.4. The 13 (factor of 4.5) dB difference between wave motion and flow noise at 0.29 Hz demonstrates that wave motion — that caused the vertical and lateral motion of the streamer — is the major limiting factor in the towed streamer CSEM. Extrapolating these results to a flow rate of 2.5 $\mathrm{m\,s^{-1}}$ at which towed streamer data are acquired and assuming that the flow pattern is laminar suggests an increase in the noise level (due to E_T, in equation (3.4)) of 45% and above the static noise level (E_n, in equation (3.4)).

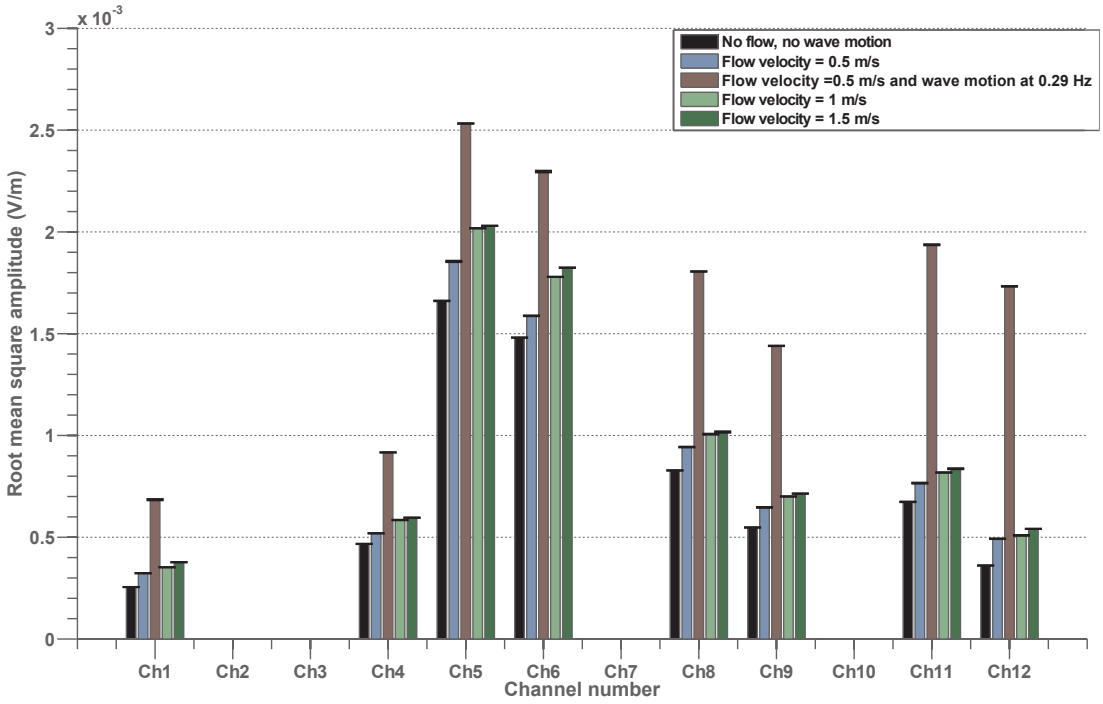

Figure 7.5: The average RMS noise level in the time domain as a function of water flow rate: 0, 0.5, 1 and 1.5 $\mathrm{m\,s^{-1}}$. The average RMS noise level for a flow rate of 0.5 $\mathrm{m\,s^{-1}}$ and a wave motion parallel to the streamer direction is shown in brown.

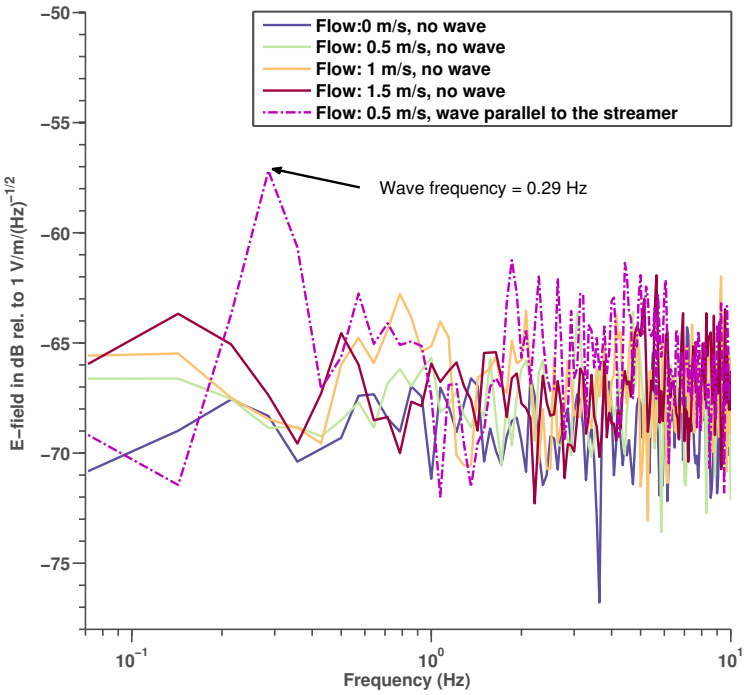

Figure 7.6: ASD of the electric field recorded for flow rates parallel to the streamer: 0 $\mathrm{m\,s^{-1}}$ (purple), 0.5 $\mathrm{m\,s^{-1}}$ (green), 1 $\mathrm{m\,s^{-1}}$ (orange), and 1.5 $\mathrm{m\,s^{-1}}$ (red). ASD for a flow rate of 0.5 $\mathrm{m\,s^{-1}}$ and a wave motion parallel to the streamer direction is shown in dashed pink.

By analysing Figure 7.4 and Figure 7.6, we can conclude that electric flow noise originates from the motion of the streamer as flow past around the streamer. Following Curtin (1970) who investigated the effect of water flow near electrode surfaces when Ag-AgCl electrodes are towed in sea, we can state that local hydrodynamic effects due to water flow near the surface of electrodes is another possible explanation for the large electric field difference generated when flow rates increase from 0 to 0.5 $\mathrm{m\,s^{-1}}$. Hydrodynamic effects result from the electrical structure interface that exists between metal electrodes immersed in electrolytes.

In Curtin (1970), the model of this interface is based on the "double layer" model developed by Helmholtz in 1871. Since then, many models of the double layer have been published in the literature. The Helmholtz double layer assumes a compact layer of ions in contact with the charge electrode surface. The next model, the Gouy and Chapman model evolved from the Helmholtz's model and suggests a model in which the ions are diffused to some distance from the solid surface. In a further development, the Stern model proposes that the electrode-electrolyte interface includes both the compact Helmholtz layer and the diffuse one of Gouy and Chapman. During our experiments, it was impossible to determine which model was in used. This is because the double layer model depends on electrode material (metals, electrode porosity, the presence of layers of either oxides or other solid materials at the surface), type of solvent, type of supporting electrolyte, the extent of specific adsorption of ions and molecules, and the temperature (Scholz, 2002). Nevertheless, the double layer consists of an inner Helmholtz plane (IHP) and an outer Helmholtz plane (OHP). The IHP is associated with solvated cation ions and the OHP is associated with absorbed ions. Figure 7.7 shows a schematic diagram of a Helmholtz double layer model.

As the water flows past the electrodes, the solvated and absorbed ions are transported and therefore, their organisations are locally disrupted at the electrode surfaces (Lauga, 2004). This established a potential difference known as the streaming potential (Lauga, 2004). This streaming potential is referred here as flow noise. To reduce the flow noise effect, Curtin (1970) carried out two experiments. In the first one, electrode surfaces were in direct contact with water flow and in the second one, the electrodes were shielded with a porous material. Curtin (1970) noted the potential difference was considerably low in the second experiment.

Moreover, the effect of wave motion is also shown in Figure 7.6 (pink dashed lines). The motionally-induced electric field due to wave motion is referred to as wave motion noise. From Figure 7.6, it can be seen that the wave motion noise is observable only at the wave frequency of 0.29 Hz. In fact, the wave motion noise is approximately 13 dB (factor of 4.5) above the flow noise level regardless of the velocity of the water.

This means that electric field noise due to wave motion is larger than the flow related noise.

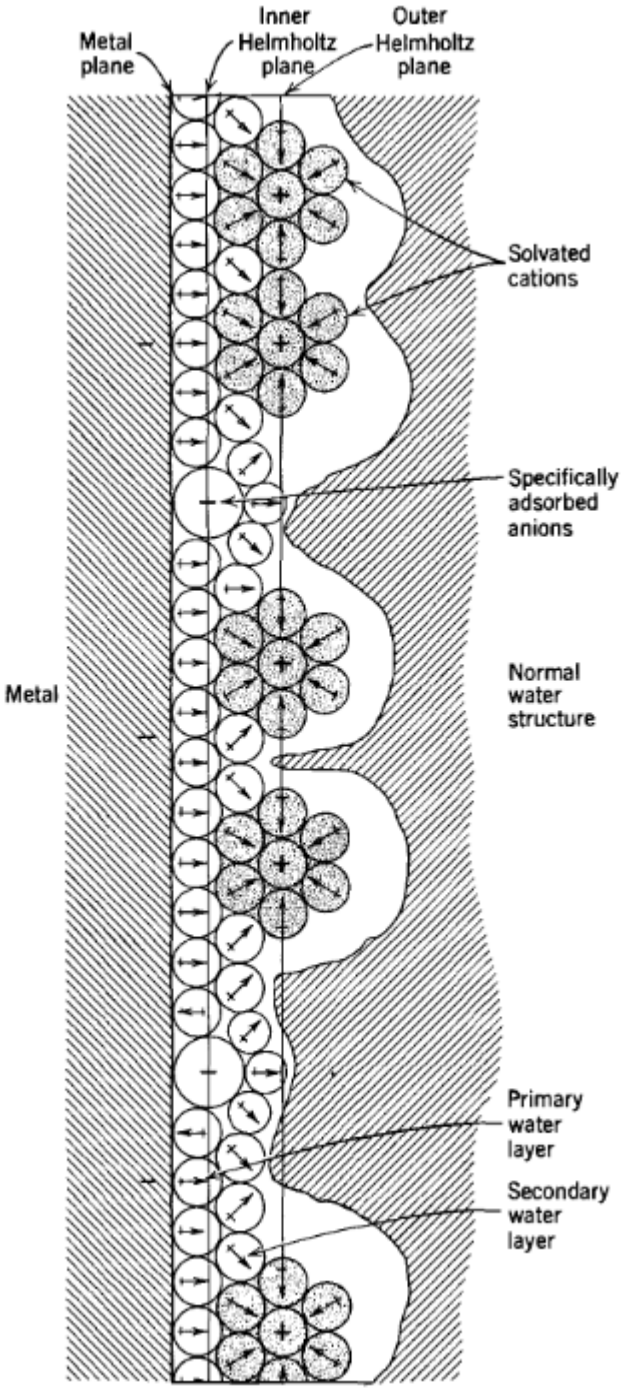

Figure 7.7: A detailed structure of the double layer model (Barlow and Macdonald, 1967). In my case, the metal is the silver-silver chloride electrode (Ag-AgCl). The electrolyte is fresh water.

7.3 The effect of wave motion - Wiring Configuration 3

In this section, I investigated the effect of wave motion on the motion of the streamer and the electric field that is measured simultaneously. Three different wave motion were analysed: waves travelling parallel, at 45°, and perpendicular relative to the streamer direction. For comparison purposes, I also plotted a constant flow rate of 0.5 $\mathrm{m\,s^{-1}}$ and no wave motion — this is similar to noise recorded with the node based CSEM system. All waves were generated at a frequency of 0.29 Hz and an amplitude of 0.1 m. Waves moved in presence of a constant flow rate of 0.5 $\mathrm{m\,s^{-1}}$ parallel to the streamer direction.

Displacement of the streamer

The displacement of the centre of the prototype streamer under the influence of the three wave motion types in the X-, Y-, and Z-direction is shown in Figure 7.8(a), (b), and (c), respectively. In each component, flow only (purple), waves propagating parallel (green), at 45°(orange), and perpendicular (red) relative to the streamer direction are displayed.

Like observed in Figure 7.3, Figure 7.8 shows that the displacement in the X-direction is negligible (± 0.005 m) compared to the displacement in the Y-direction (± 0.14 m) and Z-direction (± 0.04 m). The largest displacement is measured along the streamer's Y-direction as the wave moved perpendicular to the streamer. In the Y-direction, for example, the displacement due to a perpendicular wave motion is a factor of about 12 higher than when the wave propagates along the streamer direction and is a factor of about 2.6 higher than when the wave propagates at 45° to the streamer direction.

The ASD of the data in Figure 7.8(a), (b), and (c) are shown in Figures 7.9(a), (b), and (c), respectively. Considering Figure 7.9, the following observation can be made:

- Above 3 Hz, the amplitude of the streamer not moving is comparable to it amplitude when under the influence of wave regardless the directions. The effect of wave motion is not visible at these frequencies. The same observation was made when analysing the amplitude of the streamer's motion due to flow motion (Figure 7.4).
- Below 3 Hz, the sensitivity of the streamer to wave motion is clear. For an input wave frequency of 0.29 Hz, there is a peak in the amplitude spectrum at both the wave frequency and the second and third harmonics of 0.58 Hz and 0.87 Hz, respectively. This is indicated in Figure 7.9(b) by the arrows. Harmonics are

observed because the streamer was setting up a standing wave at these frequencies as a result of being anchored at each end. In general, the streamer motion increases as the wave motion becomes transverse relative to the streamer direction. In the Y-direction for e.g., at 0.29 Hz, the streamer motion increases by about 10 dB (factor of 3), 30 dB (factor of 32), and 40 dB (factor of 100) above the level of the static streamer as the wave moves parallel, 45°, and perpendicular to the streamer direction.

The observations made in Figures 7.8 and 7.9 are significant for the commercial towed CSEM streamer. They indicate that in practice, the streamer is highly sensitive to wave motion, particularly when the streamer motion is perpendicular to the streamer direction. The largest sensitivity of the streamer is in Y-direction regardless of the type of wave motion. Comparing these results to the one made when analysing the effect of gradually increasing the water flow rate, Figures 7.3 and 7.4, suggest that that the major source of the streamer motion is due to transverse wave motions.

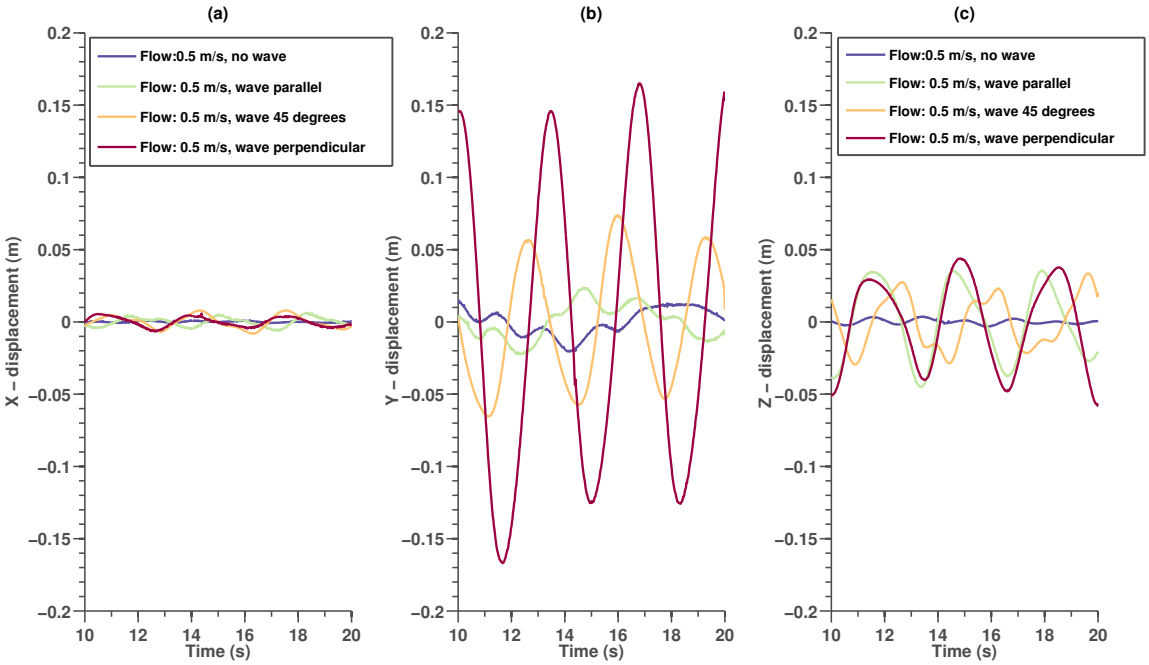

Figure 7.8: Displacement of the streamer in the X- (a), Y- (b) and Z- (c) direction in response to, a constant flow rate of 0.5 $\mathrm{m\,s^{-1}}$ parallel to the streamer (purple), a wave motion of amplitude 0.1 m travelling parallel to the streamer direction (green), at 45°to the streamer direction (orange), and perpendicular to the streamer direction (red). Wave frequency = 0.29 Hz.

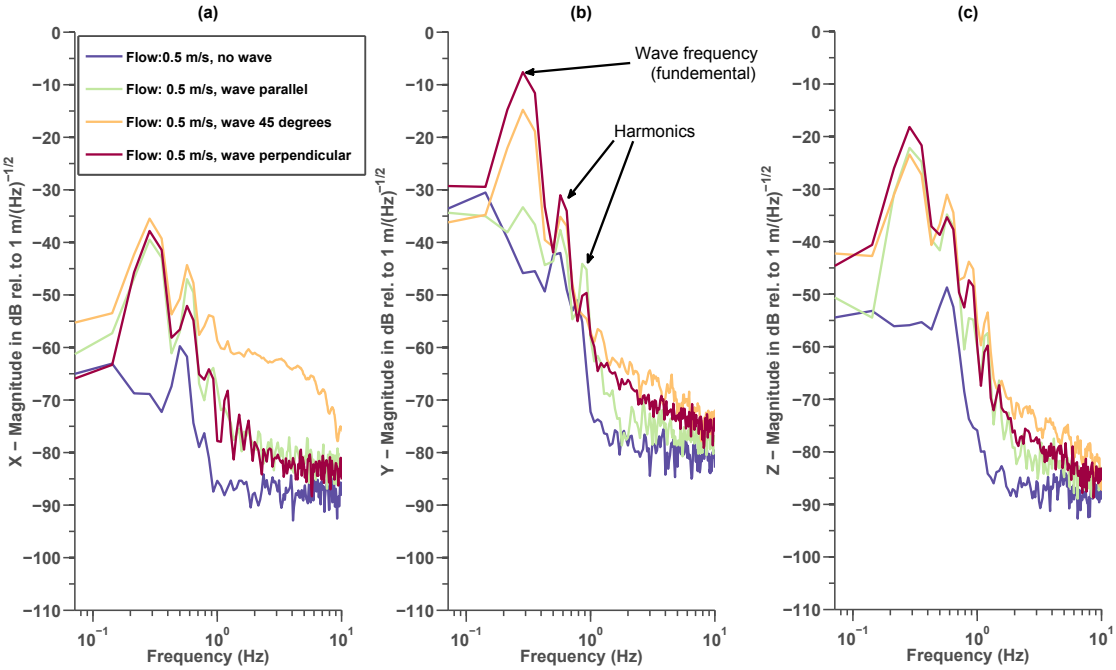

Figure 7.9: ASD of the displacement in the X- (a), Y- (b), and Z- (c) direction for data shown in Figure 7.8(a), (b), and (c), respectively.

Electric field analysis

Measurements of the electric field noise were made simultaneously as the displacement data collected Figure 7.8. From Figure 7.10, it can be seen that the RMS electric field noise levels recorded without flow and wave motion (black bar on the graphs) vary from channel to channel. This noise corresponds to E_n in Equation 3.4 as explained above in "The effect of flow" section.

The effects of waves travelling in different directions relative to the streamer are shown in Figure 7.10. The RMS noise level, due to E_T in Equation 3.4, increases on average approximately by a factor of 2.3, 2.9, and 3.1 above the static noise level (E_n, in Equation 3.4) for waves propagating parallel, at 45°, and perpendicular relative to the streamer direction, respectively. However, most of the increase occurred between the static noise level and waves parallel to the streamer.

It can be seen from Figure 7.11 that the effect of wave motion above the static noise level is noticeable only at the input frequency, that is 0.29 Hz. The wave motion noise increases by an average of 12 dB(factor of 4), 13 dB(factor of 4.5), and 15 dB (factor of 5.6) above the static noise level (E_n, in Equation 3.4) as the wave propagates parallel, 45°and perpendicular, relative to the streamer direction, respectively. This observation is consistent with the RMS analysis in Figure 7.10 and with the streamer motion analysis made in Figure 7.9.

The observations made in Figures 7.8 to 7.11 show that the wave motion electric field noise is connected to the motion of streamer. We can also conclude that the greater the transverse angle, the greater the streamer motion and the wave motion electric field noise. The relation between the wave motion and the motion of the telluric cables is investigated further in the next section: "Isolating the motionally-induced noise".

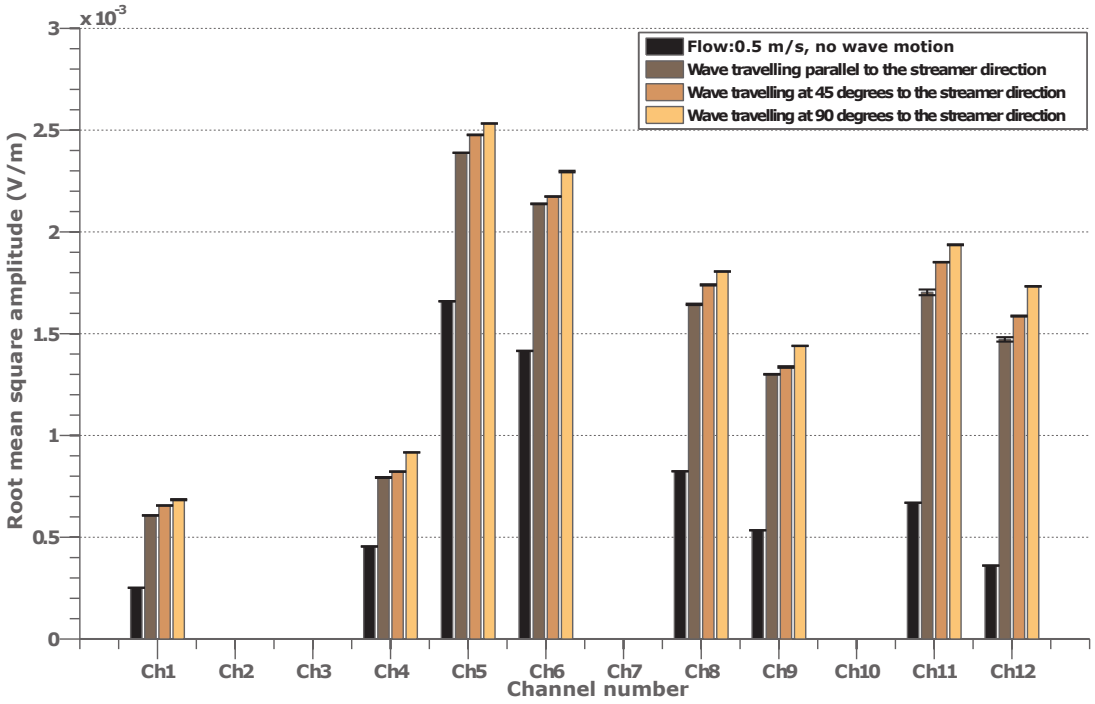

Figure 7.10: The average rms noise level in the time domain as a function of wave motion direction relative to the streamer. Electric field increases as the

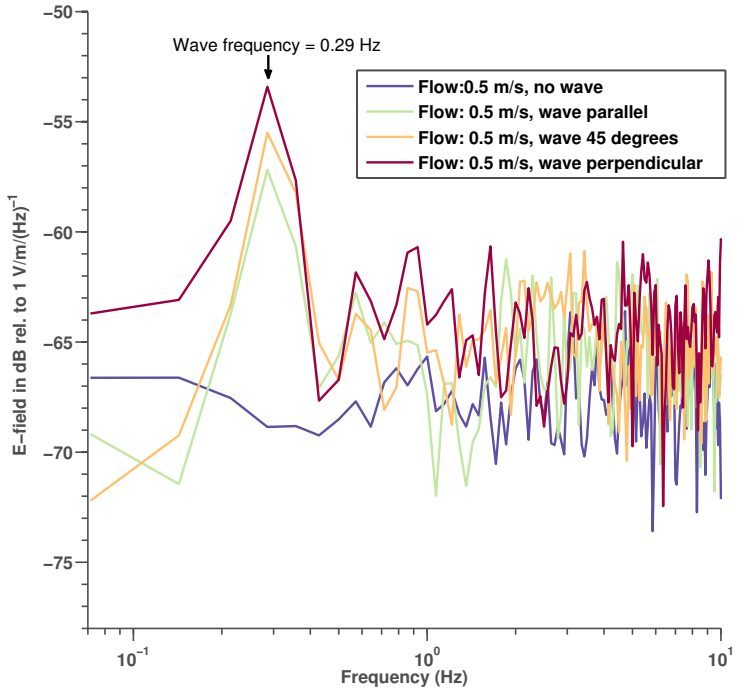

Figure 7.11: ASD of the electric field measurements in response to, a constant flow rate of 0.5 $\mathrm{m\,s^{-1}}$ parallel to the streamer (purple), a wave motion of amplitude 0.1 m travelling parallel to the streamer direction (green), at 45° to the streamer direction (orange), and perpendicular to the streamer direction (red). Wave frequency = 0.29 Hz.

The experiments carried out in the FloWave tank, to some extent, are only valid for a constant laminar flow around the streamer. In practice, this means that the streamer needs to be aligned perfectly with the mean flow and that the conditions need to remain constant for the results to be accurate. However, there are currents in the water and Elboth et al. (2010a), showed that the flow pattern around the streamer is not necessary laminar, it is mostly turbulent. During marine seismic exploration, Elboth et al. (2010a) stated that turbulent flow generation depends on the flow velocity and weather conditions. Nevertheless, the analysis of the data collected during the FloWave tank experiment provides a qualitative and quantitative picture of how the streamer and the electric field behave when under the influence of flows and waves motion.

The analysis of the effect of flow rates and wave motion indicate that flow noise is independent of the wave motion noise. The flow electric field noise is caused both by the motion of the streamer and by local hydrodynamic effects due to the disruption of ions at the electrode-electrolyte interface. The wave motion electric field noise is solely due to the motion of the prototype streamer. Moreover, in the time domain, I showed that the increase of the flow rate increases the noise level in prototype streamer. The increase of electric field due to wave motion is approximately twice that due to the increase of the flow rate relate noise. In the frequency domain, the greatest increase in noise level (15 dB (factor of 5.6) above the static noise level) is observed when the wave moves perpendicular to the streamer direction. I also showed that the component of the streamer that is most sensitive to flow rates and wave motion (regardless the direction) is the one perpendicular to the streamer direction — the Y - direction.

Next, it is reasonable to assume that the main source of high amplitude, low-frequency(0–3 Hz) electric field noise in recordings is due to transverse wave motion. At 0.29 Hz, we observed a noise peak. This noise corresponds to the input wave frequency. Following the results of our experiments, we could suggest that the prominent peak observed at 0.07 Hz, in towed CSEM electric field noise data in Figure 4.2 - Chapter 4, is due to the motion of the streamer under the influence of ocean swell. In fact, ocean swell causes the streamer to move vertically and laterally.

Based on these observations and analysis of the streamer motion and the subsequent electric field flow noise, we could suggest that under normal circumstance, the vessel velocity is not a limiting factor in the towed streamer CSEM. To reduce the effect of flow and wave motion noise, the following suggestion could be used:

- To reduce the flow noise, one way could be to use electrodes that are hydrodynamically and chemically isolated from the effect of flow passing at their surfaces by a porous material.

- To reduce the wave motion noise, limiting the lateral and vertical motion of the streamer has to be addressed. One way could be by towing the streamer deeper or increasing the streamer tension. This is an engineering problem, not a geophysics one!

7.4 Isolating the motionally-induced noise

The electric field noise data measured on the channels inside the streamer (Channel 12) was compared with the electric field measured on the fixed channels (Channel 14) outside the streamer. These data were recorded at the same time as the data shown in Figure 7.8 (orange). Figure 7.12(a) and (b) show data acquired using Channel 12 (inside the streamer, 6 m apart) and Channel 14 (fixed channel, 6 m apart), respectively. The effect of the wave motion can be seen on Channel 12 but not on Channel 14. The noise seen on Channel 12 is induced by the motion of the cable in response to the wave. The amplitude spectrum in Figure 7.12(c) clearly shows large peaks at the fundamental wave frequency (0.29 Hz) and its harmonics on Channel 12, but not on Channel 14. This is clear evidence that the motion of the streamer in the Earth's magnetic field in response to waves causes noise to be induced in the streamer.

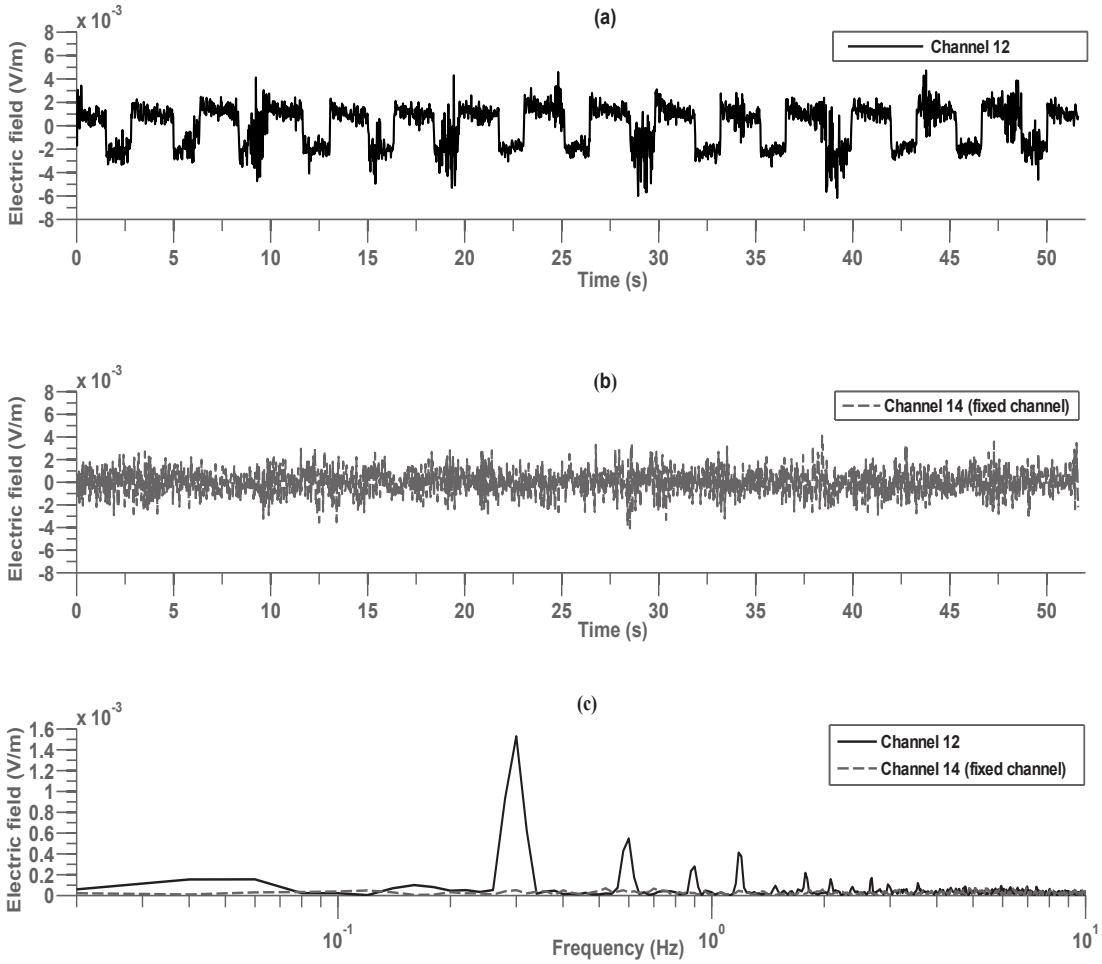

Figure 7.12: Data from Channel 12 (inside the streamer) and Channel 14 (fixed channel). (a) Electric field data recorded by Channel 12. (b) Electric field data recorded by Channel 14. (c) Amplitude spectrum data shown in (a) and (b).

Coherence analysis

Figure 7.13(a) and (b) were obtained by calculating the coherence between the electric field noise sensed by the electrodes inside the prototype streamer and the displacement of the cable at the same time. The input wave was at the frequency of 0.29 Hz (Figure 7.15(a)) and 0.45 Hz (Figure 7.15(b)).

Figure 7.13(a) and (b) show that there is a strong correlation (0.91) between channels inside the streamer and wave motion. In contrast, the correlation is very low (0.12) between the fixed channel outside the streamer and wave motion (dashed line). These results confirm that channels inside the streamer are sensitive to wave motion. Fixed electrodes with the signal cable out of the water are not sensitive to wave motion. This

clearly illustrates the effect of induction noise due to the streamer moving in the Earth's magnetic field.

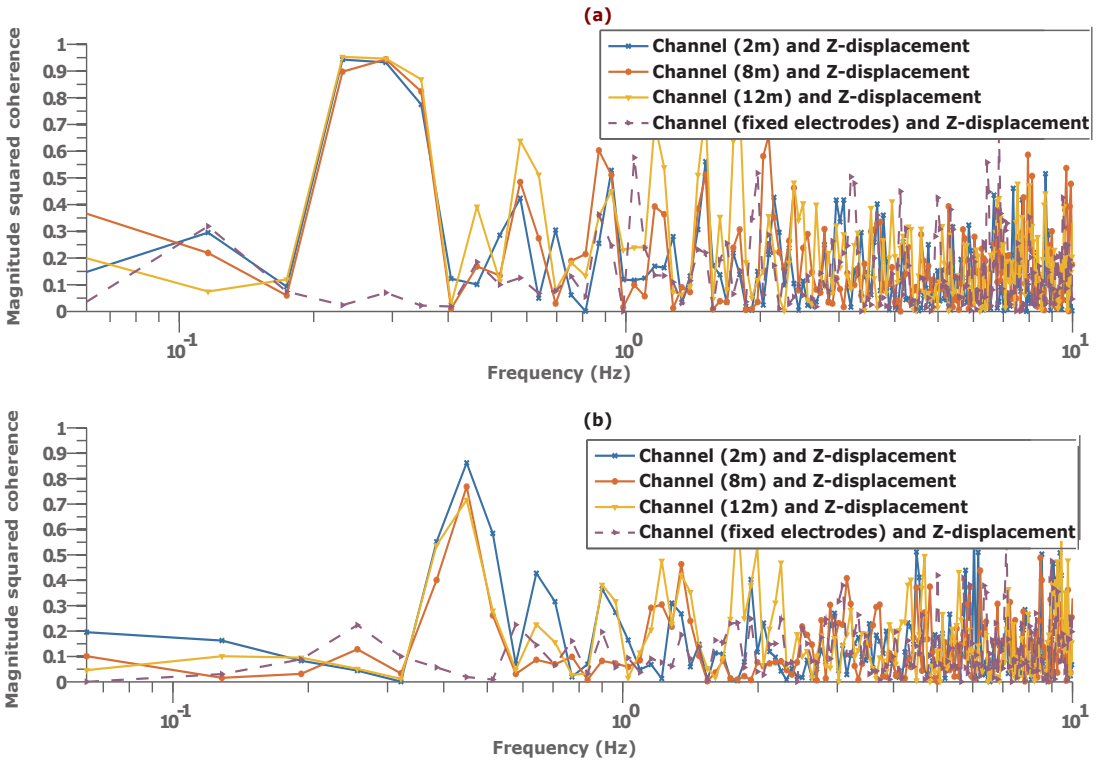

Figure 7.13: Magnitude squared coherence of electric field and Z-displacement data. (a) Wave frequency 0.29 Hz. (b) Wave frequency 0.45 Hz.

Wave motion wavelength estimation

The wavelength and the speed of the wave moving in the tank can be estimated by calculating the cross-correlation between a reference marker and other markers spread along the streamer. In this case, Marker 5C is used as the reference marker. From each cross-correlation, the maximum cross-correlation coefficient and the corresponding delay time was picked. Figure 7.14 shows the maximum cross-correlation coefficient for the 7 markers that were active during experiments in the X-(Figure 7.14(a)), Y-(Figure 7.14(b), middle), and Z-directions (Figure 7.14(c)). The circles show individual correlations. Figure 7.14 was obtained when the wave was travelling at a frequency of 0.29 Hz and at 45° to the streamer direction. The largest streamer motion was observed in the Y-direction. Therefore, to estimate the wave wavelength, Figure 7.14(b) is used. Estimating the wave motion speed is very important as it contributes to the estimation of the motionally-induced electric field noise.

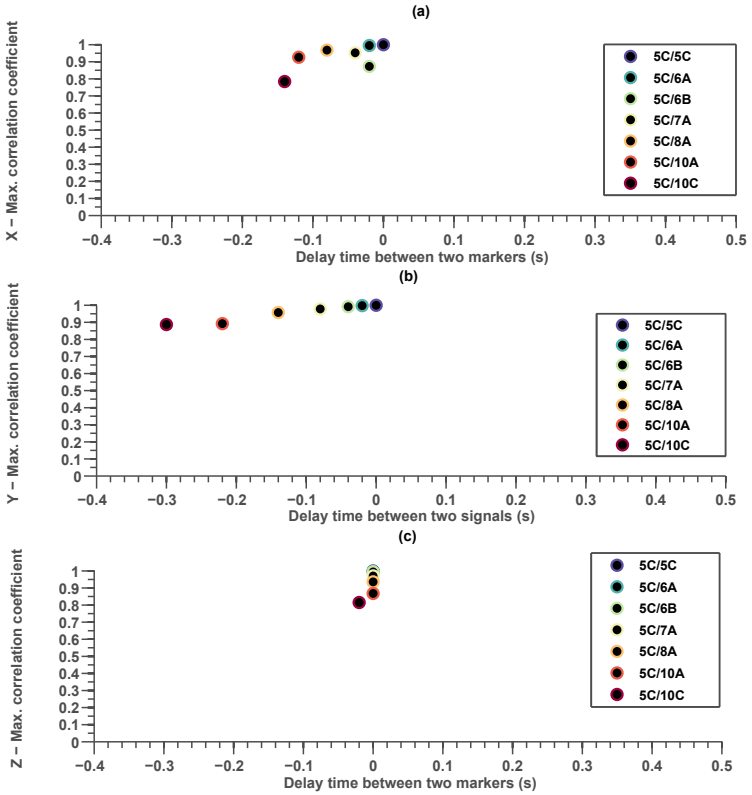

Figure 7.14: Maximum cross-correlation coefficient against time delay between marker 5C (reference) and the other markers - for e.g. 5C/10C means cross-correlation between marker 5C and 10C. The distance between Marker 5C and 10C is 1.5 m.

The wave velocity can be estimated as:

$$v_{wave} = \frac{D_{5C-10C}}{T_{delay}}\,, \tag{7.1}$$

where, D_{5C-10C} is the distance between Marker 5C and 10C which is 1.5 m from Figure 6.15. The delay time between Marker 5C and 10C is denoted by T_{delay} and is equal to 0.3 s from Figure 7.14(b). Using these values in equation (7.1), I obtain $v_{wave} = 5\ \mathrm{m\,s^{-1}}$. The wave wavelength is estimated following the relation:

$$\lambda = \frac{v_{delay}}{f}\,, \tag{7.2}$$

where f is the wave frequency. In this case, $f = 0.29$ Hz. Replacing the value of f in equation (7.2), the wavelength of the wave in the tank is about 17 m.

Estimation of the motionally-induced electric field noise

Mathematical expression

The motionally-induced voltage between a pair of electrodes in the streamer is given by the integral along the streamer length as shown in Equation 5.17.

$$\mathcal{V} = \int_{l_a}^{l_b} (\mathbf{v} \times \mathbf{B}) \cdot d\mathbf{l}, \qquad [\mathrm{V}]$$

where

$$d\mathbf{l} = \mathbf{a_x} dl_x + \mathbf{a_y} dl_y + \mathbf{a_z} dl_z \,, \tag{7.3}$$

$$\mathbf{B} = \mathbf{a_x} B_x + \mathbf{a_y} B_y + \mathbf{a_z} B_z \,, \tag{7.4}$$

$$\mathbf{v} = \mathbf{a_x} v_x + \mathbf{a_y} v_y + \mathbf{a_z} v_z \,, \tag{7.5}$$

where $\mathbf{a_x}$, $\mathbf{a_y}$, and $\mathbf{a_z}$ are based vectors in the X-, Y-, and Z-directions, respectively. B_x and B_y are the horizontal components of the magnetic field, B_z is the upwards component of the magnetic field. v_x is the streamer velocity parallel to the streamer (in the X-direction), v_y is the streamer velocity perpendicular to the streamer (in the Y-direction), and v_z is the vertical streamer velocity (in the Z-direction). Equations (7.3) to (7.5) into equation (5.17) lead to

$$\begin{aligned} \mathcal{V} &= \int_{l_a}^{l_b} \begin{vmatrix} \mathbf{a_x} & \mathbf{a_y} & \mathbf{a_z} \\ v_x & v_y & v_z \\ B_x & B_y & B_z \end{vmatrix} \cdot d\mathbf{l}, \\ &= \int_{l_a}^{l_b} (v_y B_z - v_z B_y) dl_x + (v_z B_x - v_x B_z) dl_y + (v_x B_y - v_y B_x) dl_z \,. \end{aligned} \tag{7.6}$$

In our experiment, the streamer was placed along the X-axis and in the north-south direction as shown in Figure 6.13. Therefore, equation (7.3) becomes

$$d\mathbf{l} = \mathbf{a_x} dl_x \,, \tag{7.7}$$

Equation (7.7) into equation (7.6) gives

$$\mathcal{V} = \int_{l_a}^{l_b} (v_y B_z - v_z B_y) dl_x \,. \tag{7.8}$$

The streamer has 7 active markers that recorded its displacement in the X-, Y- and Z- directions. Hence, I divided the interval length $[l_a \; l_b]$ into $n = 7$ subdivisions. That

is:

$$l_a = l_1 < l_2 < ... < l_n = l_b \tag{7.9}$$

The velocity is a function of position along the streamer and time. It is determined from the displacement data. It is estimated by the difference between the current and the previous displacement, divided by the time between successive samples, Δt:

$$v_i = \frac{l_i - l_{i-1}}{\Delta t}, \tag{7.10}$$

The magnetic field components are assumed constant for the duration of the data acquisition. Therefore, using the trapezoid rule (defined in equation (0.29)) to approximate the integral in equation (7.8), it follows that the predicted motionally-induced voltage due to the motion of the streamer is expressed, in volts as:

$$\mathcal{V} \approx \frac{1}{2}\sum_{i=1}^{n}\left[(v_{y_{i+1}}(l_{i+1})B_z - v_{z_{i+1}}(l_{i+1})B_y) + (v_{y_i}(l_i)B_z - v_{z_i}(l_i)B_y)\right](l_{i+1} - l_i) \tag{7.11}$$

where $l_{i+1} - l_i$ is the spacing between each consecutive pair points.

Results

Using equation (7.11) and the displacement data obtained when the wave was travelling at 45° to the streamer direction (Figure 7.8 (orange)), an estimation of the motionally-induced noise for the cable was computed. As shown in Figure 7.14, this wave had a wavelength of about 17 m, and was travelling at a velocity of 5 $\mathrm{m\,s^{-1}}$. This motionally-induced noise was compared to the electric field sensed simultaneously at the electrodes as the streamer was moving within the Earth's magnetic field.

Figure 7.15(a) displays the electric field noise in the time domain sensed by Channel 4 (red), Channel 5 (green), and the motionally-induced noise estimated from equation (7.11). Figure 7.15(b) shows the amplitude spectrum obtained from Figure 7.15(a). The measured electric field noise of Channel 14 (fixed channel) is also shown in black. On Figure 7.15(c), two coherence analyses are plotted: the coherence between Channel 11 and the estimated motionally-induced noise (blue), and the coherence between Channel 12 and the estimated motionally-induced noise (orange).

From Figure 7.15(a), the estimated motionally-induced noise is very well correlated with the measured electric field noise. This observation is confirmed in Figure 7.15(c),

where the correlation coefficient between the estimated motionally-induced field and the measured electric field noise is about 1 $\mathrm{Vm(Hz)}^{-1/2}$ at the input frequency of the wave (0.29 Hz). Even though the estimated motionally-induced and the electric field noise are correlated, Figure 7.15(b) shows that the measured electric field noise is higher than the estimated motionally-induced field noise by a factor of 2.7. The same results were obtained in most of the runs. This observed discrepancy in amplitude is likely to be explained by one of the two possible reasons. First, an additional noise between the electrodes and the amplifier. This could result in the addition of a specific amount of noise to the analogue potential voltage sensed at each channel.

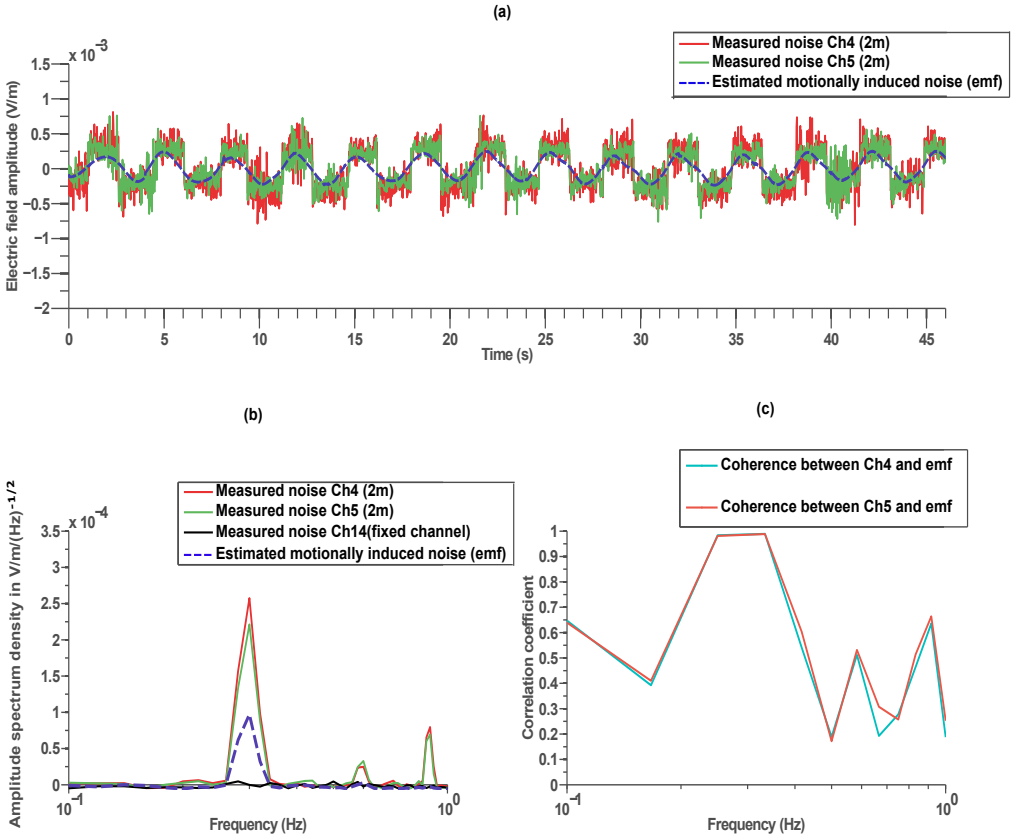

Figure 7.15: Measured electric field noise by Channel 4 (red) and Channel 5 (green), and the estimated motionally-induced field (dashed brown) due to a wave motion of frequency 0.29 Hz with wavelength equal to about 17 m travelling at 45° to the streamer direction. (a) Time domain analysis. (b) ASD of data plotted in (a). (c) Coherence analysis.

7.5 Correlation distance - Wiring Configuration 2

To estimate the distance at which the noise becomes uncorrelated, I used Wiring Configuration 2. In this configuration, all the channels extend from the same central electrode

(Channel 13), and overlap one another. The overlap distance between Channel 13 and the other channels is displayed in Table 7.1.

Channel number	Overlap length (m)
Channel 13 - Channel 12	8
Channel 13 - Channel 11	8
Channel 13 - Channel 10	6
Channel 13 - Channel 9	6
Channel 13 - Channel 8	4
Channel 13 - Channel 7	4
Channel 13 - Channel 6	2
Channel 13 - Channel 5	2
Channel 13 - Channel 4	1
Channel 13 - Channel 3	0.5
Channel 13 - Channel 2	0.25
Channel 13 - Channel 1	0

Table 7.1: Overlapping length between Channel 13 and the other channels.

Figure 7.16(a) was produced by cross-correlating the electric field noise recorded by Channel 13 with the other channels for two cases: when the water was flowing at a constant rate of 0.5 $\mathrm{m\,s^{-1}}$ without a wave motion (red circle) and with the wave travelling at a frequency of 0.29 Hz parallel to the streamer direction (green stars). From each cross-correlation, the coefficient found at zero lag was picked. The curves were then produced by using a cubic spline through the correlation coefficient values to show the spatial correlation length of flow only (red curve) and flow and wave motion (green curve) noise. The horizontal axis represents the overlap length highlighted in Table 7.1, and the vertical axis denotes the correlation coefficient. Figure 7.16(b) shows the Pearson residual which is calculated by dividing the residual by its standard deviation as expressed in equation (4.14). It is produced to evaluate how well the cubic spline function fit the data.

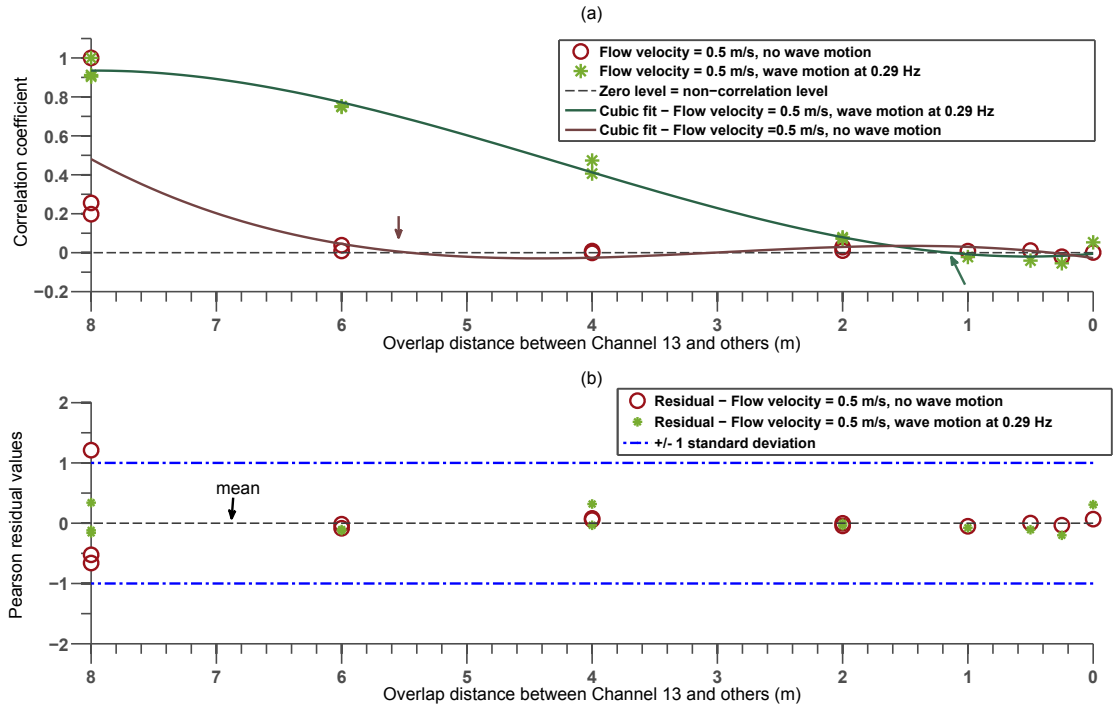

Figure 7.16: Spatial correlation distance of electric field noise recorded along the streamer. (a) For flow velocity at 0.5 $\mathrm{m\,s^{-1}}$ (red circle) and when the flow velocity is 0.5 $\mathrm{m\,s^{-1}}$ and wave motion at 0.29 Hz (green stars). The horizontal dashed black line indicates the boundary below which the noise becomes uncorrelated. (b) Residual plot from (a).

From Figure 7.16(a), it can be seen that in general, the correlation length decreases as the overlap length decreases. Figure 7.16(a) shows also that when the water is flowing at a constant velocity of 0.5 $\mathrm{m\,s^{-1}}$, the flow noise is correlated out to about 5.5 $\pm$ 0.2 m (red arrow) overlap length. When the flow is at the same velocity but with wave moving at 0.29 Hz parallel to the streamer direction, the correlation is shortened to about 1 $\pm$ 0.2 m (green arrow) overlap length. This difference in correlation length is explained therefore by the presence of low-frequency, high amplitude wave motion.

Figure 7.16(b) shows that the residual appears to behave randomly and hover around 0 (dashed line). Most of the data (apart from 1 point) are within $\pm$ 1 standard deviation (blue dash-dot lines) from the mean. This suggests that the cubic spline fits the data well.

The result of this analysis demonstrates that channels sharing the same central electrode and having 1mor less overlap length could be used to record uncorrelated motionally-induced noise regardless the state of the water. This could be investigated in future experiments.

7.6 Single channel or multiple small channels - Wiring Configuration 1

In this section, I investigate the idea that the SNR of the towed CSEM could be improved by using multiple channels of total length "L" instead of a single channel of the same length. Wiring configuration 1 is used to investigate this idea thoroughly. For the purpose of this work, the noise level of a single channel, namely Channel 1 (16 m) is compared with a group of non-overlapping channels identified as:

- Group 1: Ch2 (8 m) + Ch3 (8 m),
- Group 2: Ch4 (4 m) + Ch5 (4 m) + Ch6 (4 m) + Ch7 (4 m), and
- Group 3: Ch8 (2 m) + Ch9 (2 m) + Ch10 (2 m) + Ch11 (2 m) + Ch12 (2 m) + Ch13 (2 m) + Ch14 (2 m) + Ch15 (2 m) .

Figure 7.17 was obtained by calculating the RMS from noise recorded by each channel as the water was flowing at a velocity of 0.5 $\mathrm{m\,s^{-1}}$. A similar RMS trend was obtained with other water flow velocity. The dashed black line represents the RMS noise level of the single channel. From Figure 7.17, one can observe that Channel 1 is a factor of 1.3, 1.4, and 2 smaller than the RMS noise level recorded by Group 1, Group 2, and Group 3, respectively. This increase in RMS level as the number of channel increases within a group of channel is associated with the increase of electrode noise because of additional electrodes.

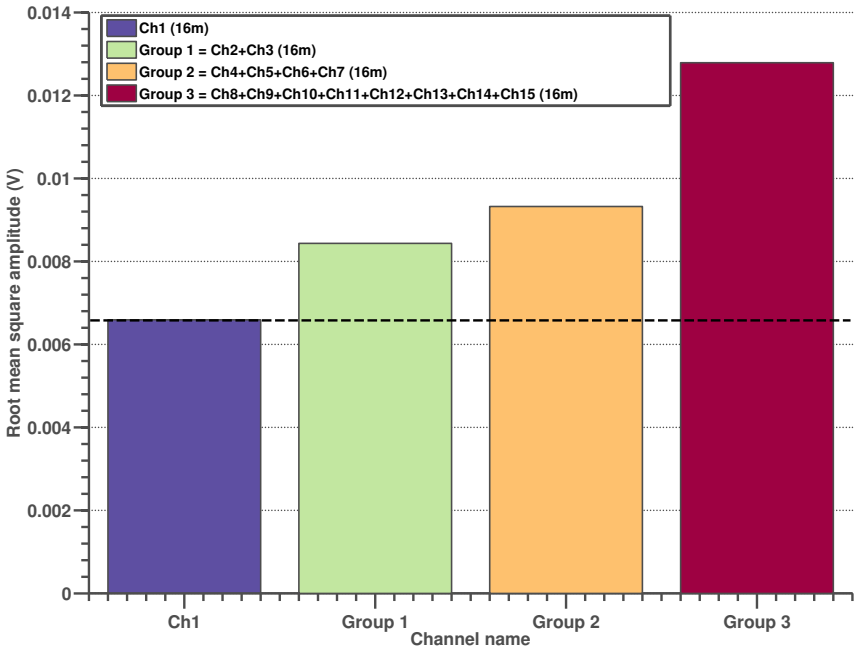

Figure 7.17: Root mean square amplitude of a single channel (Ch1 (16 m)) compared with 2 channels per 8 m group (Group 1), 4 channels per 4 m group (Group 2), and 8 channels per 2 m group (Group 3).

Placing the channels more densely in the streamer as expressed in equation (6.1), could improve the SNR only if the electrode noise issue is addressed. The need to keep the Ag-AgCl electrodes in contact with water is one of the Ag-AgCl drawbacks because of the electrochemical reaction at the surface of the electrode that generates additional noise as shown in Figure 7.17. In addition, small variations of the temperature, salinity of water lead to an increase in the electrode measurement noise at frequencies below 1 Hz (Havsgård et al., 2010; Hibbs and Nielsen, 2008; Corwin, 1973). To overcome this additional noise at the Ag-AgCl electrode, one solution could be to use capacitive electrodes because they offer a way to measure electric potential without contact with the medium and without electrochemical reactions(Constable et al., 2012). This was explained in Section 3.3, Page 62 . Therefore, the use of multiple short channel length instead of a single long channel length to improve the SNR of the towed system could be possible if the capacitive electrodes are used as sensing devices instead of the Ag-AgCl electrodes .

7.7 Implications for towed streamer CSEM

The experiment allows me to isolate and quantify the effects of flow rates relative to waves motion on the streamer. It allows also me to discriminate and quantify the contribution of flow noise compared to wave motion noise measured simultaneously with the streamer displacements. The results show how the electric field is affected by streamer motion are and are applicable to any motion of the cable, not just wave motion. Moreover, the same mechanism applies to long streamers.

The results of this experiment demonstrate that the flow noise is sizable from no flow to 0.5 $\mathrm{m\,s^{-1}}$, and precautions must be taken to reduce it. For this reason, commercial electrodes are shielded by a porous plastic that minimises the flow passing at the electrode surfaces whilst still allowing the electrode to function normally (Constable, 2013; Havsgård et al., 2010). From the result of the data collected in the FloWave tank, it is clear that the largest noise in the towed streamer CSEM originates from the lateral rotary motion of the telluric cable in the Earth's magnetic field. In fact, the variation of the velocity of the lateral motion of the telluric cable in the Earth's magnetic field causes an additional voltage to appear at the electrodes according to Faraday's law of induction, as illustrated in Figure 7.18. This theory was developed in Chapter 5.

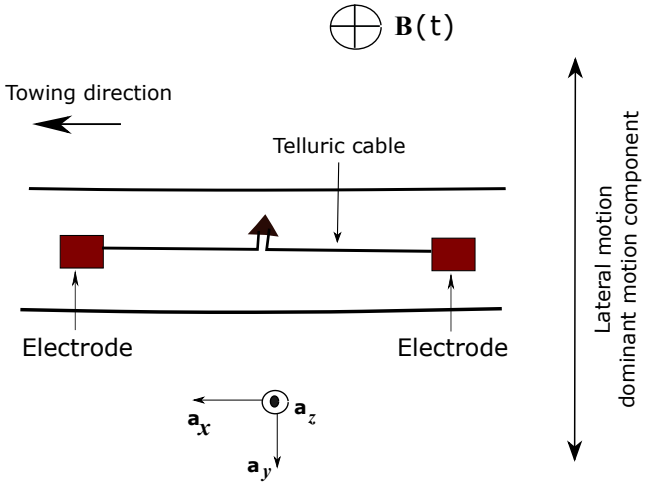

Figure 7.18: Illustration of the lateral motion of the telluric cable in the Earth's magnetic field $\mathbf{B(t)}$. The streamer is shown moving in the X-direction. Regardless of the wave motion direction relative to the streamer direction, the greatest motion is observed on the lateral component.

In the absence of any method for prediction and subtraction, the noise can only be reduced by not being recorded in the first place. This means that motionally-induced noise can be reduced by limiting the lateral motion of the cable while towing. This

motion depends on the mechanical properties of the cable, its tension, and the forces acting at its surface. The wave motion noise can therefore be reduced by the following approach:

1. Use of rigid telluric cables. This could reduce the displacement of the cables when the streamer is hit by an ocean current or swell.
2. Increase the streamer and the telluric cable tension. Increasing the tension acts as a damping force that reduces the motion of the streamer compared to water motion.
3. Tow the streamer deeper to avoid the influence of ocean swell.
4. The channel overlap distance could be about 1 m or less for the noise to be uncorrelated. This overlap distance is extremely small compared to the 300 m overlap distance between channels shown in Figure 4.1 and Table 4.3, and is unfeasible with current technology

Any combination of items 1–4 will reduce the noise and any relative improvement in 1–3 will as well. In item 4 however, unless the distances can be reduced to $\sim$ 1 m no gain will be seen from reducing to more than that.

Summary

I have looked at electromagnetic induction in a prototype streamer. The streamer was found to be sensitive to flow rates and to wave motion from any direction. The streamer experienced its largest displacement in the Y-direction when the wave was propagating perpendicular to it.

I observed that two separate phenomena were responsible for the motionally-induced electric field noise: the flow rates and the waves motion. First, the motionally-induced electric field noise due to flow rate (flow noise) is found to increase with flow velocity. Significant flow noise is generated from no flow to 0.5 $\mathrm{m\,s^{-1}}$, and increases modestly above 0.5 $\mathrm{m\,s^{-1}}$. This is caused by local hydrodynamic effects due to water flowing over the electrode surfaces. Second, the motionally-induced electric field noise (wave motion noise) is observable only at the wave frequency and increased with transverse waves motion — with the largest wave motion noise measured when the wave was perpendicular to the streamer. I showed that the wave noise was due to the motion of the telluric cable as a result of wave motion. Telluric cables inside the streamer are sensitive to wave motion, while fixed electrodes with telluric cables out of the water are insensitive to wave motion. This observation provides clear evidence that the wave noise is due to the motion of the telluric cable in the Earth's magnetic field.

In addition, I showed that the flow noise is a factor of 2 smaller than wave motion noise even for a small 16 m long streamer in the time domain. In the frequency domain, the flow noise is 12 dB (factor of 4) smaller than the wave motion noise at 0.29 Hz (input wave frequency).

I also found that the measured electric field noise was higher than the estimated motionally-induced noise by a factor of 3. The difference could be attributed to the additional noise between the electrodes in the cable and the amplifier.

I showed that the correlation length decreases with the overlap regardless of water state. However, channels with an overlap distance of about 1 m record uncorrelated noise when the wave is propagating at 0.29 Hz. I conclude that this is an "optimal" overlap distance. Finally, I showed that using multiple non-overlapping silver-silver chloride (Ag-AgCl) channels instead of a single channel increases the overall noise level.

The use of rigid telluric cables, short channels and capacitive electrodes could improve the overall signal-to-noise ratio of the marine towed streamer CSEM. This could also be improved by increasing the streamer tension at the head and at the tail, or by towing the streamer deeper. I summarised these findings and provide a list with ways to mitigate flow noise and wave motion noise recordings.

■

8

Conclusions

I have noticed that even people who claim everything is predetermined and that we can do nothing to change it, look before they cross the road.

Stephen Hawking(1942–)
Physicist

8.1 Findings

To deliver risk mitigation in the pursuit of oil and gas discovery, a towed controlled source electromagnetic (CSEM) system is faster and cheaper to operate than the conventional autonomous node based CSEM system, but it is noisier within the frequency range of interest: 0.01–1 Hz. Many sources of noise contribute to this increase in noise level including magnetotelluric (MT) noise, electrode noise, and motionally-induced electric field noise (a combination of flow noise and swell noise). At the beginning of this thesis, it was challenging to identify the contribution of each of these sources of noise. Several publications in marine CSEM suggested that the major source of noise in towed streamer CSEM is due to the motionally-induced electric field noise. However, none of these publications provided the mechanisms that generate this noise or quantify it in comparison to other noise sources. The work presented herein addressed these two last points in three ways.

In the first part of this thesis, I analysed and compared noise data collected using towed CSEM and a static CSEM ocean bottom cable (OBC) system. I showed that the towing noise is about 20 dB (factor of 10) above the level of the OBC noise in the frequency range of interest. I showed that this discrepancy is caused by the motion of the telluric cable within the Earth's magnetic field. However, I was unable to discriminate or to quantify the contribution of flow noise and swell noise (which was addressed in the final section). In the first part, I also showed that within the frequency ranges 0.03–0.1 Hz and 0.3–2 Hz, the motionally-induced electric field noise is uncorrelated across all channels, but highly correlated (0.9) at about 0.2 Hz. I suggested that the uncorrelated nature of noise is likely due to the pressure fluctuations within the turbulent boundary layer surrounding the streamer that causes the telluric cable to move with a different wavelength from one point to another. I suggested also that the correlated nature of the noise observed at about 0.2 Hz is likely due to ocean swell that causes the telluric cable to move with the same wavelength.

Stacking by averaging a set of data could be one way to improve the signal-to-noise ratio (SNR) of the system. However, stacking is optimal when noise components from channel to channel are uncorrelated. If the noise is correlated, stacking will have limited to no effect. That is why it is important to identify the mechanism that generated the correlated noise present at about 0.2 Hz. Understanding the cause of the correlated noise will help develop methods to reduce the noise, or prevent it from being recorded in the first place.

The second part of this thesis addresses the parameters that cause the motionally-induced electric field noise. I derived a quantitative theory of the motionally-induced

noise for the case of a horizontal, and a curved streamer moving in a constant and time-varying magnetic field. I showed that no motionally-induced electric field noise is generated when the streamer is horizontal and moving in a constant magnetic field. When the streamer is curved, I used a mathematical model of its shape which was obtained by taking into account the forces acting on the surface of the streamer. I then derived the expression of the motionally-induced electric field noise analytically using the aforementioned model. This expression showed that the motionally-induced electric field noise depends on the feather angle at the head and tail of the streamer and on the vertical and the lateral motion of the streamer change caused by the cross-currents. The variation over time of one of these parameters generates a motionally-induced voltage across the channels.

In the final part of this thesis, in an attempt to identify and quantify the various sources of noise in the towed CSEM data, a prototype streamer was built and used in the FloWave tank to reproduce the flow noise and the wave motion noise that affect the towed CSEM system, and to test various wiring configurations that could help to reduce the motionally-induced noise. The effect of water flow around the streamer was tested by gradually increasing flow rates parallel to the streamer from 0 $\mathrm{m\,s^{-1}}$ to 0.5 $\mathrm{m\,s^{-1}}$, 1 $\mathrm{m\,s^{-1}}$, and 1.5 $\mathrm{m\,s^{-1}}$. The effect of wave motion was also investigated by propagating wave frequencies of 0.29 Hz parallel, at 45°, and perpendicular to the streamer direction. From the data collected during the FloWave tank experiment, I was able to discriminate, quantify, and describe the mechanisms that generate flow noise and swell noise. Below are highlighted the six main findings that were made after processing the FloWave tank experiment data:

1) I showed that the streamer motion increases as flow rates increase from 0 $\mathrm{m\,s^{-1}}$ to 1.5 $\mathrm{m\,s^{-1}}$. Most of this increase occurred as flow increases from 0 $\mathrm{m\,s^{-1}}$ to 0.5 $\mathrm{m\,s^{-1}}$. The largest motion was observed in the Y-direction — 18 times and 1.5 times greater that the motion in X- and Z-direction, respectively. I also demonstrated that the flow noise increases with flow rates from 0 $\mathrm{m\,s^{-1}}$ to 1.5 $\mathrm{m\,s^{-1}}$. Most of the increase in flow noise also occurred between 0 $\mathrm{m\,s^{-1}}$ and 0.5 $\mathrm{m\,s^{-1}}$. There was a modest increase in noise above 0.5 $\mathrm{m\,s^{-1}}$. The large increase in noise from no flow to due to 0.5 $\mathrm{m\,s^{-1}}$, was due to local hydrodynamic effects caused by flow over the electrode surfaces.

2) I showed that wave motion noise was, on average, 2 times higher than flow rate related noise in the time domain. In the frequency domain, the wave motion noise was about 3.5 times greater than the flow noise at the wave frequency of 0.29 Hz. Above 0.29 Hz, the flow noise and wave motion noise have a flat spectrum and were on average similar in amplitude.

3) I showed that the streamer was highly sensitive to wave motion, regardless of the wave motion direction. The greatest displacement was observed when the wave was travelling perpendicular to the streamer direction and was measured along the Y-direction. I also showed that the electric field noise increases with the transverse wave motion. In fact, for a wave parallel to the streamer, the electric field noise was typically 12 dB (factor of 4) above the static noise at the wave frequency of 0.29 Hz. The electric field noise was about 13 dB (factor of 4.5) and about 15 dB (factor of 5.7) above the static noise level as the wave moved at 45 degrees and perpendicular to the streamer, respectively. This noise was due to the lateral motion of the telluric cable in the Earth's magnetic field.

4) When a wave of frequency 0.29 Hz and about 17 m in wavelength was travelling at 45° to the streamer direction, the estimated motionally-induced field noise deduced from the displacement of the streamer was shown to be highly correlated (0.9) with the measured electric field noise. However, this estimated motionally-induced electric field noise was, in general, a third smaller compared to the measured electric field noise. This discrepancy was likely caused by the additional noise in the telluric cable between the electrodes and the amplifier.

5) I used Wiring Configuration 2, in which one central electrode is common to each channel, to estimate the overlap correlation length of the flow and wave motion noise when the wave was moving at 0.29 Hz, parallel to the streamer direction. The overlap correlation length varied strongly from 8 m to about 1.2 m. The channels that had an overlap length of 1 m or less, recorded only uncorrelated noise. Given the 8 m maximum channel separation, this is the optimal overlap distance.

6) I used Wiring Configuration 1, to compare the noise level recorded by a single channel with the noise recorded by multiple small non-overlapping channels with the total length equal to the single channel length. I showed that placing small channels more densely in the streamer generated noise that was up to 2 times greater than the noise generated by a single long channel. The noise increases because of the additional noise originating from the electrochemical reactions at the surface of the silver-silver chloride (Ag-AgCl) electrodes with the water. I proposed that one solution to reduce the noise caused by the Ag-AgCl electrodes is to use capacitive electrodes.

8.2 Future research

As a result of the towed CSEM noise analysis, the derived quantitative expression of the motionally-induced noise, and the processing of the data collected during the FloWave tank experiment, the following research could be carried out in the future.

- During the FloWave tank experiment, I observed that the water pattern surrounding the streamer was laminar. In the future, it will be interesting to carry out the same test but by generating turbulent flow around the streamer as this more is likely to happen in offshore conditions.
- In Chapter 7, I showed in Figure 7.16 that in the presence of a constant flow velocity and wave motion propagating parallel to the streamer direction, the "optimal" overlap distance between channels for the noise to be uncorrelated noise is 1 m or less. Testing this configuration in the towed CSEM streamer could lead to the reduction of the effect of ocean swell, and therefore improve the overall SNR of the system.
- The electric field is calculated by dividing the potential voltage by the effective length of the channel. As a consequence, short channel length, ideally 1 m long, might help to eliminate the dependency of the electric field on the channel length. This implies that the channels will be placed more densely within the streamer than in the wiring configuration shown in Figure 4.1 of Chapter 4. However, as shown in Figure 7.17 of Chapter 7, the use of small Ag-AgCl channel lengths instead of a single one is disadvantageous because of the additional noise due to the addition of electrodes. An alternative to overcome the electrode noise could be to use capacitive electrodes to measure potential voltage.

References

Anderson, C., and J. Mattsson, 2010, An integrated approach to marine electromagnetic surveying using a towed streamer and source: First Break, **28**, 71–75. 34, 68, 160

Andrés, D., and L. MacGregor, 2007, Time domain versus frequency domain csem in shallow water: Presented at the SEG Technical Program Expanded Abstracts. 56

Barker, N., J. Morten, and D. Shantsev, 2012, Optimizing EM data acquisition for continental shelf exploration: The Leading Edge, **31**, 1276 – 1284. 33, 56, 60, 61, 68, 69

Barlow, C. A., and J. R. Macdonald, 1967, Theory of discreteness of charge effects in the electrolyte compact double layer: Advances in electrochemistry and electroc hemical engineering, **6**, 1–199. 15, 166

Bhatt, K. M., 2014, Microseisms and its impact on the marine-controlled source electromagnetic signal: Journal of Geophysical Research: Solid Earth, **119**, 8655–8666. 66

Brady, J., T. Campbell, A. Fenwick, M. Ganz, M. P. P. Buonora, L. F. Rodrigues, S. K. Sandberg, C. Campbell, L. Combee, A. Ferster, K. E. Umbach, T. Labruzzo, and A. Zerilli, 2009, Electromagnetic Sounding for Hydrocarbons: Oilfield Review Spring, **21**, 4–19. 62

Brigham, E. O., 1974, The Fast Fourier Transform: Prentice-Hall. 21, 22

Burger, B., and P. Toiviainen, 2013, MoCap Toolbox - A Matlab tootool for computational analysis of movement data: Presented at the Proceedings of the Sound and Music Computing Conference. 155

Burrows, M. L., 1972, On the design of a towed ELF H-field Antenna: Technical report, Lincoln Laboratory. 35, 89, 91, 105, 106

———, 1974, Motion-Induced Noise in Electrode-Pair Extremely Low Frequency (ELF) Receiving Antennas: IEEE Transactions on Communications, **22**, 540–542. 105, 106

Chave, A. D., S. C. Constable, and R. N. Edwards, 1991, Electrical exploration methods for the seafloor, *in* Electromagnetic methods in applied geophysics: Nabighian, 931 – 969. 59

Chave, A. D., and A. G. Jones, 2012, The Magnetotelluric Method: Theory and Practice: Cambridge University Press. 82

Chen, C., and L.-M. Liu, 1993, Joint Estimation of Model Parameters and Outlier Effects in Time Series: Journal of the American Statistical Association, **88**, 284 – 297. 92, 93

Cheng, D. K., 1989, Field and wave electromagnetics: Addinson-Wesly. 111

Connell, D., and K. Key, 2012, A numerical comparison of time and frequency-domain marine electromagnetic methods for hydrocarbon exploration in shallow water: Geophysical Prospecting, **61**, 187–199. 56, 60, 62, 70, 86, 99

Constable, S. C., 2010, Ten years of marine CSEM for hydrocarbon exploration: Geophysics, **75**, 75A67–75A81. 32, 44, 56, 58, 61, 69, 70

———, 2013, Review paper: Instrumentation for marine magnetotelluric and controlled source electromagnetic sounding: Geophysical Prospecting, **61 (suppl. 1)**, 505 – 532. 33, 35, 62, 63, 65, 70, 71, 105, 130, 184

Constable, S. C., and C. Cox, 1996, Marine controlled source electromagnetic sounding. Part 2: the PEGASUS experiment: Journal Geophysics Research, **101**, 5519 – 5530. 56, 70, 72

Constable, S. C., P. Kannberg, K. Callaway, and D. Ramirez, 2012, Mapping shallow geological structure with towed marine CSEM rreceiver: Presented at the SEG Annual Meeting. 34, 183

Constable, S. C., P. K. Kannberg, and K.

Weitemeyer, 2015, Vulcan: A deep-towed CSEM receiver: Geochemistry, Geophysics, Geosystems, **17**, 1042–1064. 163

Constable, S. C., A. S. Orange, G. M. Hoversten, and H. F. Morrison, 1998, Marine magnetotellurics for petroleum exploration; Part I, a sea-floor equipment system: Geophysics, **63**, 816–825. 35, 59, 63, 64, 162

Constable, S. C., and L. Srnka, 2007, An introduction to marine controlled source electromagnetic methods for hydrocarbon exploration: Geophysics, **72**, WA3–WA12. 32, 56, 58, 69

Constable, S. C., and C. J. Weiss, 2006, Mapping thin resistors and hydrocarbons with marine EM methods: Insights from 1D modeling: Geophysics, **71**, G43–G51. 63

Corwin, R., 1973, Offshore Application of Self-potential Prospecting: PhD thesis, University of California, Berkeley. 62, 63, 129, 183

Cox, C. S., N. Kroll, P. Pistek, and K. Watson, 1978, Electromagnetic fluctuations induced by wind waves on the deep-sea floor: Journal of Geophysical Research: Oceans, **83**, 431–442. 63

Cox, S. C., 1981, On the electrical conductivity of the oceanic lithosphere: Physics of the Earth and Planetary Interiors, **25**, 196–201. 32

Crona, L., T. Fristedt, P. Lundberg, and P. Sigray, 2001, Field Tests of a New Type of Graphite-Fiber Electrode for Measuring Motionally Induced Voltages: Journal of Atmospheric and Oceanic Technology, **18**, 92–99. 63

Curtin, T. B., 1970, Towed Electrodes in the Sea: Theory and Use: Master's thesis, Oregon State University. 165

Darnet, M., P. V. D. Sman, F. Hindriks, A. Sandrin, P. Christian, L. Jensen, and A. Uldall, 2010, The Controlled Source Electro-Magnetic (CSEM) method in shallow water: a calibration survey: SEG Annual Meeting, 701–705. 56

de la Kethulle de Ryhove, S., and F. Maaø, 2008, On the Removal of MT Signals from SBL Data: Presented at the 70th EAGE Conference and Exhibition. 64

Djanni, A. T., A. Ziolkowski, and D. Wright, 2014, Estimation of IInduction Noise in a Towed EM Streamer: Presented at the EAGE. 7, 109

———, 2015, Analysis of flow and wave motion in an electromagnetic streamer at the FloWave tank: Presented at the Marine Electromagnetic Conference (Marelec). 7

———, 2016, Electromagnetic induction in a towed electromagnetic streamer: Geophysics, **81**, 1–13. 7, 154

Dobrin, M. B., and C. H. Savit, 1988, Introduction to geophysical prospecting, fourth ed.: McGraw-Hill International Editions. 84

Dunn, P. K., and G. K. Smyth, 1996, Randomized Quantile Residuals: J. Comput. Graph. Statist., **5**, 236–244. 92

Eidesmo, T., S. Ellingsrud, L. M. MacGregor, S. C. Constable, M. C. Sinha, S. Johansen, F. N. Kong, and H. Westerdahl, 2002, Sea Bed Logging (SBL), a new method for remote and direct identification of hydrocarbon filled layers in deepwater areas: First break, **20**, 144 – 152. 32, 68

Elboth, T., D. Lilja, B. A. P. Reif, and O. Andreassen, 2010a, Investigation of flow and flow noise around a seismic streamer cable: Geophysics, **75**, Q1–Q9. 84, 106, 107, 148, 152, 172

Elboth, T., B. A. Reif, and Ø. Andreassen, 2009, Flow and swell noise in marine seismic data: Geophysics, **74**, Q17–Q25. 77, 159

Elboth, T., I. Vik Presterud, and D. Hermansen, 2010b, Time-frequency seismic data de-noising: Geophysical Prospecting, **58**, 441–453. 106

Ellingsrud, S., T. Eidesmo, S. Johansen, M. Sinha, L. MacGregor, and S. Constable, 2002, Remote sensing of hydrocarbon layers by seabed logging (SBL): Results from a cruise offshore Angola: The leading Edge, **21**, 972–982. 32, 56

Engelmark, F., J. Mattsson, and J. Linfoot, 2012, Efficient marine CSEM with a towed acqusition system: Presented at the 21 EM induction Workshop. 35

Engelmark, F., J. Mattsson, A. McKay, and Z. Du, 2014, Towed streamer em comes of age: First Break, **32**, 75–78. 34, 36

Evans, R., S. Constable, M. C. Sinha, C. S. Cox, and M. J. Unsworth, 1991, Upper crustal resistivity structure of the East Pacific Rise near 13 degree N on the East Pacific: Geophysical Research Letters, **18**, 1917–1920. 56

Filloux, J. H., 1973, Techniques and instrumentation for study of natural electromagnetic induction at sea: Physics of Earth and

Planetary Interior, **7**, 323–338. 110
———, 1980, Observation of very low frequency electromagnetic signals in the ocean: Journal of Geomagnetic Geoelectric, **32**, SI1–SI12. 63
Frigo, M., and S. G. Johnson, 1998, FFTW: An Adaptive Software Architecture for the FFT: Proceedings of the International Conference on Acoustics, Speech, and Signal Processing, 1381–1384. 22
Furey, D. A., 2005, The turbulent boundary layer on small diameter flexible cylinder on the wake of a streamlined towing apparatus: PhD thesis, University of Maryland. 106
Gamble, T. D., W. M. Goubau, and J. Clarke, 1979, Magnetotellurics with a remote magnetic reference: Geophysics, **44**, 53–68. 64
Havsgård, G. B., H. R. Jensen, A. Kurrasch, H. Jones, P. Austin, and A. Thompson, 2010, Low Noise Ag/AgCl Electric Field Sensor System for Marine CSEM and MT Applications: Technical report, Electromagnetic Geoservices ASA and Ultra Electronics PMES. 162, 183, 184
Hayes, M. H., 1996, Statical Digital Processing and Modeling: John Wiley & Sons. 22
Hibbs, A., and T. K. Nielsen, 2008, Compact Underwater Electromagnetic Measurement System: US Patent 2008/0246485 A1 (Application). 63, 183
Hoversten, G. M., F. Cassassuce, E. Gasperikova, G. A. Newman, Y. R. J. Chen, Z. Hou, and D. Vasco, 2006, Direct reservoir parameter estimation using joint inversion of marine seismic AVA and CSEM data. geophysics: Geophysics, **71**, C1–C13. 63
Hoversten, G. M., S. C. Constable, and H. F. Morrison, 2000, Marine magnetotellurics for base-of-salt mapping: Gulf of Mexico field test at the Gemini structure: Geophysics, **65**, 1476 – 1488. 63, 66
Ingram, D., R. Wallace, A. Robinson, and I. Bryden, 2014, The design and commissioning of the first, circular, combined current and wave test basin: Presented at the Flow -3D. 143
Ives, D. J. G., and G. J. Janz, 1961, Reference electrodes, theory and practice: Academic Press. 62
Kay, S. M., and S. L. Marple, 1981, Spectrum Analysis - A Modern Perpective: Proceedings of the IEEE, **69**, 1380–1419. 22
Kedar, S., M. Longuet-Higgins, F. Webb, N. Graham, R. Clayton, and C. Jones, 2008, The origin of deep ocean microseisms in the North Atlantic Ocean: Proceedings of the Royal Society, **464**, 777–793. 62, 66
Keith, W. L., K. M. Cipolla, D. R. Hart, and D. A. Furey, 2005, Drag measurements on long thin cylinders at small angles and high Reynolds numbers: Experiments in Fluids, **38**, 759–769. 106
Keller, G. V., 1989, Rock and Mineral Properties, *in* Misac N. Nabighian (ed.), Electromagnetic methods in applied geophysics - Theory: Society of Exploration Geophysicists, **Volume 1**, 13–51. 41
Key, K., 2003, Application of Broadband Marine Magnetotelluric Exploration to a 3D Salt Structure and a Fast-Spreading Ridge: PhD thesis, University of California, San Diego. 59
Krail, P. M., and H. Brysk, 1989, The shape of a marine streamer in a cross current: Geophysics, **54**, 302–308. 117, 119, 120, 123
Lauga, E., 2004, Apparent Slip Due to the Motion of Suspended Particules in FFlow of Electrolyte Solutions: Langmuir, **20**, 8924–8930. 165
Longuet-Higgins, M. S., 1950, A theory of the origin of microseisms: Philosophical Transactions of the Royal Society of London. Series A, Mathematical and Physical Sciences, **243**, 1–35. 66
Longuet-Higgins, M. S., M. E. Stern, and H. Stommel, 1954, The electrical field induced by ocean currents and waves, with applications to the method of towed electrodes: Massachusetts Institute of Technology and Woods Hole Oceanographic Institution, **13**. 115
Lu, X., and L. Srnka, 2009, Logarithmic spectrum transmitter waveform for controlled-source electromagnetic surveying: US Patent 7539279 B2 (Grant); Grant. 72
MacGregor, L., 1997, Electromagnetic investigation North Reykjanes Ridge near 58 North: PhD thesis, The University of Cambridge. 72
MacGregor, L., M. Sinha, and S. Constable, 2001, Electrical resistivity structure of the Valu Fa Ridge, Lau Basin, from marine controlled-source electromagnetic sounding: Geophysical Journal International, **146**, 217–236. 56, 58

MacGregor, L., and J. Tomlinson, 2014, Marine controlled-source electromagnetic methods in the hydrocarbon industry: A tutorial on method and practic: Interpretation, **2**, SH13–SH32. 32, 33

Madden, T., and W. Thompson, 1965, Low-frequency electromagnetic oscillations of the Earth-Ionosphere cavity: Reviews of Geophysysics, **3**, 211–254. 80

Martin, J., A. ?????zbek, L. Combee, N. Lunde, S. Bittleston, and E. Kragh, 2000, Acquisition of marine point receiver seismic data with a towed streamer.: Presented at the SEG 2000 Expanded Abstracts. 117

Matsushita, S., and W. H. Campbell, 1967, Physics of geomagnetic phenomena: Academic Press. 80

Mattsson, J., F. Engelmark, and C. Anderson, 2013, Towed streamer EM: the challenges of sensitivity and anisotropy: First Break, **31**, 155–159. 33, 34, 35, 55, 58

Mattsson, J., P. Lindqvist, R. Juhasz, and E. Bjornemo, 2012, Noise reduction and error analysis for a towed EM system: SEG Technical Program Expanded Abstracts, 1–5. 69, 76

McKay, A., J. Mattsson, and Z. Du, 2015, Towed Streamer EM ????? reliable recovery of sub-surface resistivity: First break, **33**, 75 – 85. 36

Miche, M., 1944, Mouvement ondulatoire de la mer en profondeur constante ou decroissante: Ann, Ponts Chaussees, **114**, –. 66

Milsom, J., and A. Eriksen, 2011, Field Geophysics, fourth edition ed.: John Wiley and Sons Ltd. The Geological Field Guide Series. 82

Mittet, R., and J. P. Morten, 2012, Detection and imaging sensitivity of the marine CSEM method: Geophysics, **77**, E411–E425. 35, 52, 56, 58, 60, 63, 65, 66, 67, 70, 99

Mittet, R., and T. Shaug-Pettersen, 2008, Shaping optimal transmitter waveforms for marine CSEM surveys: Geophysics, **73**, F97–F104. 72

Myer, D., S. Constable, and K. Key, 2011, Broad-band waveforms and robust processing for marine CSEM surveys: Geophysical Journal International, **184**, 689 – 698. 72

Nickolaendro, A., and M. Hayakawa, 2013, Schumann Resonance for Tyros: Springer. 80

Nielsen, T., G. Guy, and A. Hibbs, 2009, The Next Generation of Electromagnetic Offshore Ressource Exploration Technology: Sensors Online. 33, 63

Pinet, P. R., 2003, Invitation to oceanography, third ed.: Jones and Bartlett Learning. 66

Ronaess, M., and P. Lindqvist, 2010, Method and apparatus for reducing induction noise in measurements made with a towed electromagnetic survey system: US Patent 7671598 B2 (Grant). 119

Rutten, K., M. Valeton, and T. van Grunsven, 1972, Measurement of the signal to noise ratio in seismic profiling: Marine Geophysical Researches, **1**, 445–450. 68

Ryan, T., 1997, Modern regression methods: Wiley. 93

Sasaki, Y., and M. A. Meju, 2009, Useful characteristics of shallow and deep marine CSEM responses inferred from 3D finite-differencchallenges: Geophysics, **74**, F67–F76. 56

Scholz, F., 2002, The electrical double layer and its structure, *in* ElectroAnalystical Methods: Guide to Experiments and Applications: Springer, 3–8. 165

Shantsev, D., F. Roth, and H. Ramsfjell, 2012, Surface towing versus deep towing in marine CSEM: Presented at the SEG Technical Program Expanded Abstracts. 56, 61

Shantsev, D., F. Roth, C. Twarz, A. Frisvoll, and A. K. Nguyen, 2010, Shallow water CSEM using a surface-towed source: EAGE Technical Program Expanded Abstracts, C018. 67

Shantsev, D., L. Uri, E. Bjørdal, and M. Hansen, 2013, Marine csem in rough bathymetry: Presented at the SEG Technical Program Expanded Abstracts. 56

Simpson, F., and K. Bahr, 2005, Practical Magnetotellurics: Cambridge University Press. 64

Spies, B. R., 1989, Depth of investigation in electromagnetic sounding methods: Geophysics, **54**, 872–888. 36

Srnka, L., 1986, Method and apparatus for offshore electromagnetic sounding utilizing wavelewave effect to determine optimum source and detector positions: US Patent 4617518 A (Grant). 32

Stoica, P., and R. Moses, 2005, Spectral Analysis of Signals: Prentice Hall. 79

Summerfield, P. J., L. S. Gale, X. Lu, T. C.

Phillips, R. Quintanilla, E. A. Eriksen, A. K. Rutledge, and K. D. Solon, 2005, Marine csem acquisition challenges: SEG Technical Program Expanded Abstracts, 538–541. 35, 65, 66

Tcheheumeni, A. L., A. Ziolkowski, and D. Wright, 2013, Noise investigation of a towed marine active source EM system: Presented at the British Geophysical Association - Postgraduate Research in Progress Meeting. 7, 75

Tenghamn, S. R. L., R. J. M. Mattson, P. G. Krylstedt, M. F. Karlsson, U. P. Lindqvist, and P. A. Davidsson, 2007, Low noise, towed electromagnetic system for subsurface exploration: U.S. Patent US7737698 B2 (Grant). 35

Vander-Hyde, D., I. Fiori, and F. Paoletti, 2011, Testing the magnetic fields produced from twisted wires: Technical report, California State University. 128

Vozoff, K., 1991, The magnetotelluric method, *in* M.N. Nabighian (ed.), Electromagnetic Methods in Applied Geophysics: Society of Exploration Geophysicists, **Volume 2**, 641–711. 64

Wang, Z., M. Deng, K. Chen, M. Wang, Q. Zhang, and D. Zeng, 2014, Development and evaluation of an ultra-low noise sensor for marine electric field measurements: Sensors and Actuators, A: Physical, **213**, 70–78. 129, 130

Ward, S. H., and G. W. Hohmann, 1989, Electromagnetic Theory for Geophysical Applications, *in* M.N. Nabighian (ed.), Electromagnetic Methods in Applied Geophysics: Theory: Society of Exploration Geophysicists, **Volume 1**, 131–311. 41, 51

Webb, S. C., S. C. Constable, C. S. Cox, and T. K. Deaton, 1985, A sea-floor electric field instrument: Geomagnetism and Geoelectricity, **37**, 1115 – 1129. 60, 62, 70

Weiss, C. J., 2007, The fallacy of the shallow-water problem in marine CSEM exploration: Geophysics, **72**, A93–A97. 56

Weitemeyer, K., and S. Constable, 2010, Mapping shallow geology and gas hydrate with marine CSEM surveys: First Break, **28**, 97–102. 56, 61

Welch, P. D., 1967, The use of fast Fourier transform for the estimation of power spectra: A method based on time averaging over short: IEEE Transactions Audio Electroacoustics, **15**, 70–73. 80

Wright, D., A. Ziolkowski, and T. Djanni, 2015, Wave tank testing of noise induced in a towed EM streamer: Presented at the SEG Technical Program Expanded Abstract. 7

———, 2016, The Effect of Flow and Wave Motion on a Prototype EM Streamer: Presented at the EAGE. 7

Young, P., and C. S. Cox, 1981, Electromagnetic active source sounding near the East Pacific Rise: Geophysical Research Letters, **8**, 1043–1046. 32, 56

Zhang, Y., 2011, Electromagnetic Induction E-Sensor for Underwater UXO Detection: Technical report, QUASAR Federal Systems, Inc. 63

Zhdanov, M. S., 2009, Geophysical electromagnetic theory and methods: Elsevier. 40, 42

Ziolkowski, A., R. Parr, D. Wright, V. Nockles, C. Limond, E. Morris, and J. Linfoot, 2010, Multi-transient electromagnetic repeatability experiment over the North Sea Harding field: Geophysical Prospecting, **58**, 1159–1176. 33, 61, 64, 68, 86, 87

Ziolkowski, A., and D. Wright, 2010, Signal-to-Noise Ratio of CSEM data in Shallow Water: SEG Technical Program Expanded Abstract, 685 – 689. 56

———, 2012, The potential of the Controlled Source Electromagnetic Method: a powerful tool for hydrocarbon exploration, appraisal, and reservoir characterization: IEEE Signal Processing, **29**, 36–52. 35, 61, 64

Ziolkowski, A., D. Wright, and J. Mattsson, 2011, Comparison of pseudo-random binary sequence and square-wave transient controlled-source electromagnetic data over the Peon gas discovery, Norway: Geophysical Prospecting, **59**, 1114–1131. 56, 72